EPFL

Thèse n° 7814

Electrons leave the flatland: out-of-plane charge dynamics in layered materials

Présentée le 25 septembre 2020

à la Faculté des sciences de base
Laboratoire de physique de la matière complexe
Programme doctoral en physique

pour l'obtention du grade de Docteur ès Sciences

par

Edoardo MARTINO

Acceptée sur proposition du jury

Prof. C. Hébert, présidente du jury
Prof. L. Forró, Prof. A. Akrap, directeurs de thèse
Prof. M. Orlita, rapporteur
Prof. I. Grigorieva, rapporteuse
Prof. M. Banerjee, rapporteuse

École polytechnique fédérale de Lausanne

2020

Acknowledgements

The results and achievements presented in this thesis have been possible thanks to the fantastic support and contribution of many people. Here I would like to acknowledge them and their invaluable help.

First, I want to express my sincere and deep gratitude to my thesis director, Prof. László Forró for giving me the opportunity to conduct my research activity in his group, providing me with the great support to pursue all my experiments and collaborations. I really appreciated his continuous encouragement and the nice and positive convivial atmosphere that he promoted in the group (the LPMC family).

A very special thank goes to my thesis co-director, Prof. Ana Akrap. Her great experience, passion and patience helped me a lot to improve my understanding of physics and to explore the fascinating universe of user facilities such as synchrotron and high-magnetic field laboratories. I am very grateful for all the kind support to improve the quality of my articles and the precious corrections for this thesis.

My most profound gratitude goes to Prof. Philip Moll, for his incredible support in instructing me to the use the Focused Ion Beam and for showing me his model of great leadership and continues search for excellence. Without his assistance the high quality results presented here would have probably not been possible.

To guide me over my academic path I had the luck to meet diverse mentors, which guided me with their enthusiasm and advices: Dr. Andrea Pisoni, Dr. Edoardo Baldini, Prof. Neven Barisic and my “spiritual” mentor Prof. Davor Pavuna.

I am very thankful to Dr. Arnaud Magrez, Helmuth Berger and Philippe Bugnon for all the high-quality single crystals that they always provided me, without which there will be no experiments.

During my PhD I had the great opportunity to work with diverse teams at international user facilities or in the frame of collaborations:

- Synchrotron Soleil of beamline SMIS: Dr. Francesco Capitani, Dr. Ferenc Borodics, Dr. Christophe Sandt, Anna Celeste
- LNCMI Grenoble and Toulouse: Prof. Milan Orlita, Dr. Iris Crassee, Dr. David leBoeuf, Dr. Cyril Proust.
- ESRF Swiss-Norwegian beamline: Dr. Dmitry Chernyshov, Dr. Alla Arakcheeva.
- Brookhaven National Laboratory: Dr. Christopher Homes, Dr. Fernando Camino, Dr. Genda Gu,
- Max Plank Institute for chemical physics of solids: Prof. Andrew Mackenzie, Dr. Markus König, Dr. Maja Bachmann, Prof. Kimberly Modic, Dr. Toni Helm, Dr. Kent Shirer, Dr. Veronika Sunko.
- Humbolt University Berlin: Dr. Holm Kirmse and Prof. Christop Koch
- Institute of Physics in Zagreb: Prof. Eduard Tutiš, Prof. Ivo Batistić, Prof. Osor Barišić Dr. Petar Popčević.

I would like to acknowledge Prof. Cécile Hébert, Prof. Mitali Banerjee, Prof Milan Orlita and Prof. Irina Grigorieva for accepting to be members of the jury of my doctoral exam.

Thanks to Nicole and Anh who were always very efficient and helpful in administrative support. Thanks the CMi and CIME staff and to the ICMP technicians for the help services they provided me.

A special thanks to all the friends and colleagues who I had the pleasure to meet and work together during my PhD. The LPMC team: Andrea, Lidia, Pavao, Iness, Konstantins, Xavier, Anastasiia, Davor, Dunja, Massimo, Endre, Luka, Trpimir, Peter S., Peter M., Gaétan, Claudio, Balint, Alla and Sergiy. A special mention goes to Konstantin for being an amazing teammate in the last age of the transport lab!

The LFS team in Fribourg with who we have also shared many beam-time adventures: David, Florian, Zoran and Shai.

The QMAT team: Carsten (an absolute reference for scientific excellence), Amelia, Jonas, Xiangwei, Hung-Wei, Mark and Marteen.

I really much enjoyed the great discussion with my colleagues at EPFL: Gianmarco and Alberto for their experience in ARPES and hopefully for my help with transport. Ivan and Francesco for their support to perform electron diffraction experiments. “Il capitano” Ivica for his great support and the very interesting discussions we had.

A special thanks goes to all the students I have supervised in the lab: Ruben, Michele and Mathieu. I really enjoyed the time we spent together and the fact that working together was a learning experience for both sides.

Finally I want to acknowledge all the close friends that supported me over this time of my PhD here in Lausanne, and when I was constantly travelling around: Lucie, Chiara, Shriya, Vera, Marcello, Federico, Denis and Anna (who has been my reference point here in Lausanne since day one).

Most of all, I want to thank my parents and the members of my family for their love, support and trust in me.

Edo

Lausanne, 16 June 2020

Prologue

I believe that an experiment is not about distorting nature to make it do what we want. Nature has countless details that must be considered when seeking a truthful answer to our questions. We must listen and observe with openness and respect. The right questions must be asked. And we must stay receptive to the answers that Nature truthfully reveals, especially when it offers surprises.

The general question we asked was how electrons ‘move’ inside a material. This is a question that scientists have asked multiple times, leading us to create electronic devices, harnessing the sun's energy with photovoltaic panels and storing that energy inside batteries.

In this thesis, I investigated how electrons move between atomic planes in layered materials, a class of crystalline compounds that have today attracted considerable scientific and technological attention. I took advantage of the most advanced experimental tools so as to ask and receive the most truthful answers of Nature. The answers I obtained were occasionally surprising, and revealed many truths previously unseen.

M. C. Escher “Reptiles”, lithograph print, March 1943

A hexagonal lattice of 2D-reptiles, adventuring outside of the flatland.

Abstract

Layered materials, such as graphite and transition metal dichalcogendes, have attracted a great scientific interest over the past 50 years. In the 1970's they were investigated because of the possibility to tune their superconducting properties by intercalation of ions or organic molecules. In the 1980's the interest shifted to charge density waves, a periodic modulation of the electron density common for low-dimensional conductors. Since 2005, they returned under the spotlight of scientists and engineers, interested by the possibility to isolate atomic thin crystals by mechanical exfoliation. As the crystalline layers are weakly bounds in these materials, one can peel-off a single atomic plane and use it to create an electronic device. This offers an easy approach to exploring the physical properties of 2D conductors, initiated with the pioneering work on graphene in 2005. The scientific interests continue today, due to the possibility of combining different layers stacking them together as LEGO blocks to create artificial heterostructures. It was observed experimentally, that new physical properties can emerge when stacking different atomic layers together. Moreover, the combination of different atomic layers such as insulator, semiconductor and metals is proposed for the creation of potential future ultrathin solid state optoelectronic devices. The magnitude of the current scientific interest is remarkable. As reference, the European commission supported projects related to this topic with a 1 billion Euro budget under the Graphene Flagship program, as part of the Horizon 2020 scientific and technology work package.

The goal of this thesis is to explore the "neglected" third dimension of layered materials, by studying the interlayer charge dynamics through dc conductivity, optical spectroscopy and *ab*-initio calculations. This project was designed to respond to the growing interest in layered materials and heterostructures. It is today evident that new properties originate by the interaction between neighbouring atomic planes, but the magnitude of the interlayer coupling has so far been poorly investigated. Reliable and reproducible experiments, in particular for dc conductivity, are today made possible thanks to the recent advancements in the field of materials microfabrication through focused ion beam. Such an emerging approach has enormous potential for the advancement of condensed matter physics. In the case of this thesis, it enabled me to review long-standing scientific paradigms and verify that previous experimental results differ by more than 2 orders of magnitude from the intrinsic material property.

The subjects of study are metallic layered transition metal chalcogenides, as they offer a very flexible playground of crystalline structure and physical properties. At the same time, these materials are chemically simple, making the synthesis of high-quality single crystals accessible. The discussion will start in Chapter 3, where we will discuss the case of simple layered metals (2H-$NbSe_2$, 2H-TaS_2) or semimetal ($ZrTe_5$), for which the anisotropic transport properties can be accurately predicted by their simple band structure calculation and Fermi surface topology. The anisotropic response will be treated in a more general term by considering the effective number of carriers which contributes to charge transport along in a specific crystallographic direction.

The discussion will continue by looking at the peculiar properties of 1T-TaS_2, a prominent layered material for the rich set of charge density waves reconstruction, and the presence of a low temperature meta-insulator transition. The proposed interpretations for the physical properties of this compound, have often evoked a dominant contribution of the quasi-2D electronic properties in light of the layered structure. Recent results from band structure calculations, photoemission spectroscopy and X-ray diffraction, on the contrary, suggests

that strong interlayer interactions need to be accounted to justify the observed properties of this material. The experimental results in Chapter 4 provide a clear evidence from transport properties in support of this new interpretation of a layered material where physical properties are strongly dictated by the way different layers interact with each other. This counterintuitive result is regarded as the consequence of the intertwined relation between the charge density wave and the orbital character of the conduction electrons bands, producing a *c*-axis oriented orbital texture.

The weak bond that holds together the crystalline planes in layered materials also creates the perfect condition for intercalation, or the growth of compounds with different crystalline layers staked together, creating a natural heterostructure. In chapters 5 and 6, we will explore the new physical properties that emerged in layered transition metal dichalcogenides when different layers are combined together to form a natural heterostructure, or when magnetic ions are intercalated. The host layered material and the individual building blocks of the heterostructure, are related to the compounds discussed in the previous chapters. This helps to identify differences and similarities in the observed physical properties. Surprising results are reported from the studies of interlayer conduction properties. The interaction between the different types of layers in the natural heterostructure of 4Hb-TaS_2, influences the charge density waver and superconducting properties. In this situation, the conduction mechanism is highly anisotropic. In Chapter 6 we will see how conduction anisotropy is affected by the specific long-range magnetic order produced by the intercalated atoms.

Keywords

Layered materials, transition metal dichalcogenides (TMDC), mesoscopic physics, focused ion beam, transport properties, optical properties, conductivity anisotropy, charge density wave, high-pressure physic

Résumé

Les matériaux multicouches, tels que le graphite et les dichalcogènures de métaux de transition, ont suscité un grand intérêt scientifique au cours des 50 dernières années. Dans les années 1970, ils ont été étudiés pour la possibilité d'ajuster leurs propriétés supraconductrices via l'intercalation d'ions ou de molécules organiques. Puis, dans les années 1980, l'intérêt s'est porté sur les ondes de densité de charge, une modulation périodique de la densité électronique, commune aux conducteurs de faible dimension. Depuis 2005, ils sont revenus sur le devant de la scène, les scientifiques et les ingénieurs étant intéressés par la possibilité d'isoler des cristaux de l'épaisseur d'un atome par exfoliation mécanique. Comme les couches cristallines sont faiblement liées dans ces matériaux, on peut décoller un seul plan atomique et l'utiliser pour créer un dispositif électronique. Cela offre une approche simple pour explorer les propriétés physiques des conducteurs 2D, initiée avec les travaux précurseurs sur le graphène en 2005. L'engouement se poursuit aujourd'hui notamment, grâce à la possibilité de combiner différentes couches et de les empiler comme des LEGO pour créer des hétérostructures artificielles. Il a été observé expérimentalement que de nouvelles propriétés physiques peuvent émerger de l'empilement de différentes couches atomiques. De plus, la combinaison de différentes couches atomiques (isolante, semi-conductrice ou métallique) est une piste pour la création de futurs dispositifs optoélectroniques ultra-minces à l'état solide. L'ampleur de l'intérêt scientifique actuel est remarquable. À titre d'exemple, la Commission européenne soutient des projets liés à ce sujet avec un budget d'un milliard d'euros pour le Graphene Flagship, dans le cadre du programme de travail scientifique et technologique Horizon 2020.

L'objectif de cette thèse est d'explorer la troisième dimension souvent négligée des matériaux en couches, en étudiant la dynamique des charges entre les couches par la conductivité en courant continu, la spectroscopie optique et les calculs *ab*-initio. Ce projet a été conçu pour répondre à l'intérêt croissant pour les matériaux en couches et les hétérostructures. Il est aujourd'hui évident que de nouvelles propriétés émergent de l'interaction entre des plans atomiques voisins, mais l'ampleur du couplage intercouche a été jusqu'à présent peu étudiée. Des expériences fiables et reproductibles, en particulier pour la conductivité en courant continu, sont aujourd'hui possibles grâce aux récentes avancées dans le domaine de la microfabrication des matériaux par faisceau d'ions focalisée (focused ion beam, FIB). Cette nouvelle approche a un énorme potentiel pour l'avancement de la physique de la matière condensée. Dans le cadre de cette thèse, elle a permis de passer en revue de vieux paradigmes scientifiques et de démontrer ainsi que les résultats expérimentaux précédents diffèrent des propriétés intrinsèques réelles de ces matériaux par plus de deux ordres de grandeur.

Les objets de cette étude sont les dichalcogènures de métaux de transition en couches métalliques, car ils offrent un vaste répertoire de structures cristallines et de propriétés physiques. Dans le même temps, ces matériaux sont chimiquement simples, ce qui rend possible la synthèse de monocristaux de haute qualité. La discussion commencera au chapitre 3, où nous aborderons le cas des matériaux en couches métalliques ou semi-métalliques, dont les propriétés de transport anisotropies peuvent être prédites avec précision par le simple calcul de la structure des bandes et la topologie de surface de Fermi. La réponse anisotrope sera traitée en des termes plus généraux de nombre effectif de porteurs, qui contribuent au transport de charge dans une direction cristallographique spécifique.

La discussion se poursuivra en examinant les propriétés particulières de 1T-TaS_2, un matériau en couches connu pour le riche ensemble de reconstruction des ondes de densité de charge, et la présence d'une transition métal-isolant à basse température. Les interprétations proposées pour les propriétés physiques de ce composé ont souvent évoqué une contribution dominante des propriétés électroniques quasi 2D en se basant sur la structure en couches. Les résultats récents des calculs de structure de bande, de la spectroscopie de photoémission et de la diffraction des rayons X, au contraire, suggèrent que les fortes interactions entre les couches doivent être prises en compte afin de pouvoir expliquer les propriétés observées pour ce matériau. Les résultats expérimentaux présentés au chapitre 4 démontrent clairement que les propriétés de transport justifient cette nouvelle interprétation, pour un matériau en couches dont les propriétés physiques sont fortement dictées par la façon dont les différentes couches interagissent entre elles. Ce résultat contre-intuitif est considéré comme la conséquence de la relation entre l'onde de densité de charge et le caractère orbital des bandes d'électrons de conduction, produisant une texture orbitale orientée sur l'axe *c*.

La faible liaison qui maintient ensemble les plans cristallins dans les matériaux en couches, crée également la condition parfaite pour l'intercalation ou la croissance d'autres composés avec différentes couches cristallines, créant ainsi une hétérostructure naturelle. Dans les chapitres 5 et 6, nous explorerons les nouvelles propriétés physiques qui émergent lorsque différentes couches de dichalcogènures de métaux de transition sont combinées avec d'autres pour former une hétérostructure, ou lorsque des ions magnétiques sont intercalés. Le matériau stratifié de départ et les éléments individuels constitutifs de l'hétérostructure sont en lien avec les composés étudiés dans les chapitres précédents. Cela permet donc d'identifier les différences et les similitudes des propriétés physiques observées entre ces états. Des résultats surprenants sont observés lors de l'études des propriétés de conduction des couches intermédiaires. L'interaction entre les différents types de couches dans l'hétérostructure naturelle de 4Hb-TaS_2 influence l'onde de la densité de charge et les propriétés supraconductrices. Dans cette situation, le mécanisme de conduction parallèlement et perpendiculairement au plan des couches est hautement anisotrope. Dans le chapitre 6, nous verrons comment l'anisotropie de conduction est affectée par l'ordre magnétique spécifique à longue portée produit par les atomes intercalés.

Mots-clés

Matériaux en couches, dichalcogénures de métaux de transition (TMDC), physique mésoscopique, faisceau d'ions focalisé, propriétés de transport, propriétés optiques, anisotropie de la conductivité, onde de densité de charge, physique des hautes pressions

Contents

Chapter 1 Introduction

The availability of materials with specific functionalities has always been the practical bottleneck for technological innovations throughout human history. It is indeed according to the "most performing" available material that prehistorical ages are classified: the stone age, the bronze age, the iron age. While in prehistory, the materials' mechanical properties were the most important ones, today we take advantage of the spectrum of physical properties, such as electronic, optical and magnetic. Modern technologies, which have revolutionized our way of living, have been made possible thanks to the development and understanding of new materials. The most prominent example is the transistor, the building block of todays computer technologies, and the result of the work of physicists interested in the fundamental properties of semiconducting materials such as silicon and germanium [1].

It is well known that the properties of a material are defined by the type and spatial arrangement of the atoms that constitute it. An elegant example, is the comparison between graphite and diamond. Both materials are made of carbon atoms, but they differ in the way atoms are spatially organized. In graphite they form layers with a honeycomb structure, while in diamond the atoms create a three-dimensional network. This different organization results in considerably different properties. Graphite is an electrical conductor, and it is black because it strongly absorbs visible light. Diamond is an electrical insulator and transparent. The difference in atomic arrangement is evident in their mechanical properties. Diamond is the hardest known materials, while a graphite block can be easily destroyed by hand. Graphite is so soft that it can be "spread" over a rough surface, leaving a dark mark of fine graphite dust behind it. This is because the atomic layers can be easily detached from each other, meaning the material can be easily cleaved.

A scientist who wants to create a new material can chose to combine several among the 80 different kinds of atoms, in countless combinations and in unlimited possible spatial arrangements. According to the on-line crystallographic databases, up to date we know around 450'000 possible materials with different atoms and/or spatial arrangements [2]. Together with the type of atoms and their positions, we know that we have another degree of freedom, the material dimensionality. When the size of a material along at least one direction is shorter than 100 nm (10^{-7} meters), its properties can be dramatically changed. This is the result of quantum confinement effects, because the electrons in the materials will start to behave differently when they are confined in a smaller space. Changing the materials' properties by tuning their sizes is the aim of nanotechnology, a branch of science and engineering that has attracted ever growing attention for its potential impact in the fields related to energy, information technology and even medicine [3].

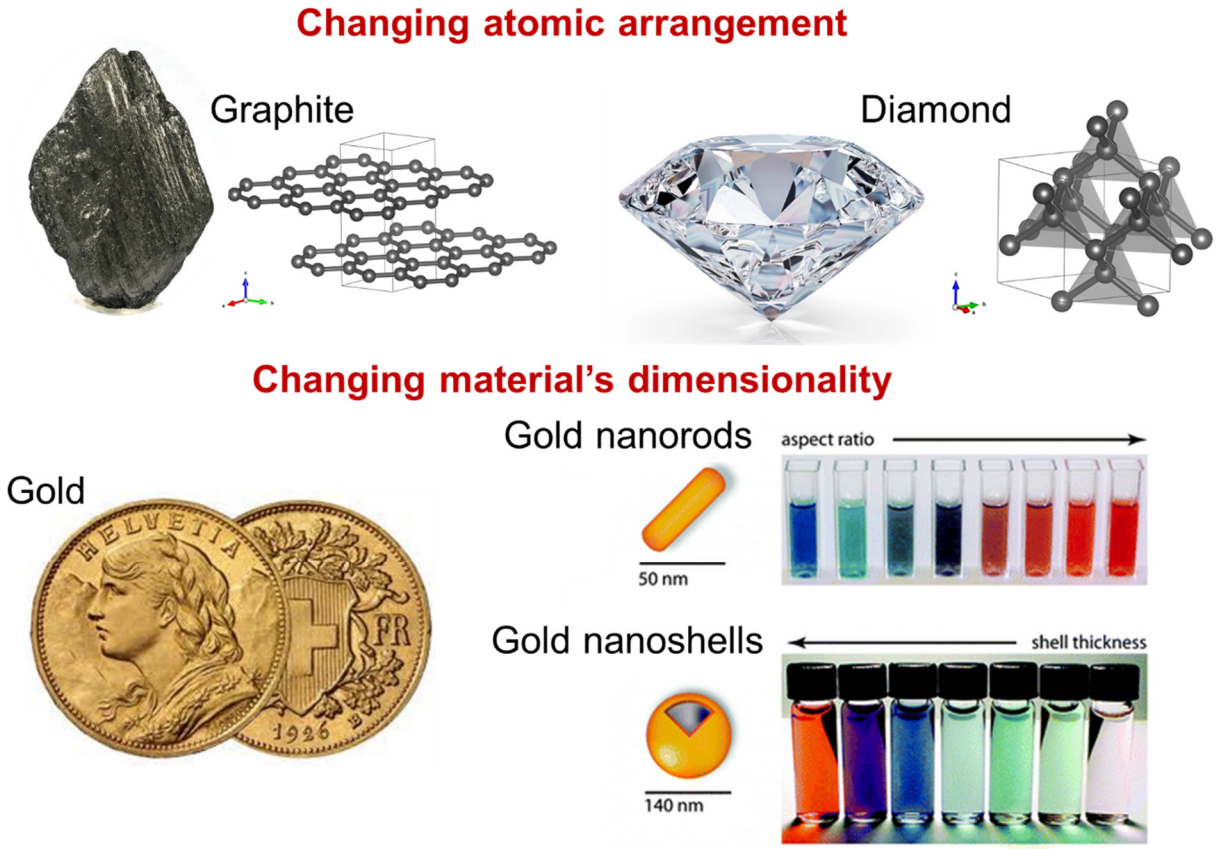

Figure 1:1 Materials properties: structure and dimensionality. Upper panel) materials properties change with atoms spatial arrangement. Graphite and diamonds are made of the same type of atoms: carbon. Their properties are considerably different as a results of the carbon atoms spatial arrangement. **Lower panel)** materials properties change with dimensionality. Gold's characteristic bright yellow colour, is a consequence of the concentration and mobility of conduction electrons in the material. When gold is reduced in size, its colour change as a consequence of the confinement effect on the electrons inside the golden nano-object. Pictures adapted from [4].

With the increase of more demanding and specialized technological applications, it became of paramount importance to create materials that are able to comply with all the desired requirements. The modern strategy for material scientists is to look for nanomaterials when standard macroscopic materials are not able to provide the required performances. Creating nanomaterial can be relatively simple. In the case of gold nanoparticles: the material is made by one element, and it forms only one type of ordered crystalline structure. Additionally, gold is stable in air and non-toxic, so with the right set of chemicals and minimum infrastructure one can easily produce nanoparticles. The potential of reduced dimensionality is evident if we look at Figure 1:1, where different solutions of gold nanoparticles are ordered according to their geometrical dimensions. We are all familiar with the bright yellow colour of gold, but when its dimensions are reduced to nanometre scale, its colour will change as a result of the electrons' confinement.

Scientists have found a variety of suitable methods to create nanomaterial, either by cutting out pieces of materials to reduce their size (top-down), or by growing them atom by atom to reach the desired nanometric dimension (bottom-up). The science and engineering of nanomaterials has now many established techniques [5]. The nanomaterials can be divided into categories according to the dimensionality of electron confinement. In 0D, electrons are confined in point-like volume as in so called quantum dots or nanoparticles, and behave like in a single atom as they are unable to move. 1D nanomaterials are called nanotubes or nanowires, and confine electrons along two directions while leaving them free along the tube/wire direction. In two-dimensional (2D) materials, electrons are confined into a very thin layer, down to a single atom thickness. As

an example, carbon atoms offer the possibility to create nanomaterials of all three possible types of dimensional confinement, along with 3D bulk compounds as graphite or diamond.

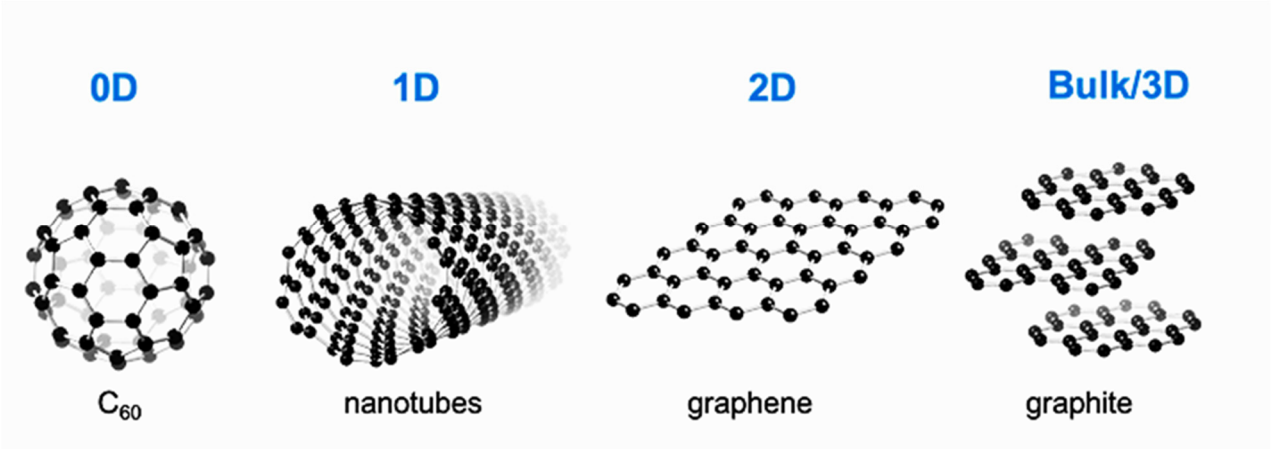

Figure 1:2 Carbon based nanomaterials Carbon atoms are able to create nanomaterials where atomic structure bearing close resemblance to the structure found in graphite. Fullerenes (C_{60}) are 0D systems, made by 60 atoms that are organized into a soccer-ball kind of structure of 1.1 nanometres in diameter. Carbon nanotubes are a 1D-type of nanomaterials, creating a tube of new nanometres in diameter which can extends over hundreds of microns. Graphene, is a single crystalline plane of graphite that has been isolated from the rest of material, is one atom thick and can be arbitrary large. Graphite is the familiar form of carbon, found in natural coal. It is made by layers of carbon atoms stacked on top of each other's. Figure from [6].

The class of 2D materials is related to this thesis subject of interest. When electrons are confined in two-dimensions, their properties can dramatically change with respect to when they are free to move in three dimensions. The interactions between electrons can be considerably enhanced, giving origin to electronic correlations and collective excitations. The limited thickness of the material also changes the electrostatic environment, producing a much poorer screening, as a result increases the Coulomb interaction between charged particles inside the material. This leads, for example, to higher excitons binding energies [7]. The physics of 2D materials shows some of the most remarkable demonstrations of quantum coherent properties in solids: the integer and fractional quantum Hall effects [8] [9] [10]. In a 3D conductor, for low values of magnetic field applied perpendicular to the current flow produces a cross voltage V_{xy}, normal to the current and magnetic field. The effect can be understood in classical terms as originating from the Lorentz force acting upon the electrons, as charged particles move in a magnetic field. The Hall resistance ($R_{xy}=V_{xy}/I_{channel}$) depends on the materials parameters, its magnitude scales linearly in magnetic field and can assume any value.

Magneto-resistance and Hall resistance measurements on 2D conductors, which have a low density of highly mobile conduction electrons, has led to surprising results. It was first observed in 1980 that at specific magnetic fields, the Hall conductance remains constant and proportional to an integer multiple of e^2/h, while magnetoresistance drops to zero [8]. This is the observation of the integer quantum Hall effect (QHE), produced by the quantization of the electron energy levels induced by the magnetic field. This first observation of quantized Hall conductance was measured on silicon field effect transistors, in which by changing the electrostatic potential of the gate, it is possible to create a two-dimensional conducting channel. It was thanks to the development of better 2D conductors, such as GaAs/AlGaAs heterostructures with electron mean free paths as long as 0.1 mm, that the fractional quantum Hall effect was observed (FQHE). In the fractional case, Hall conductance plateaus are rational fractions of the quantum of conductance [9]. This phenomenon originates from the correlated motion of electrons, resulting in a coherent quantum mechanical state in the material able to produce fractional charged excitations [10].

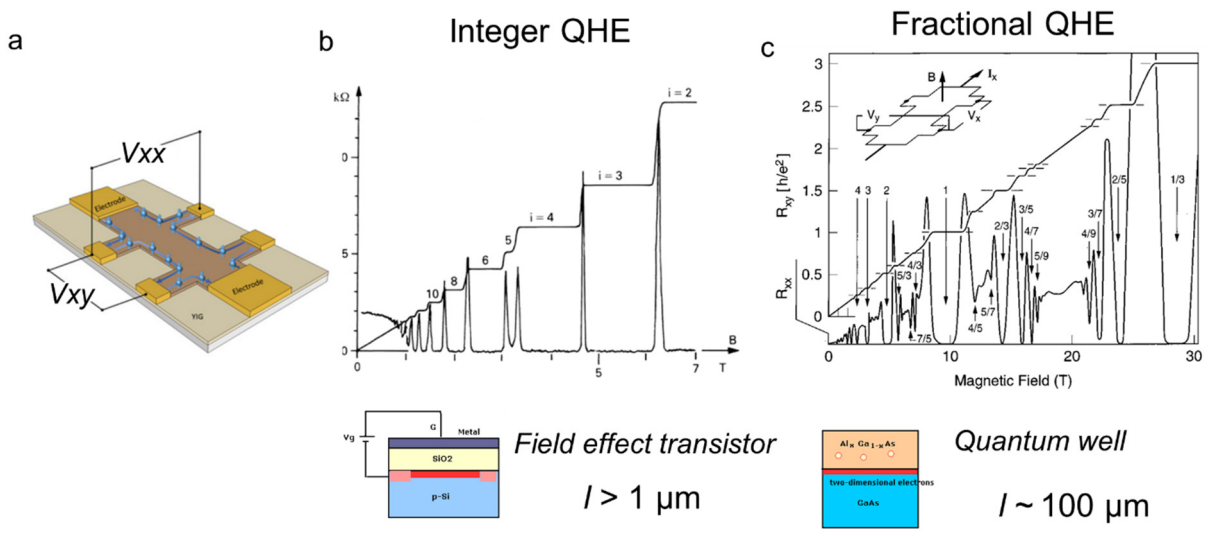

Figure 1:3 New physics in two-dimensions: quantum Hall effect. **a)** Hall bar device. Indicated the potential differences for the measurement of magnetoresistance V_{xx}, and Hall resistance V_{xy}. **b)** Integer quantum Hall effect (IQHE). For high enough magnet fields, the Hall conductance is an integer multiple of e^2/h, and magnetoresistance is zero. IQHE was first measured in a 2D-electrons gas created in silicon field effect transistors. Figure from [11]. **c)** Fractional quantum hall effect (FQHE). For 2D-electrons gas with extreme high mobility, in addition to IQHE, additional plateaus are visible where the Hall conductance is a rational fraction of the quantum of conductance. 2D-electrons gases with sufficiently high electrons mean free paths can be found in GaAs/AlGaAs heterostructures. Figure from [10].

Integer and fractional quantum Hall effects are very complex physical phenomena, but they clearly prove one point: new unexpected physical properties can emerge in two-dimensions. These properties can only be observed if the material is of very high quality: a crystalline material with limited defects and very limited impurity concentration.

2D materials, like ones used for the discovery of quantum Hall effects, can be realized thanks to machines that are able to grow high purity materials, controlling the thickness at the atomic scale. A molecular beam epitaxy (MBE) is a machine of this type, which allows creating 2D-materials, and even multiple layers of different materials stacked on top of each other. To create the engineered 2D-material, the desired chemical elements are injected into a chamber pumped to ultra-high-vacuum (10^{-8}-10^{-12} torr), ensuring maximum possible cleanness. The chemical constituents of the final material are deposited onto a suitable substrate to form a perfectly ordered nanometer thin layer of a precisely controlled stoichiometry. By using different atoms in sequence, it is possible to produce an alternated stacking of 2D materials, called heterostructures, like the GaAs/AlGaAs where FQHE was observed. The performances of this approach come at a considerable economical cost and has practical limitations. It takes a large investment to build a machine capable of creating the highest possible quality thin films, and highly specialized personnel to operate it. Moreover, it takes years of trials and optimisation to identify the correct set of parameters to produce high quality materials. Typically, one machine will be devoted to produce one specific type of material for its entire service time, or a very limited set of materials that have common chemical elements. For this reason, explorative research on new materials cannot be easily conducted using the MBE approach.

At the same time, new materials are discovered daily, and in some cases they present new and surprising properties. An example is the discovery of high temperature superconductivity at 35 K in $La_{1.85}Ba_{0.15}CuO_4$ by Bednorz and Muller in 1986 [12]. This finding was made possible thanks to the freedom the two scientists had to explore different materials and chemical variations. Their discovery was a major breakthrough for the physics community, and has fuelled an intense search for similar materials that could become superconducting at a much higher temperature. In a few years, many other materials were discovered, manifesting

superconductivity at higher temperatures, and with much more complex compositions. The record holder, $HgBa_2Ca_2Cu_3O_8$, was discovered in 1993. This material has a considerably more complex structure than the first high-temperature superconductor discovered in 1986 [13]. The physics of high-temperature superconductors has a connection to the realm of 2D conductors. The exciting electronic properties of these materials originates from their CuO_2 layers, which are separated by insulating atomic blocks. The stronger interaction of electrons confined in the CuO_2 atomic planes are seen as the primary origin for the superconducting properties at high temperature.

Controlling materials dimensionality, in particular through two-dimensional confinement, can modify the materials' properties and even produce new surprising physical phenomena, like the quantum Hall effect and high-temperate superconductivity. Today's challenge for material physicists and nanotechnology engineers is how to merge the best of these two words. They seek to create a complex material that combines different elements with a high chemical purity and crystalline order, while at the same time controlling its dimensionality on the nanometer scale.

How to explore the properties of new materials with two-dimensional electrons confinement? A solution to this question arrived for the scientific community in 2005, as a result of a Friday evening experiment conducted by Andre Geim and Konstantin Novoselov at the University of Manchester. Their interest was to measure the electrical properties of a single layer of graphite, which is called graphene [14]. In doing so, they identified an accessible approach to isolate an atomically thin crystalline material, simply by peeling it off with adhesive tape and transferring it on a flat surface such as a silicon wafer. Their idea demonstrated how to create a 2D-material using cheap tools that everybody can afford. This development was a surprise, because until 2005, the scientific community believed in the paradigm that if a flake of graphite is thinned down to a single atom thickness, it would never be thermodynamically stable. It was thought that the flake would sublimate, burn, or just fold onto itself to create something like a nanotube. Geim and Novoselov challenged this idea, and repeatedly studied the electronic properties of thin flakes of graphite by measuring resistivity and Hall coefficient. When graphene was isolated and measured, its properties were clearly different from that of graphite as a result of its reduced dimensionality. The Hall coefficient and magnetoresistance measurements gave evidence of Dirac electrons originating from the linear band dispersion (expected from symmetry and tight binding calculations), and showed a quantum Hall effect, see Figure 1:4 b [15]. The quality of graphene samples improved very quickly, thanks to better control of the detrimental interactions with the substrate. To further improve the sample quality, another layered material was used, hexagonal boron nitride (h-BN). h-BN is an insulator, and like graphite it can be exfoliated to produce atomically thin and flat flakes [16]. When graphene was sandwiched between h-BN layers, the mobility of the electrons increased considerably. As a result, it was possible to observe FQHE [17]. In only a few years since its discovery, graphene has not only achieved electronic mobility comparable to 2D-electron gas created in GaAs by MBE, but has also become considerably cheaper to make, and thereby easily accessible to a broad group of scientists.

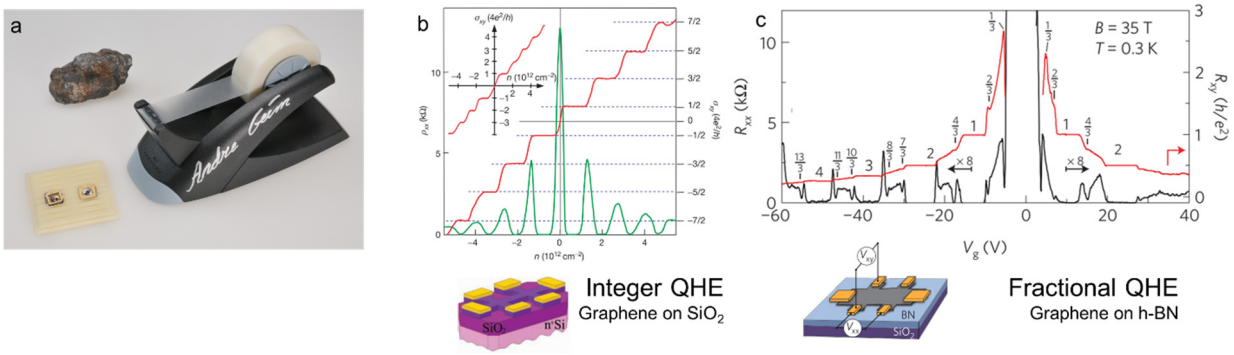

Figure 1:4 Isolation and properties of graphene. a) A chunk of graphite, adhesive tape and one of the first graphene devices, donated by Andre Geim and Konstantin Novoselov to the Nobel Museum, after receiving the physics Nobel prize in 2010 [18]. **b)** QHE in graphene, where magneto-resistivity ρ_{xx} (left - green) and Hall conductance σ_{xy} (right - red) are shown as a function of carrier concentration. Measurements was performed at B = 14 T and T = 4 K. The Hall conductance steps in graphene are half integer, as a consequence of the relativistic-like behaviour of conduction electrons (Dirac electrons). The inset is displays the behaviour for a double layer graphene, with evident integer steps. Figure from [15]. **c)** Magnetoresistance (left - black) and Hall resistance (right – red) as function of gate voltage, showing evidence of FQHE for a graphene sample on top of hexagonal boron nitride (h-BN). The insulating and atomically flat h-BN layers protects the graphene, increasing the electrons mobility. Figure from [17].

The work of Geim and Novoselov on graphene received immediate recognition, landing them the physics Nobel prize in 2010. The impact of their discovery was not limited to graphene, but it was immediately extended to many other materials that, like graphite, have a layered structure and can be mechanically exfoliated to isolate a two-dimensional atomic crystal [19]. Insulators like boron nitride, semiconductors or metals like transition metal chalcogenides, and even complex oxides like high-temperature superconductors can be readily exfoliated. Potentially, any material that has strongly covalently bound layer, which are weakly connected to each other, can be exfoliated and became a 2D material.

The variety of layered materials that can be exfoliated to atomic thickness offers a palette of physical properties. Graphene is a Dirac semimetal with extreme high electron mobilities, h-BN is a wide band gap insulator, transition metal dichalcogenides can be either metals or semiconductors with a bandgap in the 1 – 2 eV energy range. All these different 2D materials can be combined by stacking them together —like one would do with LEGO blocks— to form artificial materials, named van der Waals heterostructures (Figure 1:5) [20].

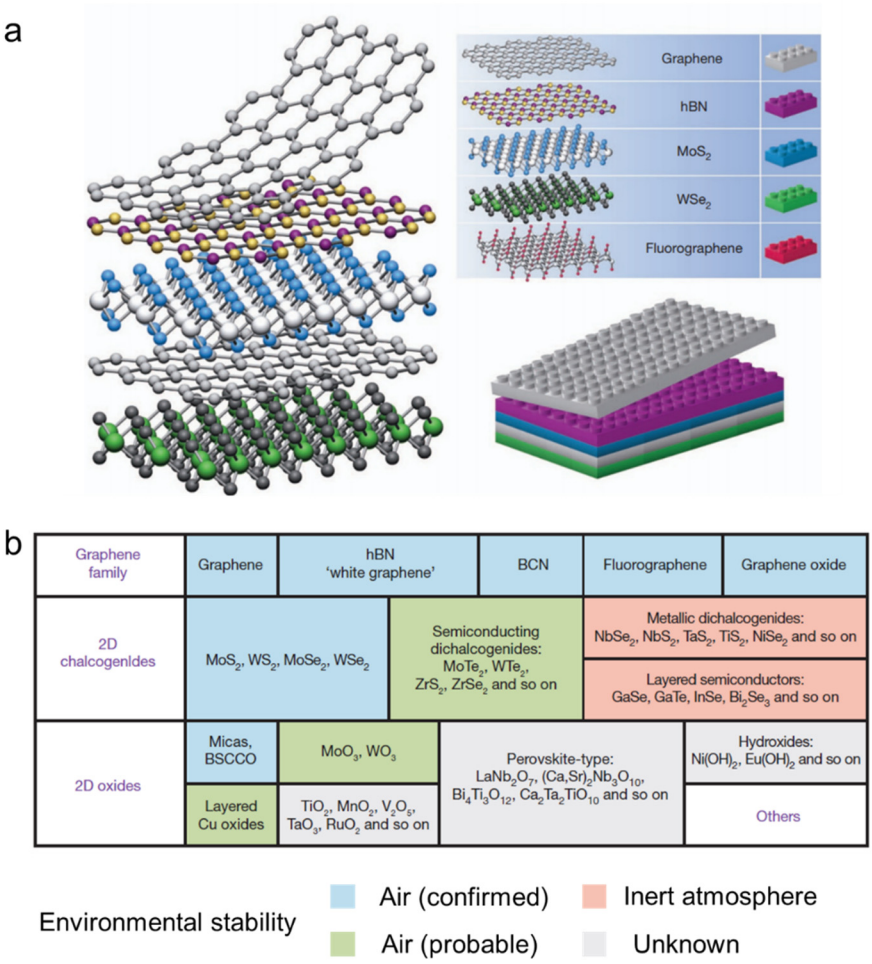

Figure 1:5 van der Waals heterostructures. a) The concept of creating artificial materials by stacking 2D materials, in analogy to LEGO blocks. This atomic scale construction process is in close resemblance to molecular beam epitaxy growth. Because of the van der Waals type of interaction between layers, materials with different lattice parameters can be combined together, which is not possible for covalently bond epitaxial heterostructures. **b)** The table shows a proposed list of materials that can be exfoliated to atomic thin crystals and combined together into heterostructures. The colour is an indication of the environmental stability. Figure from [20].

The term van der Waals refers to the weak interatomic interaction between neutral molecules, and it is responsible for the attractive force between atomic layers in materials like graphite. Materials made by alternating different atomic layers can also be created by thin film growth, for example using MBE, in which different layers are grown on top of each other. As the atoms are covalently bound, the different layers are strongly connected. The strong atomic interaction poses a practical constraint on the lattice parameters for the materials that can be combined. The difference in lattice parameters induces mechanical stresses. Beyond a certain lattice parameter difference, the materials cannot be combined anymore because the necessary deformation would destroy the material.

This is another point where exfoliated layered materials can outperform standard thin-film-grown 2D materials. Because of the weak interlayer interaction, van der Waals materials have a much wider flexibility for combining in vertically stacked heterostructures. Not only can they accommodate arbitrarily large differences in the atomic lattice parameters, but they can also combine different crystal symmetries and even allow a rotation between different layers, something impossible for covalently bound materials. The creation and study of van der Waals heterostructures is today a relevant branch of condensed matter physics, accessible to many laboratories, offering unmatched degrees of freedom. Because the creation of a heterostructure and

the synthesis of the individual atomic layers are done separately, materials with very different chemical elements and with incompatible synthesis reactions can now be combined.

The stacking of different layers in a van der Waals heterostructure can be seen as the tailored creation of new materials with specifically designed properties. Such materials already exist. A very successful example is the measurement of FQHE in graphene, which was possible in a heterostructure that combines the high conductivity of graphene, with the insulating and protecting capabilities of h-BN. Advancements in this field led to new surprising properties originating from the interaction between the stacked layers. For example, strong electronic correlations and unconventional superconductivity were discovered in twisted bilayer graphene [21], and enhanced exciton lifetime in heterobilayers of semiconducting transition metal dichalcogenides [22]. In the twisted bilayer graphene, a small rotation between the two hexagonal potentials creates an additional periodicity, a large-scale moiré pattern (Figure 1:6 a). This additional periodic potential creates new electronic states that increase the interactions between electrons, up to the point of suppressing the material conductivity. If the layers are forced closer together by applying pressure, their electronic interactions are enhanced (Figure 1:6 b). This is evident in the electrical conductivity, as for stronger electronic interaction the twisted bilayer graphene become much less conducting [23]. These results prove the fundamental role of interlayer coupling for the emergence of new properties, and are an additional motivation to study the electronic interaction between layers.

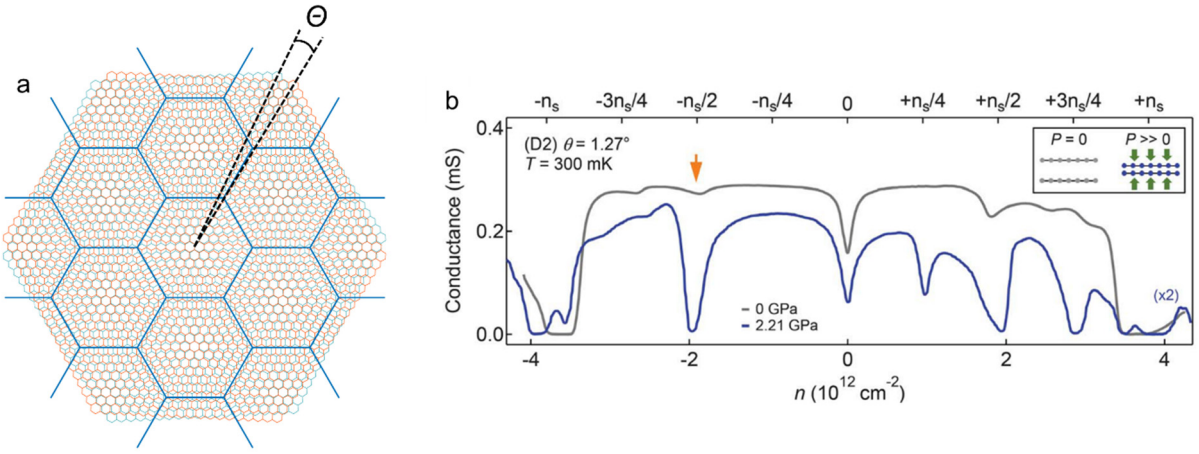

Figure 1:6 Twisted bilayer graphene and interlayer coupling. **a)** Two graphene layers twisted by a small angle Θ form a superstructure modulation (moiré pattern), shown by the thick blue hexagonal lattice. Figure from [24] **b)** Conductance measurements for a twisted bilayer graphene as a function of band filling, tuned by electrostatic doping. At half filling a correlated insulating state is marked by the dip in conductance (orange arrow). The insulating phase, produced by the superstructure modulation, is enhanced when the two layers of graphene are forced closer together by applied pressure. The higher interlayer coupling is therefore responsible for the enhanced electronic correlations. Figure from [23].

These van der Waals heterostructures are one of the new frontiers in the development of new materials. The origin of new properties come from the electronic coupling between different layers. As of today, there is not an established understanding of how electrons in two neighbouring atomic layers interact with each other, and how this can be harnessed to generate new properties. This is the central question that will be discussed in this thesis: how are 2D layers electronically coupled together?

We decided to address this question by experimentally probing how electrons move between atomic layers. This translated into measuring their electrical conductivity anisotropy, comparing the behaviour between current flowing in-plane and out-of-plane. The measurement of electrical conductivity has a double significance. It provides information on the electronic coupling between the layers, answering if they are

electrically connected or there is an energy barrier for electrons to move. At the same time, it serves as a guide on how much electrical resistance could be encountered in potential electronic devices based upon these materials, if the current is forced to move between the atomic layers. Despite the intense research on layered materials, this question has so far been overlooked, receiving only simple, dismissive answers: because the material is layered and can be easily exfoliated, the electronic properties are weakly coupled and electrons can only propagate within the crystalline planes. The objective of this work is to go beyond such simplistic statements and address interlayer physics in depth, through a careful experimental investigation.

The recent breakthrough in artificial heterostructures has been a strong motivation for this work, yet our experiments are based on the three-dimensional layered material, the source of the two-dimensional building blocks for new artificial materials. To probe the intrinsic properties of layered materials and exclude any extrinsic effects, the most effective approach is to leave the layered material “intact”. The samples used for experiments are single crystals of 3D layered materials of high purity and high crystalline quality. They are created in the lab by established chemical synthesis, and presents a stacking of the same type of layers that can extends for more than 100 μm (approximately 100’000 layers).

3D layered materials have been studied long before the advent of graphene, yet it is a formidable task to determine the interlayer coupling and out-of-plane transport properties. The few existing experimental results paint an unclear picture, with data for the same materials that are considerably scattered. The collection of reproducible and reliable data presented in this work was possible thanks to state-of-the-art modern 3D-microfabrication technologies based on focused ion beam micro-machining. In addition to advanced sample preparation, high-pressure experiments had a crucial role in this thesis. By application of enormous pressures, in the order of thousands of atmospheres, even solid materials can be compressed. For the case of layered materials, the dominant effect is the reduction of the distance between layers. The continuous tuning of interlayer distance while probing the materials physical properties is a very powerful tool to reliably address the interlayer coupling and mechanism of charge conduction between the layers.

Each chapter of this thesis describe a different dominant contribution to interlayer charge transport. In every chapter a different material is introduced and discussed, first by presenting its crystalline and electronic structure, and then by showing and discussing the anisotropic transport properties. The discussion proceeds with growing complexity, and in a certain sense with increasing surprise. First, we discuss the case of layered semimetals and metals, for which the anisotropic transport properties can be simply described by their electronic band structure. The finding is in a certain sense trivial. In a three-dimensional layered metal, electrons can move along every direction with a finite anisotropy that depends on the effective electron mass or effective number of carriers. As we progress in the thesis, special cases are introduced, where the presence of lattice reconstruction, orbital ordering, combination of different atomic layers, and even magnetic ordering can have a dominant effect on the coupling and conductivity anisotropy.

Chapter 2 Layered materials and transport anisotropy

The recent attention given to layered compounds is a consequence of their peculiar crystalline structure. In these materials the atoms share strong bonds within planes, but the planes are bound together by a much weaker van der Waals type of interaction. Because of the anisotropic crystalline structure, such materials can be mechanically exfoliated. This weak mechanical connection between atomic planes is evident when manipulating a layered material, such as graphite or molibdenite (MoS_2). Those materials can be destroyed by hand, producing a fine dust of flakes. It is indeed thanks to this property that graphite and molibdenite found their first industrial application as solid-state lubricants, taking advantage of the low friction of sliding between crystalline planes. The weak interaction between atoms in different planes results in a much higher interatomic distance compared to that observed in covalently bound compounds. From the known crystalline structure, it can be predicted whether the material is layered and if it can potentially be exfoliated. This notion can be developed into an algorithm, to explore possible new layered materials, simply by systematically searching through the inorganic crystal structures databases [25].

Crystallographic structure databases store the relevant information on all known materials, synthesised in the laboratory or found in nature as minerals, to make them accessible to the entire scientific community. These databases today host more than 450'000 entries [2] [26]. Because layered material are now of interest as source for 2D crystals, several initiatives were launched to investigate material databases in search for new layered materials. The results of this screening, are published in a few on-line repositories [27] [28]. From the large number of known materials, around a thousand are thought to be layered and exfoliable. The aim is to provide a rational guide for the time-consuming experimental exploration of new materials, as simple chemical intuition cannot be enough. Layered or isotropic materials can have very similar chemical formulas, for example the transition metal dichalcogenides molibdenite (MoS_2) and pyrite (FeS_2). Only the Mo-based material crystallizes into a layered structure. Figure 2:1 clearly shows the difference in the crystalline structure and the mineral morphology. The "wrinkles" in the molibdenite crystals are most likely due to internal cleavage planes, where the layers are detached as a consequence of mechanical deformation. At the bottom of Figure 2:1 are displayed several layered materials, that will be evoked in different discussions throughout this thesis. The difference in chemical elements and structure also reflects on the strength of interlayer adhesion, which defines how easily the material can be exfoliated.

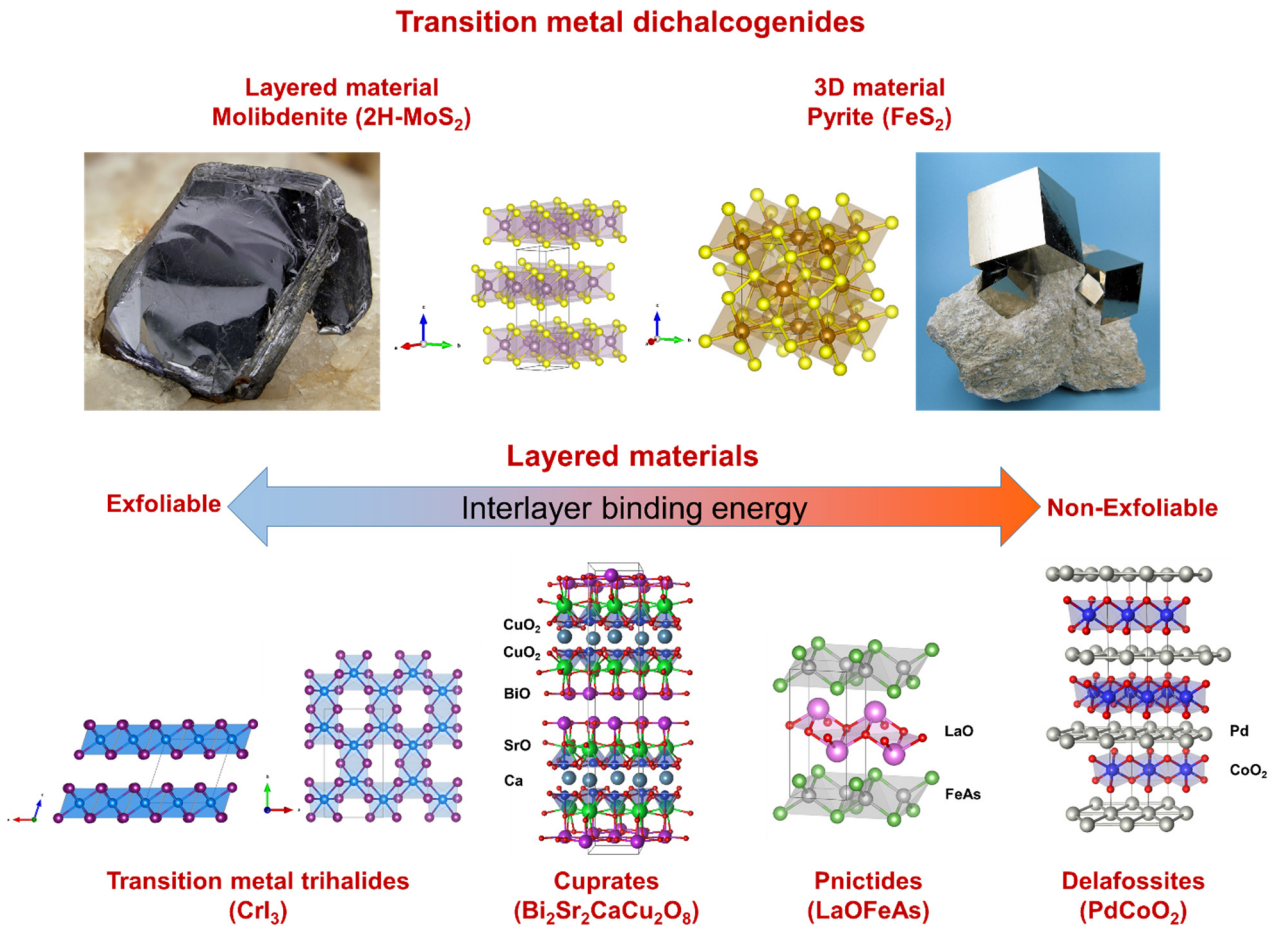

Figure 2:1 Layered vs isotropic crystals. **Top)** Comparison of the naturally grown minerals and crystalline structures of molibdenite and pyrite. The Mo-based material has a layered structure, forming crystals that can be easily exfoliated. FeS_2 forms an isotropic structure where Fe-S covalent bonds extends in all three direction. Pyrite minerals have a cubic structure, and cannot be exfoliated. Photographs from [29] [30]. **Bottom)** Different layered materials that have received considerable scientific attention. The compounds are ordered according to their interlayer bonding strength, increasing going from left to right. Crystal structures have been created using VESTA Software [24].

2.1 Layered transition metal dichalcogenides

All the materials discussed in this thesis are layered transition metal chalcogenides. With the exception of $ZrTe_5$, all the others are dichalcogenides, having a general chemical formula: MX_2 where M is a transition metal and X a chalcogen [31]. Limiting ourselves to a specific class of layered materials offers the opportunity to identify similarities and peculiarities, and to pin-point specific features that are responsible for the observed anisotropic transport properties.

Layered transition metal dichalcogenides (TMDs) are made of hexagonal M layer sandwiched, between two chalcogen planes. The three atomic layers have a 6 – 7 Å thickness. For the creation of in-plane covalent bond the transition metals provide 4 electrons to fill the bonding states, such that the oxidation state is +4 for the metal and -2 for the chalcogen [32]. Each chalcogen atom is coordinated with three metals, and one lone-pair electron to terminate the surface of the layer, which explains the weak interlayer interaction. The absence of dangling bonds on the surface renders the layers chemically stable. The metal atoms are six-folds coordinated, and the bond geometry can be either trigonal prismatic (TP) or octahedral (OC), giving two possible types of layers configuration. The energetically favoured coordination depends on the d-electron count of the transition metal. For group 4 and 7, only OC is favourable, for group 6, only TP, and for group 5 both configurations can

be observed. Two different types of in-plane coordination combined with a weak interlayer coupling give rise to a rich polymorphism of TMDs in bulk form. The most commonly encountered phases are 1T, 2H and 3R. The digit indicates the number of layers in the unit cell, and the letters stands for the crystal symmetry: trigonal (T), hexagonal (H) and rhombohedral (R). Polymorphism can also originate from different stacking orders. For example, three possible orders are observed in the "2H phase". In the 2Ha phase, found for group 5, metal atoms in different layers are vertically stacked following the AbA CbC configuration. For the 2Hc, found in group 6, the metal atom is aligned with the chalcogen of the subsequent layer (CaC AcA). The least common 2Hb is found in off-stoichiometric compounds, and its formation is driven by the transition metal self-intercalation. Polytypes with four layers present more complex sets of combinations, as they can include, within the same unit cell, a combination of layers with TP and OC coordination ($4H_b$, $4H_{dI}$, $4H_{dII}$ and 6R). The polytype present in the synthetized material depends on the growth conditions such as temperature and stoichiometry, and for particular cases metastable phases can be stabilized at room temperature by rapid quenching.

The electronic structure near the chemical potential is dominated by the transition metal *d*-orbitals. The energy levels are defined by the crystal field splitting, which differs for the two possible coordinations. In the octahedral crystal symmetry, two degenerate levels are formed: e_g (d_{z2} and d_{x2-y2}) and t_g (d_{xy}, d_{yz}, d_{xz}). In the trigonal prismatic configuration, the levels are split into three groups: a_1 (d_{z2}), e (d_{x2-y2}, d_{xy}) and e' (d_{xz}, d_{yz}). The bands are separated by a sizable gap around 1 eV. The difference in electronic properties for each transition metal group arises from the progressive filling of the *d* bands. Groups 4 and 6 have fully occupied bands and are semiconductors. Group 5 and 7 are metals with partially filled bands. The transition metal *d*-bands defines most of the electronic structure of TMDs near the chemical potential, and therefore have a crucial role in the electrical conductivity.

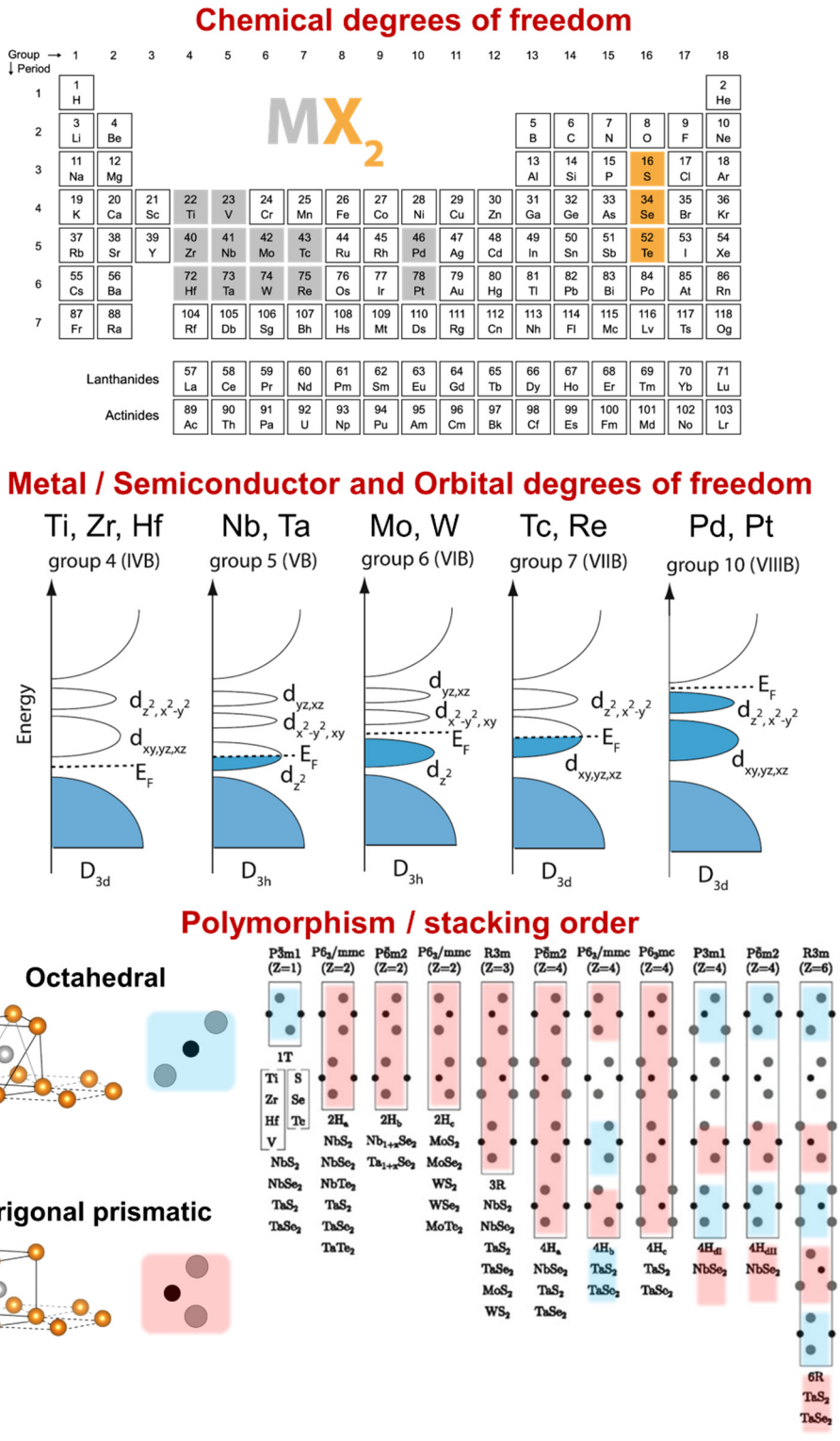

Figure 2:2 Transition metal dichalcogenides, elements and structures. **Top)** Periodic table shows the chemical elements that can form layered transition metal dichalcogenides. Shown in grey are the transition metals and in orange the chalcogens. **Middle)** Schematic representation of the band structure, with the *d*-orbital bands splitting and the occupied states for TMDs with different transition metals. Shown in blue are occupied states. Figure from [31]. **Bottom)** Observed polytypes of TMDs. Different types of layers are indicated by the background colour, red for trigonal prismatic, blue for octahedral. The unit cell is shown along the 11-20 projection of the hexagonal structure to facilitate the comparison. Figure is adapted from [33].

2.2 Out-of-plane change dynamics

Throughout this thesis, two kinds of experiments are used to gauge the charge dynamics in layered materials: dc electrical conductivity and optical conductivity. Here we will discuss the general information that can be extracted from a first glance at the experimental data. Relevant results from the literature will be presented and discussed, to familiarize the reader with the type of results and to presents some of the existing open questions related to interlayer charge transport.

In the measurement of dc electrical conductivity (σ), or electrical resistivity ($\rho = 1/\sigma$), an electrical current is forced through the material and the electrical voltage generated across it is measured. The better the material conducts electricity, the lower the voltage. From the measured sample resistance ($R = V/I$) we calculate the material specific resistivity knowing the sample geometry ($\rho = R \cdot Cross\ section/lenght$). Electrical resistivity measurement is a conceptually simple experiment, and the necessary tools to perform it —a current source and a voltmeter— are readily available. The simplicity masks some of the challenges to obtain reliable data. All electrical connections must have a low resistance and be ohmic, which can be inspected by checking the *I-V* curve for each electrode pair. But most critically, in particular for the experiments in this thesis, we have to ensure that the current flows homogenously in the material. The electric field over the material needs to be homogenous, with equipotential lines perpendicular to the expected current flow. The current distribution affects the determination of the sample resistivity in two ways:

- The sample geometrical factor is equivalent to the sample physical dimensions only if current is homogenously distributed. If the current is concentrated only in a smaller section of the sample, calculating the resistivity value from the sample cross section will lead to an overestimation of the material's resistivity.

- Electrical resistivity of a material is a tensor. To measure the resistivity along a specific direction (such as a specific crystallographic direction), the only reliable approach is to ensure that current flows exactly parallel to the desired direction. The problem is increased in anisotropic conductors, as the current will distribute and flow in the material along a path that minimizes the total resistance. This can lead to measuring a combination of the resistivity response along different directions.

The solution to these problems is a rigorous control of the sample geometry, with particular attention to the current leads, to ensure a homogenous current injection. For the specific case of layered materials, determination of transport anisotropy translates into preparing at least two different samples, one where the current flow is parallel to the layers, and one where it is perpendicular. In an electrical resistivity measurement, the electric field driving electrons motion in the material is static with respect to the characteristic time scales of electric interaction and dynamic response. To have a further insight into the dynamic aspects of electronic conduction, optical spectroscopy becomes a valuable approach. Optical conductivity refers to the complex response of the materials, with real and imaginary parts, to the oscillating electric field of incoming electromagnetic radiation. The wavelengths of interest extend from the far-infrared (10 cm^{-1}, 0.3 THz or 1.2 meV) to the UV (50'000 cm^{-1}, 1'500 THz or 6.2 eV). A common approach to determine the optical conductivity, is to measure the sample's reflectivity as a function of frequency. Light incidence is nearly normal to the polished surface of the sample, and the absolute value can be computed using an in-situ reference method by gold evaporation [34]. From the reflectivity frequency dependence, the real and imaginary part of the optical conductivity can be computed thanks to Kramers–Kronig relations. The anisotropic optical response can be investigated using polarized light. The material response is probed along the direction of the electric field of the polarized light. For a sample oriented along the *a*-*c* surface (with *a* and *c* axes orthogonal), one can probe the response along the two axes independently by a 90° rotation of the polarized light.

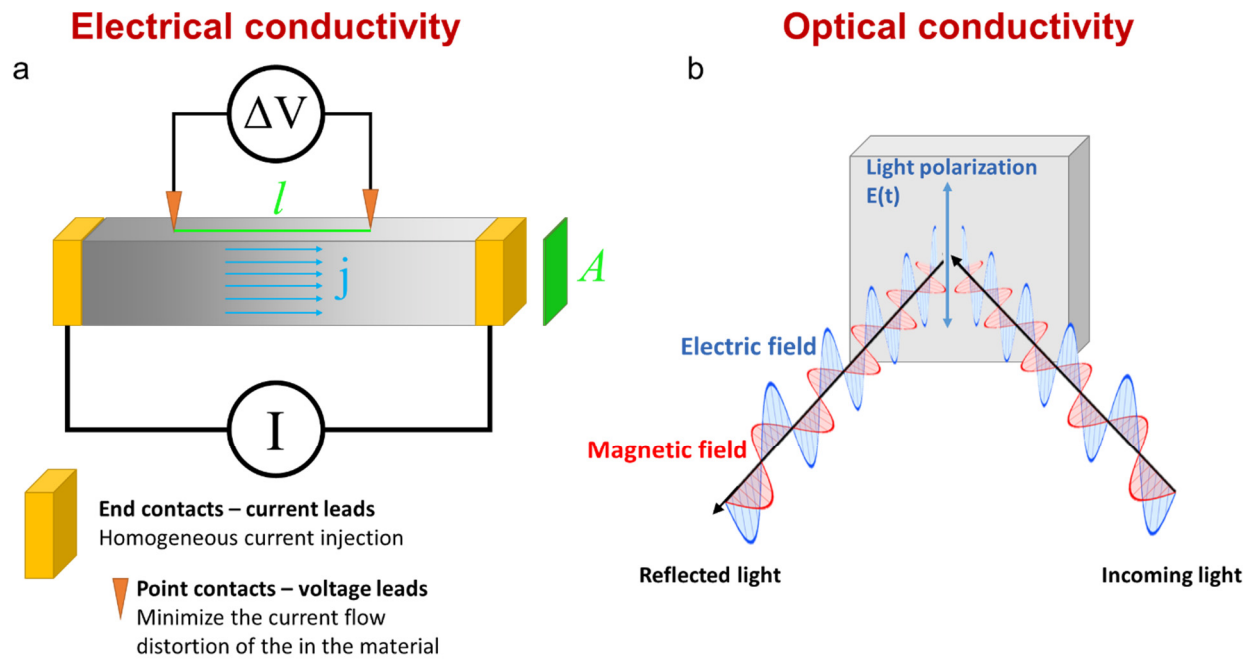

Figure 2:3 Electrical and Optical conductivities. a) Graphical representation of an ideal sample for electrical conductivity measurement. Current density inside the sample is homogeneous over the entire cross section area (A). The current leads cover the entire side surfaces to ensure uniform injection, while the voltage contacts (separated by a distance l) are point-like to interfere as little as possible with the current distribution within the sample. j is the current density. **b)** Frequency dependent optical reflectivity measurements allow to compute the material optical conductivity. The optical response of the sample can be probed in the direction of the electric field for linearly polarized light.

2.2.1 dc electrical resistivity

When measuring electrical resistivity, relevant information are immediately obtained from its absolute value and the temperature dependence. For metals, resistivity increases with temperature ($d\rho/dT > 0$) due to the enhanced scattering. In the case of semiconductors or hopping transport through localized states, the resistivity decreases with temperature ($d\rho/dT < 0$) as a consequence of the thermal activation. Concerning the absolute value, metals have a much lower resistivity, while semiconductors have diverging resistivity for $T \rightarrow 0$ K. The Drude model provides a simple description for resistivity in metals, with the assumption that electrons are moving as free and weakly interacting particles:

$$\rho = {}^{1}/_{\sigma} = \frac{m}{ne^2\tau} = \frac{mv}{ne^2 l} \qquad \text{Equation 1}$$

Here n is the density of conduction electrons, τ the scattering rate, v the electrons drift velocity and l the mean free path. Through the studies of simple alloys or elemental metals, it become evident that it is possible to define an upper limit for electrical resistivity in a metal. The ideal metals under consideration have electron density of 10^{23} cm^{-3} (each atom provides at least one conduction electron), a half-filled band, a spherical Fermi surface (electrons can acquire momentum along every direction). The approximate value of 200 μΩcm is proposed as the maximum resistivity value for metallic materials, beyond which the resistivity tends to saturate as a function of temperature and when further increasing, dρ/dT will change sign [35]. This value is the Ioffe-Regel limit [36], and it is based on the assumption that the electron mean free path cannot be shorter than the interatomic distance. From this notion, and the material specific parameter of an ideal half band metal, one can compute that the ultimate value of resistivity is around 200 μΩcm. Because all the parameters are material specific, the value for resistivity saturation depends on the material [37]. Nevertheless, metals with half-filled

bands can present values of resistivity much above the Ioffe-Regel limit. A notable case are the cuprate high temperature superconductors (HTS). In these materials, electrons interact strongly with each other. This causes the high value of electrical resistivity and is considered as one of the primary causes of the high temperature superconductivity.

Cuprates have been intensely studied, with particular attention to their electrical conductivity properties. It is generally believed that understanding the normal state transport properties might provide the necessary knowledge to create a microscopic model for their superconducting properties. Those materials are layered conductors, with metallic CuO_2 planes sandwiched between insulating layers. The quasi-2D confinement of conduction electrons is regarded as fundamental to sustain the high temperature superconducting phase. The interlayer charge dynamics in cuprates has been studied to gauge the extent of the interlayer coupling and better understand its role in the materials' electronic properties.

When charge carrier concentration is sufficient to sustain superconductivity, in-plane electrical resistivity has a metallic temperature dependence. There are a few important anomalies, such as the resistivity absolute value much higher than the Ioffe-Regel limit and its continuing linear increase with temperature, even up to 1000 K, in contrast to most metals where resistivity will tend to saturate [38]. These properties are common to all cuprates. The difference between cuprates HTS crystalline structures, are the elements and structure of the insulating block layer between the CuO_2 planes. The insulating layer has a prominent role for the interlayer distance and consequently the electronic coupling between neighbouring CuO_2 planes. Here we will review some results for the highly anisotropic $Bi_2Sr_2CaCu_2O_{8-\delta}$ (abbreviated as BSCCO). The crystal structure, visible in Figure 2:4 a, is made out of double CuO_2 layers, separated by a 15 Å thick block of BiO and SrO with rock salt structure.

The concentration of charge carriers is tuned by the oxygen stoichiometry in the rock salt layer. Optimally doped sample has the highest superconducting transition temperature. For increasing doping, at higher oxygen concentration, superconducting transition temperature and in-plane electrical resistivity are reduced, as it was reported by Forró [39]. More surprising is the resistivity of the material when current is flowing across the planes ($\rho_\perp$). For the optimally doped sample, the $\rho_\perp(T)$ has a semiconducting-like temperature dependence, with $d\rho/dT < 0$, and an absolute value much above the Ioffe-Regel limit [40]. The resistivity anisotropy is on the order of 10'000, and the temperature dependence is interpreted as tunnelling-like transport through the insulating layer between two neighbouring CuO_2 planes. For the overdoped sample, its out-of-plane electrical resistivity acquires a metallic-like temperature dependence. Since its absolute value is above 1 Ωcm, the anisotropy is around 6'000. The application of a simple Drude model estimates the electronic mean free path along *c*-axis to be about 10^{-2} Å. This is not only much shorter than the interlayer distance of 15 Å, but it is even shorter than the in-plane interatomic distance. Similar sets of experimental results have been obtained as a result of iodine intercalation [41]. Because of BSCCO's layered structure, iodine atoms can be inserted in between the BiO_2 planes by heat treatment in I_2 atmosphere [42]. This not only increases the interlayer distance by 23 %, but also results in $\rho_\perp(T)$ changing from semiconducting to metallic (Figure 2:4 c). These experimental results have not yet been understood. At the same time, they put forth a fundamental question regarding the out-of-plane conductivity in layered materials. How is it possible to have a metallic resistivity between the planes, when the mean free path deduced from resistivity is order of magnitudes lower than the lattice spacing?

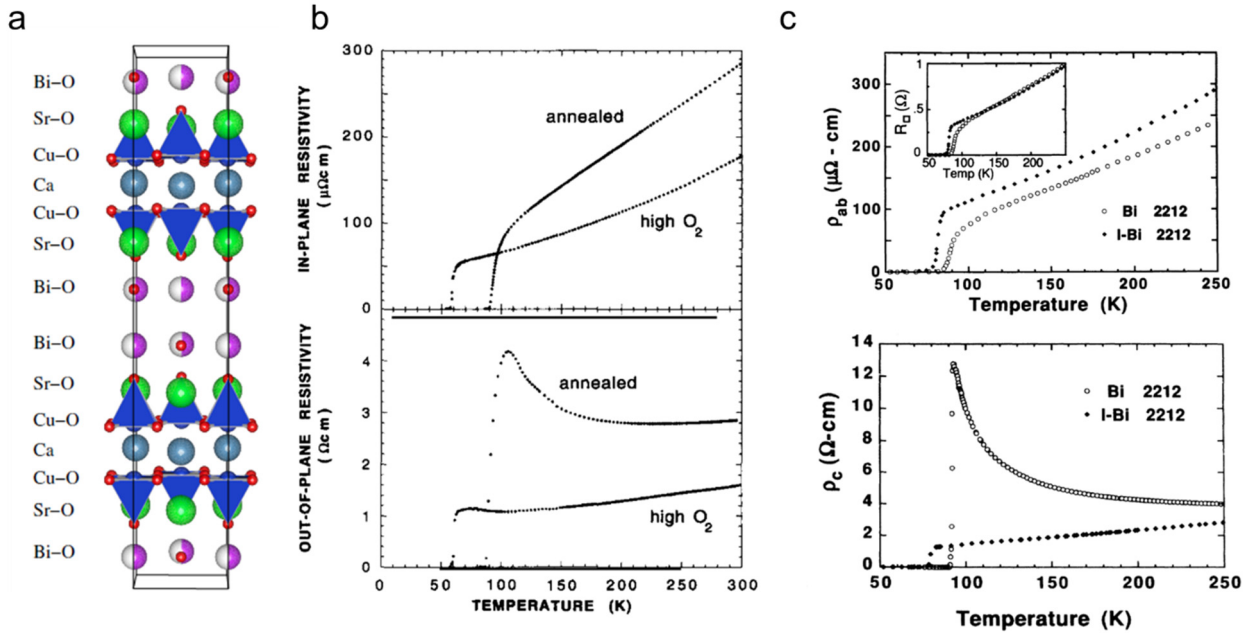

Figure 2:4 Electrical resistivity anisotropy in BSCCO. a) $Bi_2Sr_2CaCu_2O_8$ crystal structure. **b)** Resistivity anisotropy for two BSCCO samples with different doping levels controlled by the oxygen concentration. "Annealed" sample is heat treated in air to reach optimal doping, "high O_2" sample has been heat-treated in a high oxygen pressure and is overdoped. The overdoping reduces the in-plane resistivity, the superconducting transition temperature and induces a change in the derivative for the out-of-plane resistivity temperature dependence. Figure from [39]. **c)** In-plane and out-of-plane resistivity temperature dependence for optimally doped BSCCO and Iodine intercalated BSCCO. Iodine atoms are epitaxially intercalated between the BiO_2 layers. In-plane resistivity is comparable for both, with a metallic temperature dependence ($d\rho/dT > 0$). Out-of-plane resistivity has a semiconducting-like temperature dependence ($d\rho/dT < 0$) for the pristine sample, while it is metallic for the intercalated version besides the increased interlayer distance. Resistivity anisotropy is on the order of 10'000. Figure from [41].

An empirical model was presented in [39], based on the argument that $\rho_\perp$ is diffusive, and the temperature dependence is dominated by the in-plane scattering rate. Out-of-plane conductivity is described by:

$$\rho_\perp = [n(E_F)e^2 l_c^2 \tau_\perp^{-1}]^{-1} \qquad \text{Equation 2}$$

where $n(E_F)$ is the conduction electrons density, $l_c^2\tau_\perp^{-1} = D$ is the diffusion coefficient, l_c is the hopping distance and $\tau_\perp^{-1}$ is the hopping rate which is given by:

$$\tau_\perp^{-1} = (2/h)|t_\perp|^2 \tau_{//}/h \qquad \text{Equation 3}$$

Here $t_\perp$ is the interplane overlap integral and $\tau_{//}$ in the in-plane carrier lifetime. By combining the two equations one finds for the out-of-plane resistivity:

$$\rho_\perp = |t_\perp|^{-2}\tau_{//}^{-1} \qquad \text{Equation 4}$$

This shows that the in-plane and out-of-plane resistivities can be governed by the same relaxation time. The implication is that a metallic-like resistivity, can be the result of an interlayer hopping between conducting planes and not a direct signature of coherent transport between the layers.

The previous description holds for the case of resonant tunnelling, where initial and final states are at the same energy. If the energy of the two states is different, the interlayer tunnelling becomes phonon-assisted with a hopping rate:

$$\tau_{\perp}^{-1} = (\tau_{\perp}^{-1})_0 \exp(-\Delta E/k_B T)^{\alpha} \qquad \text{Equation 5}$$

where $(\tau_{\perp}^{-1})_0$ is the spatial tunnelling factor, ΔE is the energy difference between the states, and the exponent α is a function of the system dimensionality. This model still leaves many open questions when trying to explain the results on BSCCO. For example: What is the cause of the energy mismatch between conducting planes, which changes the sign of dρ/dT ? In the case of change in oxygen stoichiometry, it was proposed that the higher oxygen concentration can reduce the presence of disorder due to interlayer oxygen vacancies. The role of interlayer disorder is less clear for the case of iodine intercalation, for which the additional element in the structure would unavoidably increase the level of disorder.

To reliably answer these questions, one needs to have complete control over the material structure and properties. Despite their scientific interest, cuprates are not an ideal system due to their chemical and structural complexity. In particular, with respect to the interlayer physics, a common question is what is the amount of disorder due to intercalated or interstitial oxygen in the insulating block layers between CuO_2 planes.

In contrast, TMDs are binary materials, able to offer the necessary flexibility to explore different compositions, polytypes and intercalated compounds. We approach the problem of interlayer charge transport from the side of coherent conductivity [43] [44]. In this way it is possible to assess what material modification, in terms of disorder and enhanced interlayer spacing by intercalation, can downgrade the conduction mechanism from coherent to diffusive.

2.2.2 Optical conductivity

One limit in the interpretation of electrical conductivity measurements is that one cannot isolate the individual contributions of carrier density, effective mass and scattering rate. The frequency-dependent response of conduction electrons, measured by optical conductivity, allows us to deconvolute these parameters, and provide additional information to understand the interlayer charge transport. When electrons interact with light, they can absorb the photon if its energy matches the difference between the initial and the final state. As momentum transfer from the photon to the electrons is negligible, only transitions with $\boldsymbol{k}_{initial} = \boldsymbol{k}_{final}$ are possible. There are two kinds of electronic transitions that can be observed by optical spectroscopy on crystalline materials: intraband and interband transitions (Figure 2:5). Intraband transitions involve electrons at the chemical potential. These are the same electrons involved in the dc electrical conductivity response, and are therefore not present in insulating materials. On the other hand, interband transitions involve electrons jumping from an occupied to an empty electronic state, which can be separated by an arbitrary energy difference. In the case of semiconductors, it is the transition between the highest occupied valence band and the lowest unoccupied conduction band that defines the optical band gap.

In our discussion of electron dynamics, we are mostly interested in the low-energy intraband transitions. A simple but effective model is to consider the conduction electrons as free charged particles, with a well-defined effective mass and scattering rate. The oscillating electric field of the incoming light produces an oscillating current density in the material, related by the frequency dependent (optical) conductivity: $J(\omega) = \sigma(\omega)E(\omega)$. The real part of optical conductivity, $\sigma_1(\omega)$, is the in-phase resistive response, while the imaginary part, $\sigma_2(\omega)$, is the out-of-phase inductive response.

In the Drude model, the frequency response of conduction electrons is derived from a forced harmonic oscillator subject to a viscous damping force with a relaxation time τ. The resulting frequency-dependent optical conductivity is:

$$\sigma(\omega) = \sigma_1(\omega) + i\sigma_2(\omega) = \frac{ne^2\tau}{m}\frac{1}{1 - i\omega\tau} \qquad \text{Equation 6}$$

For the limit of dc electric field ($\omega = 0$), the conductivity reduces to Equation 1. At low frequencies, the electron response is purely resistive and in phase with the electric field. As frequency increases, the real part of the conductivity decreases, as the electrons lag while trying to follow the quickly changing electric field. The width of $\sigma_1(\omega)$ is given by the scattering rate. Materials with low dissipation will present a sharp drop in $\sigma_1(\omega)$. With further increase in frequency, the imaginary part of the conductivity becomes larger, and the crossover marks the limit for the in-phase response of electrons to the incoming electric field. Beyond a certain frequency –the screened plasma frequency– the electrons cannot follow anymore the changing electric field. In these conditions, optical reflectivity of the metal suddenly drops from its value close to unity to a few percent. In the coming discussion we will refer to the unscreened plasma frequency (ω_P), which is a function of the electron density and mass only:

$$\omega_P = \sqrt{\frac{4\pi ne^2}{m}} \qquad \text{Equation 7}$$

$$\sigma(\omega) = \frac{\omega_P^2}{4\pi}\frac{1}{1 - i\omega\tau} \qquad \text{Equation 8}$$

From the sole measurement of optical conductivity is therefore possible to separate the contribution of the scattering rate (τ), from that of the number of electrons and their mass combined together (n/m).

This simple model works very well for materials where electronic correlations are weak and mobility is very high. For isotropic metals, this is the case of gold and silver. As for the class of layered materials, a prototypical case is $PdCoO_2$. Its in-plane conductivity is comparable to that of silver and gold at room temperature, and decreases by factor 400 at low temperature (ρ_{ab}(4K) = 8 nΩcm) [45] [46]. Because of the very low scattering rate, intraband and interband optical transitions are clearly separated [47]. Figure 2:5 c shows the measured in-plane optical reflectivity. At low frequencies, reflectivity is nearly constant and close to 1, and it decreases with a sharp plasma edge at 6'000 cm^{-1}. From this data, the in plane optical conductivity is computed through Kramers–Kronig transformation (Figure 2:5 d). Optical response of conduction electrons, the Drude peak, is confined below 1500 cm^{-1}. It is only above 7000 cm^{-1}, at the onset of interband transitions, that optical conductivity increases again. The additional features that are evident at low energy are associated to infrared active phonon modes. Integrating the optical conductivity, it is possible to compute the total number of carriers and their effective mass, following the f-sum rule. The plasma frequency can be computed by limiting the integration to the conductivity contributions from intraband transitions only.

$$\int_0^\infty \sigma_1^{intraband}(\omega)d\omega = \frac{\omega_P^2}{8} \qquad \text{Equation 9}$$

In most other materials this is not so obvious to separate the contributions of intraband transitions only. A common strategy is to find an arbitrary frequency below which intraband contributions are dominant. The special case of $PdCoO_2$, because of the clear separation in optical contributions unambiguously yields a value of ω_P = 33'200 ± 600 cm^{-1} from using Equation 9. Alternatively, the fit of the low frequency Drude component gives ω_P = 33'300 cm^{-1} and $1/\tau$ = 97 cm^{-1}.

The simple Drude model considers only one frequency independent scattering rate. In real materials, multiple scattering channels are present at the same time, each with a characteristic temperature and frequency dependence [48]. The Drude model can then be generalized to include a frequency-dependent scattering rate:

$$\Gamma(\omega) = \frac{1}{\tau(\omega)} = \frac{\omega_P^2}{4\pi} Re\left[\frac{1}{\sigma(\omega)}\right] \quad \text{Equation 10}$$

In the case of a canonical Fermi liquid, the frequency and temperature dependence of the scattering rate obeys:

$$\frac{1}{\tau(\omega)} = A(\hbar\omega)^2 + B(k_B T)^2 \quad \text{Equation 11}$$

In the specific case of $PdCoO_2$, this description was used to describe the discrepancy between the in-plane scattering rate computed from dc electrical conductivity ($1/\tau_{tr}$ = 0.3 cm^{-1}) and the value extracted from optical conductivity ($1/\tau_{op}$ = 97 cm^{-1}). The optical value is the average of the frequency dependent scattering rate.

$$\frac{1}{\tau_{op}(\omega)} = \frac{1}{\omega}\int_0^\infty \frac{1}{\tau(\omega)} d\omega \cong \frac{A}{3\pi^2}\omega^2 \quad \text{Equation 12}$$

As the optical response of free carriers is captured for $\omega \approx$ 1000 cm^{-1}, the resulting optical scattering is around $1/\tau_{op}$ = 80 cm^{-1} with a residual scattering rate in the limit of $\omega \to 0$ of $1/\tau_0$ = 0.14 cm^{-1}, in agreement with transport data [47].

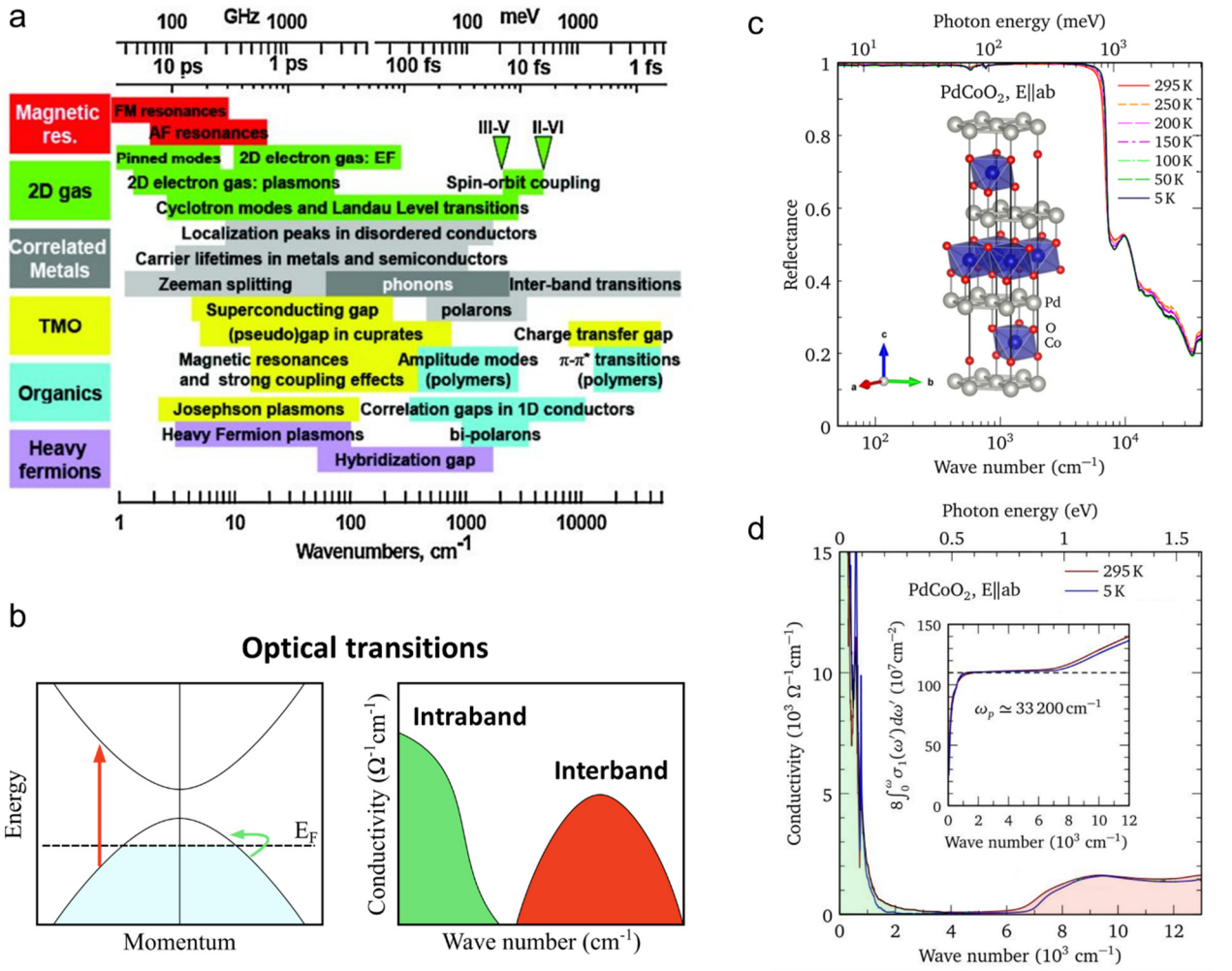

Figure 2:5 Optical conductivity. a) Schematic representation of the characteristic energy scales in correlated electron systems. These different processes can be observed in the real part of optical conductivity. TMO: transition-metal oxides. Figure from [49]. **b)** Optically active electronic transitions as seen in the band structure and in the optical conductivity: intraband transitions (in green) and interband transitions (in red). **c)** In-plane optical reflectivity of $PdCoO_2$. Reflectivity is close to 1 from the lowest measured energy up to 6000 cm^{-1}, corresponding to the screened plasma edge. **d)** Optical conductivity of $PdCoO_2$. The intra and interband transitions are completely separated in energy. The sharp, low energy contribution is the Drude peak, given by the response of conduction electrons. The optical conductivity increase above 7000 cm^{-1} is given by the onset of interband transitions. The inset shows the spectra weight associated with the conductivity, and the computed value of the plasma frequency. Figures adapted from [47].

The results on $PdCoO_2$ are an elegant example of the possibilities offered by optical conductivity measurements to unveil the conduction electron dynamics. On a conceptual level, the very same investigation can be performed for light polarized along the *c*-axis, to study and understand the interlayer charge dynamics. The practical limitation is a consequence of the conduction electrons response being limited to very low energies (far-IR range, from 10 to 200 cm^{-1}). At these wavelengths, optical reflectivity measurements are possible only for samples of few square millimeters in surface, as smaller samples will suffer from the diffraction limit. This is why only those materials that can be grown as single crystals of sufficient size can be measured. In the case of layered materials, single crystals have typical dimensions along the *c*-axis that are limited to a few hundreds of microns, incompatible with far-IR reflectivity measurements. For a few materials, the growth of crystals of sufficient dimensions was possible, and the out-of-plane charge dynamics have been investigated by means of far-IR optical spectroscopy [44] [50] [43]. Optical conductivity data can answer a

basic question regarding the interlayer charge transport: Is it a coherent or incoherent process? In the case of coherent conduction, electrons propagate as Bloch states, and their optical response will follow the Drude model. For incoherent conduction, meaning that electrons hop between localized states, the optical response will lack a sharp increase at low frequencies.

Layered materials have been shown to present both types of behaviour. Layered transition metal dichalcogenides (2H-$NbSe_2$ and 2H-$TaSe_2$) show a clear Drude peak both for light polarized along the *ab*-plane and *c*-axis. Cuprates can manifest either type of interlayer conduction according to the specific compound and carrier density. To better complete the discussion about interlayer charge dynamics probed by optical conductivity, we will review the data on $FeTe_{0.55}Se_{0.45}$ – a layered transition metal chalcogenide that also belongs to the family of Fe-based superconductors. $FeTe_{0.55}Se_{0.45}$, becomes superconducting at 14 K. Reflectance $R(\omega)$ as a function of temperature for both polarization directions is displayed in Figure 2:6 a. Reflectivity is not only much lower for light polarized along *c*-axis, but also the temperature dependence is considerably different. As temperature is reduced, $R_{ab}(\omega)$ is increased at low energy and enhanced at high. On the contrary $R_c(\omega)$ is reduced at every frequency.

More insight into the electronic response is given by the conductivity spectra (Figure 2:6 c). $\sigma_c(\omega)$ does not present a Drude peak at low frequency, suggesting instead an incoherent conduction mechanism. For the in-plane $\sigma_{ab}(\omega)$, a Drude peak is evident at low temperature (18 K). At 6 K, the Drude peak is suppressed by the onset of superconductivity. The optical conductivity data suggests that despite its simple crystalline structure and relatively short interlayer distance, the interlayer conduction in $FeTe_{0.55}Se_{0.45}$ is incoherent. The authors proposed a more general interpretation for the interlayer conduction mechanism, suggesting that it is defined by the in-plane scattering mechanism [43]. By looking at the frequency dependence of the scattering rate (Γ, Equation 10), it is possible to define if the electronic conduction is in a strong or weak dissipation regime. As a reference, if Γ at a specific frequency ω_0 is larger than ω_0 ($\Gamma(\omega_0)/\ \omega_0 > 1$), the material is in a strong dissipation regime. It was proposed that interlayer conduction is coherent, if the material has a weak in-plane dissipation, and incoherent for the strong dissipation regime. The results combining different layered materials are displayed in Figure 2:6 d. It has to be noted that the dissipation in the materials analysed are mostly due to electronic correlations, and not disorder, as proven by their manifestation of quantum oscillations.

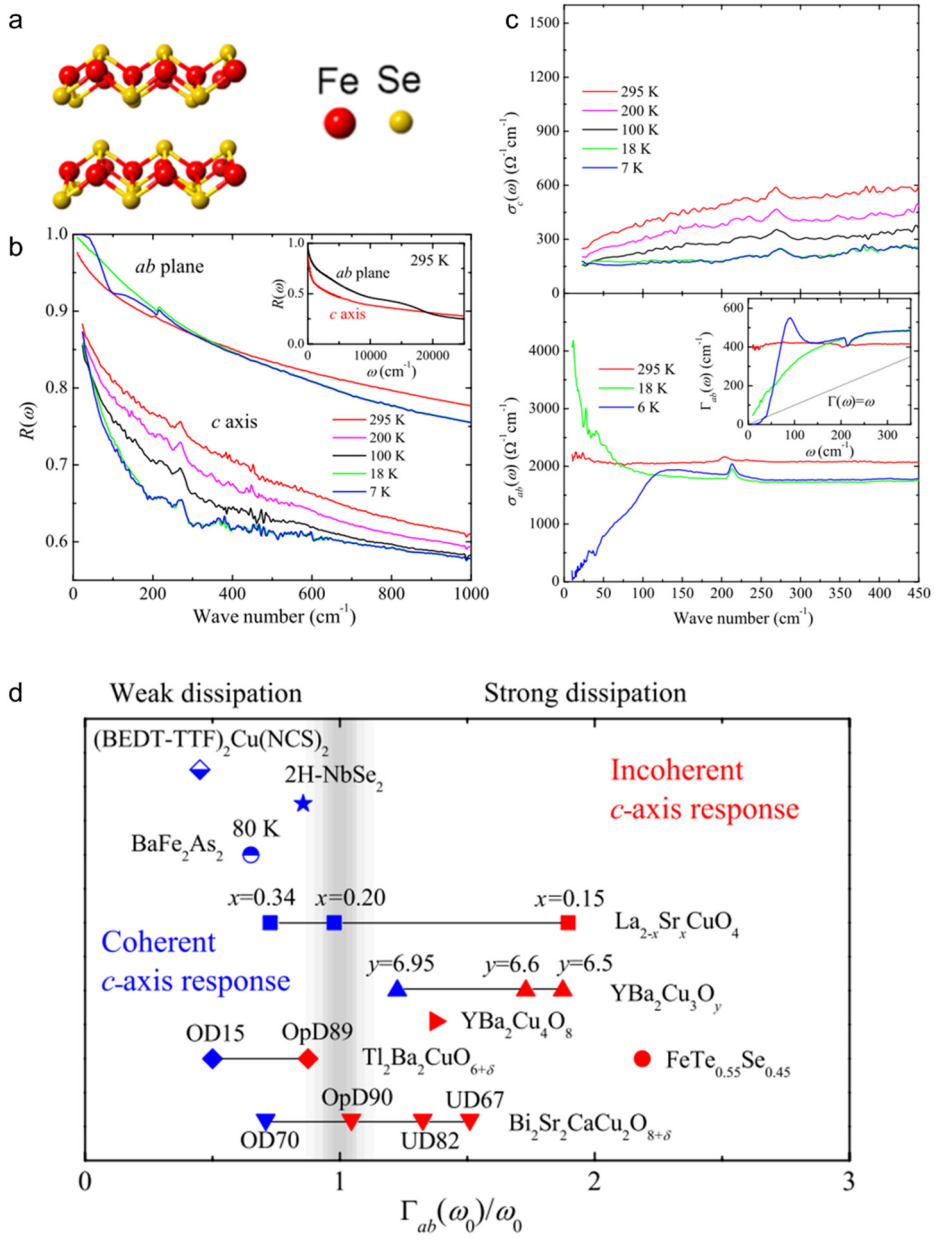

Figure 2:6 Optical conductivity anisotropy. **a)** FeSe crystal structure. **b)** Temperature dependence of the optical reflectance for $FeTe_{0.55}Se_{0.45}$ for in-plane and out-of-plane light polarization. **c)** Out-of-plane optical conductivity at different temperatures. Conductivity is suppressed with lowering temperature and there is no evidence of a Drude peak, suggesting an incoherent out-of-plane conduction mechanism. The inset shows optical conductivity on an extended scale, and the spectral weight loss at low energies with temperatures is not recovered up to 5000 cm^{-1}. Temperature dependence of the in-plane optical conductivity, data at 18 K shows a clear metallic behaviour associated with the Drude peak. Suppression of the optical conductivity at 6 K is due to the onset of superconducting state. **d)** In-plane scattering rate $\Gamma_{ab}(\omega_0)$ divided by ω_0. The value of ω_0 is defined as the frequency that accounts for 30% of intraband transitions' spectral weight. The case of $\Gamma_{ab}(\omega_0)/\omega_0 < 1$ represents weak dissipation regime, while above 1 this is a strong dissipation regime. Layered materials that present coherent *c*-axis response are in blue, and red is for incoherent response. Incoherent response is marked by an absence of Drude peak and suppression of low energy spectral weight with temperature, consistent with $d\rho_c/dT < 0$. The trend suggests that the incoherent response along *c*-axis originates in materials with strong in-plane dissipation. Figures from [43].

2.3 The experimental approach in this thesis

We have seen how the interlayer charge dynamics can be probed by the static and dynamic conductivity. In the latter case, the limitation to study the interlayer charge dynamics is given by the size of the crystal. This limitation can only be solved by developing the crystal growth technique to create high quality and large volume crystals, which was not the goal of this work. On the other side, dc conductivity measurements can be done on samples of every dimension, down to nanometre scale. For this reason the majority of the results in this thesis are based on dc conductivity measurements, for which a new sample preparation methodology has been developed to ensure a high precision in the determination of anisotropic transport properties [51] [52].

The vast majority of scientific articles that discuss interlayer charge transport have a very similar sample design. The electrical contacts are placed on the top and bottom face of a large and much thinner single crystal. The contact preparation can be either done by hand, using silver epoxy to attach the lead wires, or using a two-step lithographic process where the crystal is placed on top of a pre-patterned substrate, and later top contacts are deposited (Figure 2:7 a,b) [53]. This design can lead to two possible sources of problems, depending on the actual materials conductivity anisotropy.

For low anisotropy ($\rho_{\perp} \approx \rho_{||}$), the electrical current density will be focused in the area under the electrodes. This can lead to an incorrect reading on the neighbouring voltage contacts, and an inaccurate evaluation of the geometrical factor. This might lead to an erroneous evaluation of the absolute value

For much larger anisotropy ($\rho_{\perp} >> \rho_{||}$), the current will flow over the entire sample cross section, but its distribution will combine in-plane and out-of-plane contributions. In this situation, if the temperature dependence is different along the two directions, the information will be lost, as the probed voltage will result from a linear combination of $\rho_{\perp}(T)$ and $\rho_{||}(T)$.

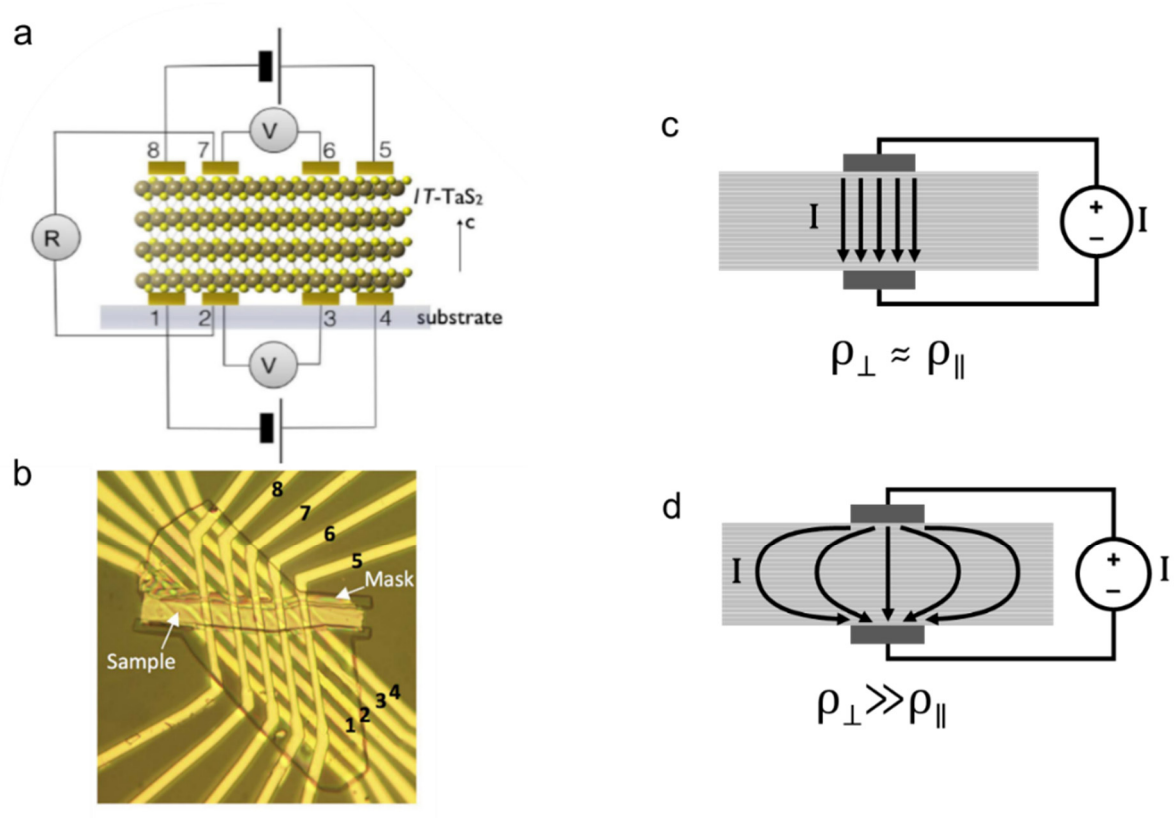

Figure 2:7 Resistivity anisotropy measurement. Schematic representation of the sample geometry for the measurement of resistivity anisotropy. **b)** Optical image of the sample depicted in panel a. Figures from [53] **c)** Current density distribution in the case of a material with low anisotropy. **d)** Current density distribution in a highly anisotropic material.

The sample geometry is imposed by the crystal morphology. To create a sample with an optimal geometry, the current leads would need to extend over the entire surfaces parallel to the *ab*-plane, and the voltage leads should be placed on the side surfaces along the *c*-axis, as displayed in Figure 2:8 a. As the crystals are a few microns thick, this is practically impossible to do by hand. On the other side, lithography does not allow to create samples with this thre- dimensional geometry.

The most practical solution arrived with the implementation of focused ion beam (FIB) microfabrication. The highly focused ions can be used to etch locally any material with a submicrometre precisions, and at the same time the imaging possibility offered by the integrated electron microscope enables a direct feedback loop for the operator. With this technique it is possible to create complex three-dimensional structures from any conducting material. Because the fabrication process does not use a mask, it can be divided into multiple steps, and integrate metal deposition by e-beam sputtering so as to create electrical contacts of the highest possible quality. A complete review on the latest advancements of this technique for the study of complex materials has been recently published in [54]. Complete details on the fabrication process can be found in the section 7.1.

Figure 2:8 b shows the electron microscopy image of a typical microstructured sample created by FIB for the investigation of transport anisotropy. The single crystal (in purple), is extracted from the starting material by removing a rectangular prism, with the largest surface along the *ac*-plane. Focused ion etching is the only approach that enables to shape the delicate layered materials without inducing undesired exfoliation. The sample is then shaped to create a continuous conducting path between the two current leads. Three sections that run along specific crystallographic directions (two along *c*-axis and one along the *ab*-plane) have pairs of

voltage leads, which are created by etching sample material. Electrical connections to the current source and voltmeter are then possible thanks to the sputtered gold film on the support substrate. The specific geometry is justified by the desire of probing at the same time both the in-plane and out-of-plane response, for the very same material in the same conditions (temperature, magnetic field, high-pressure).

It is thanks to the sophisticated sample preparation technique by FIB, that new and surprising properties of layered materials have been observed in this thesis. To further justify our results, in particular when in conflict with previous reports by several orders of magnitudes, I have performed finite elements simulations. The simulations further confirm of the validity of this approach, and the specific results can be found in section 7.1.3.

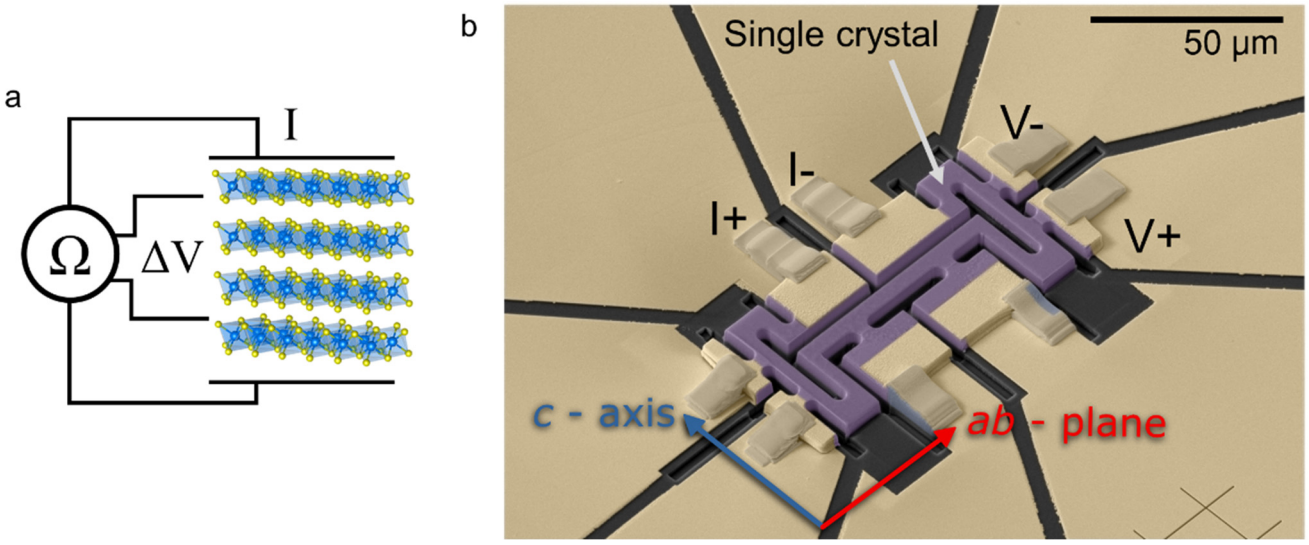

Figure 2:8 Microstructured sample. a) Ideal sample geometry for the precise determination of out-of-plane electrical resistivity. **b)** Electron microscopy image of a FIB microstructured sample of a layered material investigated in this thesis (1T-TaS_2). False colouring is used for illustrative purposes. The arrows indicate the orientation of the crystal (purple). A layer of gold (yellow) forms the conductive paths between the crystal and external leads. The rectangular ramps, created using in-situ platinum deposition, provide mechanical stability and improve the continuity of the gold layer.

Chapter 3 Transport anisotropy: a view on band structure and Fermi surface topology

In the previous chapter we introduced the experimental measurements that will be discussed throughout this thesis: dc electrical resistivity and optical conductivity. Those results used a free-electron model, in which conduction electrons are treated as classical gas of particles with an associated mass, scattering rate and carrier density. This approach is able to provide sufficiently accurate description of simple metals through the Drude equation for dc electrical conductivity (Equation 1) and Drude-Lorentz model for optical conductivity (Equation 6). Before moving on to the experimental results of this thesis, we will see in this section a more detailed description of the microscopic mechanism of charge conduction based on a semiclassical model. Conduction electrons are considered in their quantum mechanical nature, and their contribution to charge transport is intimately related to the band structure of the material in which they exist. From a precise knowledge of the material crystalline and electronic structure, one can attempt to predict the anisotropic electron dynamics. Before moving to the specific cases presented in the following sections, we need to find the answer to the following question: how do electrons move inside a material?

Electrons in a crystalline material are affected by the periodic potential of the lattice ions. As a consequence, the electrons form Bloch states. For a free electron, momentum, energy and velocity are linked by simple analytical relations. For Bloch states, their relation is more complex and is specific to the lattice symmetry and electronic bands structure. The following table summarizes the differences between the description of free electrons and Bloch states.

Table 1

	Free electron model	**Bloch state**
Quantum numbers (excluding spin)	$\boldsymbol{k}$ ($\hbar\boldsymbol{k}$ is the momentum)	$\boldsymbol{k}, b$ ($\hbar\boldsymbol{k}$ is the crystal momentum and b is the band index)
Energy	$\varepsilon(\boldsymbol{k}) = \frac{\hbar^2\boldsymbol{k}^2}{2m}$	Every band of index n, has a specific form of $\varepsilon_b(\boldsymbol{k})$. It is a periodic function in the reciprocal crystal lattice $\varepsilon_b(\boldsymbol{k}+\boldsymbol{K}) = \varepsilon_b(\boldsymbol{k})$
Velocity	Mean velocity of an electron of wave vector $\boldsymbol{k}$ is: $\boldsymbol{v} = \frac{\hbar\boldsymbol{k}}{m} = \frac{1}{\hbar}\frac{\partial\varepsilon}{\partial\boldsymbol{k}}$	Mean velocity of an electron the band n and with wave vector $\boldsymbol{k}$: $\boldsymbol{v_b}(k) = \frac{1}{\hbar}\frac{\partial\varepsilon_b(\boldsymbol{k})}{\partial\boldsymbol{k}}$

In a crystalline material the electronic states are the results of the hybridization of the different atomic orbitals of the constituting materials. The spatial configuration of the atomic orbitals' overlap affects the directions of electrons propagation, and results in the specific dependence of the electrons energy to wave vector $\varepsilon_b(\boldsymbol{k})$. The energy of the highest occupied electronic level is the Fermi energy E_F, which for the case of conducting

materials is located inside a band. Only the electrons that are in proximity of E_F in a partially filled band can contribute to the current flux inside a material. The projection in reciprocal space of the constant energy surface at E_F is called the Fermi surface, and it is specific to every material. The velocity vector of conduction electrons is perpendicular to the Fermi surface, and its geometry will be later discussed to predict the anisotropic conduction. In special situations, the Fermi surface topology approach that of a sphere, and the electron velocity will be parallel to $\boldsymbol{k}$ (the vector connecting the centre of the Brillouin zone to any point of the surface. In this case the propagation of Bloch electrons under applied electric field closely resemble that of free electrons. This is the case of alkaline metals or noble metals such as copper, silver or gold. These are very special cases, as in most metallic materials the band structure and Fermi surface have a much more complicated geometry. This can be seen in Figure 3:1, where copper and rhodium Fermi surfaces are compared. The two elementals metals share the same crystalline structure, but only for copper the surface is close to that of a sphere, while rhodium has more complex Fermi surface in which electron velocity and wave vector are not collinear. The reason for their difference is the kind of atomic orbitals involved in the formation of the band which crosses chemical potential. In copper, the *s*-orbitals are involved, producing a weak directional dependency. In the case of rhodium the presence of *d*-orbitals produces a more marked directional dependency that translates into a complex Fermi surface.

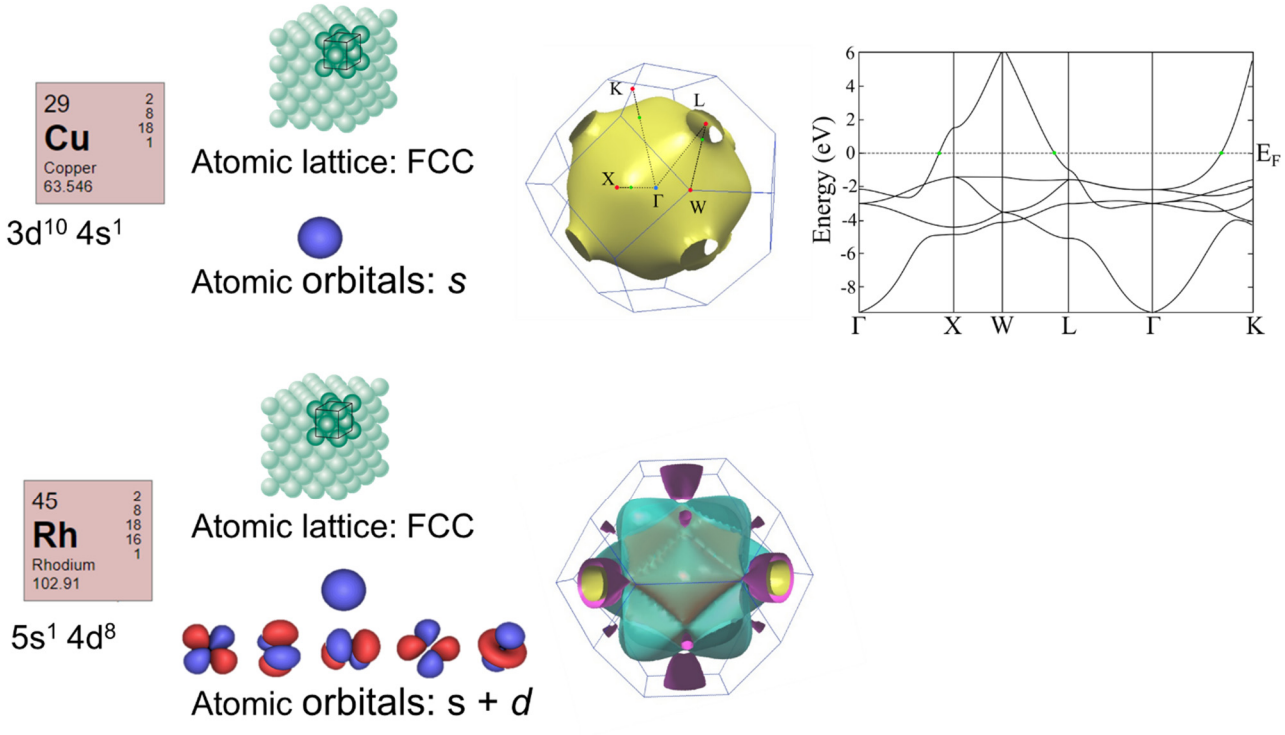

Figure 3:1 Band structure and Fermi surface of metals. The band structure of crystalline materials is created by the overlapping of atomic orbitals of all the atoms organized in the periodic lattice. The Fermi surface represents the wave vector distribution of electrons at the highest occupied state in the limit of T → 0 K. On top is the example of copper, where atoms form an FCC lattice and the highest energy level originates from *s*-orbitals. Fermi surface is nearly spherical and originate from only one electronic band. At the bottom is the example of rhodium. Rh atoms form an FCC lattice like those of copper, but electronic states at the chemical potential originate from *d* and *s* orbitals. The Fermi surface is created by different branches, marked by the colours, which come from different bands crossing the chemical potential. Figures edited from [55].

The state of all electrons in the system can be described by the semiclassical distribution function $g_b(\boldsymbol{r}, \boldsymbol{k}, t)$. Application of an external electric field $\boldsymbol{E}$, produces a net current by unbalancing the distribution of electrons wave vectors inside the material: $(t) = \boldsymbol{k}(0) - \frac{e\boldsymbol{E}t}{\hbar}$. To stop the indefinite variation of electrons momentum —that would lead to infinite conductivity—scattering events occur with a probability $1/\tau_b(\varepsilon(\boldsymbol{k}))$. In the relaxation time approximation, the distribution function under applied electric field is:

$$g(\boldsymbol{k}) = g^0(\boldsymbol{k}) - e\boldsymbol{E} \cdot \boldsymbol{v}(k)\tau_b(\varepsilon(\boldsymbol{k}))\left(-\frac{\partial f}{\partial \varepsilon}\right) \quad \text{Equation 13}$$

Here $g^0(\boldsymbol{k})$ is the equilibrium distribution function and f is the Fermi-Dirac distribution. The argument $\left(-\frac{\partial f}{\partial \varepsilon}\right)$ is zero except in the k_BT range around Fermi energy, as electrons of these energies can produce a net current flux in the material when the applied electric field disturbs their momentum distribution. The net current density produced by the electrons flux is the averaged contribution of electron velocities over all electronic states. Because of the large number of states, the sum can be converted into an integral over the number of electrons per unit volume element ($d\boldsymbol{k}/4\pi^3$).

$$\boldsymbol{j} = -e\int \frac{d\boldsymbol{k}}{4\pi^3}\boldsymbol{v}(\boldsymbol{k})g(\boldsymbol{k}) \quad \text{Equation 14}$$

The conductivity tensor, $\boldsymbol{\sigma} = {}^{\boldsymbol{j}}/_{\boldsymbol{E}}$ is the sum of the conductivity over all bands (b) crossing the Fermi energy:

$$\boldsymbol{\sigma} = \sum_b \boldsymbol{\sigma}^{(b)} \quad \text{Equation 15}$$

$$\boldsymbol{\sigma}^{(b)} = e^2\int \frac{dk}{4\pi^3}\boldsymbol{v}_b(\boldsymbol{k})\boldsymbol{v}_b(\boldsymbol{k})\tau_b(\varepsilon(\boldsymbol{k}))\left(-\frac{\partial f}{\partial \varepsilon}\right) \quad \text{Equation 16}$$

The properties of conductivity are therefore strongly related to the band structure at the Fermi energy. The computed conductivity is a tensor, and while in the free electron model **j** is parallel to **E**, for the Bloch states this condition is not necessarily true. Current and electric field will be parallel along the crystal symmetry directions, or for along any direction in cubic crystals. This is the reason behind the extreme level of precision necessary in the sample preparation done in this thesis. In the semiclassical equation of electrical conductivity there is no explicit description of the electron mass or density of electrons, and we will see how these quantities relate to the band structure and Fermi surface geometry of the material.

Electrons moving in a crystal are affected by the strong interactions with the atomic potential. In the effective mass approximation, the electrons are considered as free particles, but their mass is renormalized to account for the interaction with the lattice. The effective mass is a tensor that is defined as:

$$[\boldsymbol{M}^{-1}(\boldsymbol{k})]_{ij} = \pm\frac{1}{\hbar^2}\frac{\partial^2\varepsilon(\boldsymbol{k})}{\partial k_i \partial k_j} = \pm\frac{1}{\hbar}\frac{\partial v_i}{\partial k_j} \quad \text{Equation 17}$$

The two possible signs represent the behaviour of charge carriers as electrons or holes. In the case of hole conduction, the electrons velocity is antiparallel to the wave vector, and under an applied electric field they behave as positively charged particles. For diagonal components, it is evident that the effective mass is proportional to the electronic band curvature. It is then possible to further simplify the Equation 16, leading to the form of conductivity that depends on the effective mass tensor:

$$\boldsymbol{\sigma}^{(b)} = e^2 \int_{occupied\ states} \tau_b(\varepsilon(\boldsymbol{k}))\frac{d\boldsymbol{k}}{4\pi^3}\boldsymbol{M}^{-1}(\boldsymbol{k}) \quad \text{Equation 18}$$

The concept of effective mass, is very useful in the cases where Fermi energy is in close proximity to the top or bottom of the band, where the band curvature is well defined. This is the case of doped semiconductors and semimetals, in which only a very small portion of the band is filled. When the occupied band is nearly parabolic near the chemical potential, we recover the classical Drude expression of free electron conductivity, by putting $[\boldsymbol{M}^{-1}(\boldsymbol{k})]_{ij} = 1/m^*$.

$$\boldsymbol{\sigma}^{(b)} = \frac{ne^2\tau_b}{m^*} \qquad \text{Equation 19}$$

Here n is the total number of electrons that occupy the band b, which is the results of the integration. In Equation 19 all the contribution of the band structure to electrons conduction is contained in the effective mass. A very special condition can be observed in some materials, where the bands in proximity to the chemical potential have a linear energy dispersion. This is the case of Dirac electrons [56], as those found in graphene [15].

For the case of half-filled band metals, the general simplification of the effective mass might not be accurate as the assumption of it being independent of $\boldsymbol{k}$ may not be true anymore. In this scenario it is appropriate to look for alternative simplifications of Equation 16. Another approach is to compute the electrical conductivity from the electron velocity over the Fermi surface. In the effective mass approximation, the role of the integral was to compute the density of electrons, while in this case is to average their velocity. Band structure and Fermi velocity are determined by ab initio calculations such as density functional theory. Figure 3:2 displays for illustrative purpose the Fermi surfaces of Cu and Rh, with Fermi velocity indicated by the colour scale. For the determination of conductivity along a specific high symmetry direction (x) the Equation 16 can be further simplified as:

$$\sigma_x^{(b)} = \frac{e^2}{4\pi^3\hbar}\sum_b \iint_{S_F^b} \frac{\tau_b(\boldsymbol{k})v_{x,b}^2(\boldsymbol{k})}{|\boldsymbol{v}_b(\boldsymbol{k})|}dS \qquad \text{Equation 20}$$

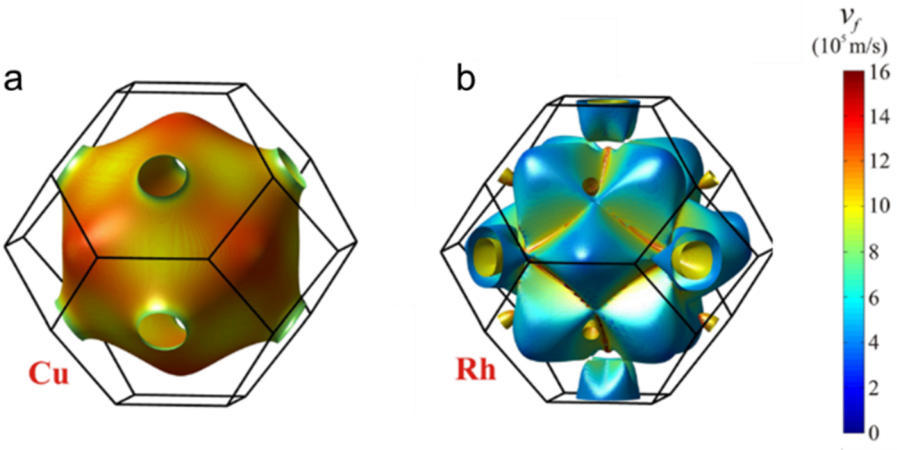

Figure 3:2 Fermi surface and Fermi velocity. *Figure from* [57].

The scattering rate is considerably more challenging to determine a priori, as it is also affected by the concentration and type of defects inside a material, which is not easy to predict. A suitable approximation can be to consider a constant relaxation time, $\tau_b(\boldsymbol{k}) = \tau$:

$$\frac{\sigma_x^{(b)}}{\tau} = \frac{e^2}{4\pi^3\hbar}\sum_b \iint_{S_F^b} \frac{v_{x,b}^2(\boldsymbol{k})}{|\boldsymbol{v}_b(\boldsymbol{k})|} dS \qquad \text{Equation 21}$$

Correspondingly one can use the concept of mean free path (l) approximation, as it is related to the relaxation time by $\tau_b(\boldsymbol{k}) = l/|\boldsymbol{v_k}(\boldsymbol{k})|$

$$\frac{\sigma_x^{(b)}}{l} = \frac{1}{l\rho} = \frac{e^2}{4\pi^3\hbar}\sum_b \iint_{S_F^b} \frac{v_{x,b}^2(\boldsymbol{k})}{\boldsymbol{v}_b^2(\boldsymbol{k})} dS \qquad \text{Equation 22}$$

The same model can describe the frequency dependence of optical conductivity produced by intraband transitions around the chemical potential. In this case, the integral of electron velocities over the Fermi surface replaces the term *n/m* in the classical Drude description, which defines the material plasma frequency.

$$\omega_P^2 = \frac{e^2}{\pi^2\hbar}\sum_b \iint_{S_F^b} \frac{v_{x,b}^2(\boldsymbol{k})}{\boldsymbol{v}_b^2(\boldsymbol{k})} dS \sim e^2\left(\frac{n}{m}\right) \qquad \text{Equation 23}$$

The above presented equations are applicable only if electrons form well-defined Bloch states along every direction inside the crystal. This is a possible problem for out-of-plane conduction in layered materials. To verify the validity of semiclassical equations of motion, one can search for the experimental fingerprints of coherent propagation of conduction electrons. In electrical conductivity this can be the temperature dependence — the case of $\mathrm{d}\rho/\mathrm{d}T > 0$ can imply that conductivity is coherent and limited by thermally excited phonon modes. A more robust proof can be the frequency dependence of optical conductivity, where the evidence of a Drude peak is a clear indication that electron conduction is coherent.

The semiclassical equations described conductivity as a tensor, and are therefore well suited for the study of anisotropic materials. In the next sections of this chapter we will apply those equations to the study of real materials, and compare the theoretical estimations with experimental results.

3.1 Electronic bands dispersion and transport anisotropy

We will begin our discussion about anisotropic charge dynamics in layered materials with $ZrTe_5$. This material is a semimetal, meaning that the bands close to the Fermi level are nearly full/empty, resulting in a low concentration of charge carriers with high mobility, a small and anisotropic Fermi surface, and most importantly, weak electronic correlations. The simple electronic structure, and the presence of only two bands in proximity to chemical potential, make it possible to write a model Hamilton to describe the electronic properties of this material. $ZrTe_5$ recently received a lot of scientific attention for its topological properties, extremely high mobility and the relativistic-like dispersion of conduction electrons [58] [59] [60] [61][62]. A band gap opens in the centre of the Brillouin zone due to the strong spin orbit interaction [63], which gives is at the origin of the material's topological properties.

Throughout this chapter we will discover that $ZrTe_5$ is a relatively simple material with respect to its electronic structure. Conduction and valence bands both have only one minimum/maximum at the centre of the Brillouin zone, divided by a small direct gap. At lowest temperature the chemical potential is just above the bottom of the conduction band. As a consequence, the Fermi surface is a single, small and symmetrical pocket. Because electron velocity is collinear to the wave vector, the simplification of quasi free electrons is accurate. The anisotropic response can be predicted from the band energy dispersion $\varepsilon_i(\boldsymbol{k})$, where i is the direction of conduction, using a similar approximation to the effective mass (Equation 17 and Equation 18).

$ZrTe_5$ is peculiar in several ways: it has a linear band dispersion in-plane, which is anisotropic as a consequence of the quasi-1D crystalline structure. The conductivity anisotropy will be studied in all the three principal crystallographic directions, and the results compared with the theoretical expectations. Because of the linear band dispersion, the concept of effective mass cannot be applied. Instead, we look at the effective number of carriers n to quantify the anisotropic response. In the semi classical description, number of carriers and effective mass are related to each other, as n/m is the results of the same integration. It is therefore possible to arbitrarily assign to one or the other the anisotropic response of the material.

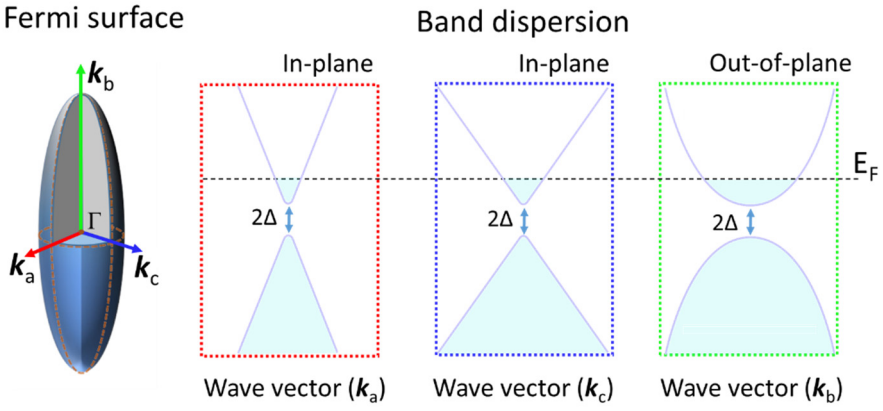

Figure 3:3 Fermi surface and band dispersion in $ZrTe_5$. Fermi surface and representation of the band dispersion along the principal lattice directions. Along the *a*-*c* plane, bands have a linear dispersion, steeper along *a*-axis. Band dispersion along the *b*-axis (out-of-plane) is parabolic. Dashed areas are occupied states below the Fermi energy. 2Δ is the magnitude of the small direct band gap.

The next section will provide a detailed description of $ZrTe_5$ band structure in close proximity to the chemical potential, and the model Hamiltonian proposed to describe its electronic properties. Optical spectroscopy and magneto-optical measurements will be used to fix the free parameters of the model Hamiltonian, necessary for the later discussion about transport properties. First the anomalous in-plane transport properties will be presented, and to conclude the anisotropic conductivity will be discussed.

3.1.1 $ZrTe_5$: crystal and band structure

The $ZrTe_5$ layered structure, can be seen as weakly bound planes made by $ZrTe_3$ chains running along the *a*-axis, with Te_2 zig-zag ladders intercalated between them, Figure 3:4 a. The interlayer distance, between the centre of two overlapping Zr chains is 7.25 Å. Because of its layered structure, it can be easily exfoliated along the *ac*-plane, but it has also a natural tendency to cleave along the Te_2 chains. When repeatedly exfoliated with the classic scotch tape approach, thin needle-like flakes are produced, while materials like graphite of TMDs produces larger flakes. The presence of two cleaving planes makes the creation of devices from thin exfoliated crystals very challenging, making it nearly impossible to create Hall bar samples. Scanning tunnelling microscopy images collected on exfoliated crystals clearly show that $ZrTe_5$ cleaves along the *ac*-plane, with atomic flat surfaces, as well as along the *a*-axis resulting in atomically sharp edges [64]. In this sense the material can be better classified as having a quasi-1D crystalline structure.

The electronic band structure has been obtained by first principle calculations, using density functional theory (DFT) with the generalized gradient approximation (GGA), and the full-potential linearized augmented plane-wave (FP-LAPW) method with local-orbital extensions in the WIEN2k implementation, as detailed in ref [65]. Figure 3:4 b,c shows the Brillouin zone and the electronic band structure. A small direct bandgap opens at the gamma point of the Brilliouin zone due to spin orbit coupling, making the material a candidate topological insulator. The energy dispersion of the conduction and valence bands is very steep and linear along the in-plane directions (*ac*-plane or *X*-*Γ*-*Z* symmetry directions), with a much weaker and parabolic energy dispersion along the out-of-plane direction (*b*-axis or *Γ*-*Y* symmetry direction) [65]. Both conduction and valence bands are based only on Te p orbitals, which are located on both the $ZrTe_3$ chains and Te_2 ladders [63]. This is a peculiarity of this transition metal chalcogenide with respect to many others presented in this thesis, mostly sulphides and selenides, where the band structure at chemical potential is dominated by the transition metal *d* orbitals.

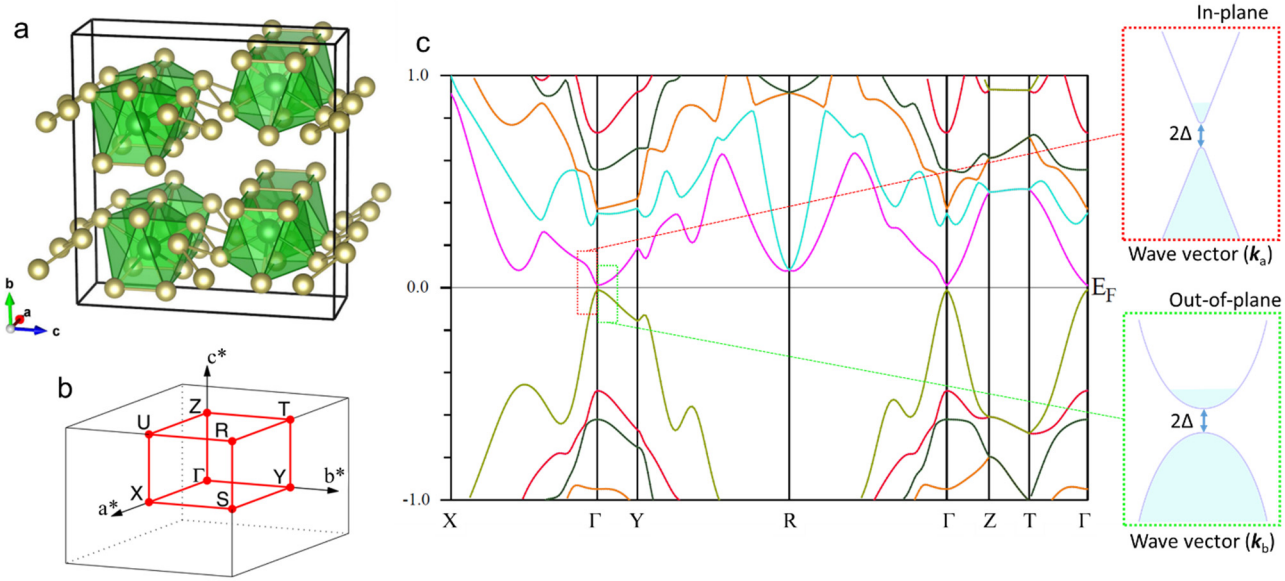

Figure 3:4 Crystal and electronic structure of $ZrTe_5$. a) Orthorhombic structure of $ZrTe_5$ in which zirconium atoms (green balls) are surrounded by tellurium atoms (yellow balls). The unit cell is shown by a solid line. The *b*-axis points perpendicular to the planes, and the zirconium zig-zag chains run along a-axis. **b)** Conventional orthorhombic first Brillouin zone of $ZrTe_5$ showing the high symmetry points. **c)** Electronic band structure determined by DFT, which considers spin-orbit coupling (SOC). Conduction and valence bands are separated by a small gap opened by SOC in Γ.

We proposed a description of the low energy electronic structure by the following effective model. The theoretical description considers a linear Dirac-like dispersion in the *ac*-plane and a parabolic energy dispersion along the out-of-plane direction (*b*-axis).

$$H = \begin{pmatrix} \Delta + \frac{\hbar^2}{2m^*}k_b^2 & \hbar v_a k_a - i\hbar v_c k_c \\ \hbar v_a k_a + i\hbar v_c k_c & -\Delta - \frac{\hbar^2}{2m^*}k_b^2 \end{pmatrix} \quad \text{Equation 24}$$

Here m* is the electron mass along the out-of-plane direction

Eigenvalues from such a Hamiltonian are symmetrical with respect to the band gap middle:

$$\varepsilon_{2,1k} = \pm\sqrt{\hbar^2(v_a k_a)^2 + \hbar^2(v_c k_c)^2 + \left(\Delta + \left(\hbar^2/_{2m^*}\right)k_b^2\right)^2} \quad \text{Equation 25}$$

This model will be later used to study the anisotropic transport properties of $ZrTe_5$. Before that, all the free parameters—band gap 2Δ, in-plane velocities v_a, v_c, out-of-plane effective mass m*— need to be determined from experimental results. To accomplish this, far-infrared optical spectroscopy measurements have been performed. Thanks to optical spectroscopy, it is possible to access information on the band structure at energy resolutions that are experimentally not accessible by angle resolved photoemission spectroscopy (ARPES), and below the error range for computational approaches. In addition, far-infrared light can probe the bulk properties of the materials, making a later comparison of the results with transport measurements more relevant.

3.1.2 Magneto-optical determination of band parameters

For materials with optical bandgap in the far-infrared energy range (2Δ < 100 meV), a convenient approach for its determination is the measurement of Landau level transitions under applied magnetic field. External field induces a quantization of the energy levels in the material band structure, whose separation in energy depends on the applied field. Under microwave irradiation, electrons can be excited between different levels, producing sharp optical absorptions at finite wavelengths. By measuring optical transmittance as function of magnetic field it is possible to determine the inter-Landau level transition and their dispersion as function of field. Figure 3:5 a,b schematically represents the band structure and density of states of $ZrTe_5$ with and without applied magnetic field.

The plot in Figure 3:5 c displays the excitations between Landau levels transition as function of magnetic field applied along the *b*-axis. The transition energy dependence on magnetic field is modelled by using the Hamiltonian presented in Equation 24.

$$\tilde{\epsilon}(B) = \pm\sqrt{2\hbar e v_a v_c BN + \Delta^2} \quad \text{Equation 26}$$

The experimental data (blue dots) are modelled by Equation 26, takin into account the selection rules between different energy levels. From the fitting of experimental data we determined a band gap of 2Δ = 6 meV, and in plane electrons velocities of v_a= 7.0 10_5 m/s and v_c= 7.0 10_5 m/s. The $\sqrt{B}$ field dependence of the Landau level transition is a direct consequence of linearly dispersing band in the a*c*-plane, which was normal to the direction of light propagation in the experiment.

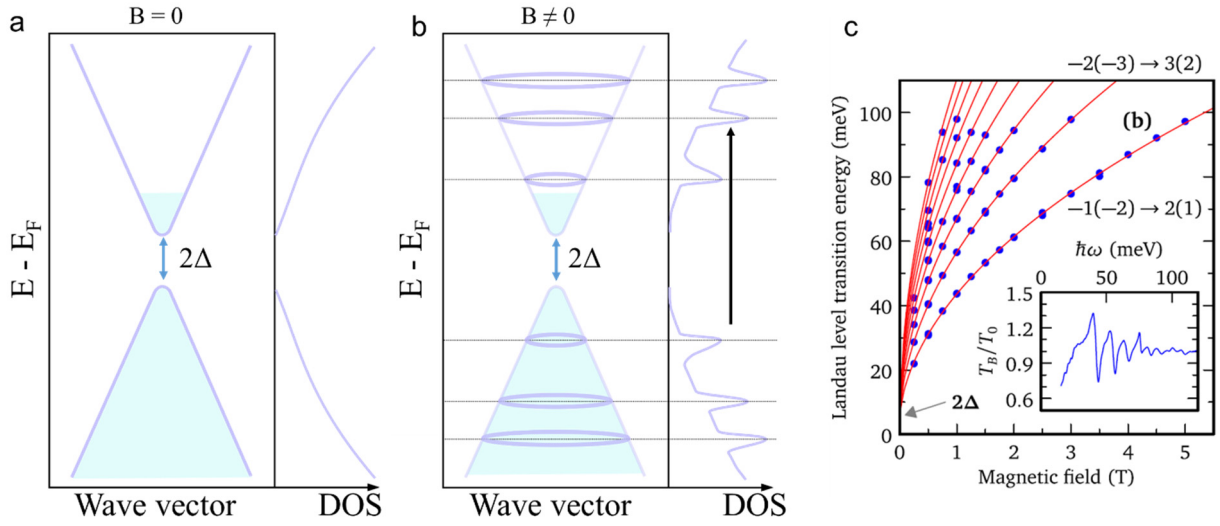

Figure 3:5 Band gap determination for $ZrTe_5$. a) Simplification of the linear dispersing bands centred in Γ. The dashed area represents occupied states in the limit of $T \rightarrow 0$ K. On the right is schematically represented the density of states as function of energy. **b)** Landau level quantization of the band structure under applied magnetic field. The vertical black arrow represent optical transitions between Landau levels. **c)** Landau level transition energies obtained from magneto-optical transmission measurements on sample A, data recorded at $T = 2$ K. Red lines are a fit to Equation 26; the gap $2\Delta = 6$ meV is indicated by the grey arrow. The two lowest observed transitions are labelled. The inset shows a relative magneto transmission spectrum for $B = 1$ T.

Because $ZrTe_5$ is a semimetal, the very low number of carriers can be strongly affected by the concentration of extrinsic defects, which are inevitably introduced during growth. The different level of doping shifts the Fermi level away from the mid-gap position, affecting the in-plane electrons velocities. Thanks to optical conductivity measurements, it was possible to determine the position of the chemical potential for two samples of $ZrTe_5$, synthesised by different techniques: chemical vapour transport and flux. Optical data have been recorded at 5 K, so that Fermi-Dirac distribution is close to a step function around E_F, and onset of interband transitions become very sharp in energy. The optical response in $\sigma_1(\omega)$ from conduction electrons is confined to frequencies below 5 cm^{-1}, due to the small Drude scattering rate. Moreover, the interband scattering rate is very small, which results in a clear separation of intra- and interband transitions. The onset energy for interband excitation, is given by the Pauli edge, which is defined as the chemical potential energy difference with respect to the band gap. Optical excitations can only occur when photon energy is twice of the chemical potential ($2E_F$), as indicated by the red arrow in Figure 3:6 a, that is the minimal energy for a vertical transition between occupied stated and the lowest energy unoccupied states. The two samples that have been investigated differ in the doping level doping, as a consequence of the different synthesis approach, tellurium flux for sample A ($E_F = 28$ meV) and chemical vapour transport ($E_F = 74$ meV) for sample B. The different growth technique affects the Te stoichiometry (typically chemical vapour transport produce chalcogen deficient materials), consequently changing the carrier density [66].

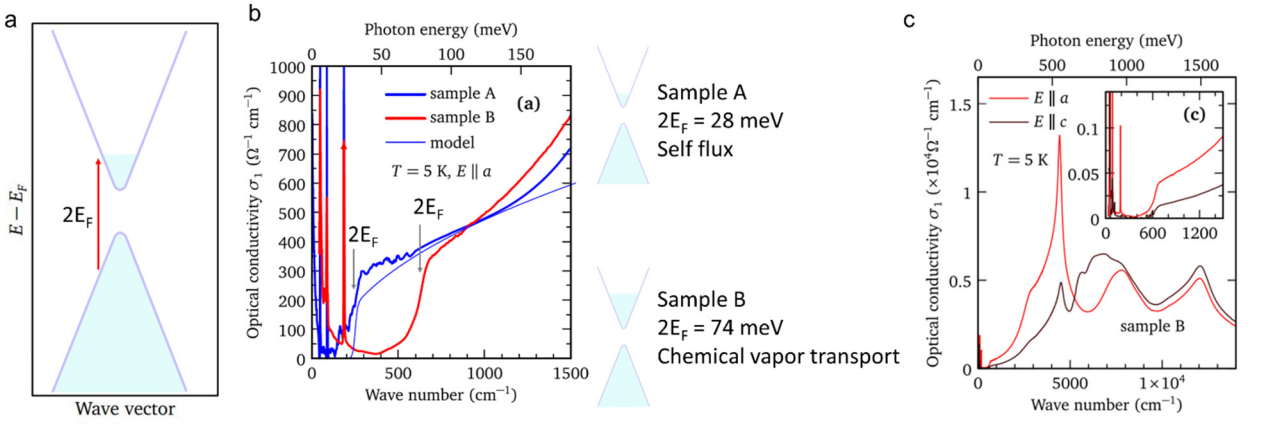

Figure 3:6 Fermi energy determination for $ZrTe_5$. a) Simplification of the linearly dispersing bands centred at the Γ point. The dashed area represents occupied states in the limit of $T \rightarrow 0$ K. **b)** Real part of optical conductivity ($\sigma_1(\omega)$) measured at 5 K for light polarized along the *a*-axis. The two thick blue and red curves were obtained on A and B samples respectively, which differ for the chemical potential energy, estimated from the Pauli blocking edge (marked by the arrow). The thin blue line is the calculated conductivity ($\sim\sqrt{\omega}$) according to Equation 27. **c)** Optical conductivity measured in a wide frequency range for two linear light polarization along the $ZrTe_5$ crystalline plane.

The frequency dependence of interband optical conductivity, for energies above the Pauli edge, can be evaluated from the model Hamiltonian (Equation 24) in the vanishing relaxation constant approximation for $T \approx 0$

$$\sigma_1(\omega) = \frac{e^2}{4\pi\hbar^2}\frac{v_a}{v_c}\sqrt{\hbar\omega - 2\Delta}\,\Theta(\hbar\omega - 2E_F) \qquad \text{Equation 27}$$

The experimental data collected on sample A are modelled using this equation, as shown in Figure 3:6 b. The value of $\frac{v_a}{v_c} = 1.5$ is experimentally determined from the ratio of optical conductivities for different light polarization along *a* and *c*-axis. Therefore, the only free parameter to model the optical response is the effective electron mass along *b*-axis, equal to $m^* = 1.8\ m_e$.

3.1.3 Transport properties of $ZrTe_5$

Before presenting the anisotropic conduction mechanism in $ZrTe_5$, we will first discuss the anomalous transport properties —resistivity, thermoelectric power, Hall coefficient— along the most conducting *a*-axis, which runs parallel to the Zr chains. The presence of anomalous features in the temperature dependence of all coefficients, was unexplained for a long time [67]. Here these anomalous features will be discussed in detail, and interpreted in light of the chemical potential shifting with temperature [59][60].

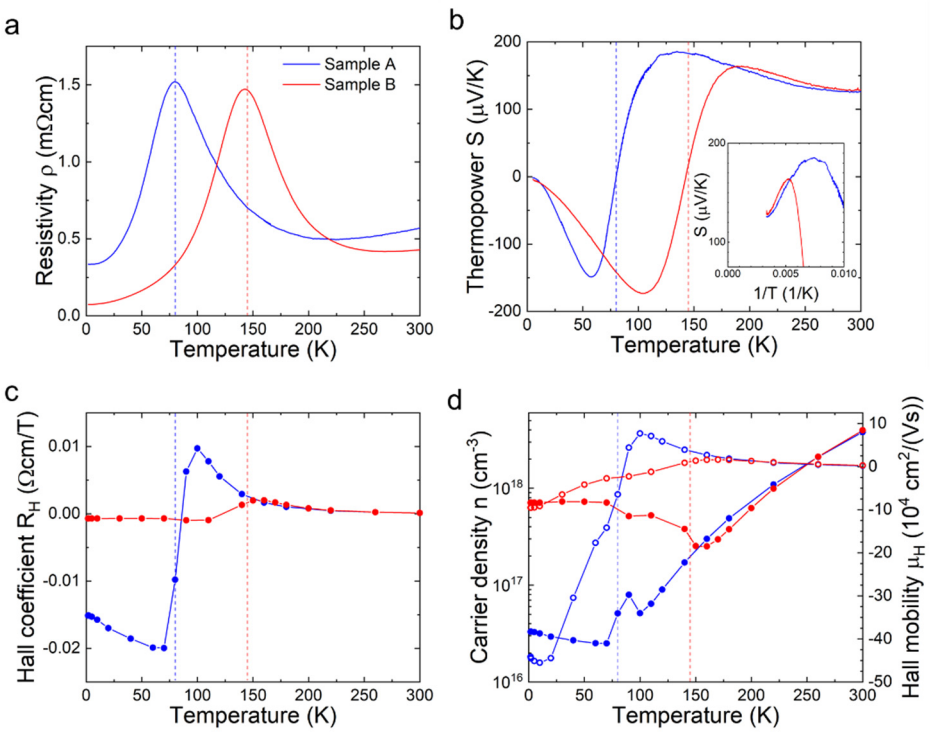

Figure 3:7 In-plane transport properties of $ZrTe_5$. a) Resistivity temperature dependence. **b)** Thermopower temperature dependence. In the inset thermopower plotted with *1/T* used to extract the chemical potential value at low temperature. **c)** Hall coefficient. **d)** Carrier density and Hall mobility. The blue and red dashed vertical lines denote the temperatures T'_A and T'_B, respectively.

Figure 3:7 shows the transport coefficients temperature dependence for two samples with different level of chemical potential (due to the different synthesis approach). Panel b displays the carrier density (n) and Hall mobility (μ_H) extracted from R_H using a single band model. It is evident that a dramatic change for all transport properties happens in both samples at temperature T', marked by a vertical dashed line. This temperature is sample dependent, with T'_A = 80 K and T'_B = 145 K, and is related to the different level of intrinsic doping in the material. These temperatures correspond to a maximum in the resistivity, a sign inversion in thermopower, Hall coefficient and Hall mobility, and a minimum in carrier density. The peculiar transport properties observed, with the non-monotonic trend as function of temperature, can be explained considering a strongly varying chemical potential with temperature, as suggested by ARPES data [59][60]. At room temperature the chemical potential is within the bandgap, with thermally excited carriers ($2\Delta < k_BT$) and a dominant hole contribution to conduction. Lowering the temperature, thermally excited carriers are reduced, while chemical potential shifts towards the conduction band. For $T < T'$, the chemical potential is within the conduction band, therefore the conduction properties become that of a metal.

Electrical resistivity (Figure 3:7 a) below T' is described by $\rho(T) = \rho_0 + AT^2$, with A_A = 0.1 μΩcm/K^2 and A_B = 0.036 μΩcm/K^2 for samples A and B respectively. The coefficient A is inversely proportional to the square of the chemical potential (E_F) [68], indicating that Fermi level in sample A is lower than B, in agreement with optical conductivity data (Figure 3:5 c). The relative high value of resistivity, above 100 μΩcm, is due to the very low carrier density, approximately 6 orders of magnitude less than in a half-filled-band metal. Thermopower coefficient temperature dependence (Figure 3:7 b) below T' can be well described by the Mott formula

$S(T) = {k_B^2 T}/{(eE_F)}$, with confirms that chemical potential is within the conduction band [69]. From thermopower measurement the computed value of E_F is 14 meV and 23 meV for samples A and B respectively.

The Hall coefficient, carrier density and Hall mobility (Figure 3:7 c) are computed in a single band analysis in the $B \rightarrow 0$ limit, and strongly differ between the two samples at temperatures below *T'*. Sample A, the one with lowest Fermi energy, has the highest mobility μ_H^A = 0.45 x 10^6 $cm^2/(Vs)$ (at carrier density of n_A = 3 x 10^{16} cm^{-3}), a remarkably high value for a bulk material.

For temperatures above 180 K the transport coefficients *S*, R_H, *n* and μ_H are very similar for both samples, suggesting that thermally activated carriers are dominant with holes as majority carriers. Thermopower temperature dependence and magnitude is that of a doped semiconductor where the dominant contribution comes from holes excited over the band gap [69]. The resistivity temperature dependence above *T'* is that of a heavily doped semiconductor, because thermal energy is larger than the bandgap, and resistivity does not diverge exponentially. The summary of the chemical potential change, at the origin of the unusual transport properties and transition from thermally excited carriers to metallic conduction are depicted in Figure 3:9. In addition photoemission data clearly show the chemical potential shifting with temperature [60].

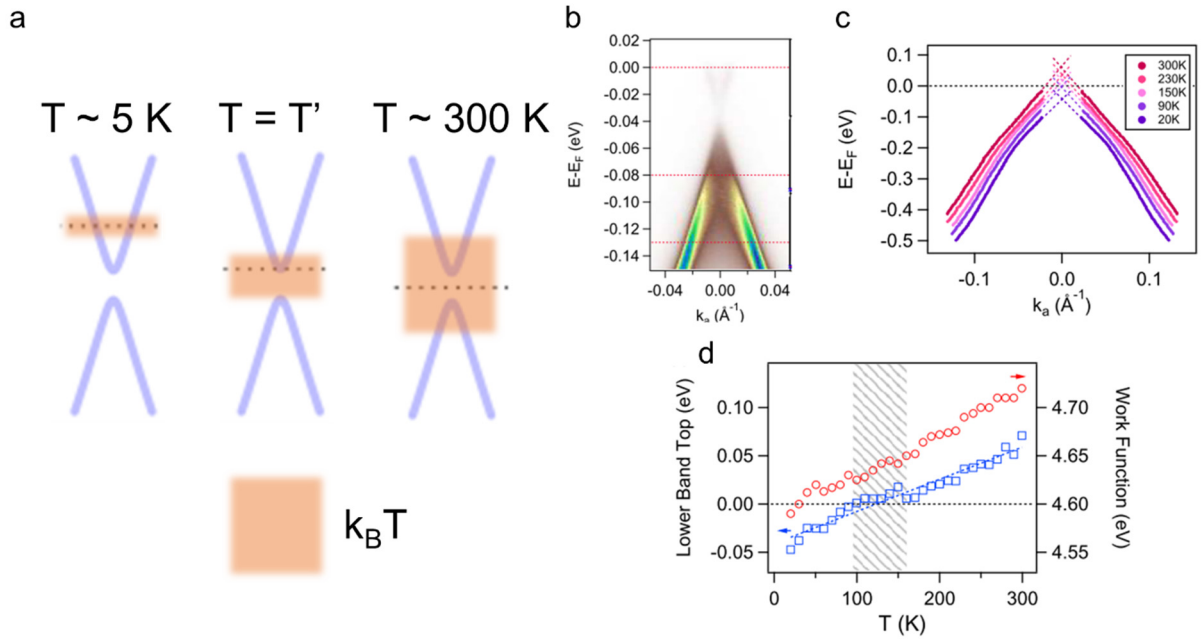

Figure 3:8 Chemical potential shift in $ZrTe_5$. a) Illustration of the chemical potential shift with temperature. **b)** Angle resolved photoemission spectrum showing both conduction and valence band, measured at 20 K. **c)** Extrapolated valence band top energy shift with temperature **d)** Energy of the valence band top as function of temperature (blue), and work function shift as function of temperature (red). Figures from [60].

3.1.4 Conductivity anisotropy

Having clarified the band structure and in-plane transport properties of $ZrTe_5$, in this section its anisotropic conduction properties will be discussed. Resistivity temperature dependence along the three principal crystallographic directions has been measured on two samples extracted from the very same single crystal and micro-machined by use of Focused ion beam (Figure 3:9 a). The two samples have been first extracted from the starting crystal as rectangular lamellas along a well-defined crystalline plane (*ab*-plane and *bc*-plane), after crystal orientation by Laue method. The lamellas, after being transferred to a substrate and coated with gold by sputtering, have been machined to create conducting paths along specific crystallographic directions. The

full procedure for sample preparation are later described in section 7.1.1. All final samples have been realized starting from a CVT grown crystal (sample B).

The resistivity temperature dependence along principal directions is shown in Figure 3:9. All curves show the same characteristic temperature dependence, with the maximum around 150 K, and a metallic behaviour (positive dρ/dT) below T'. The change in the resistivity curves for different direction is a simple multiplicative factor, of approximately 2.5 between a and c and 80 between a and b axes. Looking at the resistivity anisotropy ratio (Figure 3:9 c), it can be seen how the anisotropy changes around T'. This latter effect is not fully understood at the moment, but is attributed to possible extrinsic effects that affects the resistivity along the probed section of the sample. A possible explanation can be the presence of parasitic strain created during cool down for the interaction between the sample and the substrate. Indeed the position of resistivity maximum shows a marked pressure dependence [70], and microstructured samples prepared by FIB can be subject to parasitic strain when glued to the substrate [71].

From the measurement it is evident that the layered structure of $ZrTe_5$ affects the conductivity between crystalline planes only through a multiplicative factor. There is no dramatic contrast between the conduction in the planes, dominated by Dirac electrons, and the conduction of massive electrons "jumping" across the van der Waals bonded layers. In a certain sense this is not a surprise, as the band structure has a finite band dispersion along the out-of-plane direction; electrons propagate as coherent states between crystalline planes. The absence of electronic correlations and of a strong directionally dependent scattering mechanism are other reasons for the simple multiplicative scaling of resistivity.

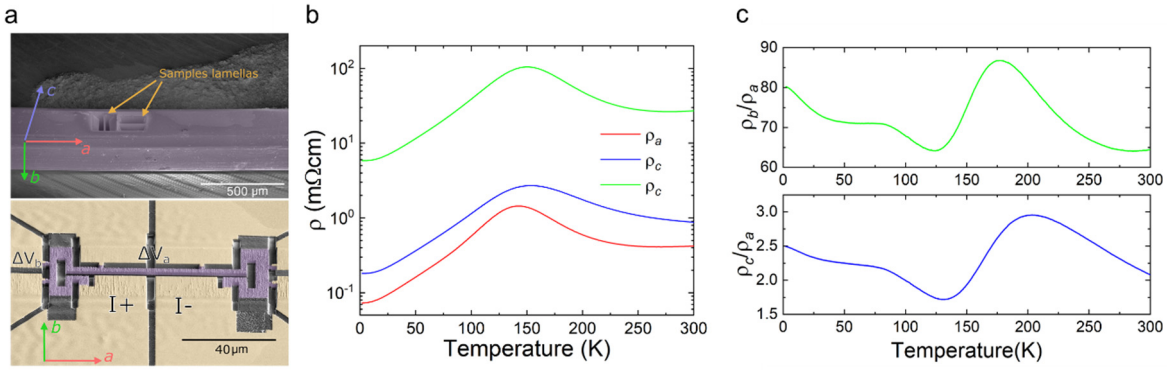

Figure 3:9 Transport anisotropy in $ZrTe_5$. a) electron microscope images of a microstructured sample prepared by focused ion beam technique. The top panel shows the single crystal from which two lamellas have been extracted. In the bottom panel, a sample prepared to probe electrical resistivity along the a- and b-axes. **b)** Resistivity anisotropy measured along all three crystallographic directions for the sample B (synthesized by chemical vapour transport, with a higher chemical potential). **c)** Anisotropy ρ_b/ρ_a and ρ_c/ρ_a as a function of temperature.

To give a more quantitative understanding of the measured anisotropy, we will use here the model Hamiltonian (Equation 24) to estimate the value of resistivity anisotropy in the $T \to 0$ K limit.

The frequency dependent conductivity tensor defined along the principal axes $\nu = a,b,c$ is:

$$\sigma_{\nu\nu}(\omega) = \frac{ie^2}{m_e}\frac{n_{\nu\nu}}{\omega + i\Gamma} \qquad \text{Equation 28}$$

with the effective concentration of charge carriers $n_{\nu\nu}$ along the conduction direction, and the relaxation constant Γ. The dc resistivity is then:

$$\rho_{\nu\nu} = 1/\sigma_{\nu\nu}(0)_{\nu\nu} = \frac{m_e\Gamma}{e^2 n_{\nu\nu}} \qquad \text{Equation 29}$$

If we assume that the relaxation rate is isotropic and constant, the effective number of charge carriers is the only relevant parameter for the resistivity anisotropy.

The effective number of carriers $n_{\nu\nu}$ is given by the sum over all the bands σ at Fermi level (one for $ZrTe_5$):

$$n_{\nu\nu} = -\frac{1}{V}\sum_{\boldsymbol{k}\sigma} m_e v_{\nu\boldsymbol{k}}^2 \frac{\partial f_{\boldsymbol{k}}}{\partial \varepsilon_{\boldsymbol{k}}} \qquad \text{Equation 30}$$

Here, the electron velocity is given by the band dispersion along the conduction direction $v_{\nu\boldsymbol{k}}^2 = (1/\hbar)\,\partial\varepsilon_{\boldsymbol{k}}/\partial k_\nu$. In the low temperature limit ($T \to 0$ K), we approximate $\partial f_{\boldsymbol{k}}/\partial\varepsilon_{\boldsymbol{k}} = -\delta(\varepsilon_F - \varepsilon_{\boldsymbol{k}})$.

For the in-plane directions (*a* and *c* axes) where band dispersion is linear $\varepsilon_{\boldsymbol{a}} = \hbar(v_{\boldsymbol{a}} k_{\boldsymbol{a}})$ we have:

$$\frac{\partial\varepsilon_{\boldsymbol{a}}}{\partial k_{\boldsymbol{a}}} n_{\nu\nu} = \frac{(\hbar v_{\boldsymbol{a}})^2 k_{\boldsymbol{a}}}{\sqrt{\hbar^2(v_{\boldsymbol{a}}k_{\boldsymbol{a}})^2 + \hbar^2(v_{\boldsymbol{c}}k_{\boldsymbol{c}})^2 + \left(\Delta + \left({\hbar^2}/{2m^*}\right)k_{\boldsymbol{b}}^2\right)^2}} = \frac{(\hbar v_{\boldsymbol{a}})^2 k_{\boldsymbol{a}}}{\varepsilon_{\boldsymbol{k}}} \qquad \text{Equation 31}$$

Along the out-of-plane direction (*b*-axis) where the band dispersion is parabolic $\varepsilon_{\boldsymbol{a}} = \left({\hbar^2}/{2m^*}\right)k_b^2$ we have:

$$\frac{\partial\varepsilon_{\boldsymbol{a}}}{\partial k_{\boldsymbol{a}}} n_{\nu\nu} = \frac{(\Delta + ck_{\boldsymbol{b}}^2)2ck_{\boldsymbol{b}}}{\sqrt{\hbar^2(v_{\boldsymbol{a}}k_{\boldsymbol{a}})^2 + \hbar^2(v_{\boldsymbol{c}}k_{\boldsymbol{c}})^2 + \left(\Delta + \left({\hbar^2}/{2m^*}\right)k_{\boldsymbol{b}}^2\right)^2}} = \frac{(\hbar v_{\boldsymbol{b}})^2 k_{\boldsymbol{b}}}{\varepsilon_{\boldsymbol{k}}} \qquad \text{Equation 32}$$

Following the integration over the entire $\boldsymbol{k}$-space, explained in details in [70], we computed the ratios for carrier density between different directions. The expected anisotropy can be then estimated using Equation 29, with no free parameters, by using the known experimentally measured values of in-plane electron velocity [61] and Fermi energy.

In-plane $$\frac{\rho_{\boldsymbol{cc}}}{\rho_{\boldsymbol{aa}}} \propto \frac{n_{\boldsymbol{cc}}}{n_{\boldsymbol{aa}}} = \frac{v_{\boldsymbol{a}}^2}{v_{\boldsymbol{c}}^2} \approx 2.2 \qquad \text{Equation 33}$$

Out-of-plane $$\frac{\rho_{\boldsymbol{bb}}}{\rho_{\boldsymbol{aa}}} \propto \frac{n_{\boldsymbol{bb}}}{n_{\boldsymbol{aa}}} = \frac{15}{105}\frac{1}{m^* v_{\boldsymbol{a}}^2}\left(\frac{15\varepsilon_F^2}{3\varepsilon_F + 2\Delta} + 4\Delta\right) \approx \frac{3}{4}\frac{\varepsilon_F}{m^* v_{\boldsymbol{a}}^2} \sim 10^2 \qquad \text{Equation 34}$$

In-plane anisotropy can be very precisely estimated because of the exact determination of the electron velocity ratio, and it agrees very well with the experimentally measured anisotropy (Figure 3:9 c). For the out-of-plane anisotropy, the model only provides a correct estimate of the order of magnitude. This can be related to the questionable assumption that relaxation coefficient is the same for in-plane and out-of-plane conductions. Even more relevant for the quantitative estimation of out-of-plane anisotropy, are the uncertainties in the absolute value of in-plane electron velocity and Fermi energy, in particular given the quadratic dependence of v_a. Nevertheless, such a simple model also provides an accurate estimate of the conductivity anisotropy.

3.1.5 Summary of $ZrTe_5$

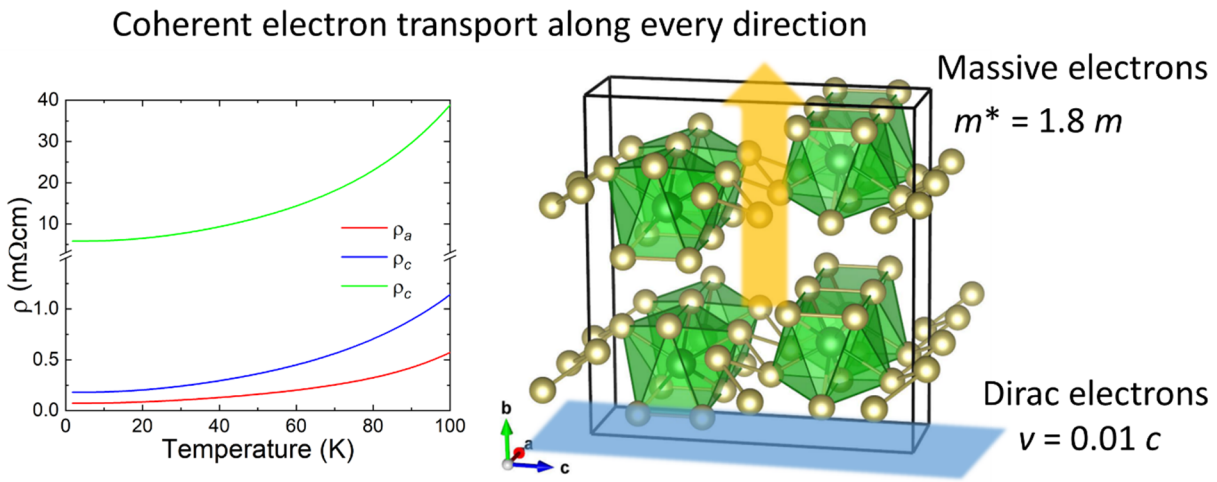

Figure 3:10 $ZrTe_5$ summary

$ZrTe_5$
$ZrTe_5$ is a layered material formed by quasi 1D $ZrTe_3$ chains connected by Te_2 ladders.
It has a simple electronic structure with only two bands in proximity of the chemical potential, separated by a 6 meV gap. The bands have linear dispersion (Dirac electrons) along the *ac*-plane and parabolic dispersion along *b*-axis.
Transport properties are unusual— resistivity maximum and majority carriers inversion at *T*'— due to the chemical potential shift from the band gap middle to the conduction band as temperature is reduced.

Interlayer transport
At low temperature, the conduction mechanism is coherent and metallic in every direction. The variation in band dispersion influences the effective number of carriers contributing to transport, resulting in a multiplicative scaling of the resistivity along different direction. Features of the temperature dependence are preserved along every direction.
Anisotropy can modelled by a simple Hamiltonian that consider the band energy dispersion. Resistivity anisotropy between out-of-plane and in-plane charge transport ($\boldsymbol{\rho}_{\perp}/\boldsymbol{\rho}_{||}$) depends on Fermi energy and in-plane electron velocity. According to our model Hamiltonian (Equation 34), the conductivity anisotropy is inversely proportional to the square of in-plane electron velocity.

Conclusion
The layered structure in a semimetal with high mobility simply induces a large resistivity anisotropy (of the order of 100) but the conduction remains coherent. There is no "tunnelling across the van der Waals gap", even if electrons within the layers have a Dirac-like energy dispersion.

3.2 Fermi Surface topology and transport anisotropy

This section compares the anisotropic properties of two isostructural and isoelectronic layered metals: 2H-$NbSe_2$ and 2H-$TaSe_2$. The two materials differ in their Fermi surface topology. In the Ta compound, the Fermi surfaces are tubulars, with a marked quasi-2D character. In the case of $NbSe_2$ there is an additional 3D Fermi surface, which originates from selenium orbitals. The effect of this different electronic structure will be investigated comparing the electrical and optical conductivity anisotropy of the two materials. The additional contribution of the chalcogen atoms to conduction in $NbSe_2$ is responsible for a less anisotropic behaviour. The layered structure and presence of quasi-2D Fermi surfaces, are also responsible for the lattice instability to form charge density waves (CDW) in both materials under investigation. The formation of CDW influences the electronic structure and the conduction properties, in particular along the *ab*-plane, where the reconstruction takes place.

Before moving to the results, we can discuss how Fermi surface defines conductivity anisotropy by looking at the simplified example Figure 3:11. We have seen in Equation 20 that conductivity along a specific direction is the integral of electron velocities projected onto that same direction. The three surfaces depicted represent the Fermi surfaces of ideal materials with markedly different anisotropic conduction properties. In the assumption that Fermi velocity is constant over the entire surface, the results of the integration is proportional to the cross section projected in the direction of charge conduction.

For the case of a 3D spherical Fermi surface, cross section is the same along every direction meaning that (n/m) will be direction independent and conduction is perfectly isotropic. In the 2D scenario, the Fermi surface forms a perfect cylinder. The electrons can move along the *x,y* plane as nearly-free electrons, but cannot acquire any velocity along the *z*-axis. The Fermi surface projection along the plane will be large, while along z-axis will be negligible, implying that $\left(\frac{n}{m}\right) = 0$, which can be either seen as the number of electrons moving along z-axis is zero ($n = 0$), or as having an infinite mass. In these conditions the electrons are effectively confined to move only along two dimensions. In real three-dimensional materials, there is always a finite dispersion along every direction, which results in warping of the Fermi surface along *z*-axis. Increasing warping will result in a larger cross section in the *z*-direction, meaning that a larger fraction of electrons can sustain out-of-plane charge transport. As the effective mass is defined by the energy dispersion and not by the shape of the Fermi surface, one can attribute to the specific shape the information on how many electrons can acquire velocity in the direction of conduction.

These concepts will be applied to investigate the anisotropic response of 2H-$TaSe_2$ and 2H-$NbSe_2$. In the discussion will be included the resistivity data collected on FIB microstructured samples and previously published optical conductivity data. Thanks to spectroscopic data, it is possible to compute the anisotropy in the plasma frequency ω_P, which is directly related to the Fermi surface cross section in the direction of applied electric field (Equation 23).

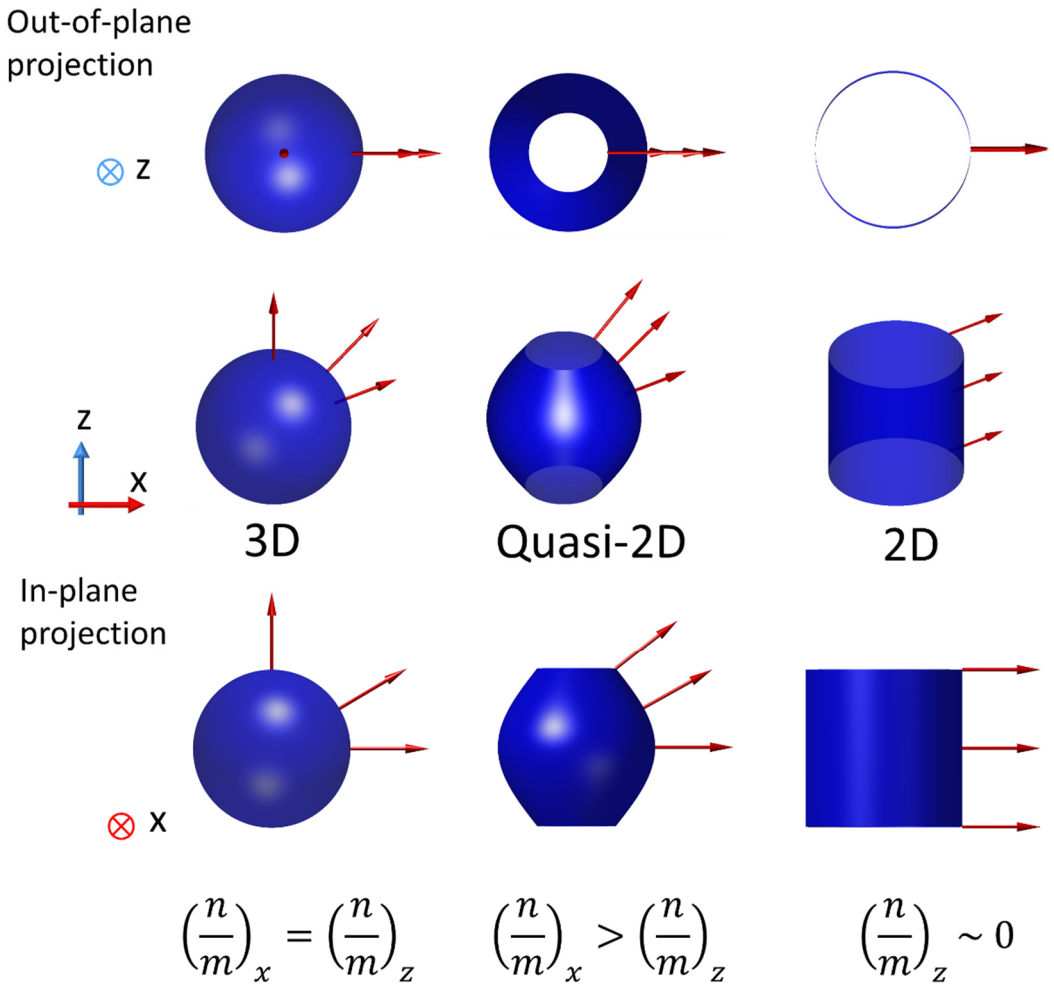

Figure 3:11 Fermi surface topology and conductivity anisotropy. Three ideal Fermi surfaces for the cases of: isotropic, quasi-2D and 2D conduction. The images show the projection of the surfaces along the in-plane (x) and out-of-plane direction (z). The cross section along each direction is proportional to (n/m), which defines the electrical conductivity. For the 2D case, this quantity is zero, meaning that the conduction along z direction is not allowed.

3.2.1 2H-$NbSe_2$ and 2H-$TaSe_2$: crystal structure and Fermi surface

2H-$NbSe_2$ and 2H-$TaSe_2$ have the identical crystalline layered structure, formed by a hexagonal plane of transition metal, sandwiched between two chalcogen layers (Figure 3:12 a). The metal is coordinated with six chalcogen atoms in a trigonal prismatic configuration. In these materials there are two layers per unit cell, stacked with the transition metals aligned along the c-axis, and the chalcogen layers rotated by 60° (Figure 3:12 b). The in-plane lattice parameter is very similar for both, with the interlayer distance 1.28 % larger in $TaSe_2$. Both materials have been extensively characterized, and their Fermi surfaces reliably determined by ARPES [72] [73] and quantum oscillations [74]. Because of the identical crystal structure, both materials have the same hexagonal Brillouin zone. The maps obtained from ARPES measurements visualize the intersection of the Fermi energy at the M-K-Γ plane Figure 3:12. In $NbSe_2$ tubular surfaces come in pairs, with one centred at Γ and other six around the zone edges K. Additional round surface is evident at the zone centre, which is the 3D-pocket produced by the chalcogen atom bands. In $TaSe_2$ the surfaces do not come anymore as pairs around the same symmetry point; six can be found around K and six around M, all with a quasi-2D character. The difference between the two materials is a consequence of the different Fermi energy, and not a different band structure. Because E_F is higher in 2H-$TaSe_2$, the 3D-pocket originating from Se orbitals is completely filled, and does not contribute to the conduction.

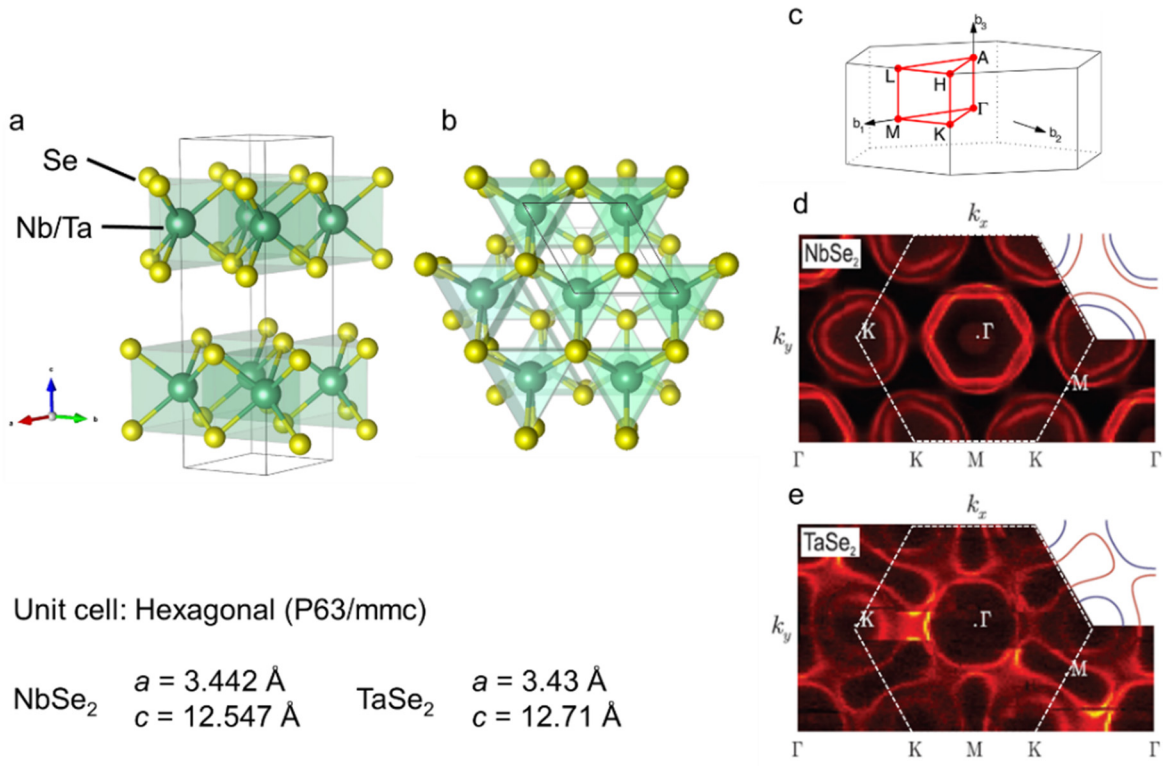

Figure 3:12 Crystal structure and Fermi surface of 2H-$TaSe_2$ and 2H-$NbSe_2$. a,b) Crystal structure seen along different directions. Both materials have the same structure, with minor differences for the lattice parameters. **c)** Hexagonal Brillouin zone, with its high symmetry points. **d,e)** Fermi surface maps measured by angle resolved photoemission spectroscopy at room temperature. In the corner the bands are schematically illustrated for clarity. Figures from [73].

Band structure calculations are able to reproduce the features seen experimentally, and offers a more clear visualization of the Fermi surfaces in reciprocal space [75] [76]. Figure 3:13 displays the individual Fermi surfaces generated by each band. The quasi 2D bands are produced by the transition metal *d*-orbitals, while the elliptical surface present in $NbSe_2$ is produced by the chalcogen *p*-orbitals, and is therefore expected to enhance the out-of-plane conductivity. The band structure was calculated by density functional theory using a linear muffin-tin orbital code in atomic sphere approximation. Perdew-Wang exchange-correlation potential and spin-orbit coupling were included in the calculations.

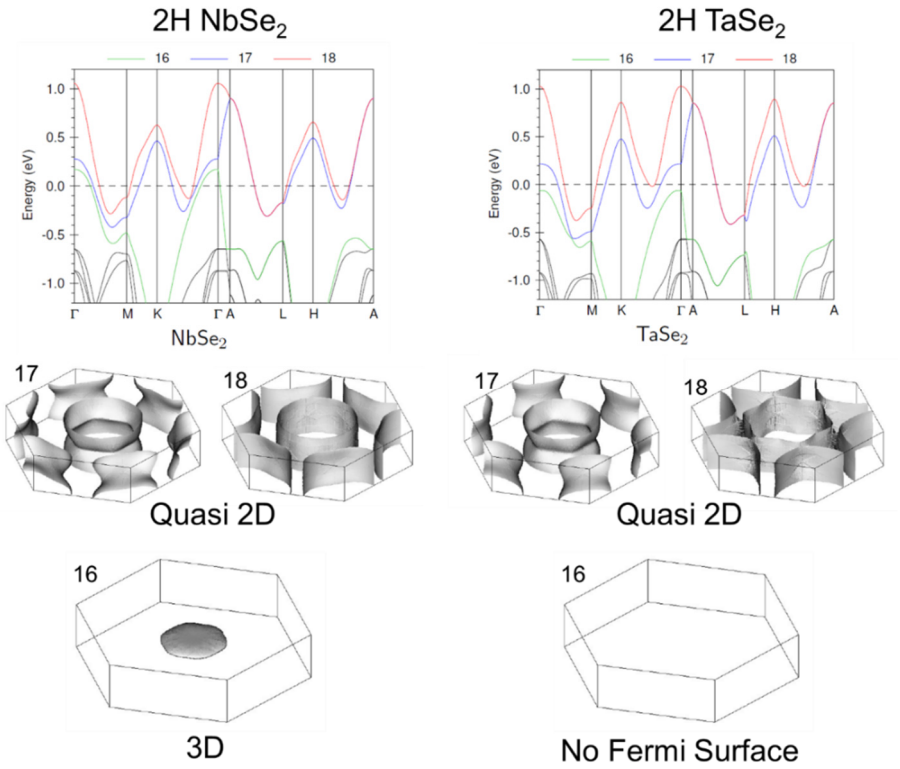

Figure 3:13 Calculated Fermi surfaces of 2H-$NbSe_2$ and 2H-$TaSe_2$ Band structure calculations, projected along the high symmetry directions. Because of the closely related crystalline structures, both materials have a very similar band structure. Bands 17 and 18 originate from the transition metals *d*-orbitals, with energy splitting originating from the interlayer interaction between the two metal ions in the unit cell. Band splitting is maximum at Γ and zero at A. Band 16 originates from Se p_z-orbitals, and crosses the chemical potential only for $NbSe_2$. Fermi surfaces are shown for each individual band. The bands 17 and 18 have a very weak dispersion along k_z, making them quasi-2D. The Fermi surface produced by the band 16 creates an ellipsoidal surface with strong dispersion along k_z, from which a 3D character is expected.

Both layered materials presented in this chapter undergo a CDW transformation. A CDW is a modulation of the conduction electron density, which comes hand in hand with a periodic lattice distortion. The additional periodicity can be described by a modulation vector, which could either be commensurate or incommensurate with the underlying lattice. The driving force is an instability of the Fermi surface, in combination with a strong electron-phonon interaction. The distortion in atomic positions creates a modulated superstructure, and induce bands structure folding as new zone boundaries are created by the additional periodicity. The energy cost of the elastic deformation of the lattice is compensated by the electronic energy reduction due to the opening of a band gap along the modulation vectors. For quasi-1D materials, the charge density wave induces a metal to semiconductor transition, known as Peierls transition [77]. For materials where electronic states have a higher dimensionality (2D and 3D), the CDW does not fully gap the Fermi surface but reduces the density of states at the chemical potential. Because of the change in electronic structure at Fermi energy, CDW formation can have a strong effect of the conducting properties of the material. Short range CDW fluctuations can exists at high temperature, inducing a strong scattering on conduction electrons. The onset of a long-range order suppresses this additional scattering mechanism [78].

Both 2H-$NbSe_2$ and 2H-$TaSe_2$ present a CDW formation with the same modulation vector $\boldsymbol{q} = 3a\ x\ 3a$. The lattice distortion, depicted in Figure 3:14 a, involves six transition metals atoms moving towards a central one, with a linear displacement of 0.05 Å [79] [80]. This lattice distortion creates a larger unit cell, with its axis

along the same direction as the non-reconstructed one, and 3 times longer. In the reciprocal space this modulation implies that the Brillouin zone becomes nine times smaller (Figure 3:14 b). The same figure is also displaying the reconstruction of the Fermi surface for 2H-$TaSe_2$. Only in 2H-$TaSe_2$ below 90 K the lattice modulation is commensurate and long range ordered. In the range between 90 K and 122 K, the lattice reconstruction is nearly commensurate as the in-plane modulation forms short range ordered domains [81]. In $NbSe_2$ the formation of long range nearly-commensurate modulation is observed below 35 K, which never reaches commensurability to the lattice [82].

The onset of long-range CDW transitions are apparent in the resistivity temperature dependence (Figure 3:14). The nearly commensurate transition in 2H-$NbSe_2$ induces a small variation in the resistivity temperature dependence below 28 K. It is a second order transition with no hysteresis in the temperature dependence. In 2H-$TaSe_2$, the onset of the nearly commensurate transition at 122 K is evident by a sharp increase in resistivity, with temperature hysteresis of approximately 1 K. After the transition, the resistivity temperature dependence becomes much steeper, with a change in dρ/dT around 90 K which is associated to the lock-in transition into the commensurate phase. Both materials become superconducting at low temperature. 2H-$NbSe_2$ has the higher T_C = 7.2 K (Figure 3:14 c), and 2H-$TaSe_2$ becomes a superconductor at 0.13 K [83].

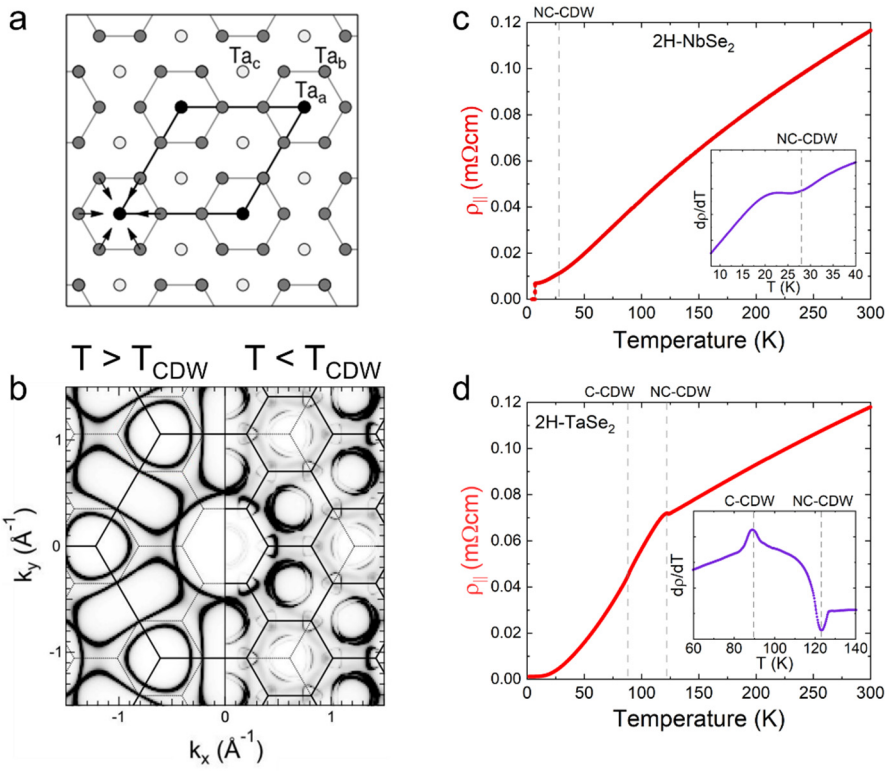

Figure 3:14 Charge density wave in 2H-TMDs a) Unit cell of the commensurate CDW reconstruction, with modulation vector $\boldsymbol{q}$ = *3a x 3a*. The reconstruction involves six metals atoms, which move towards a central one. Figure from [84]. **b)** Fermi surface cross section along the ΓMK plane in the normal state (left) and in the commensurate 3 × 3 CDW state (right) of 2H-$TaSe_2$. Figure adapted from [84]. **c)** Temperature dependence of the in-plane electrical resistivity in 2H-$NbSe_2$, where the CDW transformation is evident around 28 K from the change in the derivative dρ/dT. The lattice modulation is only short range ordered and never reaches a full commensurability with the underlying lattice. **d)** Temperature dependence of the in-plane electrical resistivity in 2H-$TaSe_2$. The CDW transformation is first noticeable at 122 K with a jump in resistivity. A second transition is marked in the derivative change at 90 K and is associated to a lock-in transition from the nearly-commensurate to commensurate CDW. The vertical dashed lines mark the onset of CDW transitions for both materials, marked at nearly-commensurate (NC-CDW) and commensurate (C-CDW) according to the long-range order of the lattice modulation.

3.2.2 Conductivity anisotropy

Metallic transition metal dichalcogenides have been investigated for over 40 years, in particular through conductivity measurements [78]. The scientific attention was first directed to the CDW and tuning of superconducting transition temperature by means of intercalation [85], both consequences of the quasi 2D character of the electronic properties and layered structure. The more recent interest is a spurred by of the possibility to explore the properties of these materials in the 2D limit, isolating few layer thick crystals by mechanical exfoliation.

The role of dimensionality and coupling between the layers is central in defining the properties of these materials. In this section we will discuss the anisotropic change dynamics. We will compare the resistivity anisotropy measured on FIB microstructure samples. The dc electrical resistivity data will be compared to the optical conductivity anisotropy measured by far-infrared optical spectroscopy [86] [87] [88]. Spectroscopy data are of particular interest because they allow to separate the scattering rate contribution from the effective number of carriers (n/m) along conduction directions.

- **dc electrical resistivity**

Figure 3:15 displays the resistivity temperature dependences for the current flowing along the planes ($\rho_{\parallel}(T)$) and out-of-plane ($\rho_{\perp}(T)$) directions. To ensure the most accurate comparison, the measurements have been collected on the very same sample for both materials. The insets display the resistivity anisotropy as a function of temperature ($\rho_{\perp}/\rho_{\parallel}$).

At room temperature $\rho_{\parallel}$ is remarkably similar for both metals, at variance with $\rho_{\perp}$. In the case of $NbSe_2$, the anisotropy at 300 K is 5.2, while for $TaSe_2$ is 18.5. The large difference in anisotropy can be immediately related to the previously discussed difference in the Fermi surface, from which a lower anisotropy for $NbSe_2$ is expected as a consequence of the 3D pocket.

Upon cooling, resistivity has a metallic temperature dependence ($d\rho/dT > 0$) along both directions, which points to a coherent conduction mechanism along the out-of-plane direction. The $\rho_{\parallel}$ has a linear temperature dependence, in contrast to $\rho_{\perp}$ which tends to saturate at high temperature. With increasing temperature, the anisotropy of both materials tends to decrease. This variation can be a consequence of the increase electron-phonon scattering, which helps to mix the two conducting channels, effectively reducing anisotropy.

At the CDW transition temperatures, $\rho_{\perp}$ presents limited variation, indication that the in-plane electronic reconstruction has a very weak effect on out-of-plane conductivity. For 2H-$NbSe_2$ the total absence of features in $\rho_{\perp}(T)$ at T_{CDW} is translated in a marked dip in the anisotropy. Following the temperature dependence of $TaSe_2$ from high temperatures, $\rho_{\perp}$ does not manifest a sharp increase around 120 K but rather a discontinuity in its derivative. With reducing temperature below 120 K, the anisotropy increases at a faster rate, following the stronger suppression in resistivity along the in-plane direction.

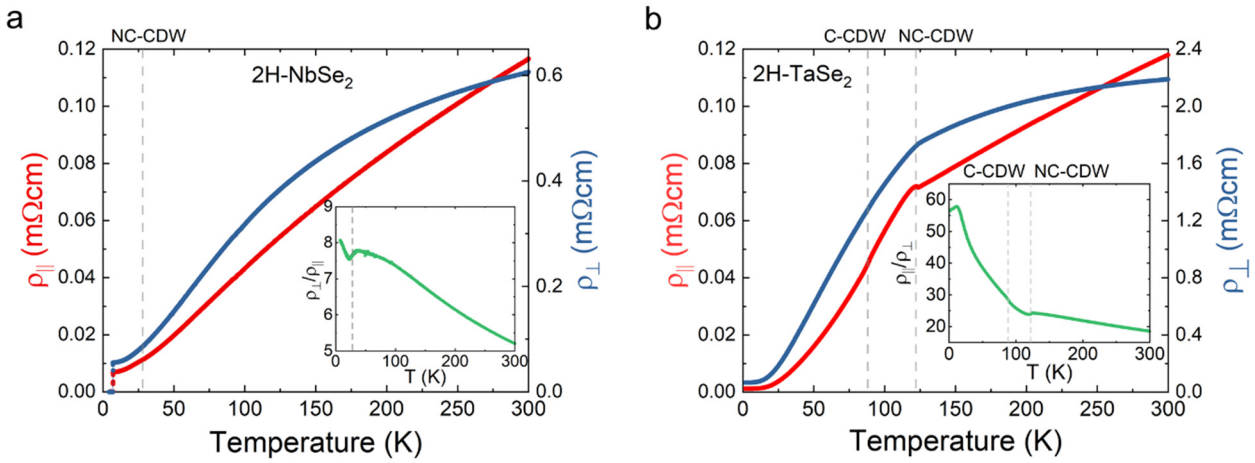

Figure 3:15 Resistivity anisotropy measured on FIB tailored single crystals a) Temperature dependence of in-plane ($\rho_{\parallel}$) and out-of-plane ($\rho_{\perp}$) resistivity for 2H-$NbSe_2$. The scale on the left is for $\rho_{\parallel}$ and the one on the right for $\rho_{\perp}$. The inset shows the resistivity anisotropy ($\rho_{\perp}/\rho_{//}$) temperature dependence. **b)** Temperature dependence of $\rho_{\parallel}$, $\rho_{\perp}$ and anisotropy for 2H-$TaSe_2$.

- **Optical conductivity**

We will discuss here the conductivity frequency dependency probed along the in-plane and *c*-axis directions. The data have been collected by optical reflectivity measurement using polarized light [86] [87] [88]. The results, after Kramers–Kronig transformations, are displayed in Figure 3:16. Common feature to both materials is the well-defined metallic Drude peak in σ_1 for $\omega \rightarrow 0$, along both polarization directions. The temperature dependence is also compatible with the results of dc resistivity, with optical conductivity increasing at lower temperatures. This is a clear evidence that electron dynamics is coherent along the interlayer direction. With increasing energy, σ_1 along *c*-axis presents a mid-infrared structure centred at 2000 cm^{-1} for 2H-$NbSe_2$ and two transitions at 2000 cm^{-1} and 6000 cm^{-1} for 2H-$TaSe_2$.

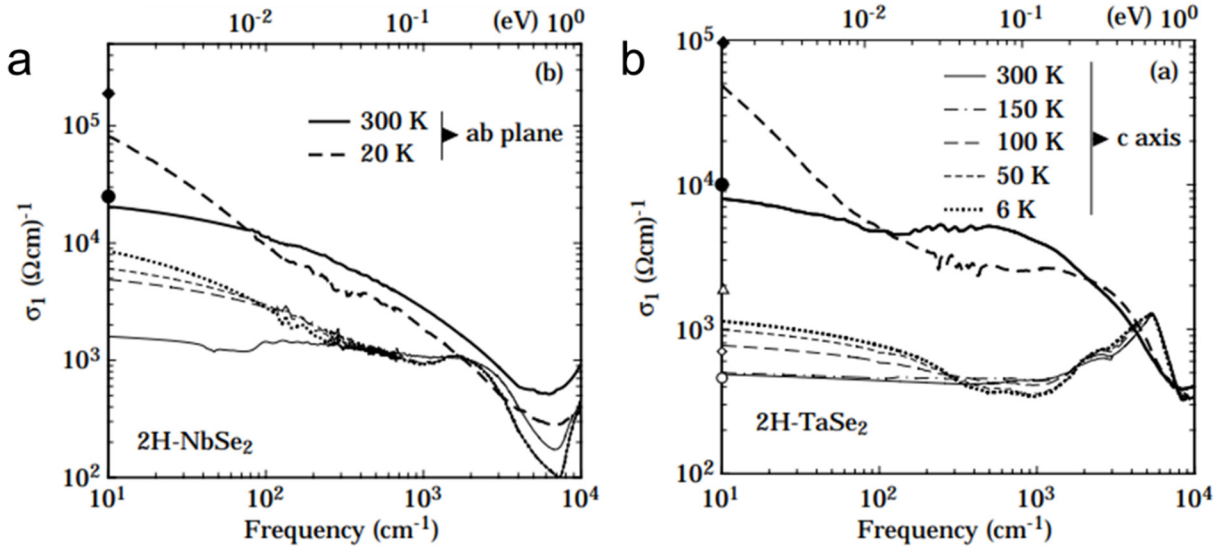

Figure 3:16 Optical conductivity anisotropy Temperature dependence of optical conductivity for light polarized along the *ab*-plane and *c*-axis. The legend for temperature refers to both figures. Results for 2H-$NbSe_2$ in **a)** and 2H-$TaSe_2$ in **b)**. Figures from [88]. The marks display the conductivity values measured with dc electrical methods. Solid for *ab*-plane and open for *c*-axis (only for 2H-$TaSe_2$).

Frequency dependence of $\sigma_1(\omega)$ along both light polarizations differs from the Lorentzian form expected by Drude theory. The extended Drude formalism (Equation 10) offers a more accurate description of the optical conductivity frequency dependency. Through this analysis the frequency dependence of the scattering rate and the plasma frequency (ω_P) was determined along each polarization direction.

Plasma frequency ($\omega_P^2 = \frac{4\pi ne^2}{m^*}$) is determined from the partial spectral weight within the range of intra-band excitations. It can be computed by integrating the real part of optical conductivity up to a cut-off frequency W below which intra-band transitions are dominant (Equation 9). Following the approach used in ref. [88], the chosen cut-off frequencies are W = 8000 cm^{-1} for *ab*-plane and W = 2000 cm^{-1} for *c*-axis for both compounds.

The low temperature (10 K) values of the plasma frequency and the scattering rate for $\omega \rightarrow 0$ are reported in the following table:

Table 2

	2H-NbSe$_2$	**2H-TaSe$_2$**
ω_P *ab*-plane	20'200 cm^{-1}	22'826 cm^{-1}
ω_P *c*-axis	13'000 cm^{-1}	6'017 cm^{-1}
$1/\tau_{ab}$ ($\omega \rightarrow 0$)	80 cm^{-1}	80 cm^{-1}
$1/\tau_c$ ($\omega \rightarrow 0$)	240 cm^{-1}	470 cm^{-1}

Both the plasma frequency and the scattering rate are anisotropic in the two materials. With respect to ω_P, the in-plane value is comparable for both materials, while along *c*-axis is lower by factor 1.5 and 3.8 for $NbSe_2$ and $TaSe_2$ respectively. Those values of plasma frequency could be interpreted as an anisotropy in the effective-mass tensor of m_c^*/m_{ab}^* of 2.25 for $NbSe_2$ and 14.4 for $TaSe_2$. As the band structure for the two materials is similar (see Figure 3:13), such large difference in effective masses cannot be easily justified. A more suitable interpretation is to consider the difference in effective number of carriers moving along the *c*-axis. The very limited Fermi surface projection along *c*-axis for $TaSe_2$, and the presence of a 3D pocket in $NbSe_2$ could better explains the experimental results. Also, the scattering rate is anisotropic and much higher along *c*-axis. In this case one has to consider the absolute value with precautions, due to large uncertainties in the extrapolation of the scattering rate at zero frequency. From the presented data, Dordevic et. al. [87] computed the electron-phonon coupling constant (λ) in 2H-$NbSe_2$ from Eliashberg analysis. The out-of-plane scattering rate $1/\tau(\omega)$ can be fully described by electron-phonon scattering, with a coupling constant λ_c = 1.59. Scattering rate for in-plane conduction cannot be explained by electron-phonon interaction alone, as electron-electron interaction appears to be relevant. From their estimation, in-plane phonon scattering appears to be much weaker, with a coupling constant λ_{ab} = 0.53. The strong in-plane electron-electron scattering, in addition to the phonon contribution, is attributed to CDW fluctuations. When CDW becomes long-range ordered, such contributions to electrons scattering are much suppressed, which explains the temperature dependence of electrical resistivity in 2H-$TaSe_2$.

It is possible to estimate the dc conductivity anisotropy from the Drude formula ($\sigma_{dc} = \omega_P^2 \tau / 4\pi$), in the zero-frequency limit:

$$\frac{\rho_c}{\rho_{ab}} = \frac{\sigma_{ab}}{\sigma_c} = \left(\frac{\omega_P^{ab}}{\omega_P^c}\right)^2 \frac{\tau_{ab}}{\tau_c} \qquad \text{Equation 35}$$

The expected low temperature anisotropies are 6.75 and 84 for $NbSe_2$ and $TaSe_2$ respectively, very close to the actual values measured in dc resistivity, see **Figure 3:15**. The frequency dependence of optical conductivity and the data measured on FIB microstructures are in very good agreement. It has to be noted that a much larger

error would occur if we tried to estimate the dc value from the extrapolation of the optical conductivity at zero frequency ($\omega \rightarrow 0$). The larger uncertainties in the determination of optical reflectivity at low photon energies, are amplified after Kramers–Kronig transformation, and lead to differences between σ_1 ($\omega \rightarrow 0$) and σ_{dc} up to an order of magnitude for low temperature data.

- **Anisotropy estimation from band structure calculation**

From the calculated band structure of 2H-$NbSe_2$ and 2H-$TaSe_2$ (Figure 3:13), it is possible to compute the anisotropic conductivity for both materials using Equation 16. The values obtained from band structure calculations do not contain information on the scattering rate anisotropy. A direct comparison to experimental data should be done with the plasma frequency anisotropy, as it is independent on the scattering rate.

Table 3

	$\boldsymbol{\sigma_{ab}/\sigma_c}$ (DFT)	$\left(\boldsymbol{\omega_P^{ab}/\omega_P^c}\right)^2$ (Optical cond.)
2H-$NbSe_2$	2.6	2.25
2H-$TaSe_2$	14.7	14.4

From the comparison it is evident that *ab*-initio calculations and experimental data show a remarkable agreement. The immediate implication is that transport is coherent along every direction, with electrons moving as well-defined quasiparticles described by Bloch states. The anisotropy can be directly related to the Fermi surface topology, as the presence of a 3D pocket strongly reduces σ_{ab}/σ_c. The following table lists the anisotropic conduction properties of each individual band. The band 16 is the one with the most favourable out-of-plane conduction, and it is present in $NbSe_2$ only.

Table 4

	2H-$NbSe_2$	**2H-$TaSe_2$**
Band 16 $\boldsymbol{\sigma_{ab}/\sigma_c}$	0.04	-
Band 17 $\boldsymbol{\sigma_{ab}/\sigma_c}$	4.2	6.6
Band 18 $\boldsymbol{\sigma_{ab}/\sigma_c}$	89.5	178.0

Because the band energy dispersion is very similar for both materials, it is hard to justify the difference in effective mass as the primary contribution to the observed behaviour. This further strengthens the interpretation through the different effective number of carriers able to transport current along *c*-axis as the primary reason for the differences between $NbSe_2$ and $TaSe_2$.

3.2.3 Summary of 2H-TMDs

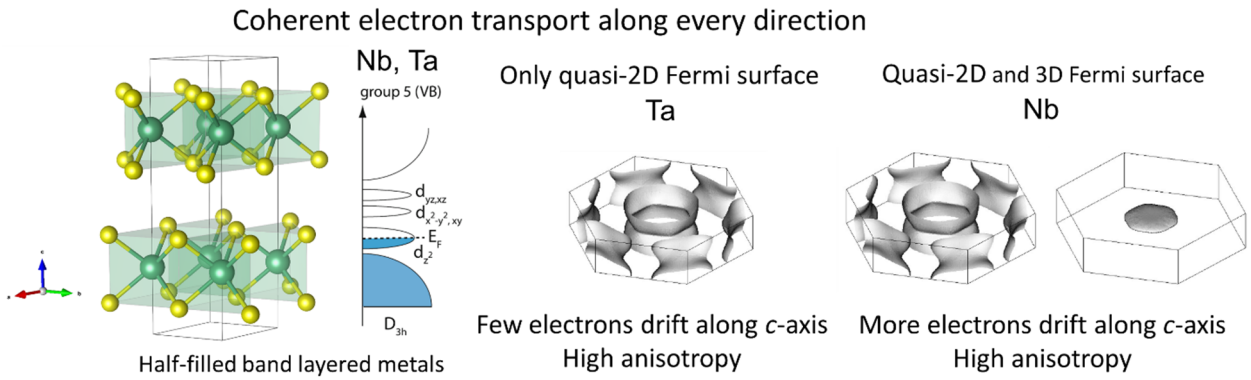

Figure 3:17 2H-TMDs summary

2H-$NbSe_2$ and 2H-$TaSe_2$
The two systems are isostructural and isoelectronic layered metals with a half-filled band ($n \approx 10^{22}$ e^-/cm^3). The band structure in proximity of the chemical potential is defined by transition metal *d*-orbitals, producing quasi-2D Fermi surfaces, and Se *p*-orbitals. Only for $NbSe_2$, the Se-band crosses the chemical potential and creates a Fermi surface with 3D topology and strong out-of-plane dispersion.

Interlayer transport
Frequency dependent optical conductivity confirms that electronic conduction is coherent along in-plane and out-of-plane directions.
Conductivity anisotropy between the two materials differs by a factor of ~ 10, the anisotropy being 8 in $NbSe_2$ and 60 in $TaSe_2$.

Conclusion
Transport anisotropy can be well understood from the Fermi surface topology, because in ordered layered metals conduction is coherent along every direction.

Chapter 4 Charge density wave, phase separation and orbital ordering: 1T-TaS_2

Layered metals are prone to formation of charge density waves (CDW), because of the quasi-2D nature of their electronic structure and anisotropic lattice bonds. This is the case for metallic transition metal dichalcogenides, such as Ti-, Nb and Ta-based compounds [84], as we have already seen in section 3.2.1. Among them, 1T-TaS_2 is the compound that exhibits the largest variety of CDW textures, all occurring in a relatively small region of a pressure-temperature phase diagram. These even include a unique complex phase, in which structurally distinct domains of a few nanometres in size form a regular lattice. The physical properties, in particular electrical conductivity, are strongly affected by the CDW reconstructions, in a more dramatic way than for 2H-polytypes. Notably, there is evidence of a metal-insulator transition at low temperature, when the CDW order becomes commensurate with the underlying lattice. Because the CDW reconstruction can only gap a small portion of the Fermi surface of a three-dimensional material, the mechanism behind the metal-insulator transition is has been highly debated. The results presented in this chapter not only uncover the accurate value of conductivity anisotropy of this complex material, but also provide new insights into the origin of the metal-insulator transition.

The investigation of the transport anisotropy in this material revealed a set of surprising results that have eluded experimental observation for over 40 years. Remarkably, we found that the resistivity anisotropy, first believed to be of the order of 1000, is actually below 1 in a broad temperature range. In addition, in a specific CDW phase, called the nearly commensurate or NC phase, the out-of-plane charge transport is preferred over the in-plane one. In this phase, only the conduction along *c*-axis appears to be coherent as in a normal Fermi liquid metal, in contrast to the non-metallic behaviour for the in-plane current flow. At the origin of these surprising properties is an intimate relation between the charge density wave and the electronic structure, dominated by Ta $\boldsymbol{d_{z^2-r^2}}$ orbitals, which direct the majority of electron density along the *c*-axis. The resulting orbital ordering contributes to the surprisingly anisotropic behaviour.

The insulating state of the low-temperature phase of 1T-TaS_2 has been originally attributed to Mott physics [89]. Recent studies, however, pointed out that the band gap can alternatively arise due to a particular stacking of the CDW-reconstructed layers. Our results provide a valuable experimental argument for the latter description, and suggest that the metal-insulator transition can be regarded as a quasi-one-dimensional instability. The formation of band gap opening resembles a quasi-1D instability oriented along the *c*-axis, reminiscent of a Peierls instability. Formation of an insulating phase appears as a consequence of dimerization between consecutive layers. Preferential out-of-plane conduction and dimerization are both the consequence of the strong interlayer hybridisation of electronic orbitals, which is enhanced by the commensurate CDW phase.

4.1 Lattice reconstruction and charge density wave

Undistorted 1T-TaS_2 has a simple crystalline structure (Figure 4:1 a), with one layer per unit cell and a trigonal symmetry (space group No 164, P-3m1). Within the layers each Ta atom is octahedrally coordinated with six S atoms. Isostructural compounds include 1T-$TaSe_2$ and dichalcogenides of group 4 metals (MS_2, MSe_2, MTe_2, where M is Ti, Zr, or Hf).

No other layered material can match the diversity of CDW textures observed in 1T-TaS_2. At ambient pressure a lattice instability occurs at a temperature as high as 550 K, which is a sign of a very strong driving force. Upon cooling, the structure discontinuously transforms between distinct CDW phases. In total four CDW reconstructions can be observed, all identified according to the degree of commensurability between the CDW modulation and the underlying lattice. In the order of appearance from the highest temperature, the different phases are called: incommensurate (IC), nearly-commensurate (NC), triclinic (T) and commensurate (C). The T phase can only be observed during heating from the C phase, while all the other phases set in for both temperatures sweep directions, but with sizeable hysteresis.

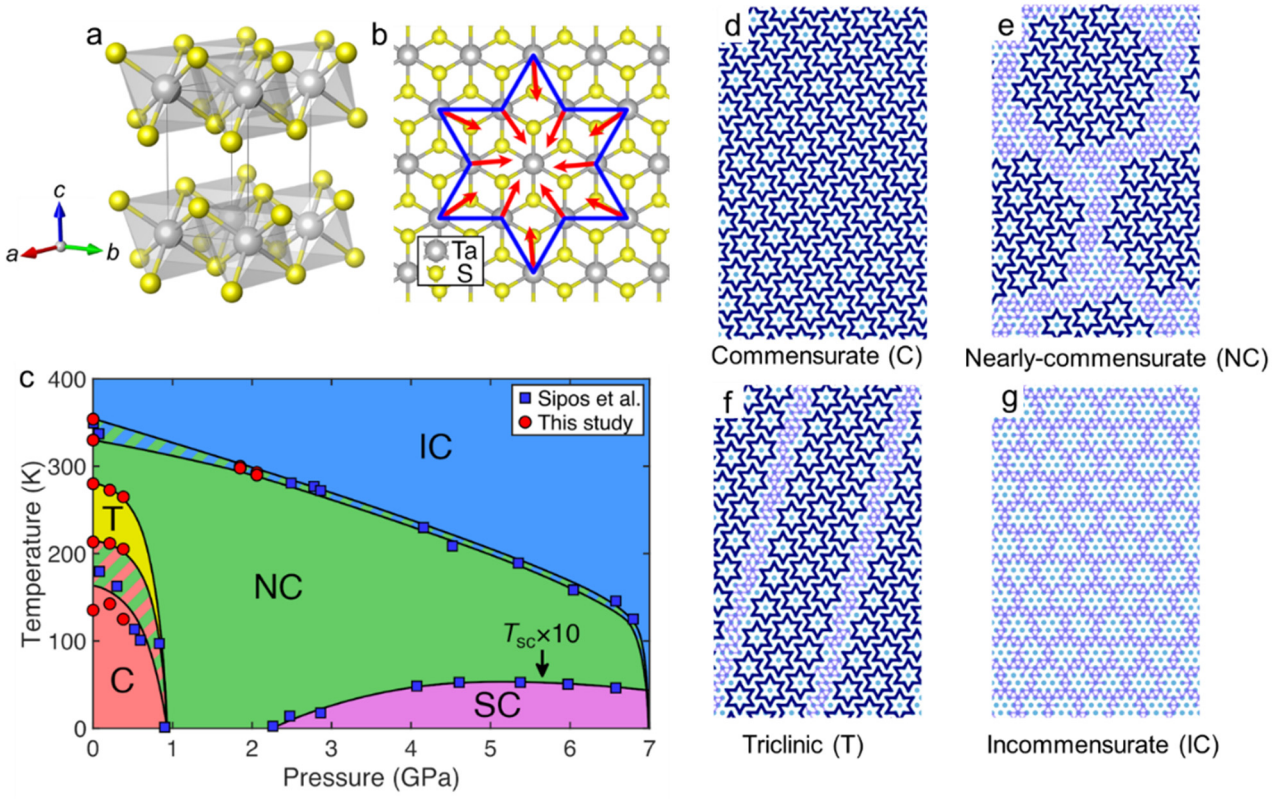

Figure 4:1 Charge density waves in 1T-TaS_2. **a)** Crystalline structure of undistorted 1T-TaS_2. **b)** In-plane lattice distortion leading to a formation of a David star cluster (DS) — a recurring element of the various CDW textures of 1T-TaS_2. The red arrows point the direction of in-plane displacements of the Ta atoms, and the blue line outline the DS. **c)** Pressure-temperature phase diagram of 1T-TaS_2, based on the resistivity data of Sipos et al. [90] and this study. The black lines represent the approximate phase boundaries. The striped areas indicate the regions where hysteresis occurs upon heating and cooling. The T phase is observed only during a warm-up. Superconducting (SC) transition temperature is multiplied by 10 for clarity. **d-g**) Schematic illustration of the in-plane reconstruction in different CDW phases. The David-star clusters are marked by the dark blue outlines, light blue dots are Ta atoms. Purple lines represent shorter Ta-Ta distances with respect to the undistorted lattice.

The instability interval for each phase can be tuned by applying hydrostatic pressure. The temperature-pressure phase diagram of all CDW orders of 1T-TaS_2 is shown in Figure 4:1 c. The low-temperature CDW phases (C, T and NC) are all characterized by the formation clusters made of 13 Ta atoms and 26 S atoms. The cluster is shaped as a Star of David (henceforth referred to as DS), with 12 Ta atoms moving towards a central one as represented in Figure 4:1 b. The DS cluster can be regarded as a building block for the different lattice reconstructions. For the C phase, the entire crystalline plane is tiled by DS clusters (Figure 4:1 d). For the NC and T phases, the DS clusters can only be observed inside nanometre-sized domains, shapes of which differ between the two type of reconstructions (Figure 4:1 e,f). In the IC phase (Figure 4:1 g), DS clusters are absent, and the lattice distortion is modulated incommensurately, which manifests as an aperiodic network of shortened Ta-Ta distances, marked with purple lines.

In comparison, the isostructural and isoelectronic 1T-$TaSe_2$ exhibits the same high temperature incommensurate (IC) and low temperature commensurate (C) phases, but has no sign of the nanocomposite phases, like the NC or T phases of 1T-TaS_2 [91]. It is the presence of these nanocomposite phases that leads to some of the most enigmatic properties of 1T-TaS_2 and makes the material so unique among other TMDs.

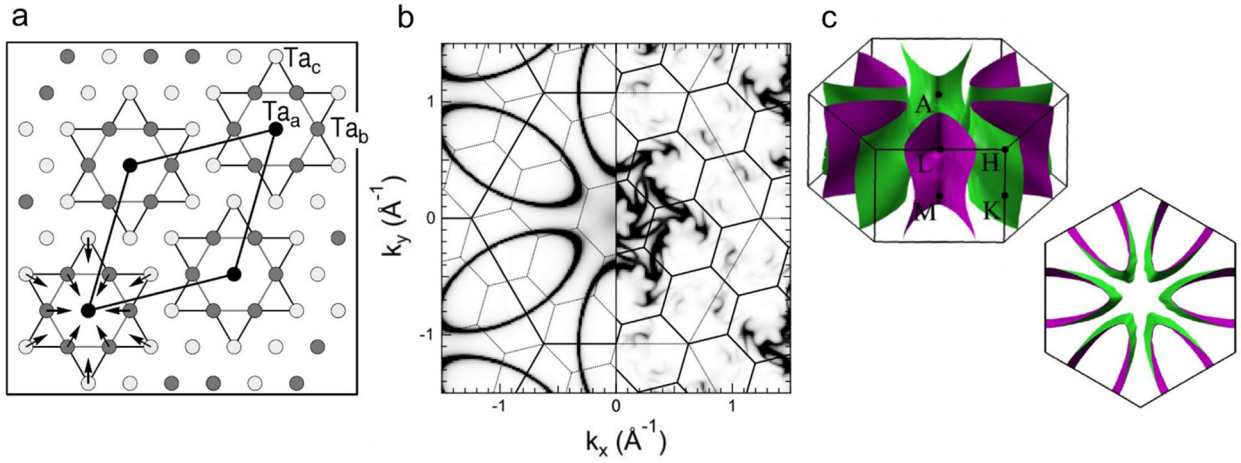

Figure 4:2 Commensurate CDW, lattice and Brillouin zone reconstruction. **a)** Unit cell of the commensurate CDW phase with modulation vector $\boldsymbol{q} = \sqrt{13}a$ x $\sqrt{13}a$. The new lattice vectors are rotated by 13.9° with respect to the undistorted unit cell. Figure from [84] **b)** In-plane Fermi surface projection and Brillouin zones folding, for the undistorted (left) and C-CDW (right) phases of 1T-TaS_2. Figure from [84]. **c)** Fermi surface of the undistorted 1T-TaS_2, indicating the quasi-2D character of the electronic structure. Figure from [92].

In the commensurate phase of the CDW in 1T-TaS_2, the new lattice modulation is rotated by 13.9° with respect to the unit cell vectors of the parent lattice (Figure 4:2 a). The rotation in the real space lattice is also reflected in the reciprocal space. The new Brillouin zone (BZ) boundaries keep the original hexagonal shape, but are again rotated by the same angle of 13.9° (Figure 4:2 b). The Fermi surface of the undistorted phase crosses the zone boundaries multiple times, and not along high symmetry directions.

The Fermi surface of the undistorted lattice (Figure 4:2 c) is composed of six quasi-tubular sheets centred at the M point of the BZ, all having a limited warping along k_z direction. Given such an electronic structure a high resistivity anisotropy is expected. The fact that only Ta *d*-orbitals are present at the chemical potential means that all electronic properties can be understood in terms of a single electronic band.

4.2 Transport anisotropy

From the precise determination of resistivity anisotropy in 1T-TaS_2, comes one of the most surprising findings reported in this thesis. Resistivity anisotropy for this material has already been presented and discussed in a few earlier publications [93],[94],[53]. All of them report anisotropy ($\rho_\perp/\rho_\parallel$) to be between 500 and 2000, and with a very similar temperature dependence along both directions.

Conducting the in-plane and out-of-plane resistivity measurements with an improved sample geometry, thanks to FIB microfabrication, provided an unmatched signal to noise ratio, and never observed details in the temperature dependence. In particular, we observed differences in resistivity temperature dependence for current flowing along or perpendicular to the atomic planes, and the evidence of a very low anisotropy, between 4.3 at 400 K and 0.6 at 1.8 K.

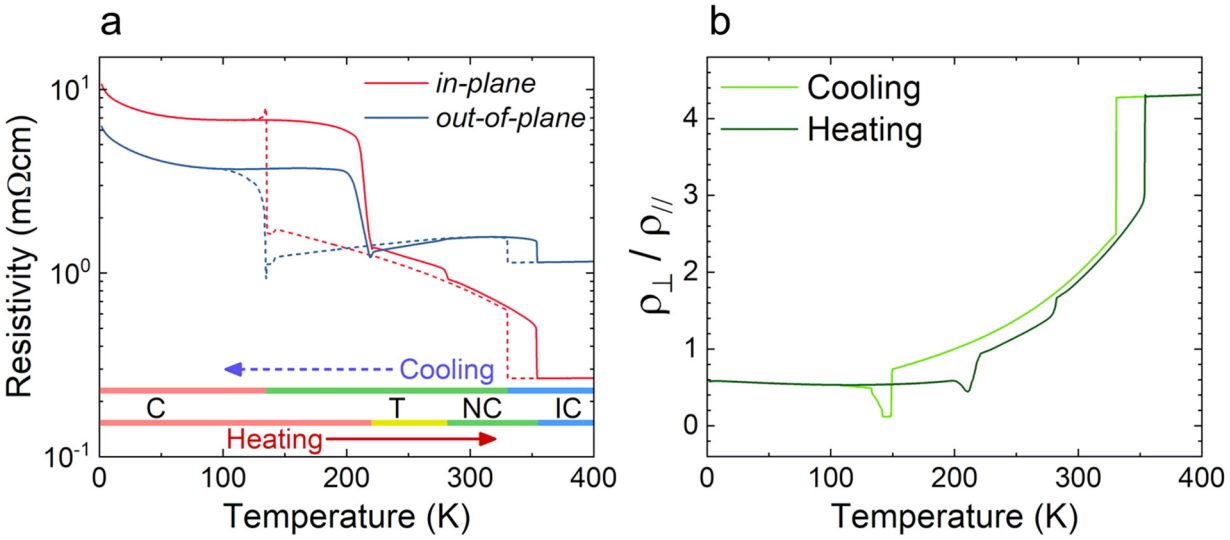

Figure 4:3 Resistivity anisotropy of 1T-TaS_2. a) Temperature dependence of the electrical resistivity of 1T-TaS_2 for current flow along the in-plane ($\rho_\parallel$) and out-of-plane ($\rho_\perp$) directions, during cooling (dashed lines) and heating (solid lines). The bars in the bottom part of the plot indicate the temperature intervals for different CDW phases encountered throughout sweeping the temperature during cooling and heating. Sharp dips and jumps in resistivities, accompanying their dominant changes around 135 K are associated with temporary internal stresses experienced by the sample due to a sudden change in the crystal volume occurring at the CDW transition. **b**) Resistivity anisotropy ($\rho_\perp/\rho_\parallel$) as a function of temperature during cooling and heating.

The temperature dependences of electrical resistivities along the two principal current directions, in the range from 1.8 K to 400 K are shown in Figure 4:3 a. For reference, all the observed CDW phases and the corresponding temperature intervals are indicated in the bottom part of the plot. Resistivity displays a hysteretic behaviour at every transition (with the exception of the T to NC), as they are all first order phase transitions. The computed anisotropy, plotted as a function of temperature in Figure 4:3 b, decreases with cooling from 4.3 at 400K to 0.6 below 100 K, with discontinuous jumps after every transition. In the high-temperature IC phase, where DS clusters are absent, the anisotropy is substantial, as expected for a layered conductor, but still 2 orders of magnitude lower than the values proposed previously. Following the IC to NC transformation, the anisotropy is suddenly reduced. The temperature dependence along different directions presents a surprising behaviour, with the out-of-plane resistivity decreasing on cool down—expected for a metallic system—while the in-plane one increases. This dual behaviour observed in the NC phase will be further discussed in the coming section. An interesting outcome is the crossing of the two curves around 200 K, temperature below which the out-of-plane resistivity is lower than the in-plane one. Around 135 K, at the onset of the C phase, a metal-semiconductor transition is evident, with resistivity showing a thermally activated behaviour. The T

phase, which can only be observed during heating from the C phase, is similar to the NC phase, as it consists of nanometer-sized domains hosting DS, but with a different geometry. The transition from T to NC phase resembles a second order phase transition, which can be explained through a reorganization of the DS domains.

A pair of drawbacks of the focused ion beam microfabrication are noticeable in the measurement. The first is the presence of a thin layer amorphous of material (a few nm) on the surface exposed to the ion beam. The exact composition is unknown, but it is highly probable that it consists predominantly of Ta which was either left over due to the preferential ablation of the chalcogen, or was redeposited from sputtered materials during the ion beam etching. A more detailed discussion can be found in section 7.1.4. Such a layer is typically conductive and in certain cases even superconducting (with observed T_C of 4.4 K). Presence of this layer in 1T-TaS_2 affects the measured resistivity of the C phase most noticeably, as this is the state with the lowest conductivity. The effect is mitigated by a careful polishing of the sample by ion milling at a grazing angle, and subsequent oxidation of the metal layer by its exposure to air. Samples that have been measured a few weeks after the fabrication present a more pronounced insulating behaviour of the C phase, because of the complete oxidation of the thin Ta crust around the sample.

When 1T-TaS_2 is cooled down, at the onset of the C-CDW transition is associated with a lattice expansion along the *c*-axis in the order of 3 % [95],[96]. This generates another drawback for FIB microstructured sample, since mechanical stresses can be temporarily acting on the material during cool down. The mechanical effect originates from the coupling between the sample and the sapphire substrate. The stresses can be amplified if the sample is fixed to the substrate using an adhesive [97], or held in place by van der Waals attraction as the surface of both the sample and the substrate are polished to nanometre roughness. The presence of residual stresses is considered responsible for the sharp dips and jumps observed in resistivity temperature dependence at the NC to C transition. These artefacts are absent, or less pronounced in bulk and free-standing samples. The effect is also diminished after a few thermal cycles, which probably helps to decouple the sample from the substrate and relax the induced stresses. Nevertheless, the aforementioned shortcoming distorts the data negligibly, the presented results are genuine and intrinsic to the studied compound. The observations have been reproduced across multiple samples, after many thermal cycles, and after surface oxidation over a long term exposure to air.

Because the results presented here are in stark contrast with the existing literature (Figure 4:4), we will discuss the origin of this large discrepancy. We justify our results by identifying flaws of the earlier experiments, and by comparing our data with finite elements simulations (Figure 4:5).

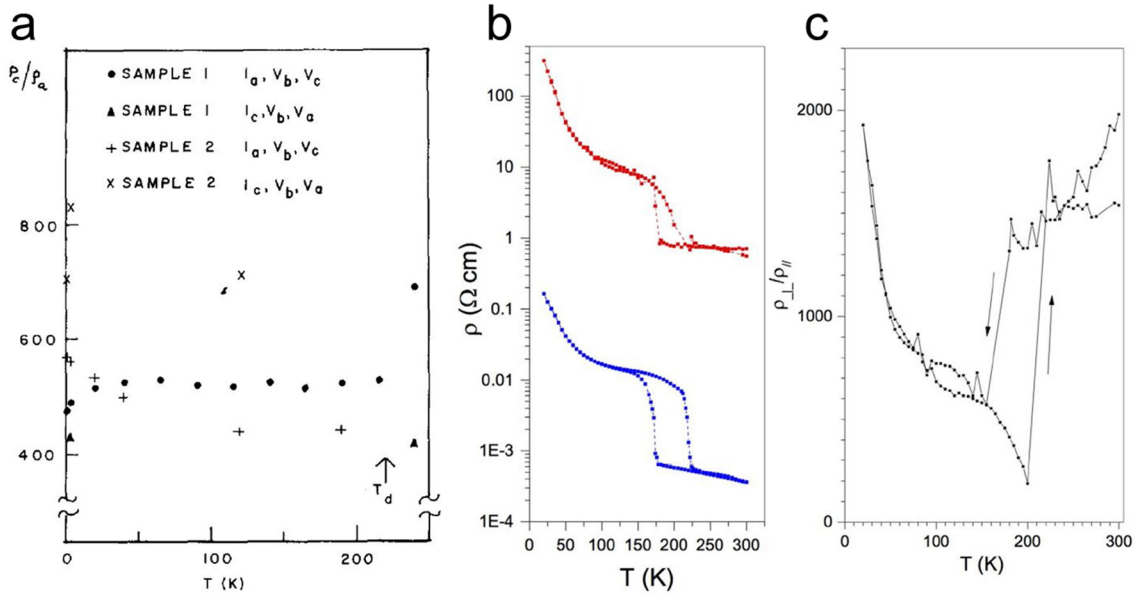

Figure 4:4 Existing reports of 1T-TaS_2 resistivity anisotropy. a) First report of resistivity anisotropy for 1T-TaS_2 was published in 1980 [93]. Out-of-plane resistivity is approximately 500 times higher, and no evident difference in the temperature dependence is observed compared to the in-plane flow. **b)** The temperature dependence of the in-plane (blue) and out-of-plane (red) resistivities. **c)** Computed resistivity anisotropy as a function of temperature, reaching 2000 [53].

The previously published data on resistivity anisotropy of 1T-TaS_2 are presented in Figure 4:4. The reported anisotropy is in the range from 500 to 2000. At the same time, there is no noticeable difference in the temperature dependence for $\rho_{\perp}(T)$ and $\rho_{\parallel}(T)$. The reported resistivity data are also missing any features associated with the T to NC transition. This transition, has been observed by other techniques, such as scanning tunnelling microscopy (STM) [98], X-ray diffraction (XRD) [99] and specific heat [100]. Previous measurement of resistivity anisotropy have been performed on thin samples contacted on the top and bottom surface with point-like electrodes. Two opposed contacts were used as current leads, and the geometry was justified by the assumption that the expected high resistivity anisotropy would distribute the current evenly in the entire basal plane of the crystal. Starting with the assumption of high conductivity anisotropy, two different approached have been used by Svetin et al.[53] and by Hambourger & Di Salvo [93].

In the case of Svetin et al. the resistivity measurements have been performed on a very thin flake of 1T-TaS_2 (the dimensions of 110 µm x 10.5 µm x 90 nm are provided in the article), which has been probed via 8 electrodes, with 4 located on each side of the flake (Figure 2:8). The out-of-plane resistance was measured via the two-point method, with subsequent determination and subtraction of the contact resistances. When converting resistance to resistivity, the authors assumed that the current was distributed across the whole area of the flake, which would have been correct had the resistivity anisotropy of 1T-TaS_2 been much more than 1. According to our results, this is not the case, therefore the much higher $\rho_{\perp}$ can be explained by the massive overestimation of the current-carrying cross-section area. Another issue is the fact that the plots of $\rho_{\parallel}$ and $\rho_{\perp}$ against temperature provided in the article by Svetin et al. have almost the same shape. Given the small thickness of the sample, if the contacts used for the interlayer resistivity measurements have been misaligned by more than several tens of nanometers, the resultant current path must have had a substantial in-plane component. Voltage drop due to this contribution could have been large enough to dominate over the genuine out-of-plane signal, resulting in effectively the same quantity being measured for the two nominally different current flow directions.

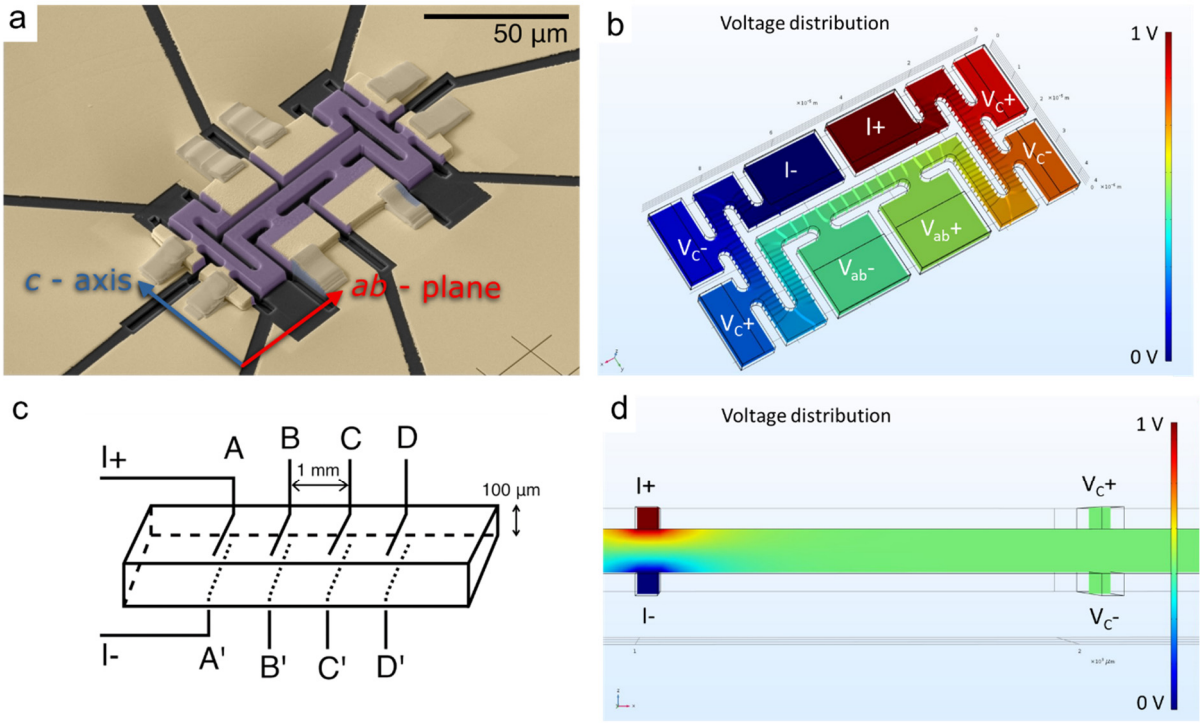

Figure 4:5 Sample geometries for resistivity anisotropy measurement. **a)** Scanning electron microscopy image of a FIB microstructured single crystal or 1T-TaS_2 (in purple). False colours are used for clarity. The gold film (yellow) is sputtered to ensure electrical connection to the external electrodes. Pt ramps (grey) are created by FIB in-situ deposition to ensure mechanical stability and continuity of the gold film over the side surfaces of the lamella. **b)** Finite element simulation for the voltage distribution in the same sample geometry as shown panel **a**. The resistivity anisotropy used for the simulation is 10. **c)** Schematic representation of the sample geometry used in the experiment presented in [93]. **d)** Finite elements simulations of the voltage distribution in the sample configuration as presented in ref [93]. The resistivity anisotropy used for the simulation is 10.

The experiment of Hambourger & Di Salvo utilised a similar sample geometry to Svetin et al. (Figure 4:5 c), but an unusual method to compute resistivity anisotropy. Using the notation introduced in the figure, and defining $V_{BB'}$ and $V_{CC'}$ as the potential differences between contacts B and B' as well as C and C', respectively, the authors claimed that resistivity anisotropy should have been inversely proportional to $(\ln V_{BB'} - \ln V_{CC'})^2$. In the scenario of low anisotropy, most of the current is expected to flow only in a small portion of the sample, in close vicinity of the contacts A and A', making the voltages $V_{BB'}$ and $V_{CC'}$ extremely small and therefore difficult to measure. In order to verify this statement, we used the finite element analysis package COMSOL Multiphysics™ for calculating the distributions of current density and voltage throughout the sample during a measurement.

Figure 4:5 d shows the model used for the calculations. Following the information provided in the paper, the sample was represented by a rectangular block of 5 mm length, 1.5 mm width and 100 µm thickness (*c*-axis extent). The spacing between the electrodes was 1 mm and the electrodes themselves were chosen to be 50 µm wide. The excitation current was set to 5 mA, the same value as quoted in the paper. The virtual sample was assigned the in-plane resistivity value equal to that of 1T-TaS_2 at room temperature (0.78 mΩcm). Imposing resistivity anisotropy of 10 results in the voltage distribution shown in Figure 4:5 d. As expected, effectively all the current flowed directly between the electrodes A and A', making $V_{BB'}$ and $V_{CC'}$ differs by less than the resolution limit of 1 nV. Such a weak signal could have been easily overshadowed by various contributions due to systematic errors. With the sample design proposed by Hambourger & Di Salvo, resistivity anisotropy could have been correctly measured only if $\rho_\perp/\rho_{//} > 10^4$.

4.3 NC-CDW transport anomalies

Among the peculiarities of 1T-TaS_2, the structure and properties of the NC phase are the most prominent and unique. This CDW phase is characterized by the formation of a nanometric array of DS domains, separated by regions of aperiodic lattice distortion. The rich set of structural information, collected during and before this thesis, provides a clear picture of the size of the domains, their orientation relative to the underlying lattice and their evolution as a function of temperature and pressure [101][102].

Domain formation in the NC phase is driven by the existence of different "modulation phases" for the periodic distortion induced by the charge density wave. The formation of a David Star cluster can be centred on any Ta atom. Once the position is defined for one cluster, the location of the neighbouring ones is unequivocally assigned. But it is possible to create another identical domain where the clusters are shifted by one atomic site (*a*) only. If the two domains are placed in proximity, they will create a boundary region where a complete cluster of 13 atoms cannot be created.

In the NC phase, the CDW modulation vector is close to being commensurate to the lattice. To accommodate the difference from commensurability, the lattice reconstruction forms domains where the CDW is commensurate and forms a DS cluster. The lattice mismatch manifests at the boundaries where CDW develops a phase shift and discommensuration occurs. Such regions are noticeable in Figure 4:6 a by their absence of DS clusters. What happens at the NC to C phase transition is the uniform coverage of the atomic plane by DS clusters, because only one of the possible modulation phases will be "selected" by the lattice reconstruction and no discommensurations will be present. Domains containing DS are long-range-ordered to create a "super-superstructure" that can be observed by XRD [102] and STM [103]. Each domain includes around 30 to 50 of DSs, and has a typical size of 5 to 10 nm. The arrangement of the domains was often described as "Kagome-like", as each single domain is approximated as hexagonal in shape and connected to the neighbouring ones in a corner sharing configuration[102]. From the refinement of our X-ray diffraction data, it is revealed that the DS domain lattice deviates from an ideal corner sharing Kagome lattice (Figure 4:6). The domains are stacked in a well-defined order. Besides the in-plane displacement of atoms, formation of a DS also involves an out-of-plane expansion of the S-Ta-S layer, as S atoms are pushed away from the plane of Ta atoms. Each domain can therefore be seen as a region locally inflated in the out-of-plane direction. To minimize the elastic energy of the three-dimensional lattice area, domains in neighbouring layers must maximally avoid each other. The resultant order has a 3-layer periodicity and an FC*C*-like configuration of AB*C*-type stacking, illustrated in Figure 4:6 b. With changing temperature or pressure, the in-plane configuration and size of the domains change. Upon increasing temperature or pressure, the domains shrink, reducing the number of DSs they contain, and changing their relative distance [102] [104]. Also, the relative orientation is modified, with a rotation of the domains away from a Kagome-like structure towards a honeycomb-like as shown in Figure 4:6 c.

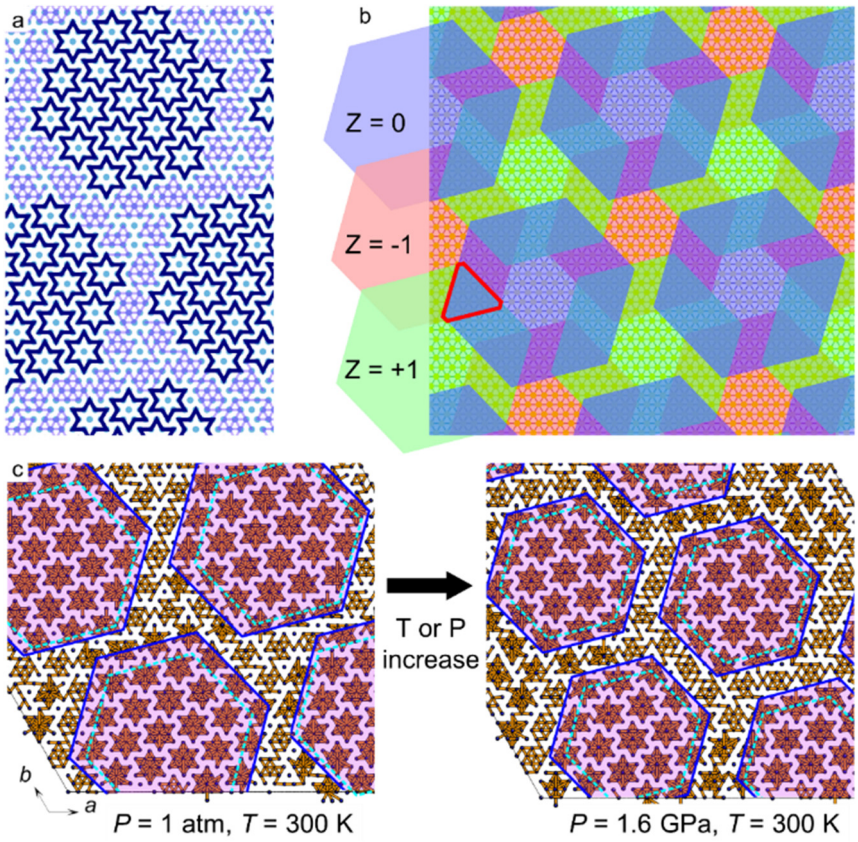

Figure 4:6 CDW domains in the nearly-commensurate phase of 1T-TaS_2. a) In-plane structure of the NC phase, simplified from room temperature X-ray diffraction data refinement. The complete DS are shown in dark blue, and the shortened Ta-Ta bonds as purple lines. **b)** DS domain stacking follows an FC*C*-like pattern (ABC). Domains from three different layers are visualized in different colours. Domains from neighbouring layers partially overlap with each other. The red triangle marks the area where the domains overlap over the three layers. **c)** Room-temperature in-plane lattice structures in the nearly-commensurate phase of 1T-TaS_2 at ambient pressure (left) and at 1.6 GPa (right), visualised based on the powder X-ray diffraction data. Ta atoms are represented by dots, which are connected if the interatomic separation is below an arbitrarily chosen threshold value. The hexagonal outlines mark the commensurately reconstructed domains, with the incomplete DS clusters included (solid blue) or excluded (dashed cyan). An increase in temperature (T) or pressure (P) both lead to the same transformation – rotation from corner-sharing towards side-sharing arrangement, shrinkage of domains and reduction of the domain lattice period.

Having clarified the periodic lattice distortion of the NC phase, we now look at the anomalous transport properties that emerge in this "nanocomposite" structure. From the electronic structure point of view is hard to imagine how the composite structure, with multiple lattice modulations coexisting, will affect the material properties. It is also completely unclear what happens to the electronic states that sit at the edges of the DS domains: Will those edges act as grain boundaries even if the material is monocrystalline? Because the lattice modulation is segmented into domains, the translation symmetry is broken along the *ab*-plane. This begs the question how the conduction electrons are affected by the loss of commensurability, and if this hinders the formation of Bloch states. All of this only applies to the in-plane translation. In the out-of-plane direction the modulation of lattice distortion is commensurate and has a period of $3c_0$.

To extend the NC phase down to the lowest achievable temperature, and see the effect of a changing interlayer distance and domain size on the electronic properties, we conducted resistivity measurements at different pressures, up to 2.1 GPa. Temperature dependence of electrical resistivity for the in-plane ($\rho_{\parallel}$) and out-of-plane ($\rho_{\perp}$) directions of the current are reported in Figure 4:7. Above the pressure of 1 GPa, the C phase is fully suppressed, and the NC extends to the lowest temperature. With pressure increasing further, resistivity along

both directions tends to decrease, with a faster rate of change for $\rho_{\perp}$. While the resistivities change, their temperature dependences do not show sizeable variation.

The surprising contrast in the behaviour of the two resistivities behaviour is clearer in Figure 4:7 c, where the data at 2.1 GPa for both current directions are shown together. For $\rho_{\perp}$ we observe a typical behaviour of a metal, with a relatively high value and low RRR, but still preserving the positive temperature coefficient and a Fermi-liquid like behaviour at lowest temperature, $\rho_{\perp}(T) \propto T^2$. The in-plane resistivity shows an opposite trend, increasing on cool-down, with a nearly linear slope and a saturation at the lowest temperature. No model has been proposed so far to describe the temperature dependence of the in-plane resistivity, but it is interesting to note its close resemblance to that of quasicrystals and disordered metals [35]. A very interesting analogy is the case of decagonal quasicrystals. Those crystalline metallic materials have quasiperiodic planes due to a broken translational symmetry. However, along the out-of-plane direction the periodicity in preserved, and this is very reminiscent of the NC phase. The temperature dependence of the resistivity and its anisotropy have a very similar behaviour to 1T-TaS_2 in the NC phase, with $d\rho/dT > 0$ for current along the periodic direction, as well as $d\rho/dT < 0$ and higher resistivity for current along the quasiperiodic plane [105]. Another example is the charge transport anisotropy in highly oriented pyrolytic graphite (HOPG). In this case the very high density of stacking faults breaks the translational symmetry along the out-of-plane direction. In-plane charge transport is therefore metallic, while the out-of-plane one exhibits $d\rho/dT < 0$ and saturates at low temperature [106][107]. For perfectly crystalline graphite the out-of-plane resistivity is also metallic, as translational symmetry is preserved.

To better understand why 1T-TaS_2 conducts better in the out-of-plane direction than in the in-plane one, we compared its room temperature resistivity values with those of 2H-$NbSe_2$ and 2H-$TaSe_2$. Both of these materials show coherent transport in all directions (Figure 4:7). The out-of-plane resistivity of 1T-TaS_2 sits between the corresponding values for the other two materials, therefore we interpret the conduction along this direction as coherent transport, which can take place through the overlapping DS domains and is not a percolative-type conductivity along the discommensuration areas. It is the comparatively high in-plane resistivity of 1T-TaS_2 that causes its very low anisotropy. A tentative explanation for this behaviour is the enhanced scattering rate for in-plane charge transport that originates from the composite nature of the CDW reconstruction.

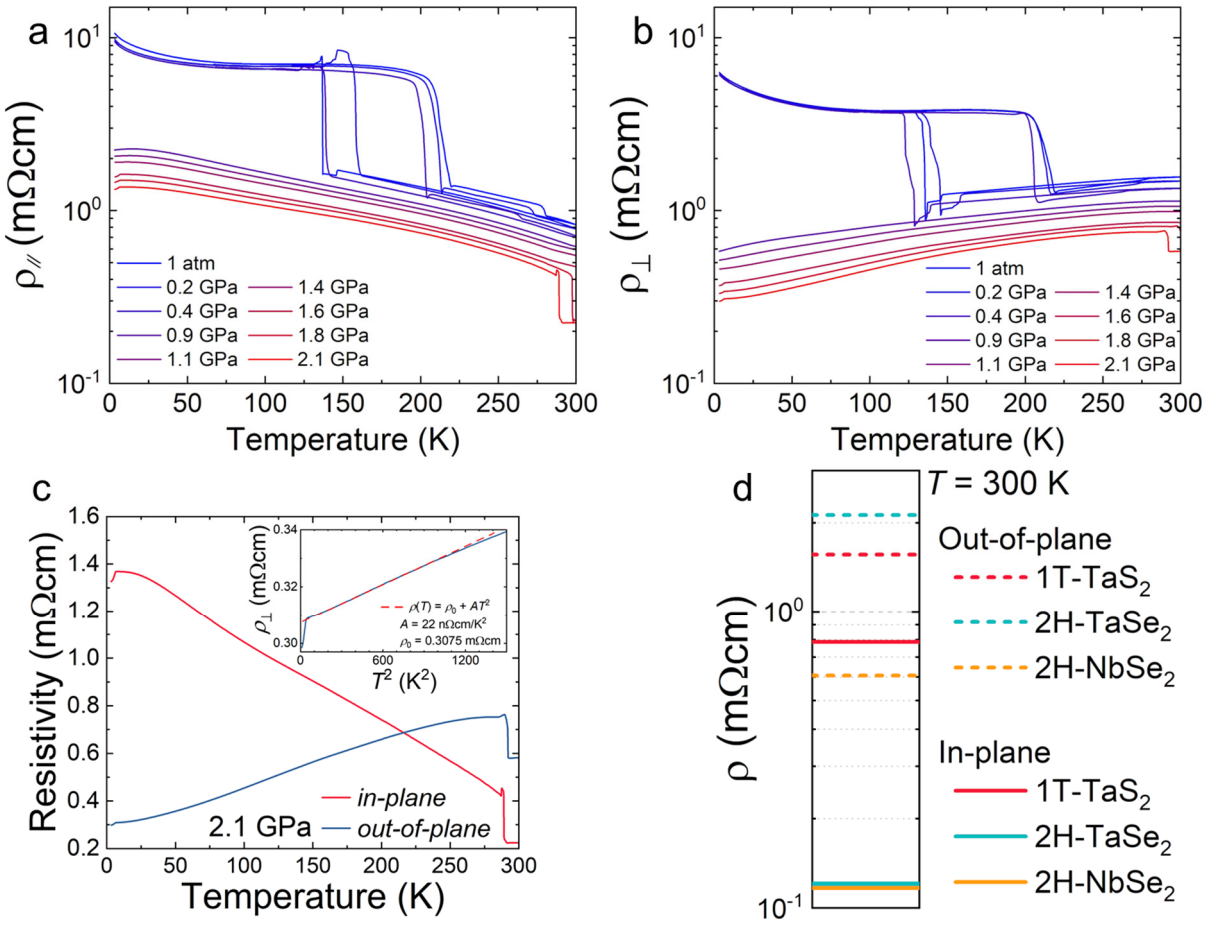

Figure 4:7 Resistivity anisotropy in the NC-CDW phase of 1T-TaS_2. a) In-plane and **b)** out-of-plane electrical resistivities of 1T-TaS_2 ($\rho_{\parallel}$ and $\rho_{\perp}$, respectively) as functions of temperature for different applied hydrostatic pressures. **c)** Temperature dependences of resistivities along the two directions at 2.1 GPa pressure. The inset shows a quadratic power-law fit to the out-of-plane resistivity between 7 K and 30 K. **d)** Comparison between the room temperature in-plane and out-of-plane resistivity values of 1T-TaS_2 and two other metallic transition metal dichalcogenides: 2H-$TaSe_2$ and 2H-$NbSe_2$.

4.4 Orbital ordering and revision of the Mott phase

The scope of this section is to discuss in detail the electronic structure of the C phase, and the origin of the associated metal-insulator transition. The mechanism of electron localization in 1T-TaS_2 is one of the most commonly investigated aspects of the compound, and it was initially classified as a Mott localization after the work of Tosatti and Fazekas in 1976 [89]. Following this definition, the absence of a magnetic order associated with this transition fuelled the idea of a possible quantum spin liquid state [108], as the Mott state should typically be accompanied by an antiferromagnetic order, which was never observed in1T-TaS_2.

The central argument for the Mott-type localization is that the: charge density wave is not able to fully gap the Fermi surface in a quasi-2D system, leaving a residual density of states at the Fermi level and an expected metallic behaviour. On the other hand, the electron density within every DS cluster is moved from the 12 peripheral Ta atoms towards the central one. The argument in favour of the Mott scenario was that the 12 electrons would be localized on the respective atoms, resulting in a lattice of half-filled sites at the centres of the 13-atom DS clusters. Such a system can then be turned into an insulator by the strong Coulomb interaction between the electrons at the centre of each DS. This description was proposed in the context of a quasi-2D picture, where the electronic properties are dominated by the in-plane interactions only. The new results in this

work suggest that interlayer interaction is actually very important in this material, and this will be revealed later, when discussing the origin of the insulating phase.

Before that, there is a different aspects of the CDW structure that needs to be assessed. The electronic structure of 1T-TaS_2 at the chemical potential is dominated by the Ta $\boldsymbol{d_{z^2-r^2}}$ orbital. This orbital structure is characterized by larger lobes protruding along the *c*-axis. Inside a DS cluster, as the electron density is transferred to the central Ta atom, the size of the electron density lobes is enhanced, as shown in Figure 4:8 a. If we look at the C phase, combining the electron density and orbital character, it is evident that hybridization along out-of-plane is much more favoured with respect to the in-plane one (Figure 4:8 b,c). With this image in mind, it is certain that the interlayer interaction has a significant effect on the electronic properties of 1T-TaS_2. Experimentally, the C phase does not appear to be stable in atomically thin samples, suggesting that it might be stabilized by interlayer interactions [109].

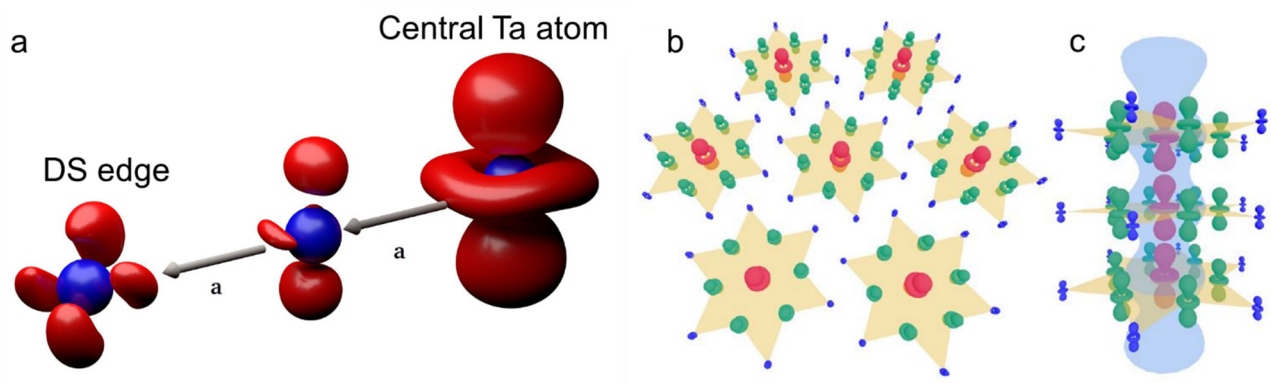

Figure 4:8 Ta-orbitals in the David star clusters. **a)** Electronic orbitals on Ta atoms in different inequivalent positions in the DS cluster, figure from [110]. **b-c)** Pictorial representation of the C phase in-plane **b)** and out-of-plane **c)** orbital structure, figures from [92].

Few theoretical works have addressed the properties of 1T-TaS_2 in the C phase, where the large Ta *d*-orbitals will significantly interact along the out-of-plane direction. Contrary to the well-defined *c*-axis periodicity observed in the NC phase, no obvious out-of-plane modulation vector can be seen from the X-ray data for the C phase. Given a pair of commensurately reconstructed layers, there are 3 possible inequivalent arrangements between the two subsequent layers. The centre of a DS in one layer can be located above: the central atom of the star, a Ta atom closest to the central one, or one of the outermost edges of the star. The electronic properties as function of different stacking order were addressed in the works by Ritschel [110], and Lee et. al [111], and part of it was reproduced in the work of this thesis, in Figure 4:9.

In the case of vertically stacked DS (A-stacking as defined by Lee et. al. [111]), the perfect *c*-axis orbital ordering produces a surprising quasi 1D character along out-of-plane direction. Such electronic structure presents a complete twist, in view of the expected electronic properties of 1T-TaS_2 it is a layered materials that could hosts a quasi 1D electronic structure oriented out-of-plane (Figure 4:9 e). This result has been reported many times [112] [113] [114], but has received little attention it conflicted with the belief that 1T-TaS_2 is a quasi 2D conductor. Also, for the staircase stacking (L-stacking, Figure 4:9 b), the band structure produced by the merging of the Ta orbitals implies that the preferential direction of conduction goes approximately along the line which joins the centres of the nearest-neighbour DS clusters located in the adjacent layers.

These findings can help interpret the robust out-of-plane metallicity, but can also provide an alternative understanding for the origin of the insulating state. For the A-stacking configuration, the electronic state that forms is that of a quasi 1D electronic system. Because of the proposed low dimensionality, the C phase of

1T-TaS_2 is prone to a lattice dimerization, a Peierls-like instability, which minimizes the electronic energy by opening of a band gap at the chemical potential. In their research, both Ritchel and Lee have independently demonstrated that for a stacking configuration in which DS clusters dimerise, a band gap of approximately 200 meV should open at E_F [110][111]. Their value estimated from DFT is remarkably close to the experimental determination by optical spectroscopy [115]. The formation of dimers is indeed suggested by structural data coming from X-ray diffraction [110], electron diffractions [116] and NQR [117]. Because the stacking of dimers is not well ordered, there is no evident modulation along *c*-axis. The experimental evidence of sizeable interlayer coupling, suggested by the small transport anisotropy we determined, is a strong support to the description of the metal-insulator transition in 1T-TaS_2 as driven by a Peierls-like instability.

To summarize, by employing the state-of-the-art FIB-based sample preparation process, we conducted reliable and accurate measurements of the in-plane and out-of-plane electrical resistivities of 1T-TaS_2 in multiple CDW phases. The experiments revealed unusually anisotropic charge transport character in presence of the NC CDW order: the out-of-plane conduction is metallic, yet for the in-plane direction the material becomes less conductive upon cooling. The in-plane resistivity in the NC phase is substantially enhanced compared to the typical values observed in other metallic TMDs. We conjecture that such an effect is caused by an additional charge carrier scattering mechanism, stemming from the aperiodic composite character of the lattice. At the same time, the out-of-plane conduction is favoured by the formation of the quasi-one-dimensional *c*-axis oriented chains of electronic orbitals. Those chains propagate through the overlapping regions of DS domains, and serve as a source of previously unobserved coherent *c*-axis metallicity. Such a description is supported by our DFT calculations in Figure 4:9. Consequently, the layered 1T-TaS_2 has an uncharacteristically low resistivity anisotropy, exhibiting nearly 5 times lower out-of-plane resistivity than the in-plane one under certain conditions. Moreover, we interpret the NC to C phase transition as a quasi-one-dimensional instability, and support the idea of the C phase being a band insulator, rather than a Mott state, as has been thought previously. Our findings are also valuable in the context of efforts to functionalize the compound. Exploiting the interlayer conduction nearly doubles the resistivity change upon the low temperature phase switching, compared to the difference seen in the in-plane charge transport. This would lead to a more robust performance of a potential device. Furthermore, miniaturisation and production scalability requirements additionally favour utilisation of the out-of-plane charge transport. 1T-TaS_2 serves as a neat example of how interlayer interactions in a van der Waals material lead to unexpected properties, warranting a more systematic study of resistivity anisotropy in other compounds.

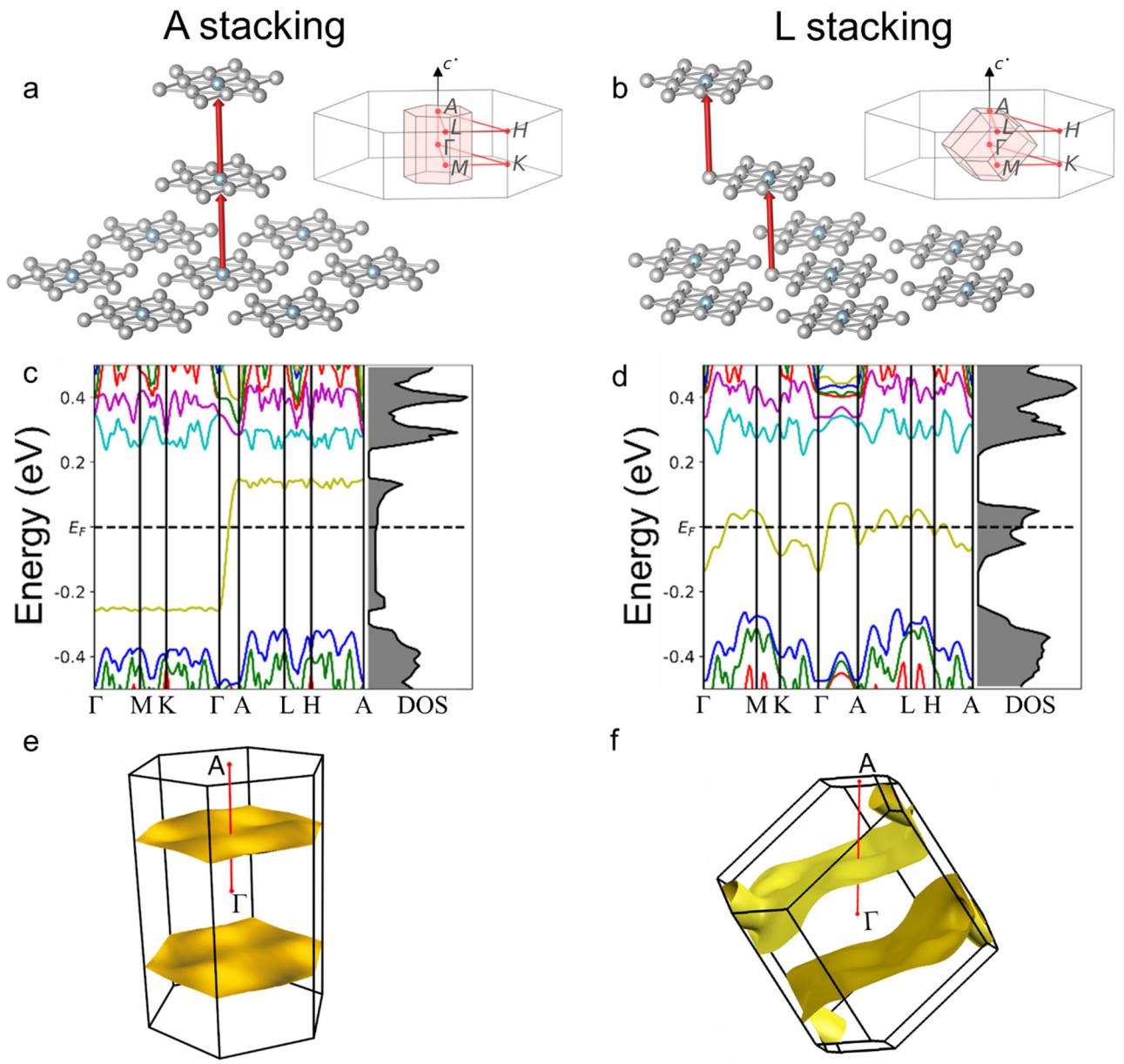

Figure 4:9 Possible electronic structure in the C-CDW phase of 1T-TaS_2. a,b) Possible relative arrangements of the David-star-shaped clusters (only Ta atoms are shown) in successive layers of commensurately distorted 1T-TaS_2, considered for our density functional theory (DFT) calculations. These configurations are denoted to as the A stacking (a) and the L stacking (b), after [111]. The red arrows join the Ta atoms sharing the same lateral position. The top right sections of both panels display the first Brillouin zones (pink polyhedra) for the corresponding lattices in relation to the first Brillouin zone for the completely undistorted 1T-TaS_2 (black wireframe). **c,d)** The respective electronic band structures and densities of states (DOS) predicted by the DFT calculations for relaxed lattices and with the on-site electron-electron interaction energy U = 2.41 eV. The directions traced in the reciprocal space are visualised in the panels a and b. The plots use different colours for different electronic bands. For both types of stacking the electronic structure contains a single metallic band (yellow) with a strong dispersion along the *Γ-A* direction. **e,f)** The respective Fermi surfaces in the first Brillouin zones of the reconstructed lattices (see panels a and b). The presence of extended open sheets in both surfaces indicates a quasi-one-dimensional character of the corresponding electronic structures.

4.5 Summary of 1T-TaS_2

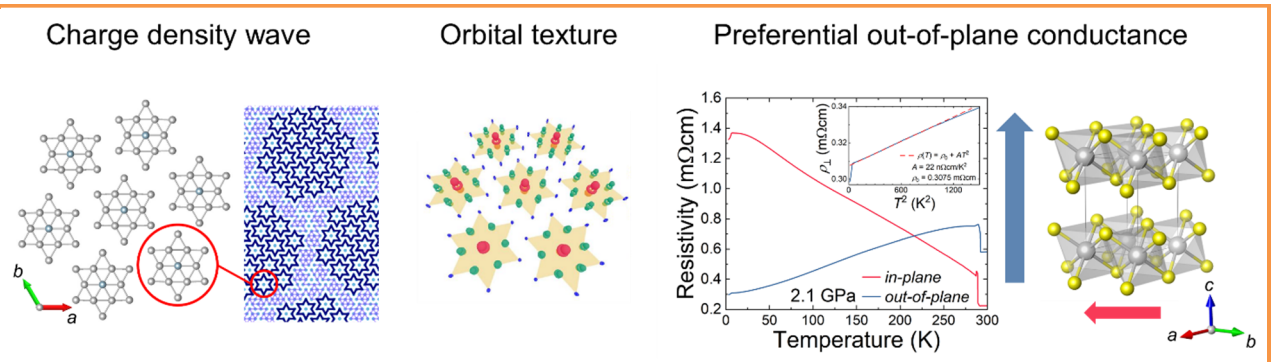

Figure 4:10 1T-TaS_2 summary

1T-TaS_2
The electronic properties of this material are dominated by the charge density wave formation. Ta atoms self-organize in 13-atom clusters with a characteristic David star shape. Around room temperature, the CDW phase is broken into domains in a nano-composite structure (NC-CDW). In this configuration, the in-plane translational symmetry is broken, while it is preserved along the *c*-axis. The complex lattice reconstruction comes together a simple single band electronic structure, dominated by Ta $\boldsymbol{d_{z^2-r^2}}$ orbitals, which are characterized by electron density lobes protruding along the *c*-axis.

Interlayer transport
1T-TaS_2 surprises with its anisotropic electronic conduction properties, in particular for the NC-CDW phase. In this phase, $\boldsymbol{\rho_\perp}/\boldsymbol{\rho_{||}}$ can be much lower than 1, meaning that out-of-plane conduction is preferred. While $\boldsymbol{\rho_\perp}$ has a characteristic metallic behaviour, $\boldsymbol{\rho_{||}}$ is non-metallic in nature, with an increasing resistivity at lower temperatures.
The peculiar combination of CDW and orbital order is responsible for the strong out-of-plane metallic coherence and weak in plane coupling.

Conclusion
1T-TaS_2 is a material of remarkable complexity because of its multitude of CDW transformations, but the simple-band electronic structure allows to draw a general conclusion: out-of-plane coupling is the driving interaction behind the unusual properties in this material.

Chapter 5 Natural heterostructures: $4H_b$-TaS_2

Among the various recent directions of research concerning layered materials, the most fruitful one is the field of artificial heterostructures [20]. The opportunity to create artificial materials by combining different atomically thin crystals has frequently lead to the emergence of new physical properties [21] [22]. In stark contrast to artificial heterostructures made by epitaxially grown thin films, creation of van der Waals heterostructures does not require the combined layers to have matching lattices, which enables vastly more combinations of materials their and arbitrary relative orientation. Yet a fundamental scalability problem remains. As of today, such artificial materials can only be created in the laboratory and manually. Their production is time consuming and characterized by a low success rate. For these reasons the current approach can only remain confined to specially equipped laboratories, and industrialization of the production requires a new paradigm.

A possible solution to overcome this technical bottleneck is to search for heterostructures that form spontaneously. Some layered materials, can indeed be grown with alternating-layer structures: remarkable examples are delafossite and cuprates HTS (Figure 2:1). Both of these classes of materials are composed of alternatively stacked conducting and insulating layers, and they exhibit peculiar properties such as ballistic electron transport and high temperature superconductivity, respectively. Up to date, the exploration of natural heterostructures has still been very limited, and there is no clear insight if these compounds can indeed offer similar platforms for the emergence of new properties, in the same way as artificial heterostructures have proved to do.

This chapter presents the structure and properties of a natural heterostructure, made out of two different types of crystalline layers of TaS_2, stacked in an alternating order. Such atomic structure can be created by taking advantage of the polymorphism of layered materials. This is the case of 4Hb-TaS_2, which contains four layers in the unit cell, two with the octahedral coordination (T-layers) as in 1T-TaS_2, and two with trigonal prismatic coordination (H-layers) as in 2H-phase. The different layers are stacked in a regular alternated order. By comparing this material with the previously studied 2H and 1T phases (Chapters 3.3 and 4), we have the opportunity to better recognize the emergence of new properties produced by the alternated stacking, where coupling between layers of the same type is reduced. The study of interlayer conductivity, is a perfect tool to gauge the electronic coupling and understand how the alternate stacking of different CDWs can affect the charge transport. As we have seen in the previous chapter, the electronic properties of 1T-TaS_2 are strongly influenced by the presence of a CDW and the interlayer overlap of Ta $\boldsymbol{d_{z^2-r^2}}$ orbitals at the centres of the star-of-David clusters. In 4Hb-TaS_2 the T-layers host the same CDW, but are divided by additional metallic planes (the H-layers), which do not host the same CDW reconstruction. Before diving into the details of the interlayer interaction in this material, the aspects of the electronic structure and the occurrence of CDW in each type of layer will be revised. The existing literature suggests that electronic properties of 4Hb-TaS_2 can be attributed almost entirely to the individual contributions of the two constituent species of layers: of octahedral (T) and trigonal prismatic (H) metal-chalcogen coordination.

In addition, the T-layers undergo the same C-CDW reconstruction as 1T-TaS_2, to form a superlattice of David star clusters. As we have seen in 1T-TaS_2, this CDW also comes with an electronic structure formed by *c*-axis

oriented $d_{z^2-r^2}$ orbitals. However, due to the T-layers in 4Hb-TaS_2 being interleaved by the H-layers, the low temperature state of the compound exhibits a new CDW reconstruction, and charge transport properties that cannot be linked to a specific kind of layer alone.

5.1 4Hb-TaS_2 crystal structure

The atomic structure of 4Hb-TaS_2 is displayed in **Figure 5:1**, with the layers of identical coordination marked with the same colour. The layers are stacked with all the transition metal atoms vertically aligned, as in 1T-TaS_2 and 2H-TaS_2. The alternated stacking is produced during the crystal synthesis by tuning the growth conditions. The stabilization of the desired phase is determined not only by the growth temperature, but also by the reactant stoichiometry, with excess sulphur stabilizing the 1T phase. Regarding growth temperature, 1T phase is stable at higher temperatures while 2H is stable at lower growth temperature [118]. The target temperature for stabilizing the 4Hb phase, is in between, such that formation energy for both metal-chalcogen coordinations is similar. These conditions of thermodynamic "ambiguity" result in the formation of an ordered material where the two types of coordination are alternately stacked.

In 4Hb-TaS_2, the sub-lattice of H-layers is identical to those in 2H-TaS_2. The sub-lattice made by T-layers differs from 1T-TaS_2. There are two T-layers that coexist in the same unit cell, where one is the mirror copy of the other. This configuration adds a glide plane symmetry operation along the *c*-axis with respect to 1T-TaS_2. 2H and 4Hb hexagonal lattices are described by the same symmetry operations *P63/mmc*, while 1T is trigonal and its symmetry operations are *P-3m1*. The presence of two T-layers in the unit cells will be of relevance later when studying the CDW. The C-CDW modulation is rotated with respect to the parent lattice, the rotation can be of +13.9° or -13.9°. The interlayer distance between the vertically aligned Ta atoms in 4Hb-TaS_2 is the same as in 1T-TaS_2 (~ 5.90 Å) and shorter than in 2H-TaS_2 (~ 6.05 Å). In plane lattice parameter is a = 3.332 Å, between that of 2H-TaS_2 (a = 3.315 Å) and 1T-TaS_2 (a = 3.36 Å). Among layered TMDs, this alternated stacking has only been observed for TaS_2 and $TaSe_2$. A plausible reason is the close energies of formation of the layers of the two types of coordination.

Table 5 reports the growth conditions for obtaining specific polytypes of TaS_2. In all cases the synthesis is performed via chemical vapour transport, using iodine as the transport agent. To obtain the 1T phase elemental Ta and S are used in combination with SnS_2, which provides the excess sulphur. Since the 1T phase is stable at higher temperatures than the 2H phase, obtaining crystals of 1T-TaS_2 at room temperature requires the growth process to be concluded by a rapid quench. For synthesizing the 2H and 4Hb phases, prereacted TaS_2 powder is used. The powder is obtained from high-purity Ta and S, sealed in an evacuated quartz ampoule (10^{-8} Torr) and reacted at 950 °C for 2 weeks. To obtain a high-purity 2H phase, excess sulphur is added for the transport stage, and the synthesis is followed by a low-temperature annealing. The 4Hb phase is stable at an intermediate temperature, and its formation is favoured when the metal and chalcogen stoichiometric amount is nominal.

Table 5

Phase	T cold	T hot	Transport agent	Reactants	Annealing
1T-TaS_2 [119]	950 °C	900 °C	Iodine	Elemental Ta and S + 0.5% wt. SnS_2	Rapid quench
2H-TaS_2 [78]	780 °C	820 °C	Iodine	TaS_2 powder + excess S	600 – 500 °C for 2 days
4Hb-TaS_2 [120]	700 °C	820 °C	Iodine	TaS_2 powder	none

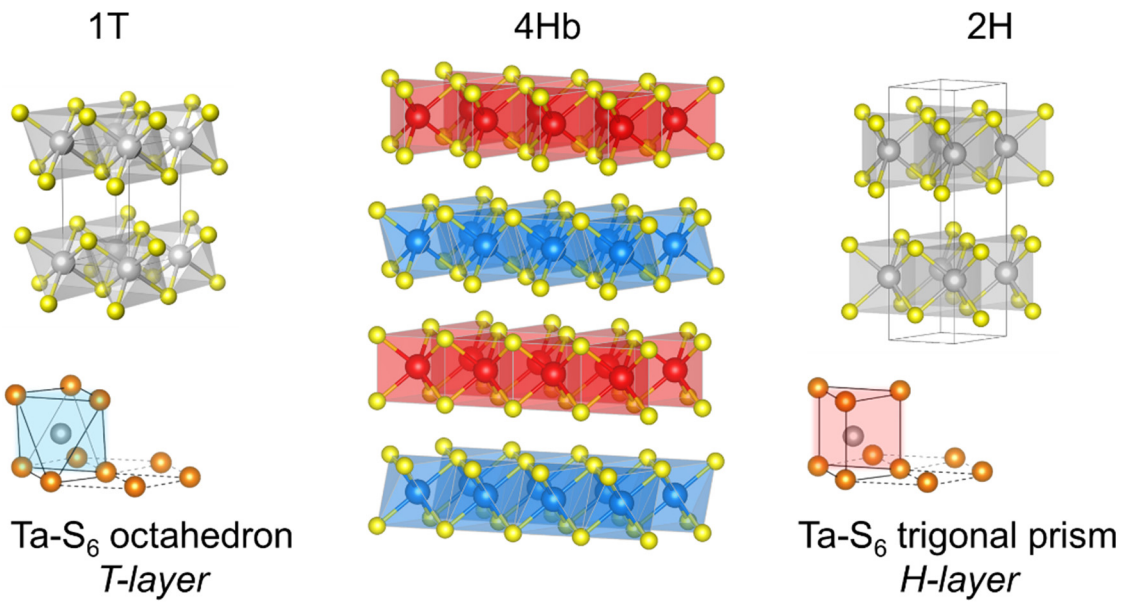

Figure 5:1 Crystal structure of 4Hb-TaS_2. The structure of 4Hb-phase can be understood as the combination of one unit cell of 2H-TaS_2 and two cells of 1T-TaS_2. In 2H and 1T, only one type of metal-chalcogen coordination is present in the crystalline structure: trigonal prismatic and octahedral, respectively. For illustrative purposes, the trigonal coordinated planes are highlighted in red, and the octahedral in blue. Within the same unit cell of 4Hb-TaS_2, pairs of layers of the same coordination are mirrored with respect to each other.

5.2 4Hb-TaS_2 electronic structure

The two types of layers in 4Hb-TaS_2 have the same hexagonal in-plane symmetry, and lattice parameters. The hexagonal Brillouin zones of both layers are therefore identical and aligned, making it possible to create a new hybrid electronic structure, closely related to that of the two individual types of layers.

The electronic structures of 1T-TaS_2, 2H-TaS_2 and 4Hb-TaS_2 have been investigated by *ab*-initio calculations and ARPES measurements. Figure 5:2 displays the constant energy cut at the Fermi energy for the three materials. From the photoemission results it is evident that the Fermi surface of 4Hb-TaS_2 is formed by the combination of the bands present in 1T-TaS_2 and 2H-TaS_2 phases, with only minor changes. Energy dispersion along high symmetry lines, computed by DFT [121], also shows that the Fermi surface originates from two pairs of Ta-bands, a pair per each type of layer, and in close resemblance to those of the 2H and 1T phases. All the bands have very limited dispersion along the *c*-axis direction, making the Fermi surface topology quasi-2D.

4Hb-TaS_2 can be seen as two layered metals that are weakly interacting with each other, given the limited hybridization of bands. Because of the alternating stacking, layers of the same type are weakly coupled to each other, evidenced by the smaller band splitting at the Γ point compared to 2H-TaS_2. This natural heterostructure therefore has the potential of being a bulk material in which properties of the T and H layers approach those of exfoliated monolayers. Conductivity anisotropy measurements were performed to estimate the degree of interlayer coupling.

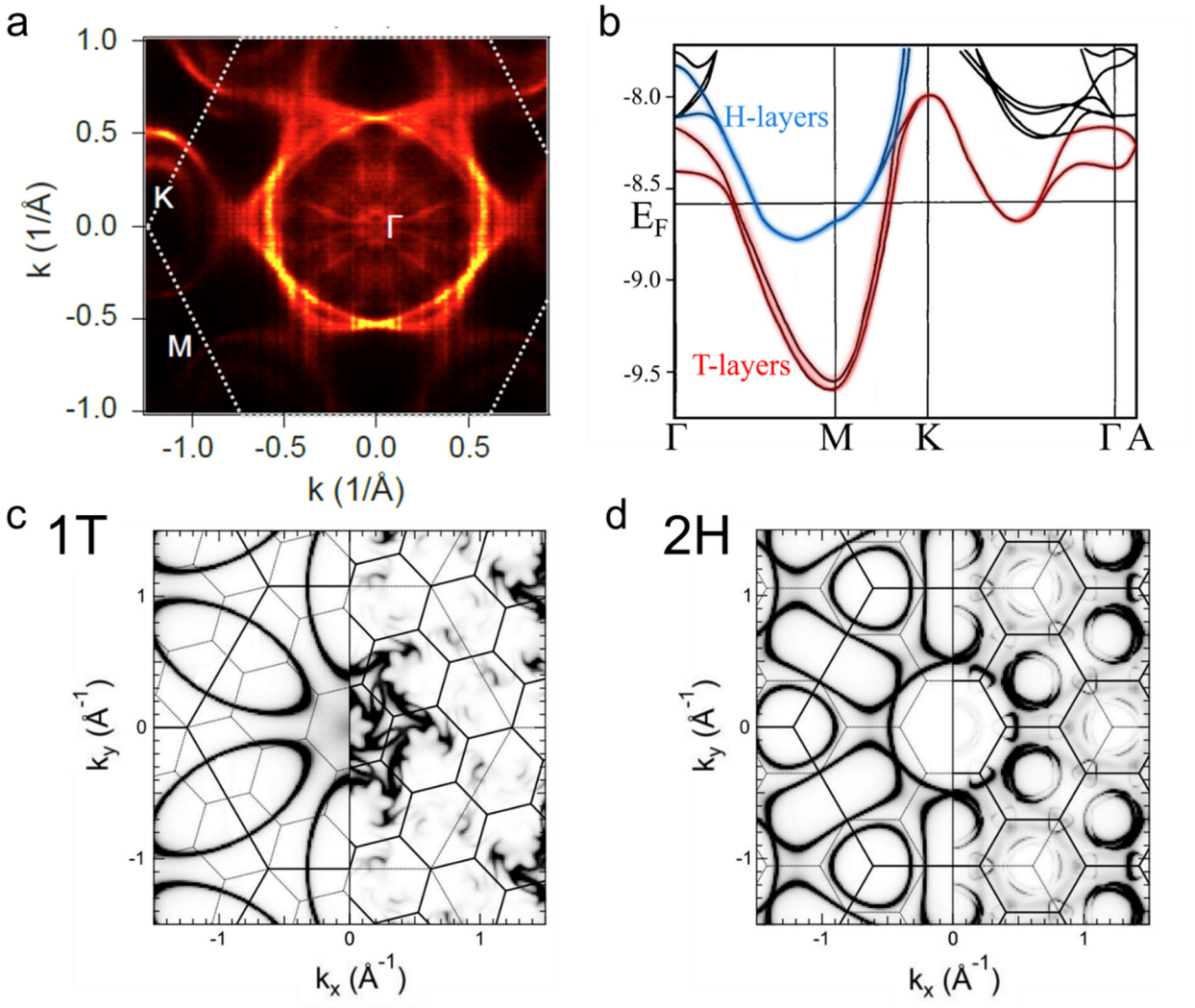

Figure 5:2 Electronic structure of 4Hb-TaS_2. a) Fermi surface cross section observed by ARPES in 4Hb-TaS_2. The band structure is a combination of bands of 2H-TaS_2 and of CDW reconstructed 1T-TaS_2 which were rigidly shifted towards the Fermi level. The image was obtained at T = 15 K using 72 eV photon energy [118]. **b)** The dispersion of energy bands along the high symmetry directions, computed by DFT [121]. Bands originating from the Ta atom in the T and H layers are indicated. **c)** Simulated Fermi surface cross section along the ΓMK plane, for 1T-TaS_2, in the unreconstructed state (left) and in the commensurate $\sqrt{13}$a x $\sqrt{13}$a CDW state (right). The Brillouin zones of the two phases are indicated. Figure from [84]. **d)** Simulated Fermi surface cross section for 2H-$TaSe_2$ (which closely resembles that of 2H-TaS_2), in the unreconstructed state (left) and in the commensurate *3a x 3a* CDW state (right). The Brillouin zones of the two phases are indicated. Figure from [84].

5.3 Charge density waves

In the previous chapters we have seen how the 2H-$TaSe_2$ and 1T-TaS_2 undergo different CDW reconstructions (Figure 3:14 and Figure 4:1). The 2H-TaS_2 and 2H-$TaSe_2$ are isostructural and display the same CDW modulation, in addition their physical properties are very similar [78]. The transitions induce periodic lattice distortions, with the $3a$ x $3a$ modulation in 2H-TaS_2 and $\sqrt{13}a \; x \; \sqrt{13}a$ in 1T-TaS_2, which can be detected from the presence of satellite reflections in X-ray and electron diffractions. The CDW transition is also evident in the transport properties. In 2H-TaS_2 it causes a reduction of resistivity and a more pronounced temperature dependence (analogous to 2H-$TaSe_2$ reported in 3.3) [78]. In 1T-TaS_2 every CDW transition causes a sudden increase in resistivity, with the low-temperature commensurate $\sqrt{13}a \; x \; \sqrt{13}a$ CDW inducing a metal-

semiconductor transition. Strong interlayer coupling and orbital ordering are proposed as the origin for the electronic transition [114] [111].

In 4Hb-TaS_2 it has been demonstrated by multiple techniques (XRD, electron diffraction, STM), that layers with octahedral metal-chalcogen coordination undergo a commensurate $\sqrt{13}a \times \sqrt{13}a$ reconstruction, creating 13-atom David star (DS) clusters, like in 1T-TaS_2 [122]. The transition takes place at 310 K, with a very narrow hysteresis. Contrary to the 1T-polytype, there is no formation of intermediate nearly-commensurate phase (NC), in which the CDW would form nanometre-sized domains. In the H-layers, the occurrence and symmetry of the CDW transition is much less clear, with a few reports suggesting the presence of the same $3a$ x $3a$ modulation below 30 K, but struggling to provide unambiguous evidence [123].

The CDW transitions and the lattice distortions have been investigated in this thesis by combined in-plane electrical resistivity and electron diffraction measurements as a function of temperature, from 400 K to 1.8 K. Electrical resistivity (Figure 5:3) presents a first sharp increase at 310 K, because of formation of DS cluster in the T-layers. In stark contrast to 1T-TaS_2, the commensurate CDW does not induce a metal-semiconductor transition, and resistivity continues to decrease on cooldown with a metallic temperature dependence. Below 35 K, a second transition takes place, reducing the resistivity by a factor of 2. This effect is unique, as commonly CDW transitions in layered materials tend to produce increases in resistivity below the onset temperature (Figure 3:14 and Figure 4:3). As the temperature decreases further, the onset of a superconducting transition occurs at around 2.5 K. The transition is very broad, and resistivity remains finite even at 1.8 K. In comparison, 2H-TaS_2 has a sharper superconducting transition at 0.7 K; the transition temperature increases up to 2.2 K when the sample thickness is reduced to a few layers [124]. In the case of 2H-TaS_2, the enhancement of Tc when approaching the 2D limit is tentatively explained by the increased electron-phonon coupling. For 4Hb-TaS_2 it is not clear why Tc is higher and the transition is very broad, but the alternating stacking might have a prominent role. The discussion of the superconducting phase of 4Hb-TaS_2 will continue at the end of this chapter, in relation to its evolution under applied pressure. Images of transmission electron diffraction in 4Hb-TaS_2, collected using a transmission electron microscope (TEM), are displayed in the top panel of Figure 5:3. The areas shown are centred on the main reflection from the undistorted unit cell (marked by a green circle), all the additional reflection are satellites produced by the CDW transformations. The colours of the outlines of the electron diffraction images indicate the temperature ranges (marked in the plot) in which the respective patterns are observed.

In the investigated temperature range (1.8 – 400 K), three CDW phases can be observed. Ordered from the highest to lowest temperature these are denoted as IC-CDW, C-CDW, LT-CDW. The first transition takes place at 310 K, followed by the second one at 30 K. Above 460 K, there should be no lattice reconstruction, and another transition is expected [122].

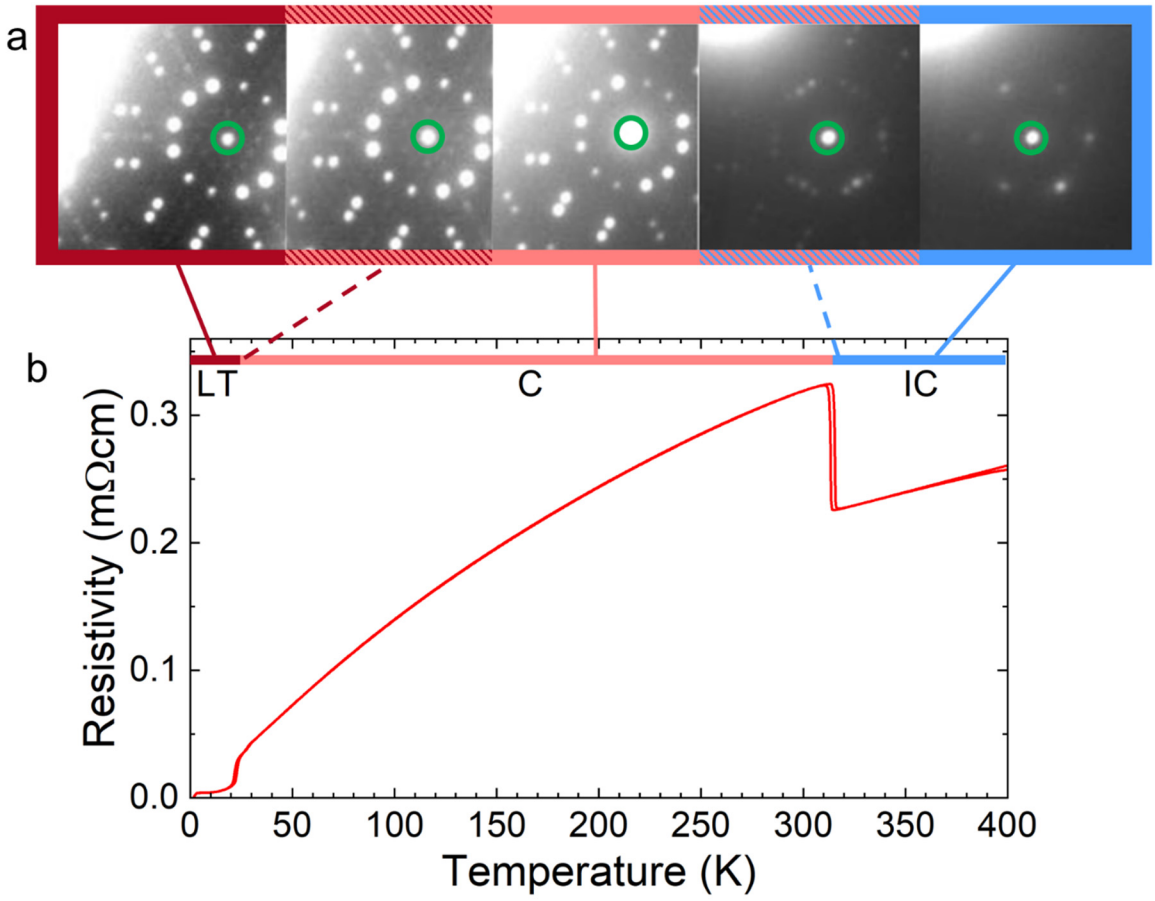

Figure 5:3 Charge density waves in 4Hb-TaS_2. a) Electron diffraction images obtained using a transmission electron microscope in diffraction mode, using a 100 nm thin sample. **b)** In-plane resistivity temperature dependence. The temperature range of each CDW phase is marked by the thick coloured lines. Same colour code is used for the electron diffraction images. A coexistence of two sets of satellite reflections can be observed in the images market with a textured background, because of temperature inhomogeneity of the sample under electron irradiation in the TEM.

Here we will discuss individually the CDW phases observed in the 1.8 K to 400 K temperature range in 4Hb-TaS_2. Together with the symmetry and the real space reconstruction, each CDW will be assigned to the specific layer involved.

- **IC-CDW phase (315 K < T < 460 K)**

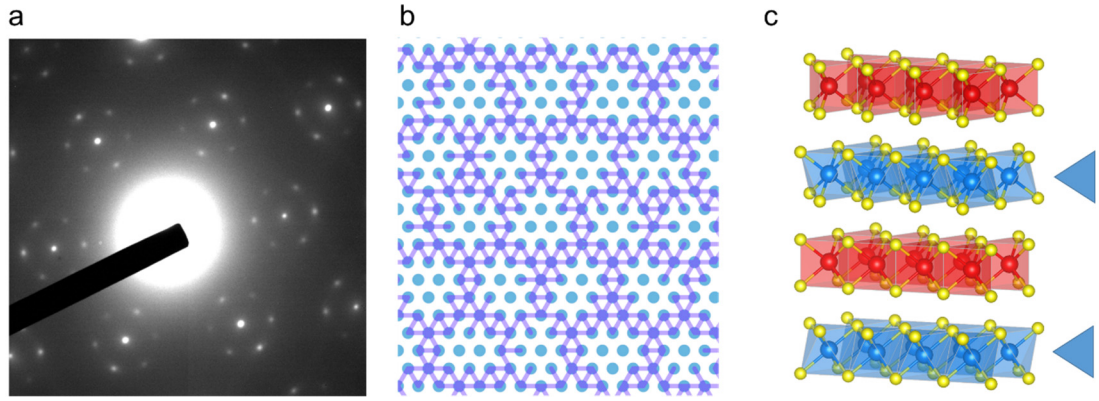

Figure 5:4 I*C*-CDW in 4Hb-TaS_2. a) Electron diffraction image recorded at 330 K. **b)** Lattice reconstruction of the incommensurate CDW, shorter Ta-Ta bonds are marked by purple lines. Each blue dot represents a Ta atom. **c)** 4Hb-TaS_2 unit cell, the T-layers which hosts the CDW reconstruction are highlighted in blue.

Above 315 K electron diffraction image shows the presence of 6 satellite peaks along the principal axis direction, and with modulation wavevector $\boldsymbol{q} = 0.26a^*$ (Figure 5:4 a). This vector is identical to the one of the IC phase in 1T-TaS_2 above 350 K. The lattice distortion involves formation of shorter Ta-Ta bonds in an anti-star configuration, with the shorter bonds forming a circle around a central Ta atom (Figure 5:4 b). The anti-stars' incommensurate modulation has a hexagonal symmetry, with the same orientation as the undistorted unit cell. This transition takes place in the T-layers, inherited from 1T-TaS_2. There is no precise determination of the upper temperature limit for this phase. From high temperature electron diffraction experiments it appears that satellite reflections are no longer visible above 460 K [122]. For comparison, in 1T-TaS_2 the IC-CDW extends up to 550 K [90].

- **C-CDW phase (30 K < T < 315 K)**

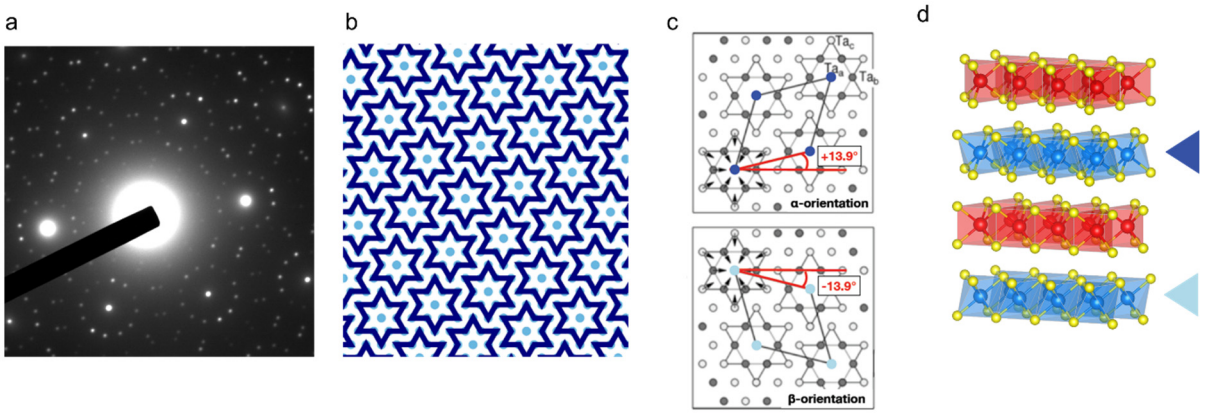

Figure 5:5 C-CDW in 4Hb-TaS_2. a) Electron diffraction image recorded at 290 K. **b)** Lattice reconstruction of the C-CDW highlighting the formation of David star clusters. Light blue dots are single Ta atoms. **c)** Two possible orientations (α and β) with respect to the undistorted unit cell for the commensurate CDW d) 4Hb-TaS_2 unit cell, the T-layers which host the CDW reconstruction are highlighted in blue.

As temperature is reduced under 315 K, resistivity exhibits a sharp 30 % increase and the satellite reflections change as a result of a first order CDW transition, as seen in previous studies [120] [122] . When crossing the transition temperature, the 6 satellite reflections of the IC phase disappear and are replaced by 12 satellites (Figure 5:5 a). The reflections can be indexed as two sets of satellites with hexagonal symmetry, rotated by +13.9° and –13.9° with respect to the undistorted cell, sharing the same modulation vector of $\boldsymbol{q} = 0.277a* (1/\sqrt{13})$. The single set of six-fold symmetric reflections are caused by the formation of David star clusters in the T-layers, as in the commensurate phase of 1T-TaS_2. Low temperature STM measurements confirm this interpretation [120]. The presence of two sets of lattice modulation is the consequence of the rotation of the superstructure by 13.9° with respect to the undistorted unit cell. This rotation creates two possible chiral configurations of charge density waves (called α and β orientations), coexisting in the same material. The diffraction pattern does not change when scanning the beam over the sample, and the intensity redistribution points to an equal concentration of the two orientations. This suggest that in 4Hb-TaS_2 α and β orientations of the C–CDW phase coexist thanks to the physical separation of layers. Powder X-ray diffraction measurements suggest that both orientations are present in the same unit cell, possibly a consequence of the two T-layers being mirrored with respect to each other [122]. Single crystal X-ray diffraction pattern can be refined by a 3 + 2 dimensional commensurate modulation with the double $\sqrt{13}a\ x\ \sqrt{13}a$ modulation of α and β domains [125]. Refinement of individual atomic positions shows the formation of 13-atom David star (DS) clusters in the T-layers. To form each DS, Ta atoms are displaced along the *ab*-plane, while chalcogen atoms are pushed away from the plane of Ta atoms. As a consequence of this three-dimensional distortion, the lattice modulation is also evident in the H-layers, caused by an elastic interaction with its neighbouring layers. The reconstruction in the T-layers is therefore also expected to induce a superstructure modulation in the H-layers sandwiched in between. This effect will be discussed in this Chapter. Structural refinement cannot clarify the sequence which the α and β orientations follow throughout the crystal, as well as their relative vertical alignment. A stochastic distribution is therefore suspected. A weak interaction between the T-layers, due to the interleaved H-layers, is the probable reason why long-range domain order cannot be established along the *c*-axis.

Based on diffraction experiments, single crystals of 1T-TaS_2 that have been slowly cooled down to the C phase exhibit only one orientation of the superlattice. Because of the strong interlayer interaction, a single specific orientation is adopted and enforced throughout the entire thickness of the crystal. The presence of two orientations in 1T-TaS_2, can be observed near domain walls, which occur along dislocations or can be introduced in the C phase after ultrafast light or current pulses [122] [126].

- **LT-CDW phase (T < 30 K)**

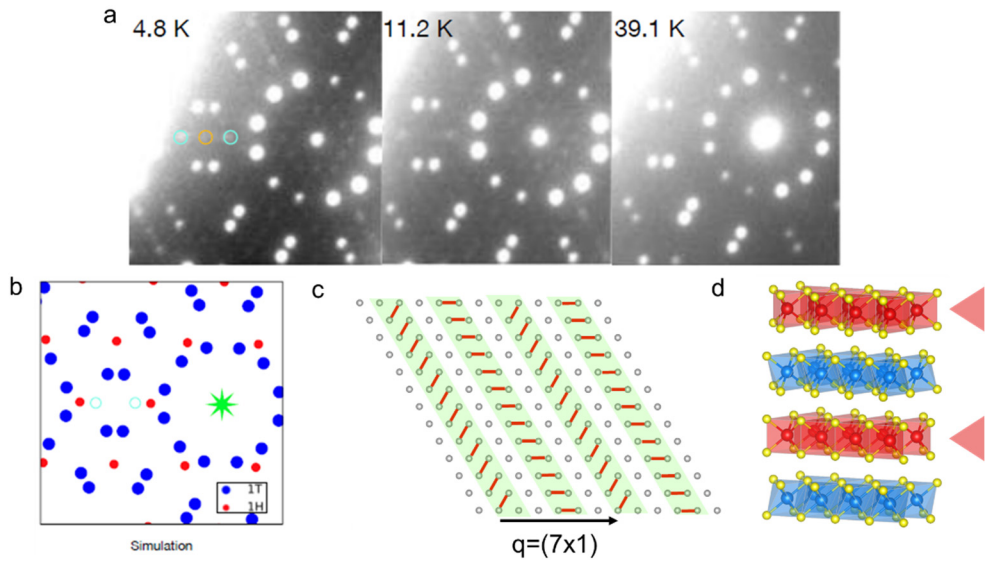

Figure 5:6 LT-CDW in 4Hb-TaS_2. a) Electron diffraction images recorded at low temperatures. Below 30 K, twelve satellites with a wave vector $\boldsymbol{q} \approx 7a^*$, aligned with the main axes of the undistorted lattice, appear around the central reflection. The reflection marked by the orange circle can be indexed as $\boldsymbol{q} = 2a^*$, and appears at the lowest temperature. Additional pairs of reflections (cyan circles), first appear below 30 K as broad diffuse peaks and become defined better as the temperature is lowered. **b)** Simulated reflections for the coexistence of modulations with $\boldsymbol{q} = \sqrt{13}a \times \sqrt{13}a$ (α and β domains) and $\boldsymbol{q} = 3a \times 3a$ in blue and red, respectively. The reflections expected for $\boldsymbol{q} = 3a \times 3a$ are absent in the electron diffraction images in panel **a**. The cyan circles mark the positions of the reflections that appears at low temperature, seen in panel **a**. The green star is the position of the central reflection of the undistorted unit cell. **c)** Proposed striped CDW phase in 4Hb-TaS_2 formed by doubling of the unit cell and modulation $\boldsymbol{q} = 7a \times 1a$. Each grey dot represents a Ta atom and red lines are shortened Ta-Ta bonds. The green highlight marks individual stripes. **d)** 4Hb-TaS_2 with the H-layers, involved in the CDW transition, pointed out.

Below 35 K a new CDW transition is evident from the anomalous reduction of resistivity and by the appearance of new satellites reflection. It was proposed that at such temperature a $3a \times 3a$ CDW modulation happens in the *H-layers*, analogous to the one observed in 2H-TaS_2. This interpretation is not compatible with the electron diffraction data, and was not clearly observed in STM data as well [123]. Simulated diffraction pattern for the $3a \times 3a$ CDW is marked in panel **b** of Figure 5:6 by the red dots. In the experimental data, there are no visible reflections in the positions expected in the case of a $3a \times 3a$ CDW. The twelve new peaks around the central reflection are spaced much more densely and are not rotated with respect to the undistorted lattice. This suggests that they are associated with a modulation with a wave vector different than for C-CDW. The 12-fold symmetry can plausibly originates from a pair of six-fold symmetric lattices, rotated by 30° with respect to each other. The approximate modulation vector is $7a$, different from any other commonly observed CDW modulation in TMDs. The new reflection at the lowest temperature can be related to $2a$ modulation, marked by the orange circles in Figure 5:6 a. In line with it, a pair of reflections, marked by the cyan circles, evolve as temperature is reduced, from broad diffusive to sharper peaks. This change can be related to a progressive ordering of CDW domains inside the H-layer. Although a clear refinement of the LT-CDW phase is currently missing, a plausible interpretation is the formation of CDW domains in the H-layer.

A tentative interpretation can be made considering the possible formation of a striped CDW. Such configuration can be seen in 2H-$TaSe_2$, when upon warming up, the commensurate $3a \times 3a$ superstructure is broken into stripe like domains divided by discommensuration regions. Formation of striped phase is enhanced

under application of external pressure [81]. In the case of 4Hb-TaS_2, the equivalent pressure be mimicked by the distorted T-layers, whose chalcogen atoms protrude out of their planes. Stripes can then be formed by lines made of Ta-Ta dimers—which would explain the 2*a* reflection—creating a modulated structure with $\boldsymbol{q} \approx 7a$ x 1*a*. Other layered TMDs, for example $IrTe_2$, host such a kind of striped lattice reconstruction. The striped domains are a few nanometres in size, with the stripes extending along one of 3 equivalent directions, so the overall diffraction pattern from the crystal preserves the six-fold symmetry. Because the diffraction pattern originates from a smaller volume fraction of the crystal, the satellite reflections are much less intense, in agreement with the collected diffraction patterns.

The distortion induced by the T-layers, generated by the out-of-plane chalcogen distortion, and highly protruding Ta-$\boldsymbol{d_{z^2-r^2}}$ orbital at the centre of each DS, could explain the creation of this textured CDW in the H-layer. The T-layer distortion can also justify the occurrence of a 12-fold symmetry in the satellite reflection, which might originate from different interaction of the H-layer with α and β domains. Surface techniques, such as STM and bulk techniques as X-rays or electron diffraction (typical simple thickness is 100 nm) might give entirely different results, as the H-layer on the surface is free of constrains imposed by the T-layers.

5.3.1 Transport anomalies and superconductivity

Lattice distortion coupled to CDW is highly sensitive to externally applied pressure, as evident in the case of 1T-TaS_2 (Figure 4:1). Electrical resistivity of 4Hb-TaS_2 was measured as function of pressure, with a particular attention to the changes of the low temperature charge transport anomaly and the superconducting state (Figure 5:7). Temperatures of CDW transitions are reduced with increasing pressure, which can be well distinguished for the IC to C phase transition. This transition is linearly reduced from 310 K at 1 atm, to 220 K at 1.5 GPa. The low temperature transition has a qualitatively different evolution under pressure. At 1 atmosphere, the resistivity is reduced by a factor of 2 over a few Kelvin range. As pressure is increased, the magnitude of resistivity change is progressively reduced, together with the width of the hysteresis loop as a function of temperature. This can be interpreted as a suppression of the low temperature CDW transformation. Definitive proof can be provided by high pressure and low temperature X-ray diffraction experiments, which have so far not been performed. The suppression of the low temperature CDW transition has a marked effect on the residual resistivity, which increases from 4 μΩcm at 1 atm to 32 μΩcm at 1.5 GPa. The transition temperature suppression is in agreement with the previous publication, but the higher accuracy results collected here show the monotonous scaling of resistivity value with pressure [127].

The effect of pressure does not only strongly affect the CDW transitions, but also the superconducting phase. At ambient pressure, the superconducting onset temperature is around 3 K, but the very broad transition does not lead to zero resistivity down to the lowest probed temperature (1.8 K). Signature of bulk superconductivity can be observed in specific heat only below 1.1 K, and the limited amplitude of the heat capacity anomaly could signify that only a small fraction of the sample becomes superconducting [128].

A very small increase in pressure, only 0.2 GPa, has a dramatic effect on the superconducting state. The onset of superconducting transition moves to 3.9 K, and the transition become much sharper reaching zero resistivity state. Increasing pressure further enhances the superconducting transition temperature. This large variation could be related to the competing effect of low temperature CDW and superconductivity. At ambient conditions, a small fraction of layers host superconductivity. These are probably layers in proximity to a specific stacking configuration of CDW in the T-layers, which suppresses the LT-CDW formation. As pressure is applied and the low temperature transition is suppressed in every layer, bulk superconductivity emerges. In the scenario involving formation of stripes in the LT-CDW phase, the evolution of lattice distortion and superconductivity under pressure is reminiscent of the behaviour observed in another layered TMD, $IrTe_2$ [129]. In this layered material striped charge order and superconductivity compete, producing a very similar behaviour of

resistivity as a function of temperature and pressure. Interplay of charge order, striped phases and orbital textures might be at the origin of the peculiar properties observed in 4Hb-TaS_2.

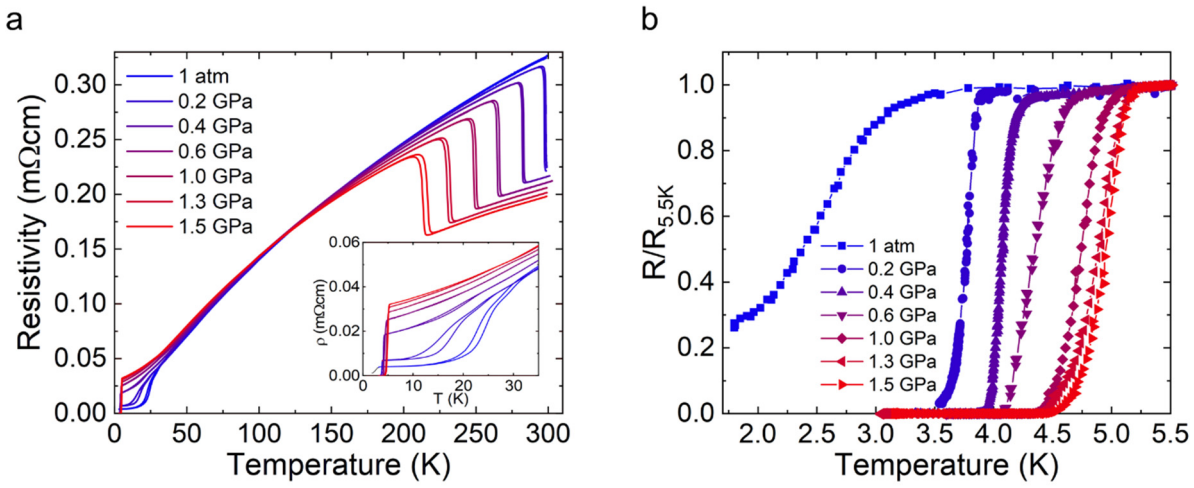

Figure 5:7 High-pressure study of 4Hb-TaS_2. a) Temperature dependence of the in-plane resistivity for different applied pressures. The C-CDW transition temperature is reduced under pressure, and the resistivity change at the LT-CDW is suppressed (inset provides an enlarged view). **b)** Normalized resistivity at 5.5 K to compare the evolution of superconducting transition upon increasing pressure.

5.3.2 Orbital texture

A peculiarity of 4Hb-TaS_2 is the coexistence of different CDW orders in neighbouring layers. As we have seen for 1T-TaS_2 (section 4.4), at the centre of each David star cluster there is a region of high electron density, which protrudes from the T-layer along the out-of-plane direction. It is therefore expected that such a large and periodically modulated density might have a strong effect on the H-layer sandwiched in between, as it is also suggested by the single crystal X-ray diffraction [125]. Scanning tunnelling microscopy (STM) measurements have successfully in identified the two possible surface terminations on 4Hb-TaS_2, and show the evidence of the formation of DS in the T-layers (1T in Figure 5:8 a) [123]. When the STM tip is located over the T-layer, the $\sqrt{13}a\ x\ \sqrt{13}a$ periodicity is clearly visible for a wide range of voltage bias. For low voltage, when scanning over the sample at a constant current, a vertical modulation of 3.5 Å is seen over the centre of each DS as a consequence of the expanded $\boldsymbol{d_{z^2-r^2}}$ orbitals. Tunnelling spectra show a clear metallic profile for the H-layer termination, in contrast to a wide band gap for the T-layer termination. Such insulating state on the surface raises a question of whether the T-layers are also insulating in the bulk. This is currently unknown.

Interesting results are obtained when the STM tip is located over an H-layer. For low applied bias, the STM map shows the atomically resolved hexagonal lattice, which hints at a possible weak reconstruction. For higher positive bias (300 meV) the $\sqrt{13}a\ x\ \sqrt{13}a$ periodicity of the electronics density, originating from the DS located in the layer beneath, is clearly visible. In the bulk, each H-layer is sandwiched between two layers hosting DS reconstruction, which creates a more complex modulation of electron density.

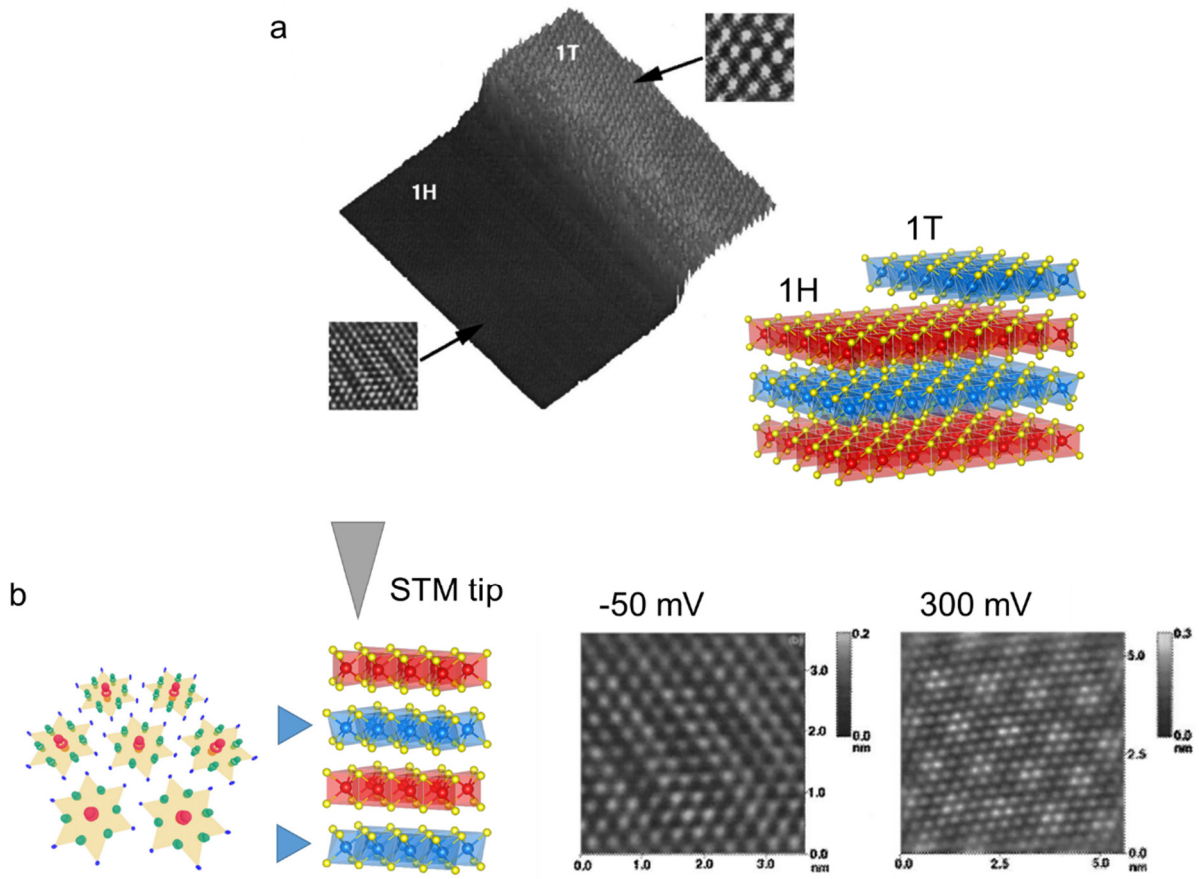

Figure 5:8 Orbital texture in 4Hb-TaS_2 seen by STM. **a)** STM image over a step, where both type of layers are visible, image area is 450 x 450 Å. Higher resolution images acquired over the two different terminations are shown in the top right and bottom left. The $\sqrt{13}a$ x $\sqrt{13}a$ reconstruction is evident for the T-layer termination. The lattice on the right schematically represents the structure of the probed surface. **b)** STM images over H-layer. For low voltage, weak modulation of the lattice was observed with atomic resolution. For positive voltage (300 mV) electrons tunnelling trough the T-layer beneath create a well defined $\sqrt{13}a$ x $\sqrt{13}a$ modulation.

The peculiar orbital character of the $\sqrt{13}a\ x\ \sqrt{13}a$ CDW can induce a potential of additional periodicity in the adjacent H-layers. The modulation vector depends on how the two CDWs in the T-layers are oriented relative to each other. Electron diffraction shows that layers with α and β orientations coexist within the same crystal. This coexistence translates into a more complex periodicity coming from the two different $\sqrt{13}a\ x\ \sqrt{13}a$ modulations.

Figure 5:9 shows a possible configuration for the superstructure generated in the H-layers by the orbital textures of the neighbouring layers. Currently, there is no experimental evidence regarding the relative stacking of DS in two consecutive T-layers. For illustrative purposes, we consider the case of alternating α and β configurations, with vertically aligned DS centres. The individual CDW superstructure is represented by dark and light blue dots. Each dot corresponds to the centre of a DS. The result is a hexagonal moiré pattern potential, with a periodicity of 13a, and supercell vector parallel to the axes of the undistorted unit cell.

Such moiré potential could have a strong enough influence on the H-layers, and be responsible for the observed electronic properties, such as the peculiar CDW reconstruction, superconductivity, and the overall temperature dependence of electrical conductivity.

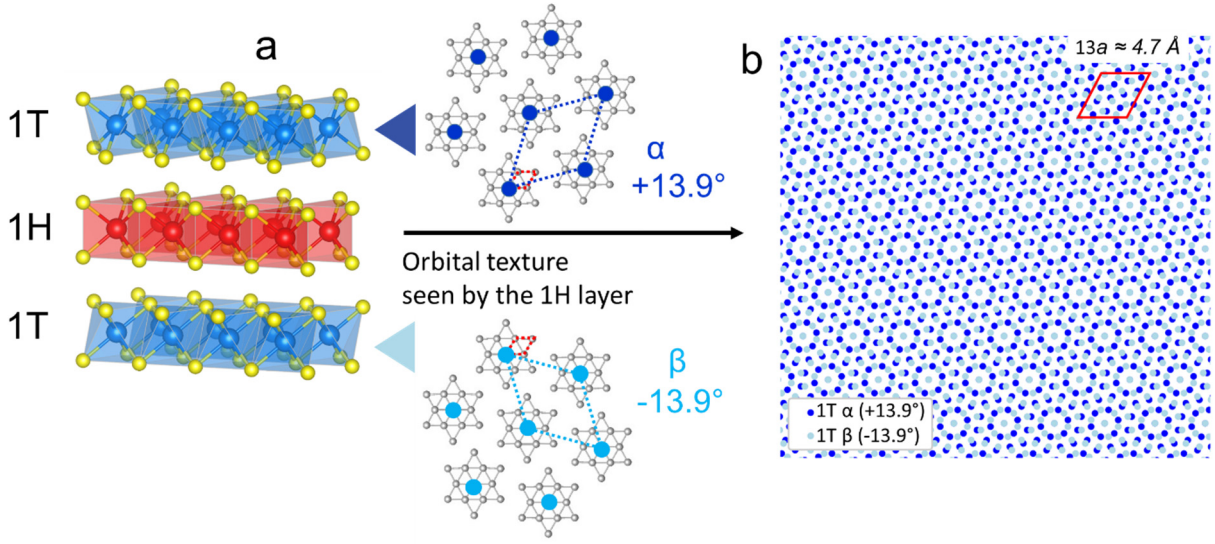

Figure 5:9 Possible configuration of the orbital textures in bulk 4Hb-TaS_2. a) $\sqrt{13}a$ x $\sqrt{13}a$ reconstruction in the T-layers with two different orientations (α and β). The larger electron density at the centre of each David star cluster is marked by a dot, dark and light blue for α and β, respectively. **b)** Moiré pattern generated by the two modulations, where contributions from CDWs of distinct orientations are marked by different colours. The moiré pattern forms a hexagonal lattice, with a modulation vector of 13a aligned to the undistorted unit cell.

5.4 Transport anisotropy

Conductivity anisotropy, and in particular the out-of-plane charge transport, have been investigated for 4Hb-TaS_2 by utilising focused ion beam microfabrication. The temperature dependence of electrical resistivity for directions parallel and perpendicular to the layers can be found in Figure 5:10 a. For temperature below 310 K, when the T-layers host DS clusters, the two temperature dependences are clearly different. While $\rho_{\parallel}$ has a positive slope, $\rho_{\perp}$ constantly increases with decreasing temperature, contrary to the behaviour expected for a metal. Anisotropy ratio monotonically increases (Figure 5:10 b), starting around 10 at 400 K. Upon entering the C-CDW phase there is a small jump in anisotropy, followed by a smooth increase at lower temperatures, going from 16 up to 400. Below 30 K, when the CDW transition takes place in the H-layer, the anisotropy suddenly increases, reaching 4'000. This large change is due to the strong reduction of $\rho_{\parallel}$ and an increase in $\rho_{\perp}$ upon entering the LT-CDW phase.

Among the layered materials discussed so far, 4Hb-TaS_2 is the first case where $\rho_{\perp}$ has a clear non-metallic temperature dependence, and an anisotropy higher than 1'000. These results are an indication of an incoherent interlayer charge transport. This peculiar temperature dependence has already been observed, and it was interpreted as electron tunnelling between the metallic H-layers trough the insulating T-layers [130]. The tunnelling interpretation is based on two assumptions: First assumption is that the T-layers are insulating, as a consequence of the C-CDW formation. Second assumption is that in presence of alternating metal and insulator layers, the charge transport occurs by tunnelling and is incoherent. However, it is an open question whether the monolayers of 1T-TaS_2 are insulating. In the bulk 1T-TaS_2 , the gap opens as a result of the interlayer interactions, but those interactions are much weaker in the 4Hb polytype. Concerning the second assumption, a few relevant examples can show precisely the opposite. In delafossites ($PdCoO_2$ or $PdCrO_2$, shown in Figure 2:1), a case of natural heterostructures of this kind, conducting layers of Pd atoms are sandwiched between insulating CoO_2 or CrO_2 layers. Both materials manifest a clear out-of-plane metallicity despite the alternating stacking of metallic and insulating layers [131] [132] [133]. According to the model proposed by Moon et. al [43], the incoherent out-of-plane transport is a consequence of a strong in-plane scattering mechanism. This is

in agreement with the high $\rho_{\parallel}$ at room temperature, but it is not so evident when considering of the low resistivity in the LT-CDW phase.

A clear understanding of the unusually large anisotropy is currently missing. At the same time, the peculiar charge density wave reconstruction which takes place in this material is expected to have a strong effect on its transport properties, as in the case of 1T-TaS_2. The most peculiar transport properties are indeed observed below 30 K, when multiple CDW orders coexist. We have seen how the in-plane resistivity is strongly reduced, which is a possible sign of a long-range ordering. On the contrary, the out-of-plane resistivity shows a local maximum at the low-temperature transition, at 19.4 K upon cooling and 22.2 K on warming. The presence of a narrow peak in the temperature dependence of resistivity is fairly unusual (Figure 5:10 c), and it might be related to an enhanced scattering due to lattice reorganization following the CDW transition.

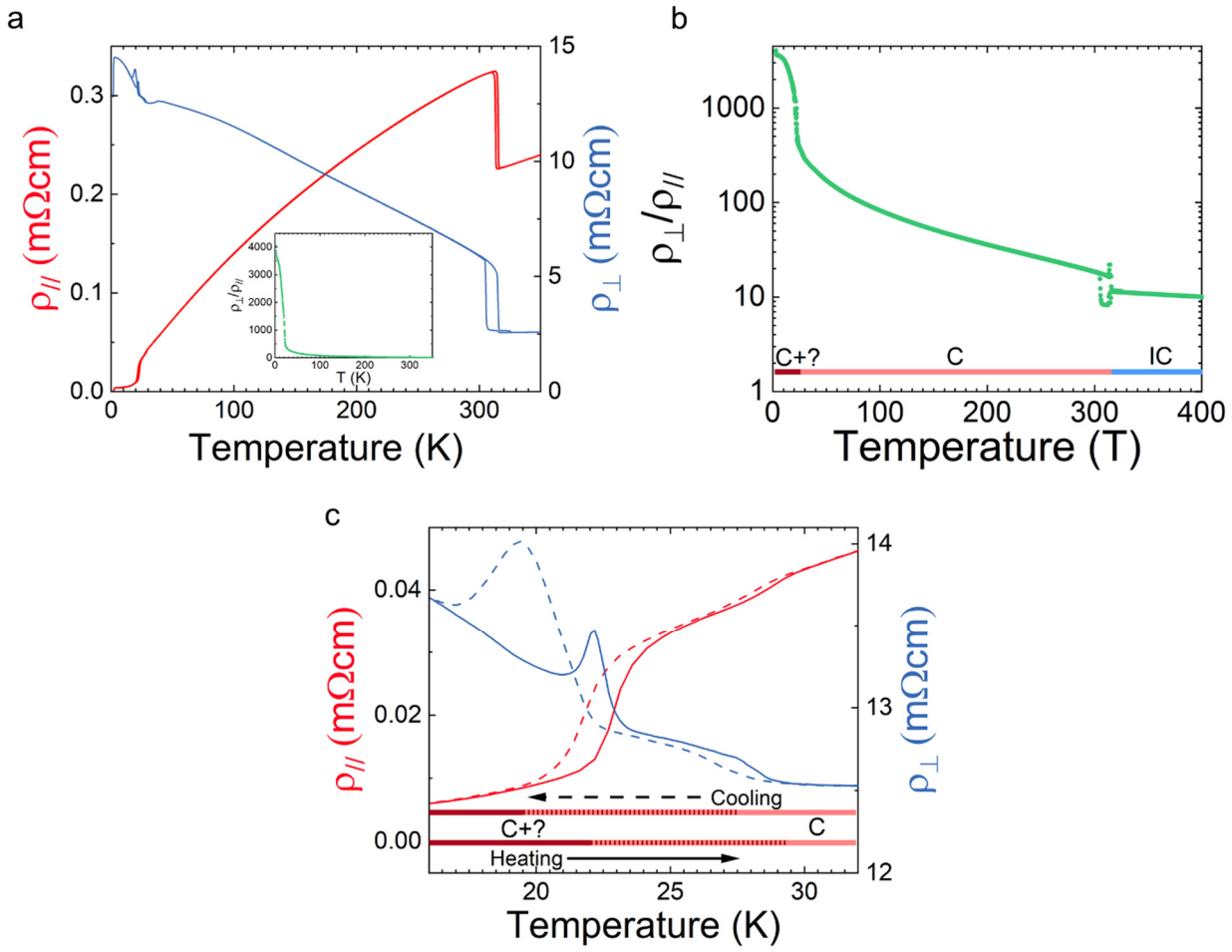

Figure 5:10 Charge transport anisotropy of 4Hb-TaS_2. a) Temperature dependence of the electrical resistivity of 4Hb-TaS_2 for current flowing along the in-plane ($\rho_{\parallel}$) and out-of-plane ($\rho_{\perp}$) directions. The $\rho_{\perp}$ was measured on a FIB microstructured sample. The resistivity anisotropy ratio is shown in the inset. **b)** Temperature dependence of resistivity anisotropy, plotted on a log-scale. The coloured lines at the bottom indicate the temperature range of each CDW phase. **c)** Temperature dependence of the in-plane and out-of-plane resistivities around the low-temperature transition, marking the onset of the LT-CDW order in the H-layers. Solid and dashed lines represent heating and cooling down, respectively. While $\rho_{\parallel}$ is reduced by a factor of 2 across the transition, $\rho_{\perp}$ continues to increase and has a local maximum at the lowest end of the CDW transition, where the hysteresis loop closes.

5.5 Summary of 4Hb-TaS_2

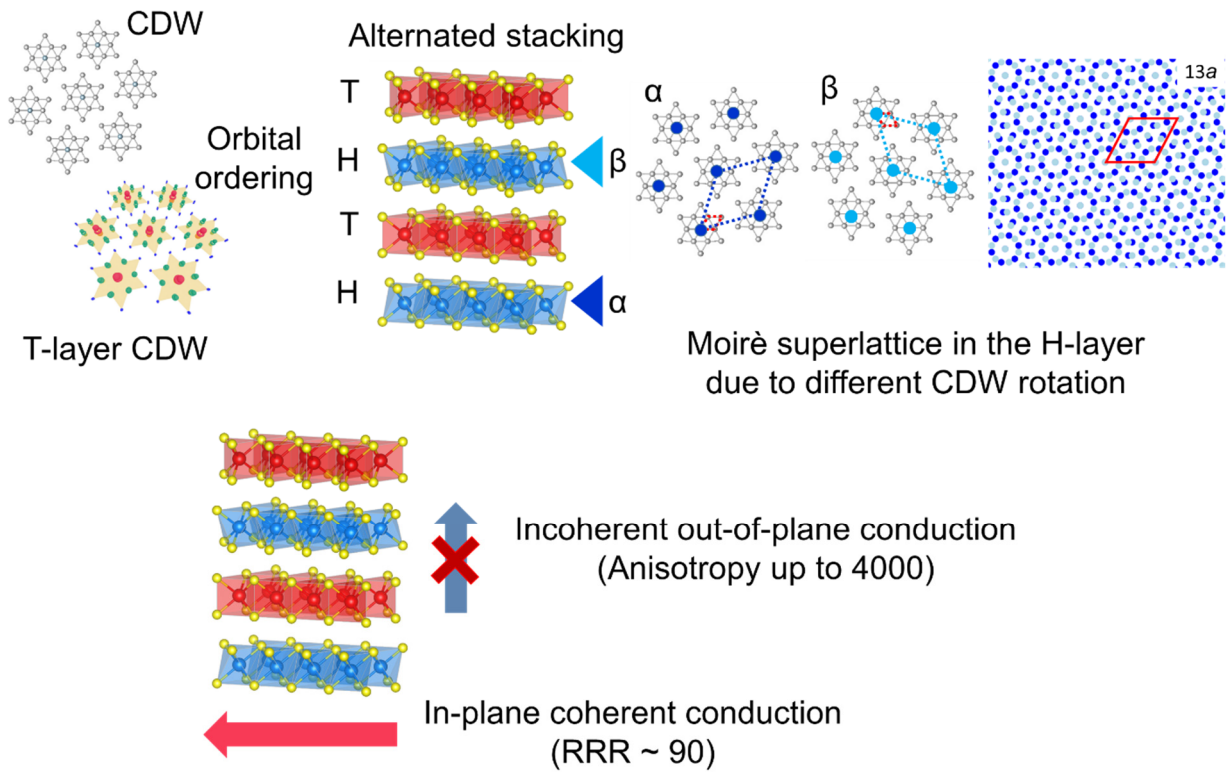

Figure 5:11 4Hb-TaS_2 summary

4Hb-TaS_2
This is a natural heterostructure, with ordered alternated stacking of TaS_2 layers of two types of metal-chalcogen coordination. This is possible thanks to the similar energies of formation of TaS_2 with trigonal prismatic (TP) or octahedral (OC) coordination. The two types of layers present different CDW orders that sets in at different temperatures. The complex interaction of different lattice modulations and orbital ordering produces a moiré potential, which may affect the electronic properties.

Interlayer transport
Out-of-plane charge transport appears to be incoherent, as the *c*-axis resistivity has a negative slope as a function of temperature, and anisotropy at low temperatures becomes higher than 1000. This result is unique among all the investigated layered transition metal dichalcogenides.

Conclusion
Currently there is not a clear interpretation for the observed behaviour, but the alternating stacking and coexistence of different CDWs are the primary possible explanations of the observed properties.

Chapter 6 Intercalation and magnetic ordering

In this chapter, we will discuss how the insertion of guest species between the layers affects the properties of the host materials, in particular the transport anisotropy and interlayer coupling. The ability to host ions and molecules between weakly coupled layers is one of the key properties that makes layered materials interesting for both science and applications. For example, the controllable and reversible intercalation of ions is widely exploited in layered materials used as electrodes in batteries – graphite for the anode and a layered transition metal oxide for the cathode, with Li ions intercalated and moving between the two electrodes during charge-discharge cycles.

From the perspective of materials science, intercalation offers a great degree of freedom to create new materials thanks to the multitude of possible combinations of host compounds and intercalants [134] [135] [136]. This can occasionally result in the emergence of new functionalities, such as superconductivity [85] [137] [138] or magnetically ordered phases [139]. Layered materials can be intercalated via different approaches. We will refer to a single-step process, when the intercalation takes place during the growth of the host material. Alternatively, a two-step process can be used, when the host material is synthesized first, and intercalated afterwards. The results of the intercalation process can be classified according to: the fraction of interlayer sites that host guest species (intercalation stage), the stoichiometry of the intercalated species in relation to the host compound, and the degree and type of resulting long-range intercalant ordering between the layers.

Intercalation during the growth of layered materials (single-step) takes place at high temperatures (600 – 900 °C). This limits the possible intercalants to elemental species, such as transition metals ions. This synthesis route can provide a stage 1 intercalation, with a high concentration of intercalants which form a long-range-ordered sub lattice. High quality single crystals can be grown by standard chemical vapour transport or flux, using the process similar to the one used for producing the non-intercalated material. Samples grown by these techniques ($Co_{0.25}$-NbS_2, $Co_{0.33}$-NbS_2 and $Mn_{0.33}$-NbS_2) will be the subject of the following sections. In these sections, we will focus on magnetic ordering produced by localized spins on the intercalated ions, and the effect of this magnetic order on the charge transport anisotropy.

With a two-step intercalation process, neutral or charged molecules can be inserted between the layers of the host material after it has been synthesized. This reaction can be performed at room temperature, giving the opportunity to intercalate organic or metalorganic molecules, which would not be stable at high temperatures. To intercalate ions, the process can be driven electrochemically, with the layered material connected to an electrode of a voltage source, or in the same configuration as the one used for ionic liquid gating. To intercalate neutral molecules, the only driving force can be diffusion driven by the concentration gradient, making the complete intercalation of a large crystals a long process.

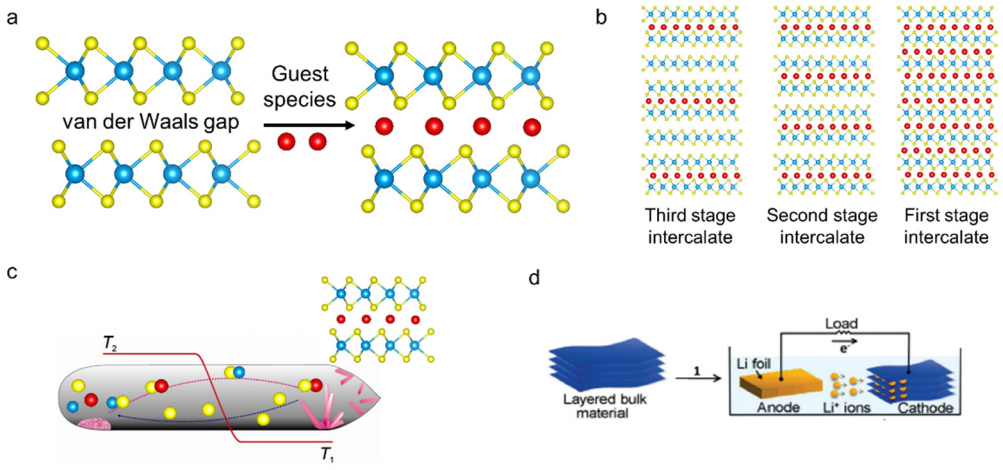

Figure 6:1 Intercalation of layered materials **a)** Schematic diagram of intercalation in layered TMDs, where guest species can be inserted into the van der Waals gap by diverse methods. **b)** Representation of different intercalation stages. In the first stage, intercalation guest species are present between every layer. **c)** Single-step intercalation process. Intercalation takes place during the growth of the host layered material. The case represented is the chemical vapour transport growth, where the reactants sublimate in the hotter end of the ampoule and the growth of single crystals takes place at the colder end. **d)** Two-steps intercalation process. After the growth of a layered material, different ions or molecules can be intercalated using different methods, such as diffusion (assisted by high pressure) or electrochemical intercalation. Figure from [140].

6.1 Organic molecules intercalation

One of the projects described in this thesis concerns the intercalation of organic and metalorganic molecules. The goal was two-fold. First, we wanted to master the intercalation process in order to produce high quality single crystals. Second, we wanted to study the influence of intercalated molecules on the electronic properties of layered materials, and in particular on the interlayer coupling. We made several attempts to intercalate 2H-$NbSe_2$ with organic (ethylenediamine, $[C_2H_8N_2]$) and metalorganic molecules (cobaltocene or $CoCp_2$, $[Co(\eta_5C_5H_5)_2]$). The procedure used for the intercalation of $NbSe_2$ crystals was the same as the one reported in published articles [141] [142]. The crystal was immersed into the solution containing the intercalate molecules, and kept at temperatures around 70°C, from a few days up to 3 weeks, in order to accelerate the process. The insertion of the guest molecules was later verified by X-ray diffraction, measuring the change in the angular position of the 00*l* reflections. The diffraction patterns in Figure 6:2 b act as the proof of successful intercalation of both organic and metalorganic molecules.

The scope of this project was not initially limited to the successful intercalation procedure. Yet, the investigation of physical properties of the intercalated crystals proved to be complex. The results were dominated by extrinsic effects. One problem we encountered was an uneven distribution of intercalated molecules in the host material. The intercalants enter the crystal from the side surfaces, and the molecules need to diffuse between the layers over the length of a few hundred microns. It was possible to track the diffusion of cobaltocene between $NbSe_2$ layers using X-ray fluorescence, see Figure 6:2 c. From the elemental maps it is evident how $CoCp_2$ molecules diffused only across a limited distance from the edges of the crystal. Based on the data collected from samples obtained at different times throughout the process, we estimated the propagation speed of 50 μm/week for $CoCp_2$ dissolved in acetonitrile or toluene at the temperature of 70 °C. The second, and more severe problem which prevented us from investigating the physical properties, are the chemical changes that happen to the layered material during the intercalation reactions. From the elemental mapping shown in Figure 6:2 c, it is evident that in a portion of the crystal which was intercalated by $CoCp_2$, the concentration of chalcogen was reduced. In addition, traces of chalcogen were found in the intercalant solution after the reaction, indicating that Se is gradually lost from the crystal. The loss of chalcogen during

the intercalation process produces a high density of Se-vacancies, and in turn induces a high concentration of static defects. These defects increase the conduction electron scattering and change the overall carrier density.

It is hard to draw conclusions regarding the observed changes in the physical properties after the intercalation, when we know that intercalant distribution is inhomogeneous and the chalcogen is depleted. One example is 2H-$NbSe_2$ that was successfully intercalated with cobaltocene, where we verified by X-ray fluorescence that the intercalation was complete. The intercalated material shows no sign of superconductivity down to 1.8 K, as opposed to the starting material with the T_C of 7.2 K. It is, however, unclear whether the suppression of superconductivity is due to the larger interlayer distance (weaker interlayer coupling), the change in chemical potential due to a transfer of electrons to the intercalant molecules, or the change in the chalcogen stoichiometry. Additional doubts were cast by the recent published study of the same material (2H-$NbSe_2$ intercalated with cobaltocene), where intercalation appears to hardly affect superconductivity, which has $T_C \approx 7$ K and only displays an enhanced critical field anisotropy [143].

The experiments performed on TMDs intercalated via the two-step process lead to the following conclusions:

- The intercalation of molecules, even complex metalorganic ones, is feasible and easy to achieve.
- The complex and uncontrolled chemical modifications of the host lattice make it difficult and unstraightforward to determine the intercalated material's physical properties.

Following the described experience, this chapter therefore focuses on single-step-intercalated materials, which offer high quality crystals with reproducible properties.

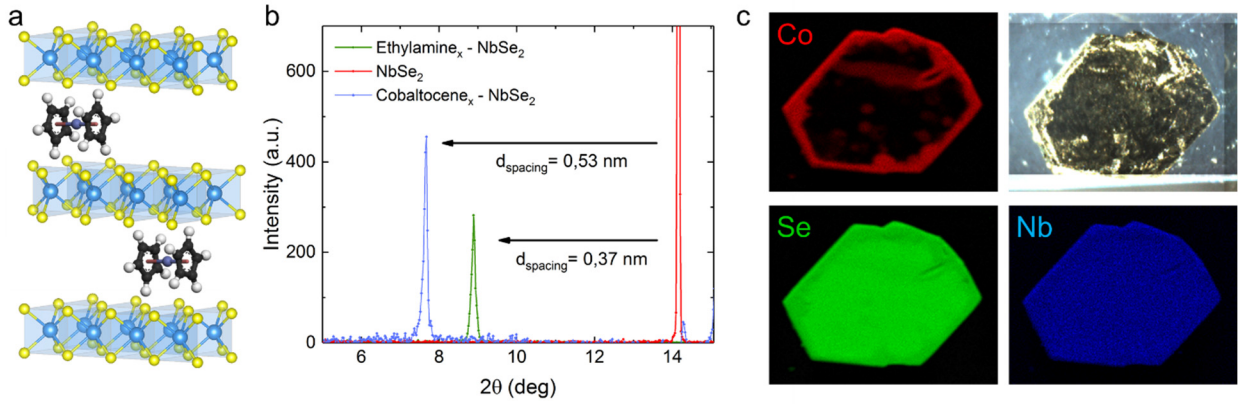

Figure 6:2 Intercalation of small molecules a) Cobaltocene molecules intercalated between $NbSe_2$ layers. The orientation of cobaltocene molecules, with the benzene rings perpendicular to the layers, is the most likely configuration given the measured lattice expansion [142]. **b)** X-ray diffraction patterns of 2H-$NbSe_2$, and $NbSe_2$ intercalated with cobaltocene and ethylamine. The diffraction peaks are the 002 reflections, which were used to compute the lattice expansion as a result of intercalation. For the sample intercalated with cobaltocene, a small peak around 14° is due to a portion of the crystal that has not been intercalated. The arrows point at the reduction in angular position of the diffraction peaks, which correspond to an interlayer spacing increase of 0.37 nm and 0.53 nm for ethylamine and cobaltocene intercalation, respectively. **c)** Microscopy images and chemical composition maps from X-ray fluorescence spectroscopy of a crystal intercalated with cobaltocene and kept at 65°C for two weeks. The signal from Co atoms is limited to the edge of the crystal, due to the very slow diffusion of the intercalant.

6.2 Transition metal intercalation and magnetic order

Layered materials intercalated with transition metals can host long-range magnetic order, originating from the localized spins of the intercalates. The great advantage of intercalation is the chemical degrees of freedom, allowing us to choose between different elements while keeping the crystalline structure identical. According to the intercalated element, the ordered superlattice of transition metal ions can produce a variety of magnetic orders, ferromagnetic (FM) or antiferromagnetic (AFM) [139]. For NbS_2 and TaS_2, the different magnetic orders and their respective transition temperatures are summarized in Figure 6:3. All the mentioned materials have the same crystalline structure as shown in Figure 6:3. Spin order in FM compounds forms a chiral helimagnetic structure, with the magnetic moment rotating in the *ab*-plane as we move along the helical *c*-axis. External magnetic field applied along the *ab*-plane flips the spins in the same direction, which then changes the spin helix pitch, and produces chiral spin soliton states [144] [145]. Antiferromagnetic order in $Co_{0.33}NbS_2$ forms a complex magnetic texture, as a result of the magnetic frustration caused by the triangular lattice of localized spins. Data coming from neutron diffraction experiments were fit with a collinear AFM structure, whose magnetic unit cell is twice the size of the crystalline unit cell [146]. The magnetic structure can be described as "hexagonal ordering of the first kind", according to Corliss et al [147]. From a neutron scattering experiment on a single crystal, six equally probable symmetry-related in-plane $\boldsymbol{q}$ vectors have been identified, suggesting a multi-domain magnetic structure. The currently available data still leave a degree of uncertainty regarding the presence of a ferromagnetic contribution to the magnetic ordering (canting along the *c*-axis), in particular in light of the large anomalous Hall effect observed in $Co_{0.33}NbS_2$ [148].

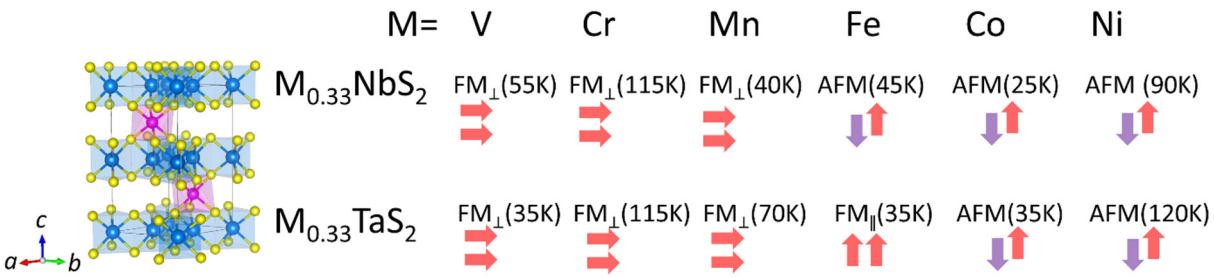

Figure 6:3 Magnetic orders for TMDs intercalated with transition metals. Crystal structure of intercalated compounds $M_{0.33}NbS_2$ and $M_{0.33}TaS_2$. M is the intercalated transition metal, shown in pink in the crystalline structure. For each compound, the figure shows the type of order, ferromagnetic (FM) or antiferromagnetic (AFM) and the transition temperature. For FM order, the notation $\parallel$ or $\perp$ refers to the direction of the easy axis of magnetization with respect to the crystalline *c*-axis. Data from [139].

Layered crystals intercalated with magnetic ions create a rich playground to tailor the physical properties of materials. Of particular interest is the interaction between itinerant electrons and magnetism. Charge transport properties are strongly affected by the presence of the magnetic ions due to the following contributions:

- Intercalated transition metal atoms transfer electrons to the conducting layers. In the first approximation, using a rigid band description, this can be seen as shifting the Fermi energy. From the Hall coefficient measurement on all the compounds reported in Figure 6:3, charge carrier density is reduced by approximately one order of magnitude with respect to 2H-NbS_2, as conduction band becomes nearly filled [139] [78].

- Conduction electrons are scattered by the localized magnetic moments of the intercalants. Such additional scattering mechanism is suppressed when a long-range order is establishment, be it ferromagnetic or antiferromagnetic.

In this chapter only compounds of NbS_2 intercalated with Co or Mn will be discussed.

6.3 M_xNbS_2 crystal structure and physical properties

Before diving into the physical properties of layered materials intercalated by ions of transition metals, we will give an overview of the crystalline structure of these materials. The intercalation process is simultaneous with the layered material growth at high temperature. Because of the high temperatures, which enhance the mobility of ions, and the controllable environment inside a sealed ampoule, this method results in ordered crystalline structures, with predictable stoichiometry and sample stability.

In the case of Co intercalation (Co_xNbS_2), two different stoichiometries were studied. The difference in Co ion content comes together with a change in crystalline order. For $x = 0.33$, Co atoms form an ordered lattice while for x = 0.25, their distribution is disordered. To obtain high quality structural information about Co_xNbS_2, X-ray diffraction experiments were carried out at the Swiss-Norwegian Beamlines at the ESRF synchrotron. Diffraction data were collected at room temperature using the PILATUS@SNBL diffractometer, using $\lambda = 0.6804$ Å wavelength. Experimental diffraction patterns and the refined structures are shown in Figure 6:4.

From the refined structure it is evident that Co atoms are located between the NbS_2 layers and are vertically aligned with the Nb atoms of the two neighbouring layers. This also places the intercalants inside octahedral cavities created by the S atoms in the two layers. The NbS_2 sub-lattice is the same as for the 2H polytype. It is interesting to note that intercalation stabilizes the 2H type of stacking with respect to the 3R type (see Figure 2:2). For the non-intercalated NbS_2, the stability region of the 2H-polytype is much more narrow, resulting in a high concentration of stacking defects [149]. The refinement also confirmed that only for $x = 0.33$ the Co atoms are long range ordered in a $\sqrt{3}a \times \sqrt{3}a$ supercell of 2-layer periodicity. In the sample with $x = 0.25$, the Co atoms are stochastically distributed across all possible sites between the NbS_2 layers. In $Mn_{0.33}NbS_2$, the intercalated Mn ions assume the same configuration like Co within $Co_{0.33}NbS_2$ (Figure 6:4 b).

Table 6 displays the unit cell parameters for 2H-NbS_2 and the derived compounds intercalated with transition metals. All unit cells are hexagonal and contain two NbS_2 layers. It is interesting to note that intercalation of transition metals induces minor changes in the *c*-axis parameter. Intercalation by Mn induces an expansion by 4.9 %, while the Co intercalation induces a contraction by 1.5 %.

Table 6

Material	Unit cell parameters, Å	Intercalated ions sublattice
2H-NbS_2	$a = b = 3.324(5)$ $c = 11.96(1)$	/
$Mn_{0.33}$-NbS_2	$a = b = 5.807$; $c = 12.550$	$\sqrt{3}a \times \sqrt{3}a$
$Co_{0.33}$-NbS_2	$a = b = 5.7345(2)$; $c = 11.7869(4)$	$\sqrt{3}a \times \sqrt{3}a$
$Co_{0.25}$-NbS_2	$a = b = 3.3165(1)$; $c = 11.7859(8)$	Stochastic distribution

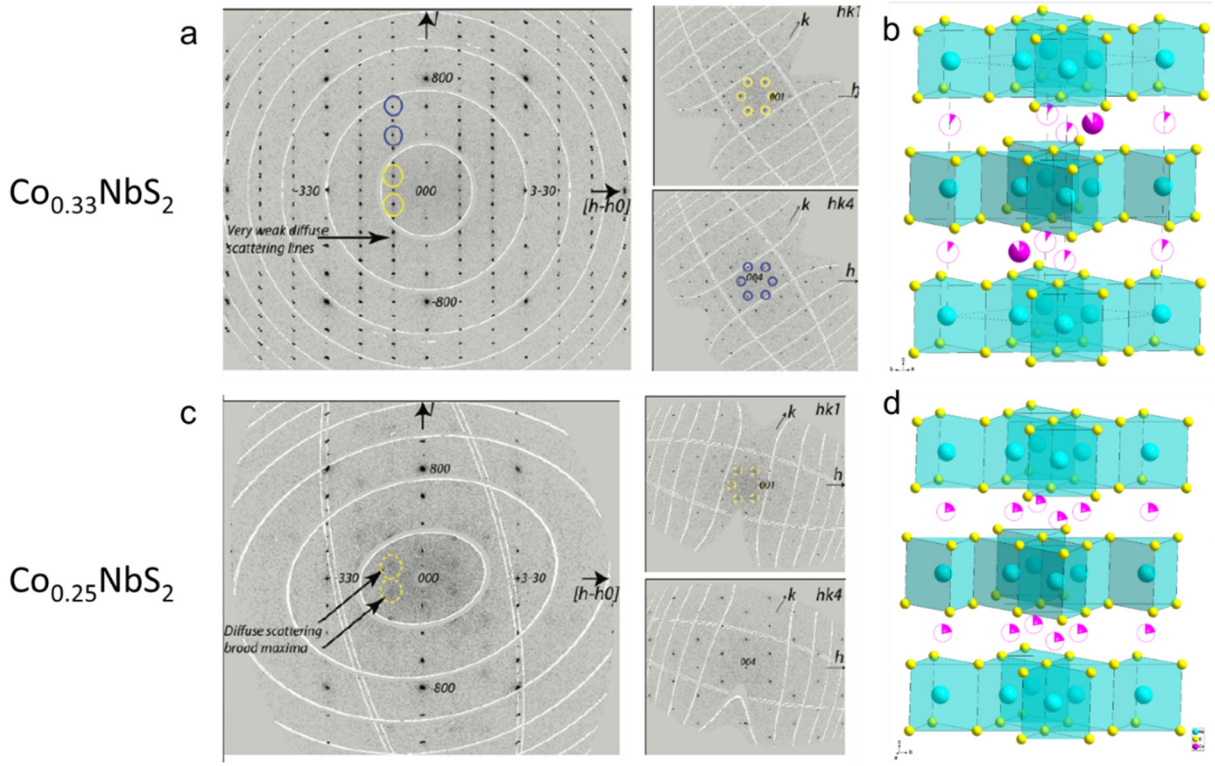

Figure 6:4 Crystal structure of Co intercalated NbS_2 a) Single crystal X-ray diffraction patterns for $Co_{0.33}NbS_2$. The Co atoms are ordered, forming a hexagonal lattice with a modulation vector $\sqrt{3}a \times \sqrt{3}a$, as can be seen from the satellite reflections. The blue and yellow circles identify the same satellite reflection in different diffraction planes. Weak diffusive scattering is produced by disorder in the distribution of Co atoms. **b)** Reconstructed crystal structure from the experimental XRD data. The filling of Co atoms represents the occupation probability of each site. **c)** Single crystal X-ray diffraction patters for $Co_{0.25}NbS_2$. The Co atoms are randomly distributed between the NbS_2 layers, as indicated by the broad diffusive scattering of the satellite peaks. **d)** Reconstructed crystal structure, where Co atoms occupy every site with equal probability, resulting in the absence of a long-range order.

The temperature dependence of the in-plane electrical resistivity for the considered materials is displayed in Figure 6:5 a. A first observation we can make is that there is a large increase in room temperature resistivity for all the intercalated samples. In the compounds with ordered intercalants ($Co_{0.33}NbS_2$ and $Mn_{0.33}NbS_2$), electrical resistivity is sharply suppressed after the onset of magnetic order — at 25 K for antiferromagnetic order in Co-intercalated compound, and 40 K for ferromagnetic order in Mn-intercalated compound. For disordered Co intercalation ($Co_{0.25}NbS_2$), there is no magnetic transition and its resistivity has a very weak temperature dependence. Such a weak temperature dependence of resistivity can be understood in terms of a strong, temperature-independent scattering caused by the stochastically distributed Co atoms. This is analogous to other metallic materials with high concentration of stochastically distributed defects or aperiodic structures [150].

While the transport properties of $Co_{0.33}NbS_2$ and $Mn_{0.33}NbS_2$ are very similar at ambient pressure, they behave completely differently once pressure is applied. This is a direct result of distinct magnetic orders. Under hydrostatic pressure of 2 GPa, the AFM order in $Co_{0.33}NbS_2$ is fully suppressed, while the Curie temperature in $Mn_{0.33}NbS_2$ remains unchanged. The suppression of magnetic order can be detected via transport measurements and via elastic neutron scattering. These data were used to complete the phase diagram in Figure 6:5 c. After the suppression of AFM order, the low temperature resistivity data show a logarithmic upturn. We interpret the upturn as caused by Kondo scattering from the interaction of conduction electrons with the localized spins on Co atoms.

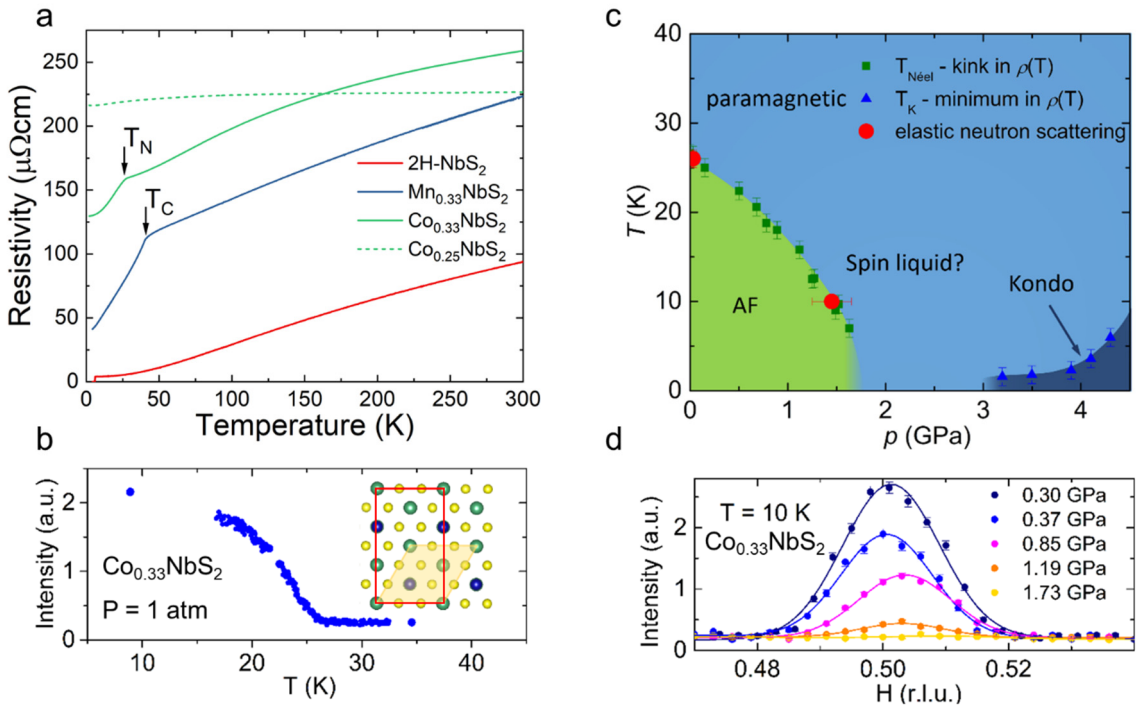

Figure 6:5 Magnetic transition and transport properties of intercalated NbS_2. **a)** Resistivity temperature dependence for 2H-NbS_2 and NbS_2 intercalated with Co or Mn. Samples with ordered intercalated ions show a low-temperature magnetic transition, which results in a sharp decrease of resistivity. For $Co_{0.25}NbS_2$, since the intercalants are disordered, there is no sign of magnetic transition and the resistivity has a very weak temperature dependence. **b)** Temperature dependence of the intensity of the [0.5, 0.5, 0] magnetic peak of the elastic neutron diffraction of single crystalline $Co_{0.33}NbS_2$. The crystalline (yellow) and magnetic (red) unit cells are depicted in the inset. **c)** Magnetic phase diagram of $Co_{0.33}NbS_2$ as a function of pressure and temperature. The critical temperatures of each magnetic transitions were experimentally determined via transport and neutron diffraction measurements. **d)** Pressure dependence of the intensity of the [0.5, 0.5, 0] magnetic peak, confirming the suppression of magnetic order by pressure.

6.4 Transport anisotropy and magnetic order

Before presenting the results of transport anisotropy in magnetically intercalated NbS_2, the following questions can be considered:

- How are the conduction electrons, propagating along different directions, affected by the magnetic order?
- Does the metallic intercalation act as a “bridge”, favouring the out-of-plane conduction?

To answer the first question, conductivity anisotropies of Mn- and Co-intercalated materials will be compared to each other. We have seen that upon magnetic ordering, the in-plane resistivity decreases for both materials. This is understood in terms of a simple notion that a commensurately ordered magnetism does not scatter conduction electrons, in contrast to the spin disorder which contributes to the resistivity at high temperature [139].

Figure 6:6 displays the results of resistivity anisotropy measured on microfabricated samples. There is a certain discrepancy in the in-plane resistivity of $Co_{0.33}NbS_2$, with respect to the values reported in Figure 6:5. This is because the crystal used for the microstructure came from a different batch that had lower crystalline quality (higher disorder of intercalated Co atoms). This difference in resistivity values, however, does not change the

main conclusions. In the paramagnetic phase, the two materials have a lower resistivity anisotropy compared to 2H-NbS_2 (16 at 300 K). In particular, for the Co-intercalated compound the anisotropy is below 2 because the out-of-plane resistivity is reduced and the in-plane resistivity increased. As expected, the intercalants contribute to the out-of-plane conduction, reducing the resistivity anisotropy.

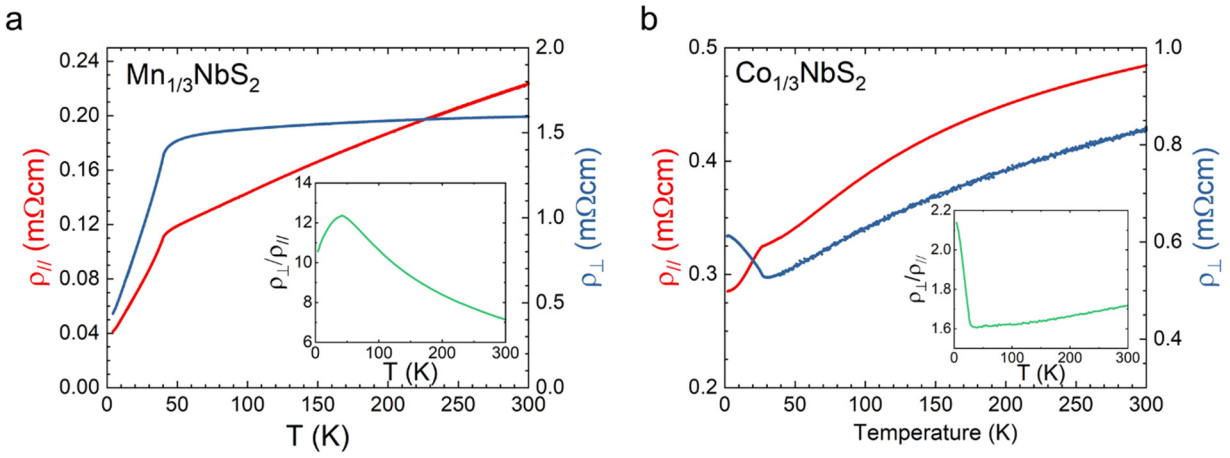

Figure 6:6 Transport anisotropy measured on FIB microfabricated samples. **a)** Temperature dependence of resistivity for $Mn_{0.33}NbS_2$ for current flow along the *ab*-plane (red) and *c*-axis (blue). In the inset the resistivity anisotropy ratio is plotted as a function of temperature. Below T_C, the resistivity decreases for both directions. **b)** Temperature dependence of resistivity for $Co_{0.33}NbS_2$ for current flow along the ab-plane (red) and *c*-axis (blue). In the inset the resistivity anisotropy ratio is plotted as a function of temperature. Below T_N the in-plane and out-of-plane resistivities have opposite trends, with an unusual increase of $\rho_\perp$ in the magnetically ordered phase upon cooling.

The difference in magnetic ordering of the two materials is reflected in the temperature dependences of the respective resistivity anisotropies. For the ferromagnetically ordered $Mn_{0.33}NbS_2$, both in-plane and out-of-plane resistivities decreases below T_C, as the spins become more ordered. In the case of antiferromagnetic order in $Co_{0.33}NbS_2$, the response of conduction electrons to magnetism is more surprising. The out-of-plane resistivity increases below T_N, in contrast to in-plane behaviour or to the case of FM order. The temperature dependence of resistivity has a negative slope, presenting us with yet another case of a "non-metallic metal", similarly to 1T-TaS_2 (Chapter 4). In this case, the temperature dependence has a close resemblance to the magnetic order parameter, proportional to the intensity of the magnetic peak shown in Figure 6:5 b.

We interpret the out-of-plane charge transport in the AFM state as dominated by a scattering mechanism analogous to a spin-blockade [151], resulting from the alternation of spin polarization between neighbouring layers. The uniqueness of $Co_{0.33}NbS_2$ is that it may be an analogue of a spin-valve in form of a bulk material, which is produced via a well-established and widely accessible process of chemical vapour transport. Spin valves are constructed by thin films of magnetic transition metals, separated by a non-magnetic spacer. The resistance through the device depends on the relative spin orientation of the magnetic layers. Opposite magnetization (antiferromagnetic coupling) induces an additional spin-flip scattering rate, suppressing conductivity. When magnetization of the two layers is the same, the device is in the low resistance state. Application of external magnetic field can change the magnetization of individual layers, switching the device resistance between high and low state [151]. In contrast to an actual spin valve, the AFM configuration in $Co_{0.33}NbS_2$ does not appear to be tuneable by an external magnetic field, and remains in the high-resistance state up to the highest applied field of 14 T.

In the case of $Fe_{0.33}NbS_2$, it has recently been demonstrated, that in-plane current pulses can rotate the in-plane component of AFM order. The rotation of magnetic configuration results in a change of resistivity, when

measured along specific directions in a multi-terminal device [152]. The proposed interpretation implies a rotation of polarisation direction of multiple AFM domains in the single crystal by spin transfer torque induced by the current pulse. This polarisation rotation within the domains is responsible for the change in the measured resistance along direction perpendicular with respect to the current pulse. A similar experiment has not been repeated on $Co_{0.33}NbS_2$, but because of the possible existence of multiple AFM domains a similar effect may be anticipated. The two intercalated compounds are isostructural, but their AFM orders have different easy axis of magnetization which might be a reason to expect a different behaviour [139].

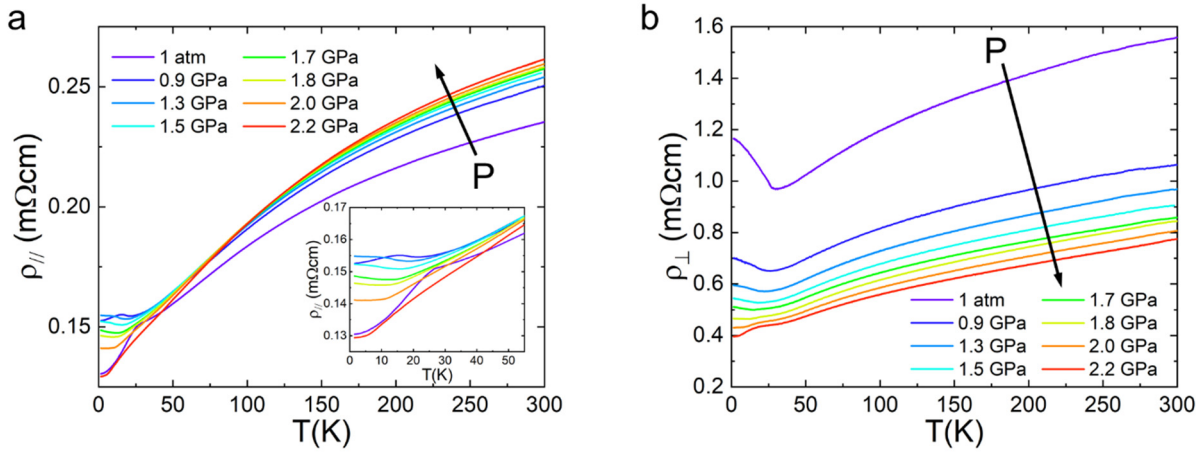

Figure 6:7 High-pressure transport anisotropy in $Co_{0.33}NbS_2$. a) Temperature dependence of the in-plane resistivity as a function of pressure. The inset shows the data in a narrow temperature range, in the vicinity of the magnetic transition. **b)** Temperature dependence of the out-of-plane resistivity as a function of pressure.

Electrical resistivity anisotropy measurements have also been carried under out applied pressure, in order to study the effect of interlayer spacing and the suppression of magnetic order (Figure 6:7). The out-of-plane resistivity has been measured on a single crystal without the use of FIB microfabrication. The pairs of voltage and current contacts have been made to the two opposite faces parallel the *ab*-plane, in the "ring and dot" configuration, with the larger ring-shaped electrodes for the injection of the current and the central smaller electrodes for probing the voltage.

This simpler sample preparation was favoured over the FIB-based approach due to working more reliably at high pressures; the method for creating FIB-microfabricated samples robust enough to withstand experiments in pressure cells was developed at a later point (details in section 7.1.2). We expect resistivity values obtained in this particular experiment to have a few-percent uncertainty, yet they still provide reliable information about the relative changes of resistivity with pressure. From the room temperature resistivity as a function of pressure, $\rho_{//}$ constantly increases in contrast to the marked decrease of $\rho_{\perp}$. The opposing trends indicate a different role of the Co atoms in the electronic conduction along different crystallographic axes. For both directions, pressure is expected to enhance the coupling between Co-orbitals and itinerant electrons of the NbS_2 layers. For the in-plane transport, the spin disorder on Co atoms acts as a scattering centre, and the higher coupling increases the scattering rate. Consequently, $\rho_{||}$ becomes higher. On the other hand, for transport along out-of-plane direction, the Co atoms have the effect of a "bridge" between the layers, and this contribution dominates over the spin-disorder scattering, reducing the out-of-plane resistivity as coupling improves. The role of Co atoms in the enhancement of the interlayer conductivity was captured in band structure calculations using DFT. Upon intercalation, the Fermi surface of NbS_2 acquires an additional "pot-shaped" pocket. The 3D nature of this Fermi surface component, gives electrons a higher velocity component along the *c*-axis. The bands responsible for the "pot-shaped" pocket originate mostly from the orbitals of the Co atom. This is a

further indication that the intercalant species contribute to the interlayer conduction. Sulphur atoms have a similar contribution to the Fermi surface, meaning that the orbitals of the chalcogen atoms also contribute to the out-of-plane transport. The behaviour of in-plane resistivity below 40 K is rather complicated, as already discussed in [153], and originates from the interplay of competing magnetic interactions. After a complete suppression of the magnetic order, above 1.8 GPa, the temperature dependence of resistivity becomes relatively featureless. The out-of-plane transport has a more pronounced response to pressure, and the onset of AFM state can be clearly identified by the resistivity minimum. The monotonic suppression of magnetic order parameter with pressure also reduces the magnitude of the out-of-plane resistivity increase below T_N, until its full suppression above 1.8 GPa.

6.5 Summary of TMD intercalated with magnetic ions

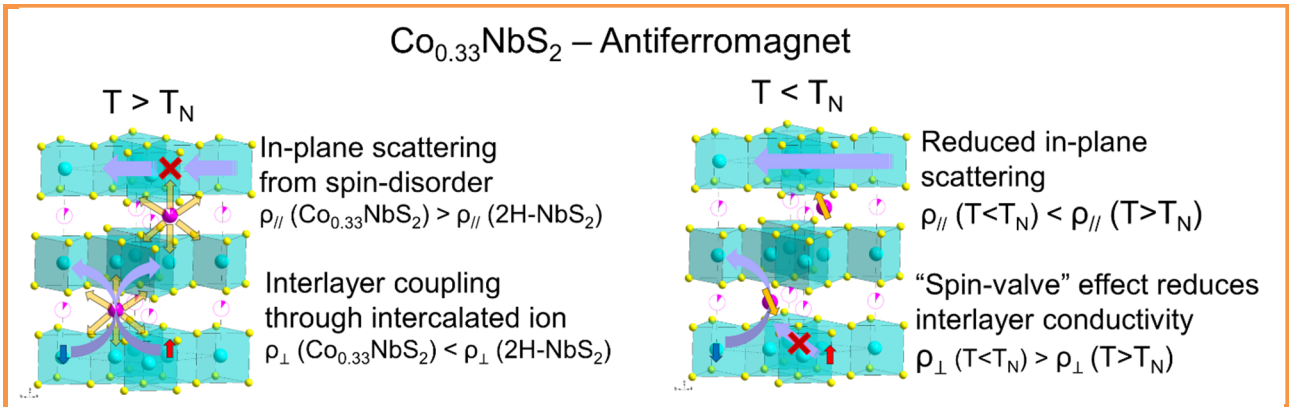

Figure 6:8 Intercalated magnetic TMDs summary

Intercalated TMDs

Thanks to their weak interlayer coupling, transition metal dichalcogenides (TMDs) can be readily intercalated with a variety if ions and molecules. Intercalation can take place during the growth of the layered material (single-step), or after the material has been synthesized (two-step). The latter approach is compatible with a variety of molecules because the low reaction temperatures, but offers lower control of the final product quality. 3d transition metals can be intercalated via a single-step approach, and their localized spins can order at low temperature in ferromagnetic or antiferromagnetic configurations.

Interlayer transport

- Paramagnetic phase: spin-disorder increases the in-plane scattering rate, intercalated ions increase the interlayer coupling.
- FM order: spin-disorder scattering rate is reduced isotropically.
- AFM order: opposite spin polarization between the planes reduces the interlayer conductivity, in resemblance to spin-gate devices.

Conclusion

Intercalation of layered materials can create new functionalities and tune transport properties through a non-trivial interplay of temperature, magnetic field and pressure.

Chapter 7 Experimental details

7.1 Focused ion beam microfabrication

The new results presented in this thesis, were possible thanks to the use of focused ion beam (FIB) for the preparation of samples for charge transport measurements. FIB is a microscopic imaging and fabrication tool, whose working principle and components are closely related to those of a scanning electron microscope (SEM), with the main difference being the use of accelerated ions instead of electrons. The energy transfer during ion-atom collisions exceeds the surface binding energy and causes the starting material to become ablated. Repeated scanning of the specimen surface with the ion beam leads to progressive removal of material from the imaged area. This enables machining of crystals with sub-micrometre precision, with the minimum feature size determined by the diameter of the ion beam spot. The development of FIB started in the 1980's, as a tool for reparation and inspection of microcircuits, first adopted in the semiconductor industry [154]. Thanks to the rapid increase in demand, commercial systems were soon developed and become fairly common in research institutes. The systems available today are usually of dual beam type, incorporating SEM and FIB columns in the same machine (Figure 7:1). The SEM offers the high-resolution imaging capability, while the FIB is used for localised milling and in-situ metal deposition. FIB is commonly used in materials science for the preparation of lamellae for transmission electron microscopy (TEM), as the localized etching on a sub-micrometre scale can be used to polish any electrically conducting material into a specimen of less than 100 nm in thickness. The possibility to deposit metal in-situ is also used to attach the lamella to a TEM sample holder. More recent development is the use of FIB for condensed matter research, in particular for preparing samples for electronic transport measurements [155]. The advantage comes from the freedom to structure any material in three dimensions, without the need of a mask and with an immediate feedback obtainable via the SEM imaging. The approach is therefore complementary to the standard lithography techniques. A common source of scepticism concerning FIB is the possibility to damage and alter the studied material by ion irradiation and implantation. We will see that extrinsic effects can largely be mitigated by following a particular fabrication procedure. In addition, samples prepared for this thesis have a cross section around 5 x 5 μm^2, and since the damaged layer extends only over the tens of nm, its contribution to transport measurement is minimal. To completely mitigate the problem and reduce any extrinsic contribution, the damaged surface layer can be completely removed by plasma etching or converted into an insulator by oxidation.

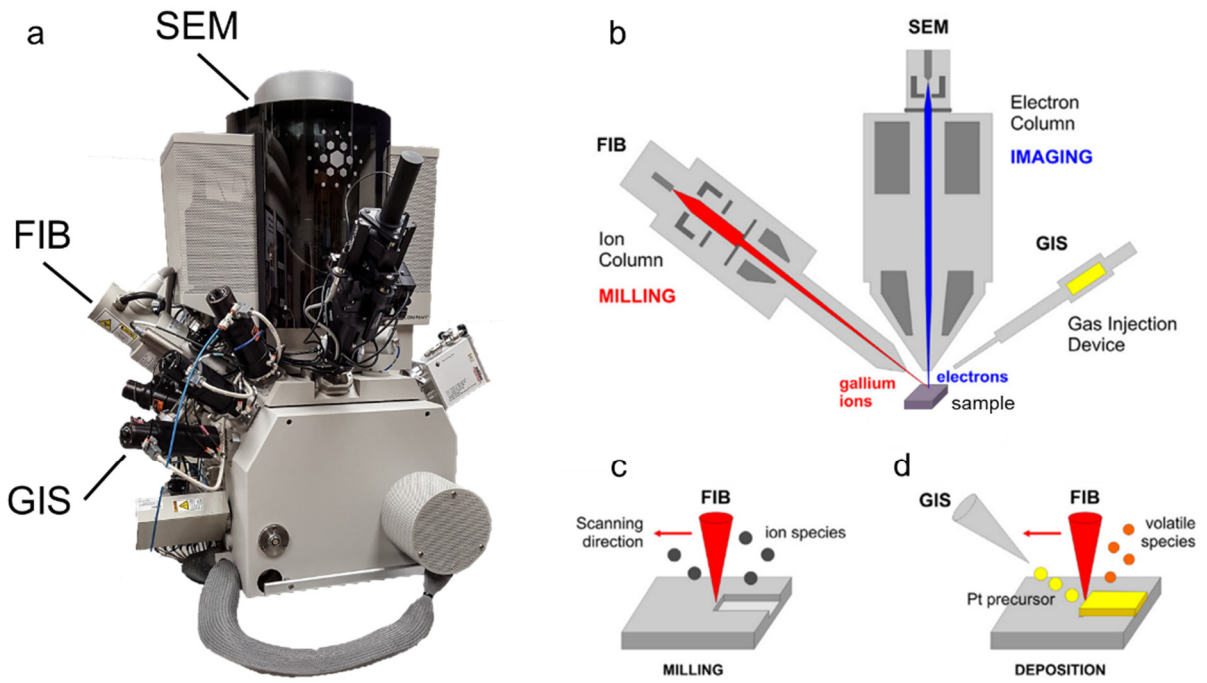

Figure 7:1 Focused ion beam microscope a) Picture of a commercial focused ion beam microscope, FEI Helios G4 Dual beam. A similar system was used for the preparation of the samples studied in this thesis. Ion column uses Ga as the source. **b)** Schematic diagram of a dual beam configuration with scanning electron microscope (SEM) and focused ion beam (FIB) of gallium ions. Gas injection system (GIS) is used for releasing metal-organic precursor gas in close proximity to the sample for in-situ ion-assisted deposition. Figure from [156]. **c)** Sample milling by a focused beam of ions. **d)** Ion-beam-assisted deposition: the ion beam is used for dissociating the precursor molecules released from a gas-injection needle and depositing their metallic part onto the specimen surface.

7.1.1 Microfabrication process

In this section the steps for producing a microstructured sample for transport measurements using FIB will be described in detail. Each step is shown in Figure 7:2, represented schematically in the left panel (a), while the actual SEM images are on the right (b). Sample preparation begins with the isolation of a lamella from a single crystal of the chosen material (Figure 7:2 1-3 or i). The process is analogous to the well-established TEM lamella preparation [157], with appropriate adjustment of sample dimensions. A typical lamella for transport measurement has a size of approximately 150 × 100 × 5 μm^3. Before the lamella is extracted, its sides are polished at a grazing angle with a beam of lower current in order to reduce the extent of the damaged surface layer and ensure the sides are parallel [158]. The analytical capabilities of dual-beam systems, such as electron backscatter diffraction, energy-dispersive X-ray spectroscopy, and high-resolution SEM are helpful to identify the optimal location to isolate a lamella and the orientation of a crystal. In the case of layered materials used in this thesis, the *c*-axis direction is evident form the morphology of crystals. The lamella preparation is completed by thinning down a small bridge (< 1 μm), which connects the lamella to the parent crystal. Once ready, the lamella is transferred onto a suitable substrate, such as a silicon or sapphire chip, used to create electrical connections. The transfer can be done either ex-situ or in-situ, using a micromanipulator needle together with FIB-assisted localised metal deposition. The former approach is used more frequently. The lamella is gently pushed by a thin microneedle in order to break the bridge and is then transferred while being held by electrostatic attraction using materials such as Kapton™ [159] (**4**). The lamella can be fixed to the substrate by epoxy glue, or by creating metallic anchoring points using in-situ metal deposition. The sample is then sputter-coated with a conducting layer, which will be used for making electrical connections. The

secondary purpose of the fixtures is to create a smooth profile between the top surface of the lamella and the substrate, ensuring the continuity of the sputtered layer. The deposited metal film covers the entire sample and most of the substrate, but will be later etched by FIB to create individual electrodes for the probing the sample. The standard process uses 150 nm of Au and 15 nm of Ti as an adhesion layer. Etching the surface with Ar plasma for 5 min before the deposition ensures that the contacts between the sample and the film have a low resistance (lower than 5 Ω). Before proceeding with the final step of the sample fabrication, thin gold or silver wires are connected to the sputtered film at the edges of the substrate by silver-loaded epoxy glue. The wires provide electrical grounding of the sample during the subsequent ion beam milling, and will be later used to connect the sample to the external leads of the measurement setup.

The sample is then moved to the FIB for the final phase of the fabrication. It starts by etching away the gold layer from the probed region of the sample (**iii**). The exposed part of the crystal is then machined into the desired final geometry (**iv**). A good practice is to finish the preparation with a few passes of low voltage grazing angle polishing of the side surfaces of the sample. This helps to minimize the extent of the damaged surface and remove material re-deposited onto the sample during the milling process.

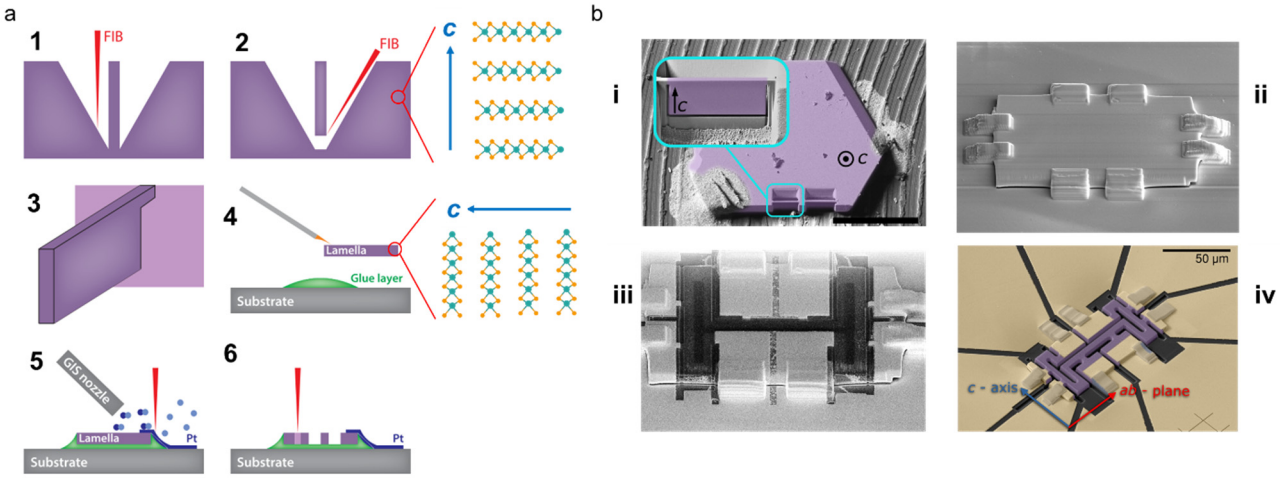

Figure 7:2 Step-by-step illustration of the sample preparation process a) Schematic visualization of the preparation of a sample for measurements of the out-of-plane transport measurement. The crystallographic orientation of the material is shown. **1)** Coarse trench cutting for isolating a freestanding slab. **2)** Undercutting the slab in order to disconnect it from the parent crystal **3)** Thinning of the lamella bridge and its polishing by grazing angle milling. Three-dimensional representation of the undercut lamella connected to the parent crystal by a thin bridge. **4)** Separation and transfer of the lamella onto a substrate using a micro-Kapton loop moved by a micromanipulator. The lamella is freed from the parent crystal by mechanically breaking the thin bridge. The lamella can be fixed by a small drop of glue or by using in-situ platinum deposition **5)** Metal deposition by gas injection system is used in order to mechanically stabilize the lamella and prepare the electrical connections. Gold sputtering is often used for creating high quality electrical contacts. **6)** Fine-structuring of the sample into the final desired geometry. Figure adapted from [155]. **b)** SEM images of samples during different phases of the preparation. **i)** Single crystal of a layered TMD with two lamellae ready to be extracted. The undercuts are shown in the inset. **ii)** Lamella placed over a sapphire substrate, held in place by 4 pairs of Pt strips deposited in-situ. The entire sample is coated with gold for electrical connections. **iii)** Selective gold etching to define the sample and electrode areas. **iv)** Completed sample, the particular geometry is used in order to homogenize the current flow through the sections of the sample where the voltage difference is measured. It also allows to measure the resistivity reliably along both axes in the identical conditions of temperature, pressure and magnetic field. False colours are added for illustrative purpose. The microstructured single crystal is highlighted in purple, and the gold film – in yellow. Crystallographic axes are also indicated.

7.1.2 Design optimization for high-pressure experiments on layered materials

Due to a weak mechanical interlayer coupling of the materials investigated, the final microstructure is extremely vulnerable to delamination induced by shear stresses. Throughout this study, mechanical failures of this kind resulted in several FIB-structured samples getting irreversibly damaged, particularly during the high-pressure experiments. Through an iterative process, the sample design has evolved to minimize the shear stresses potentially experienced by the microstructure. A first step was to use a "free-standing" configuration, where the sample is only weakly coupled to the substrate by a few metallic anchoring points instead of being connected by epoxy glue. The use of metallic connections leaves the sample partially lifted from the substrate, and in this way stresses created by differential thermal contraction are reduced [71]. The small air gap can also be filled by the liquid pressure medium during high-pressure experiments, which is necessary for ensuring quasi-hydrostatic environment and avoiding sample failure due to pressure inhomogeneity.

The geometry of the sample has been optimized to increase its mechanical stability. Among those optimizations, adjusting dimensions of each feature, rounding of the convex edges and minimising surface roughness were crucial ingredients for the successful measurements. The idea to optimize the radius of curvature and smoothing the sample surface comes from the basic knowledge of fracture mechanics [160]. Stresses are intensified in the vicinity of sharp corners, which, for materials as brittle as layered compounds along the *c*-axis, leads to a formation and propagation of cracks. In Figure 7:3, two designs of samples of the same material are compared. The one with sharp corners suffered catastrophic failure under pressure. The sample with rounded corners and polished edges was able to sustain multiple cycles of compression up to 2 GPa and decompression.

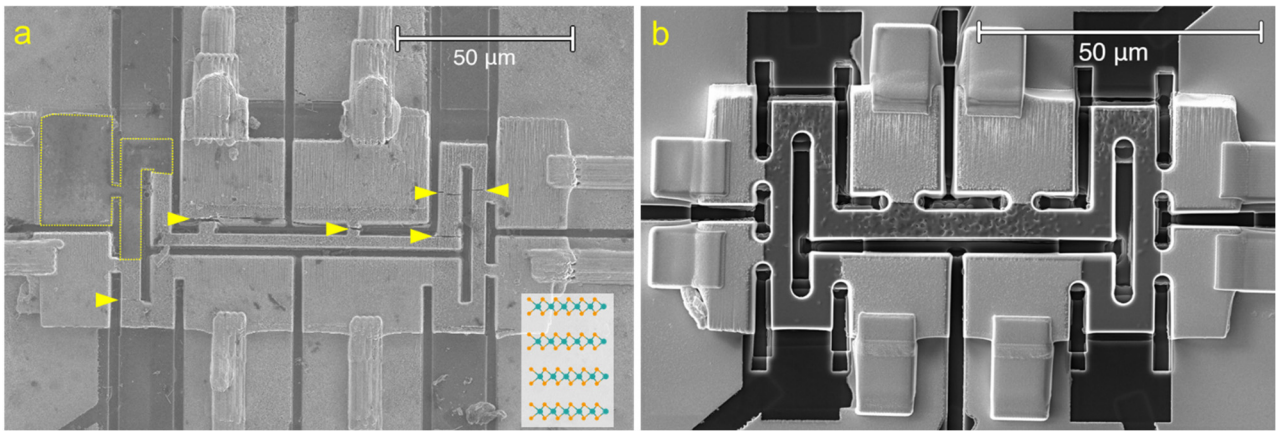

Figure 7:3 Optimisation of sample geometry for high-pressure experiments. a) Scanning electron microscope image of a microstructured TMD sample damaged during a high-pressure experiment. Multiple cracks (yellow arrows), propagating along the crystalline layers, can be seen near convex edges of the sample, where mechanical stresses are enhanced. A large section of the sample is missing, marked by the yellow dashed line. **b)** Image showing the same material as in panel **a**, microstructured with an optimal design for high-pressure experiments. In order to reduce the likelihood of mechanical failures, the minimum feature size was increased and all the convex edges were rounded. The sample successfully survived multiple pressurisations to 2 GPa without any irreversible change (image taken before applying pressure). In both images the *c*-axis of the crystal is oriented vertically.

7.1.3 Finite element simulations

Finite element simulations were performed to prove the reliability of the experimental results and assess the applicability of the chosen sample geometry for resistivity anisotropy measurements. The commercial finite element analysis package COMSOL Multiphysics^{TM} was used in order to calculate the current density and voltage fields in a model replicating the microstructured sample (Figure 7:4 a,b). The simulations were carried out for the case of 1T-TaS_2, as the results for this compounds were the most surprising and in contrast with existing literature. The general conclusion can be extended to other materials.

A fixed in-plane resistivity $\rho_{\parallel}$ = 0.78 mΩcm (room temperature value for 1T-TaS_2) was imposed for the simulations, and it was investigated how the measured resistivity anisotropy, calculated from the potential differences across the voltage probes, corresponds to the actual anisotropy, dictated by the variable out-of-plane resistivity $\rho_{\perp}$. As can be seen in Figure 7:4 c, for anisotropy values between approximately 0.1 and 100 we expect measurements to provide reliable values of $\rho_{\parallel}$ and $\rho_{\perp}$.

Figure 7:4 d-f show the computed current density field inside the sample for the anisotropy values of 0.1, 1 and 100. It can be seen that for the highest and lowest values of $\rho_{\perp}$ and $\rho_{\parallel}$ the current jetting effects result in a slight divergence of the current flow lines along some of the probed sections of the crystal. In the isotropic case, which, according to our data, is the closest to the real situation in 1T-TaS_2, the current flows homogeneously between every pair of voltage probes. For anisotropy lower than 0.1 — a scenario highly unlikely for layered materials — current jetting along *c*-axis affects the determination of $\rho_{\perp}$. For highly anisotropic materials, current distribution will be homogeneous along the *c*-axis. In this case, and for the same sample geometry, $\rho_{\parallel}$ cannot be reliably measured anymore. For the case of materials with $\rho_{\perp}/\rho_{\parallel} > 200$, such as 4Hb-$TaS_2$, the in-plane resistivity was measured on a large single crystal with gold wires connected by silver epoxy.

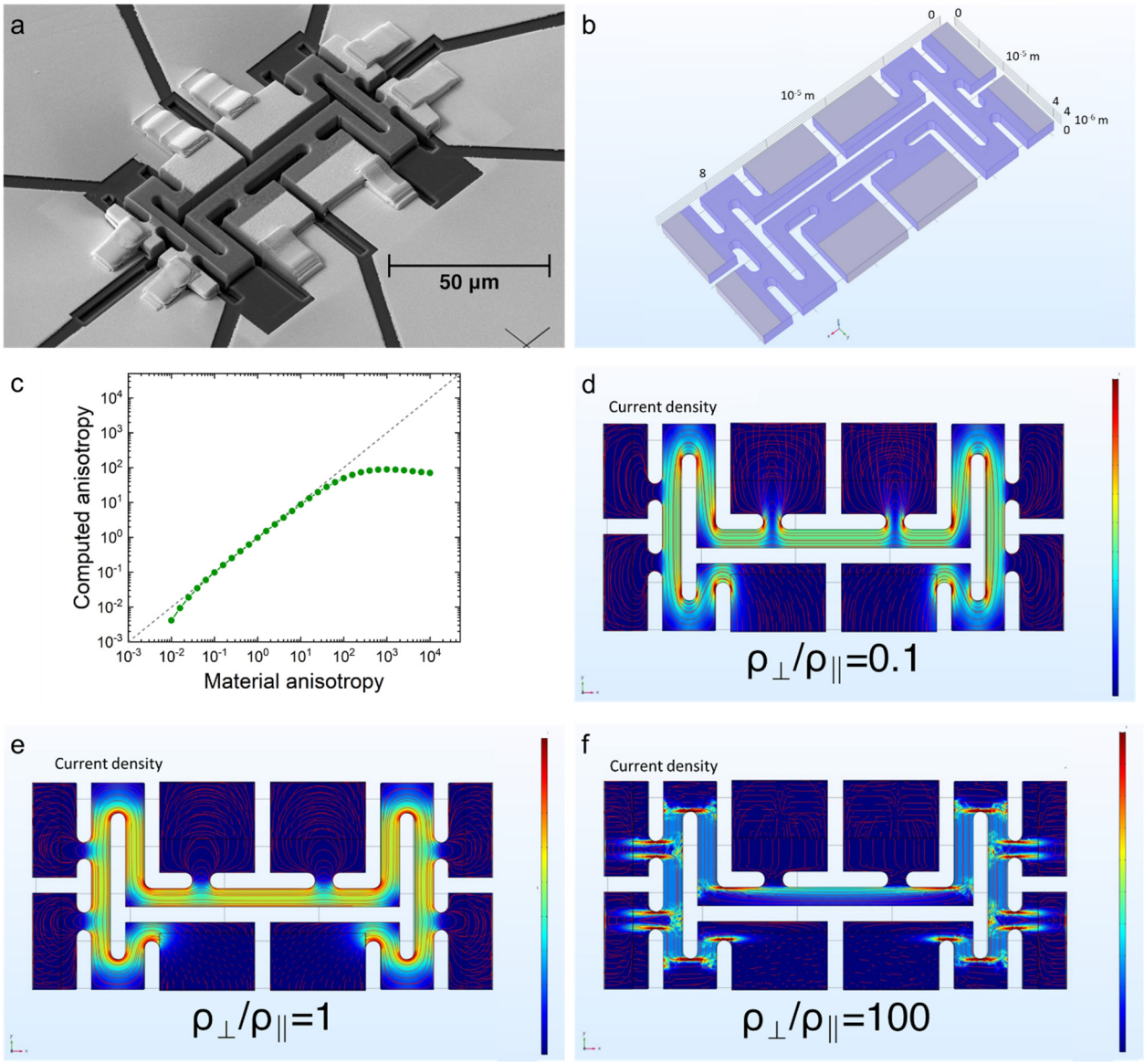

Figure 7:4 Finite elements simulations. a) Scanning electron microscope image of the focused-ion-beam-structured sample of 1T-TaS_2 used for our study **b)** A virtual model of the sample created for conducting finite element simulations of the current flow. Blue — 1T-TaS_2, grey — gold layer. The dimensions of the actual sample and the model match. **c)** Finite element calculations were used to compute the voltages at the probing points of the microstructured sample, which were used to calculate the apparent resistivity anisotropy (Computed anisotropy). The computed anisotropy is plotted (green dots) against the imposed intrinsic anisotropy (Material anisotropy). The dashed line indicates the perfect agreement between the values of the two anisotropies. The chosen sample geometry can be used to reliably measure the out-of-plane ($\rho_\perp$) and in-plane resistivities ($\rho_\parallel$) if the ratio of the between them is roughly between 0.1 and 100. **d-f)** The plots show the magnitude of the current density (colour map) and the current flow trajectory (red lines) predicted by the finite element calculations for the focused-ion-beam-structured sample. The calculations were done for three different values of resistivity anisotropy ($\rho_\perp/\rho_\parallel$): 0.1 (**d**), 1 (**e**) and 100 (**f**). The *ab*-plane and *c*-axis are aligned, respectively, with the horizontal and vertical directions. In the $\rho_\perp/\rho_\parallel = 1$, case the current flows homogeneously along all the probed sections of the sample. For $\rho_\perp/\rho_\parallel = 0.1$ small current jetting can be observed in the *c*-axis oriented parts of the sample. For $\rho_\perp/\rho_\parallel = 100$ some inhomogeneity in the current density can be seen inside the in-plane channel.

7.1.4 FIB Sample surface

The sample fabrication by ion-milling inevitably produces a thin layer of damaged material. Under ion irradiation, the structured material becomes amorphous for the first few tens of nm [158]. In addition, the accelerated ions are implanted, which can be a concern when Ga ions are used on semiconducting materials. For materials with more than one element, such as transition metal chalcogenides or pnictides, ion etching tends to leave a non-stoichiometric surface due to the difference in surface binging energies. This effect was clearly observed in NbAs, as a thin superconducting Nb layer was created by ion irradiation [161].

Polishing the samples with low-current ion beam helped to reduce the thickness of the damaged surface layer down to the several nanometers. Since dimensions of the probed parts of the samples were no less than a few microns, the resultant extrinsic effects on the charge transport properties are expected to be negligible. In the case of transition metal dichalcogenides, the amorphous surface layer is metal-rich and has a natural tendency to oxidise, when exposed to air. The resultant layer of oxide is typically highly insulating, which further reduces its contribution to the measured resistivity.

A more detailed investigation of the sample surface was done on a FIB-microstructured sample of $ZrTe_5$ with confocal Raman spectroscopy. The Raman spectra from the surface of the sample were recorded a few days after fabrication. These spectra presented a broad peak centred at zero frequency, which is an indication of amorphous material, and a pair of broad active modes centred at 130 cm^{-1} and 150 cm^{-1}, which could be attributed to off-stoichiometric zirconium oxide [162]. The surface of the sample was then been gently etched using an RF-plasma cleaner with N_2 gas. The state of the surface was periodically checked with the Raman spectroscopy. After a total etching time of 120 min, which corresponds to few tens of nanometres of material removed, the Raman spectrum of pristine $ZrTe_5$ became visible (**Figure 7:5**). From the optical images taken before and after the etching, there is no evident variation in the appearance of the sample, which is a further proof of the small extent the amorphous layer.

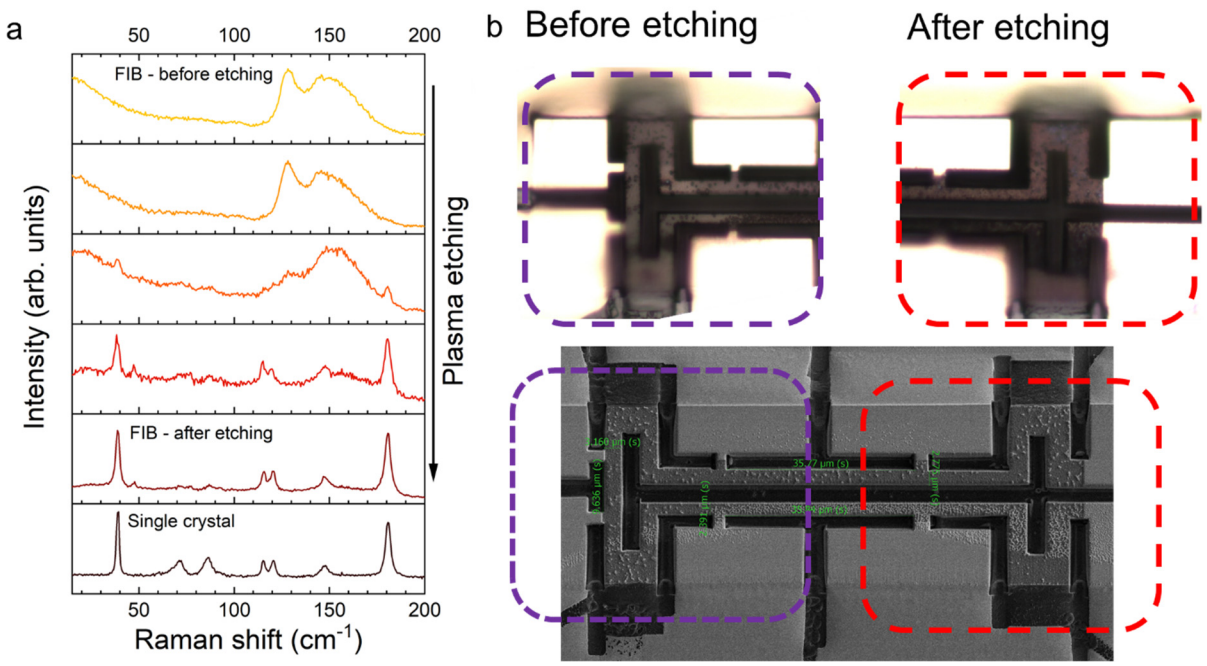

Figure 7:5 Surface state of FIB-sample. a) Confocal Raman spectra recorded on a microstructured $ZrTe_5$ sample, upon etching the surface by RF N_2 plasma. The spectrum at the bottom corresponds to a pristine single crystal and serves as a reference. **b)** Optical microscopy images of the $ZrTe_5$ sample before and after plasma cleaning. Since the thickness of the material etched away is a few nanometers, there is no evident difference in the appearance of the surface. The SEM image at the bottom indicates the portions of the sample shown in the optical photographs (marked by the coloured boxes).

7.2 High-pressure experiments

By applying external pressure, it is possible to continuously tune the lattice period of materials and consequently their electronic properties. In the scope of the research presented in this thesis, the application of high pressure to layered materials allows to observe how their properties change as the interlayer distance is reduced. Today, there exists a number of commercially available devices for creating quasi-hydrostatic pressures of up to 25'000 atmospheres (2.5 GPa), with a possibility to simultaneously probe electrical resistivity of the sample as a function of temperature or magnetic field [163].

The high-pressure transport experiments presented in this thesis were performed using a commercially available piston cylinder cell supplied by C&T [164]. The device is a composite cylinder, with parts made of Cu:Be and Ni-Cr-Al alloys. The sample is located in the bore of the cylinder, sealed inside a Teflon™ tube filled with a pressure transmitting medium. A feedthrough, through which measurement leads pass between the high-pressure and ambient-pressure regions, seals one end of the bore. A piston is located at the opposite end and is held in a fixed position by an adjustable screw. The pressure is increased by pushing the piston deeper into the bore using a hydraulic press. After applying the desired force (on the order of a few tons), the load is stored by tightening a locking nut, holding the piston in position, and the cell is ready to be loaded into the cryostat. Continuous monitoring of pressure inside the sample space is done by measuring the electrical resistance of a reference sample, such as Pb. Its normal state resistivity and superconducting transitions temperature have a pronounced pressure dependence [165]. The pressure medium used with most success for FIB microstructures is a 1:1 pentane-isopentane mixture. The choice is motivated by the good quasi-hydrostaticity [166], and by its low boiling point. Once the cell is opened the liquid completely evaporates leaving no residues inside the microstructure. Because there is not remaining contamination onto the sample, it is possible to inspect it with the SEM or even to repair it with the FIB. On the contrary, using a non-volatile

medium like Daphne oil makes it impossible to repair the sample after high-pressure experiments. The residual oil is trapped inside the sample and polymerizes under exposure to the electron of ion beam, completely covering the sample with an insulating layer. It is then impossible to obtain high quality SEM images or attempt a reparation using the FIB.

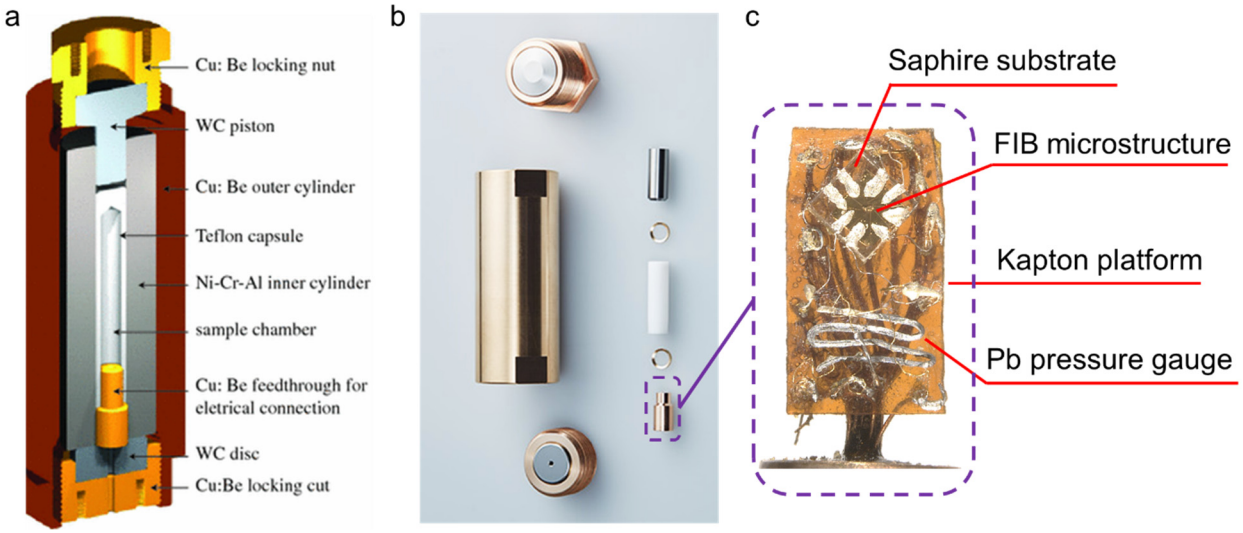

Figure 7:6 Piston-cylinder pressure cell. a) Schematic drawing of a double-layer piston-cylinder pressure cell. Figure from [163] **b))** Image of the individual components of a C&T piston cylinder cell, the orientation of the components is the same as in panel **a**. Image from [164] **c)** Sample stage set up for measurements, located on the top of the feedthrough (marked by the box in panel b). The space between electrical wires is sealed by stycast epoxy. A perforated Kapton foil is used to create a support platform for the sample preparation, and holds the wires in position. The lead strip bent into a meandering shape is located on the bottom side of the stage. Having a longer strip increases its resistance and therefore the signal-to-noise ratio of the measurement. The FIB-structured sample sits on top of a sapphire substrate.

The use of liquid pressure-transmitting media in high-pressure experiments ensures quasi-hydrostatic conditions in the sample space, which allows even brittle materials not to be destroyed. Subjecting a crystal to high pressure results in it being strained, meaning that the lattice parameters change. For materials that do not have cubic symmetry, the lattice contraction is direction-dependent and we need to represent compressibility with a tensor. The relation between lattice compression along each high-symmetry direction and the applied pressure can be experimentally determined by high-pressure X-ray diffraction experiments.

Figure 7:7 displays the variation of normalized cell parameters for different TMDs as function of pressure. Data for 1T-TaS_2 have been collected for the project conducted for this thesis, while results in the panel b are a summary of already published results [167] [168] [169]. For low pressures ($P < 5$ GPa) the compressibility along the *c*-axis is approximately 3 times higher than for the in-plane direction. For very high pressures, when the layers are moved much closer together, the relation between compressibility and applied pressure deviates from linearity. For pressures above 15 GPa, the in-plane and out-of-plane compressibilities have the same slope, making the response of the materials to external forces nearly isotropic.

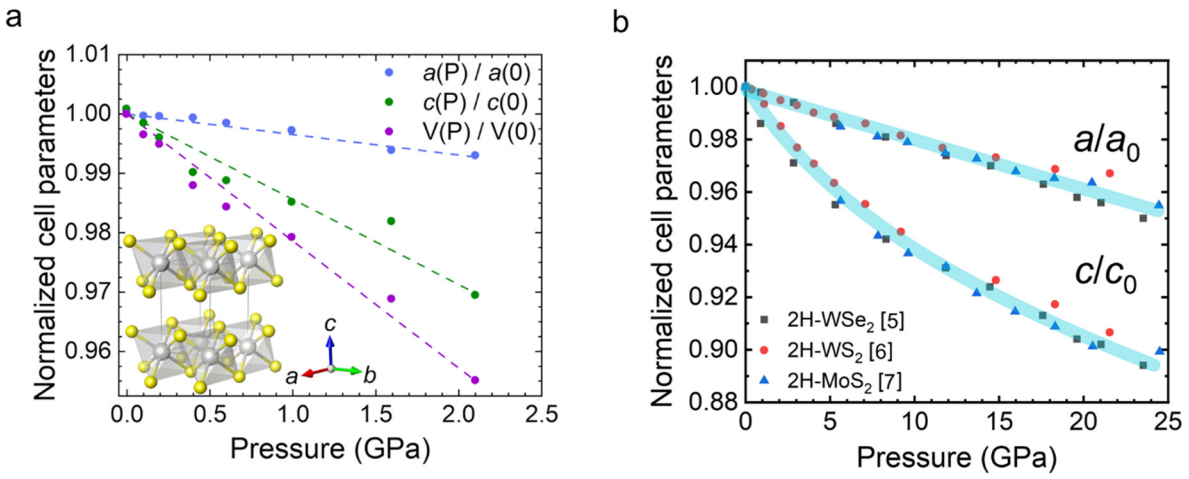

Figure 7:7 Compressibility of layered TMDs. a) Pressure dependence of the mean Ta-Ta distances within (*a*) and between (*c*) layers as well as the overall volume change (*V*). For the given pressure range the changes can be approximated as linear, which is illustrated with the fitted dashed lines. The crystal structure is visualised in the bottom left (grey – Ta, yellow – S). **b)** Normalized unit cell parameters for layered transition metal dichalcogenides: 2H-MoS_2, 2H-WS_2 and 2H-WSe_2. The three materials follow the same trend. The blue lines are guides for the eye.

Conclusion

The work presented in this thesis is intended to be a structured and systematic investigation of the interlayer physics of selected layered materials. The experimental results are introduced and discussed in order of increasing complexity of the investigated material. At the same time, the interlayer physics becomes more and more peculiar, and the understanding of the microscopic conduction mechanisms less intuitive. Today we know of more than one thousand crystalline materials with a layered structure. The same type of experiments as reported here could be repeated on any other layered material, and new properties may emerge, originating from the interlayer charge dynamics. In this sense, one of the most important achievements of this thesis is that it demonstrates a new and reliable experimental approach to study layered materials.

Most of the new results presented in this thesis have been possible thanks to the implementation of FIB microfabrication. This tool makes it possible to microstructure any material into a complex geometry, introducing a negligible amount of defects and no mechanical stress. For the study of interlayer dc conductivity, this is the only practical approach that one can adopt. The additional cost in time and resources to create a sample with FIB is paid off by the outstanding quality of the experimental data and the robustness of the sample. During this thesis, the very same samples have been measured for more than 2 years, undergoing various thermal cycles down to 1 K, high-field experiments up to 34 T and high-pressure experiments up to 25'000 atmospheres.

The discussion of experimental results started with our study of $ZrTe_5$, 2H-$NbSe_2$ and 2H-$TaSe_2$. Those layered materials where chosen and investigated because of their relative simplicity in crystalline and electronic structure. The conductivity anisotropy determined experimentally has been compared to the estimated values, computed from the band structure and Fermi surface topology of the materials. Agreement between experiments and theory is remarkable, which proves that the electronic conduction between the layers of those materials is a coherent process. The layered structure does not imply electrons are confined within the crystalline layers, but it simply induces a marked anisotropy of the material's plasma frequency, which is proportional to *n/m*. The anisotropy cannot be unambiguously attributed to the effective mass, in particular as we have seen in the case of 2H-$NbSe_2$ and 2H-$TaSe_2$. Instead, it appears more useful to consider the effective number of carriers *n* that can contribute to charge transport along the specific crystalline direction.

Surprising set of results was observed in the case of 1T-TaS_2, as a consequence of the CDW induced lattice reconstruction and orbital ordering. This material has been long investigated for its peculiar electronic properties, with particular attention paid to the low temperature metal-insulator transition. The most interesting results have been observed when the CDW reconstruction forms nanometre-sized domains, in the so-called NC-CDW phase. In this unusual electronic phase of 1T-TaS_2, charge transport has an anomalous non-metallic behaviour when electrons are propagating within the planes, and a conventional metallic behaviour is observed along the perpendicular direction. To understand this, we evoked the strong interlayer coupling. This coupling results from the orbital character of the conduction band which is formed by Ta $\boldsymbol{d_{z^2-r^2}}$ orbitals protruding along the *c-axis* direction. In the specific case of this material, the data collected on FIB microstructured sample are in stark contrast to previously reported results. The anisotropy that we found varies between 4 and 0.6, while previously it was considered to be above 1000. This large difference can be entirely attributed to the measurement geometry, which was suboptimal in the previous experiments. This example further proves the advantages of FIB microfabrication in the investigation of new materials.

Another relevant property of layered materials is the opportunity to create intercalated compounds, taking advantage of the weak interlayer bond strength. We first discussed this on the example of 4Hb-TaS_2, where two different types of TaS_2 layers with different coordination are interleaved to form a natural heterostructure. The interaction between neighbouring layers has a strong effect on the CDW reconstruction and the superconducting phase. Contrary to all the similar compounds investigated in the preceding chapters, in the case of alternately stacked 4Hb-TaS_2, charge transport is highly anisotropic and out-of-plane conduction appears to be incoherent, as the resistivity increases upon cool down. What could cause this change in conduction regime from coherent to incoherent? – This question is left open for discussion.

When intercalating layered metals with magnetic ions, the conductivity anisotropy appears to be affected by the specific magnetic order type. For ferromagnetic coupling, the long-range magnetic order induces a sharp reduction of resistivity along every direction, as the scattering of fluctuating spins is suppressed. On the contrary, antiferromagnetic order displays a peculiar anisotropic behaviour. In the specific case of the antiferromagnetic order of $Co_{0.33}NbS_2$, the out-of-plane charge conduction becomes less favourable in the magnetically ordered phase, possibly a consequence of the opposite polarization of vertically aligned Co ions.

There are still many open questions related to the microscopic mechanism of interlayer charge dynamics observed in the experiments that were discussed here. Throughout this thesis, many other peculiar effects have been observed, but as their explanation is still in an early phase, they have not made their way into this thesis. An example is a very challenging set of experimental results related to the role of stacking faults in the conduction anisotropy and physical properties of layered materials. To fully address this question, one needs accurate structural information, which can be obtained through very sophisticated structural refinement from single crystal X-ray diffraction or high resolution TEM imaging. This analysis is ongoing.

Such defects can be induced in high concentrations for specific compounds, when different polytypes have very similar formation energies. This is the case of 2H-NbS_2, in which nearly 15 % of the layers form stacking faults in a 3R-type of configuration. At low temperature, the out-of-plane resistivity shows an unusual, insulating-like behaviour. Such insulating state appears to be suppressed when a magnetic field is applied along the *c*-axis, resulting in a negative magnetoresistance. The suppression of resistivity under applied magnetic field continues without saturation up to the maximum explored magnetic field of 34 T. This problem is a challenge that we look forward to resolving.

There are many “low hanging fruits” that are in reach to anybody who has access to a FIB, and can repeat the same sample preparation procedure. Because the interest for layered materials is constantly increasing, the study of interlayer charge transport using FIB is bound to become a routine approach. With this thesis, the new challenges in layered materials are a step closer to being solved.

References

[1] "The Nobel Prize in Physics 1956 - NobelPrize.org." [Online]. Available: https://www.nobelprize.org/prizes/physics/1956/summary/. [Accessed: 17-Feb-2020].

[2] "ICSD - Basic Search & Retrieve." [Online]. Available: https://icsd.fiz-karlsruhe.de/search/basic.xhtml;jsessionid=013059B285FEAB74D104329ED84B1725. [Accessed: 21-Feb-2020].

[3] B. BHUSHAN, *Springer handbook of nanotechnology*. 2017.

[4] E. C. Dreaden, A. M. Alkilany, X. Huang, C. J. Murphy, and M. A. El-Sayed, "The golden age: Gold nanoparticles for biomedicine," *Chemical Society Reviews*, vol. 41, no. 7. Royal Society of Chemistry, pp. 2740–2779, 07-Apr-2012.

[5] D. C. Agrawal, *Introduction to nanoscience and nanomaterials*. 2013.

[6] "Carbon Nanomaterials Dimensionality And Hybridization - Diamond Graphite Sp2 Sp3, HD Png Download , Transparent Png Image - PNGitem." [Online]. Available: https://www.pngitem.com/middle/xowTib_carbon-nanomaterials-dimensionality-and-hybridization-diamond-graphite-sp2/. [Accessed: 01-Apr-2020].

[7] T. Mueller and E. Malic, "Exciton physics and device application of two-dimensional transition metal dichalcogenide semiconductors," *npj 2D Materials and Applications*, vol. 2, no. 1. Nature Publishing Group, pp. 1–12, 01-Dec-2018.

[8] K. V Klitzing, G. Dorda, and M. Pepper, "New method for high-accuracy determination of the fine-structure constant based on quantized hall resistance," *Phys. Rev. Lett.*, vol. 45, no. 6, pp. 494–497, 1980.

[9] R. Willett, J. P. Eisenstein, H. L. Störmer, D. C. Tsui, A. C. Gossard, and J. H. English, "Observation of an even-denominator quantum number in the fractional quantum Hall effect," *Phys. Rev. Lett.*, vol. 59, no. 15, pp. 1776–1779, 1987.

[10] H. L. Stormer, D. C. Tsui, and A. C. Gossard, "The fractional quantum Hall effect," *Rev. Mod. Phys.*, vol. 71, no. SUPPL. 2, 1999.

[11] D. Tong, "The Quantum Hall Effect TIFR Infosys Lectures," 2016.

[12] "The Nobel Prize in Physics 1987." [Online]. Available: https://www.nobelprize.org/prizes/physics/1987/summary/. [Accessed: 20-Feb-2020].

[13] A. Schilling, M. Cantoni, J. D. Guo, and H. R. Ott, "Superconductivity above 130 K in the Hg-Ba-Ca-Cu-O system," *Nature*, vol. 363, no. 6424, pp. 56–58, 1993.

[14] K. S. Novoselov *et al.*, "Electric field in atomically thin carbon films," *Science.*, vol. 306, no. 5696, pp. 666–669, Oct. 2004.

[15] K. S. Novoselov *et al.*, "Two-dimensional gas of massless Dirac fermions in graphene," *Nature*, vol. 438, no. 7065, pp. 197–200, 2005.

[16] C. R. Dean *et al.*, "Boron nitride substrates for high-quality graphene electronics," *Nat. Nanotechnol.* |, vol. 5, 2010.

[17] C. R. Dean *et al.*, "Multicomponent fractional quantum Hall effect in graphene," *Nat. Phys.*, vol. 7, no. 9, pp. 693–696, 2011.

[18] “Grafene - Wikipedia.” [Online]. Available: https://it.wikipedia.org/wiki/Grafene. [Accessed: 23-Mar-2020].

[19] K. S. Novoselov *et al.*, “Two-dimensional atomic crystals,” *Proc. Natl. Acad. Sci.*, vol. 102, no. 30, pp. 10451–10453, 2005.

[20] A. K. Geim and I. V Grigorieva, “Van der Waals heterostructures,” *Nature*, vol. 499, no. 7459. pp. 419–425, 2013.

[21] Y. Cao *et al.*, “Unconventional superconductivity in magic-angle graphene superlattices,” *Nature*, vol. 556, no. 7699, pp. 43–50, Apr. 2018.

[22] Z. Wang *et al.*, “Evidence of high-temperature exciton condensation in two-dimensional atomic double layers,” *Nature*, vol. 574, no. 7776. Nature Publishing Group, pp. 76–80, 03-Oct-2019.

[23] M. Yankowitz *et al.*, “Tuning superconductivity in twisted bilayer graphene,” *Science*, vol. 363, no. 6431, pp. 1059–1064, 2019.

[24] “Puzzle Solution: Magic Moiré in Graphene | Quanta Magazine.” [Online]. Available: https://www.quantamagazine.org/puzzle-solution-magic-moire-in-graphene-20190726/. [Accessed: 31-Mar-2020].

[25] M. Ashton, J. Paul, S. B. Sinnott, and R. G. Hennig, “Topology-Scaling Identification of Layered Solids and Stable Exfoliated 2D Materials,” *Phys. Rev. Lett.*, vol. 118, no. 10, 2017.

[26] “Crystallography Open Database.” [Online]. Available: http://www.crystallography.net/cod/. [Accessed: 21-Feb-2020].

[27] “2D Structures List.” [Online]. Available: https://www.materialscloud.org/discover/2dstructures/dashboard/list. [Accessed: 21-Feb-2020].

[28] “2Dmatpedia.” [Online]. Available: http://www.2dmatpedia.org/summary. [Accessed: 21-Feb-2020].

[29] “Le parole sono pietre preziose: MOLIBDENITE (Molybdenite) - Solfuri - Sulphides.” [Online]. Available: http://mineralsauvage.blogspot.com/2016/01/molibdenite-molybdenite-solfuri.html. [Accessed: 27-Mar-2020].

[30] “Pyrite - Wikipedia.” [Online]. Available: https://en.wikipedia.org/wiki/Pyrite. [Accessed: 27-Mar-2020].

[31] A. V Kolobov, *Two Dimensional Transition Metal Dichalcogenides*. Singapore: Springer Singapore, 2016.

[32] M. Chhowalla, H. S. Shin, G. Eda, L. J. Li, K. P. Loh, and H. Zhang, “The chemistry of two-dimensional layered transition metal dichalcogenide nanosheets,” *Nature Chemistry*, vol. 5, no. 4. pp. 263–275, 2013.

[33] H. Katzke, P. Tolédano, and W. Depmeier, “Phase transitions between polytypes and intralayer superstructures in transition metal dichalcogenides,” *Phys. Rev. B - Condens. Matter Mater. Phys.*, vol. 69, no. 13, pp. 1–8, 2004.

[34] C. C. Homes, M. Reedyk, D. A. Cradles, and T. Timusk, “Technique for measuring the reflectance of irregular, submillimeter-sized samples,” *Appl. Opt.*, vol. 32, no. 16, p. 2976, Jun. 1993.

[35] J. H. Mooij, “Electrical conduction in concentrated disordered transition metal alloys,” *Phys. Status Solidi*, vol. 17, no. 2, pp. 521–530, 1973.

[36] O. Gunnarsson, M. Calandra, and J. E. Han, “Colloquium: Saturation of electrical resistivity,” *Rev.*

Mod. Phys., vol. 75, no. 4, pp. 1085–1099, 2003.

[37] C. C. Tsuei, "Nonuniversality of the Mooij correlation the temperature coefficient of electrical resistivity of disordered metals," *Phys. Rev. Lett.*, vol. 57, no. 15, pp. 1943–1946, 1986.

[38] M. Gurvitch and A. T. Fiory, "Resistivity of La1.825Sr0.175CuO4 and YBa2Cu3O7 to 1100 K: Absence of saturation and its implications," *Phys. Rev. Lett.*, vol. 59, no. 12, pp. 1337–1340, 1987.

[39] L. Forro, "Out-of-plane resistivity of Bi2Sr2CaCu2O8+x high temperature superconductor," *Phys. Lett. A*, vol. 179, no. 2, pp. 140–144, Aug. 1993.

[40] J. R. Cooper, L. Forró, and B. Keszeit, "Direct evidence for a very large penetration depth in superconducting Bi2Sr2CaCu2O8 single crystals," *Nature*, vol. 343, no. 6257, pp. 444–446, 1990.

[41] X. D. Xiang *et al.*, "Metallization of the resistivity tensor in Bi2Sr2CaCu2Ox through epitaxial intercalation," *Phys. Rev. Lett.*, vol. 68, no. 4, pp. 530–533, 1992.

[42] X. D. Xiang *et al.*, "Iodine intercalation of a high-temperature superconducting oxide," *Nature*, vol. 348, no. 6297, pp. 145–147, 1990.

[43] S. J. Moon *et al.*, "Incoherent c-axis interplane response of the iron chalcogenide FeTe 0.55Se0.45 superconductor from infrared spectroscopy," *Phys. Rev. Lett.*, vol. 106, no. 21, pp. 1–4, 2011.

[44] S. V. Dordevic *et al.*, "Optical properties of the quasi-two-dimensional dichalcogenides 2H-TaSe2 and 2H-NbSe2," *Eur. Phys. J. B*, vol. 33, no. 1, pp. 15–23, 2003.

[45] M. Tanaka, M. Hasegawa, and H. Takei, "Growth and Anisotropic Physical Properties of PdCoO2 Single Crystals," *J. Phys. Soc. Japan*, vol. 65, no. 12, pp. 3973–3977, Nov. 1996.

[46] C. W. Hicks, A. S. Gibbs, A. P. Mackenzie, H. Takatsu, Y. Maeno, and E. A. Yelland, "Quantum oscillations and high carrier mobility in the delafossite PdCoO 2," *Phys. Rev. Lett.*, vol. 109, no. 11, p. 116401, Sep. 2012.

[47] C. C. Homes, S. Khim, and A. P. Mackenzie, "Perfect separation of intraband and interband excitations in PdCoO2," *Phys. Rev. B*, vol. 99, no. 19, p. 195127, 2019.

[48] S. V. Dordevic and D. N. Basov, "Electrodynamics of correlated electron matter," *Ann. der Phys.*, vol. 15, no. 7–8, pp. 545–570, Jul. 2006.

[49] D. N. Basov, R. D. Averitt, D. Van Der Marel, M. Dressel, and K. Haule, "Electrodynamics of correlated electron materials," *Rev. Mod. Phys.*, vol. 83, no. 2, pp. 471–541, 2011.

[50] D. N. Basov and T. Timusk, "Electrodynamics of High-T c Superconductors," *Rev. Mod. Phys.*, vol. 77, no. 1, pp. 1–63, 2005.

[51] P. J. W. Moll, "The role of anisotropy in iron-pnictides addressed by focused ion beam sample fabrication," ETH, 2012.

[52] A. Pisoni, "Pressure-tuned Transport Properties of Novel Iron-based Superconductors and Topological Insulators," 2016.

[53] D. Svetin, I. Vaskivskyi, S. Brazovskii, and D. Mihailovic, "Three-dimensional resistivity and switching between correlated electronic states in 1T-TaS2," *Sci. Rep.*, vol. 7, 2017.

[54] P. J. W. Moll, "Focused Ion Beam Microstructuring of Quantum Matter," *Annu. Rev. Condens. Matter Phys.*, vol. 9, no. 1, pp. 147–162, Mar. 2018.

[55] "3D (VRML) Fermi Surface Database." [Online]. Available: http://www.phys.ufl.edu/fermisurface/.

[Accessed: 26-Mar-2020].

[56] N. P. Armitage, E. J. Mele, and A. Vishwanath, “Weyl and Dirac semimetals in three-dimensional solids,” *Rev. Mod. Phys.*, vol. 90, no. 1, 2018.

[57] D. Gall, “Electron mean free path in elemental metals,” *J. Appl. Phys.*, vol. 119, no. 8, 2016.

[58] Q. Li *et al.*, “Chiral magnetic effect in ZrTe5,” *Nat. Phys.*, vol. 12, no. 6, pp. 550–554, Jun. 2016.

[59] G. Manzoni *et al.*, “Ultrafast Optical Control of the Electronic Properties of ZrTe5,” *Phys. Rev. Lett.*, vol. 115, no. 20, 2015.

[60] H. Xiong *et al.*, “Three-dimensional nature of the band structure of ZrTe5 measured by high-momentum-resolution photoemission spectroscopy,” *Phys. Rev. B*, vol. 95, no. 19, p. 195119, 2017.

[61] Y. Liu *et al.*, “Zeeman splitting and dynamical mass generation in Dirac semimetal ZrTe5,” *Nat. Commun.*, vol. 7, 2016.

[62] R. Y. Chen *et al.*, “Optical spectroscopy study of the three-dimensional Dirac semimetal ZrTe5,” *Phys. Rev. B - Condens. Matter Mater. Phys.*, vol. 92, no. 7, p. 75107, 2015.

[63] H. Weng, X. Dai, and Z. Fang, “Transition-metal pentatelluride ZrTe5 and HfTe5: A paradigm for large-gap quantum spin hall insulators,” *Phys. Rev. X*, vol. 4, no. 1, pp. 1–8, 2014.

[64] X. B. Li *et al.*, “Experimental Observation of Topological Edge States at the Surface Step Edge of the Topological Insulator ZrTe5,” *Phys. Rev. Lett.*, vol. 116, no. 17, pp. 1–5, 2016.

[65] E. Martino *et al.*, “Two-Dimensional Conical Dispersion in ZrTe5 Evidenced by Optical Spectroscopy,” *Phys. Rev. Lett.*, vol. 122, no. 21, pp. 1–6, 2019.

[66] P. Shahi *et al.*, “Bipolar Conduction as the Possible Origin of the Electronic Transition in Pentatellurides: Metallic vs Semiconducting Behavior,” *Phys. Rev. X*, vol. 8, no. 2, 2018.

[67] T. E. Jones, W. W. Fuller, T. J. Wieting, and F. Levy, “Thermoelectric power of HfTe5 and ZrTe5,” *Solid State Commun.*, vol. 42, no. 11, pp. 793–798, 1982.

[68] X. Lin, B. Fauqué, and K. Behnia, “Scalable T2 resistivity in a small single-component Fermi surface,” *Science (80-.).*, vol. 349, no. 6251, pp. 945–948, 2015.

[69] Z. M. Gibbs, H.-S. Kim, H. Wang, and G. J. Snyder, “Band gap estimation from temperature dependent Seebeck measurement—Deviations from the 2e|S|maxTmax relation,” *Appl. Phys. Lett.*, vol. 106, no. 2, p. 022112, Jan. 2015.

[70] D. Santos-Cottin *et al.*, “Probing intraband excitations in ZrTe5: a high-pressure infrared and transport study,” 2019.

[71] M. D. Bachmann *et al.*, “Spatial control of heavy-fermion superconductivity in CeIrIn5,” *Science*, vol. 366, no. 6462, pp. 221–226, 2019.

[72] K. Rossnagel *et al.*, “Fermi surface of 2H-NbSe2 and its implications on the charge-density-wave mechanism,” *Phys. Rev. B - Condens. Matter Mater. Phys.*, vol. 64, no. 23, pp. 1–6, 2001.

[73] D. S. Inosov *et al.*, “Fermi surface nesting in several transition metal dichalcogenides,” *New J. Phys.*, vol. 10, no. 12, p. 125027, Dec. 2008.

[74] R. Corcoran *et al.*, “Quantum oscillations in the mixed state of the type II superconductor 2H-NbSe2,” *J. Phys. Condens. Matter*, vol. 6, no. 24, pp. 4479–4492, 1994.

[75] M. Johannes, I. Mazin, and C. Howells, “Fermi-surface nesting and the origin of the charge-density

wave in NbSe2," *Phys. Rev. B*, vol. 73, no. 20, p. 205102, May 2006.

[76] M. D. Johannes and I. I. Mazin, "Fermi surface nesting and the origin of charge density waves in metals," *Phys. Rev. B - Condens. Matter Mater. Phys.*, vol. 77, no. 16, 2008.

[77] G. Grüner, *Density waves in solids*. 2018.

[78] M. Naito and S. Tanaka, "Electrical Transport Properties in 2H-NbS2, -NbSe2, -TaS2 and -TaSe2," *J. Phys. Soc. Japan*, vol. 51, no. 1, pp. 219–227, 1982.

[79] D. E. Moncton, J. D. Axe, and F. J. DiSalvo, "Neutron scattering study of the charge-density wave transitions in 2H-TaSe2 and 2H-NbSe2," *Phys. Rev. B*, vol. 16, no. 2, pp. 801–819, 1977.

[80] R. L. Withers and L. A. Bursill, "Comments on the neutron scattering study of the charge-density-wave-periodic-structural-distortion transition in 2H-TaSe2 and 2H-NbSe2 by Moncton, Axe, and DiSalvo," *Physical Review B*, vol. 26, no. 3. pp. 1469–1470, 1982.

[81] D. B. McWhan, J. D. Axe, and R. Youngblood, "Pressure dependence of the striped-to-hexagonal charge-density-wave transition in 2H-TaSe2," *Phys. Rev. B*, vol. 24, no. 9, pp. 5391–5393, 1981.

[82] C. J. Arguello *et al.*, "Visualizing the charge density wave transition in 2H - NbSe2 in real space," *Phys. Rev. B - Condens. Matter Mater. Phys.*, vol. 89, no. 23, p. 235115, 2014.

[83] K. I. Yokota, G. Kurata, T. Matsui, and H. Fukuyama, "Superconductivity in the quasi-two-dimensional conductor 2H-TaSe2," *Phys. B Condens. Matter*, vol. 284–288, no. PART I, pp. 551–552, Jul. 2000.

[84] K. Rossnagel, "On the origin of charge-density waves in select layered transition-metal dichalcogenides," *Journal of Physics Condensed Matter*, vol. 23, no. 21. 01-Jun-2011.

[85] F. R. Gamble, J. H. Osiecki, M. Cais, R. Plsharody, F. J. DiSalvo, and T. H. Geballe, "Intercalation complexes of lewis bases and layered sulfides: A large class of new superconductors," *Science*, vol. 174, no. 4008, pp. 493–497, 1971.

[86] B. Ruzicka, L. Degiorgi, H. Berger, R. Gaál, and L. Forró, "Charge Dynamics of 2H-TaSe2 along the Less-Conducting c-Axis," *Phys. Rev. Lett.*, vol. 86, no. 18, pp. 4136–4139, Apr. 2001.

[87] S. V. Dordevic, D. N. Basov, R. C. Dynes, and E. Bucher, "Anisotropic electrodynamics of layered metal 2H-NbSe2," *Phys. Rev. B*, vol. 64, no. 16, p. 161103, Sep. 2001.

[88] S. V Dordevic *et al.*, "Optical properties of the quasi-two-dimensional dichalcogenides 2H-TaSe2 and 2H-NbSe2," *Eur. Phys. J. B*, vol. 33, no. 1, pp. 15–23, 2003.

[89] E. Tosatti and P. Fazekas, "ON THE NATURE OF THE LOW-TEMPERATURE PHASE OF 1T-TaS 2," *Le J. Phys. Colloq.*, vol. 37, no. C4, pp. C4-165-C4-168, Oct. 1976.

[90] B. Sipos, A. F. Kusmartseva, A. Akrap, H. Berger, L. Forró, and E. Tutǐ, "From Mott state to superconductivity in-1T-TaS 2," *Nat. Mater.*, vol. 7, no. 12, pp. 960–965, 2008.

[91] Y. Liu *et al.*, "Nature of charge density waves and superconductivity in 1T-TaSe2-xTex," *Phys. Rev. B*, vol. 94, no. 4, p. 45131, 2016.

[92] X. L. Yu *et al.*, "Electronic correlation effects and orbital density wave in the layered compound 1T-TaS2," *Phys. Rev. B*, vol. 96, no. 12, Sep. 2017.

[93] P. D. Hambourger and F. J. di Salvo, "Electronic conduction process in 1T-TaS2," *Phys. B+C*, vol. 99, no. 1–4, pp. 173–176, 1980.

[94] A. Ribak *et al.*, "Gapless excitations in the ground state of 1T-TaS2," *Phys. Rev. B*, vol. 96, no. 19,

Nov. 2017.

[95] O. Sezerman, A. M. Simpson, and M. H. Jericho, “Thermal expansion of lT-TaS2 and 2H-NbSe2,” *Solid State Commun.*, vol. 36, no. 9, pp. 737–740, 1980.

[96] W. Wang, D. Dietzel, and A. Schirmeisen, “Lattice Discontinuities of 1T-TaS 2 across First Order Charge Density Wave Phase Transitions,” *Sci. Rep.*, vol. 9, no. 1, Dec. 2019.

[97] M. D. Bachmann *et al.*, “Spatial control of heavy-fermion superconductivity in CeIrIn5,” *Science (80-.).*, vol. 366, no. 6462, pp. 221–226, Oct. 2019.

[98] R. E. Thomson, B. Burk, A. Zettl, and J. Clarke, “Scanning tunneling microscopy of the charge-density-wave structure in 1T-TaS2,” *Phys. Rev. B*, vol. 49, no. 24, pp. 16899–16916, 1994.

[99] B. Burk, R. E. Thomson, J. Clarke, and A. Zettl, “Surface and bulk charge density wave structure in 1T-TaS2,” *Science (80-.).*, vol. 257, no. 5068, pp. 362–364, 1992.

[100] S. C. Bayliss, A. M. Ghorayeb, and D. R. P. Guy, “Thermal and transport evidence for a phase transition in 1T-TaS2 observed at 282K upon warming,” *J. Phys. C Solid State Phys.*, vol. 17, no. 21, 1984.

[101] A. Spijkerman, J. L. de Boer, A. Meetsma, G. A. Wiegers, and S. van Smaalen, “X-ray crystal-structure refinement of the nearly commensurate phase of in-dimensional superspace,” *Phys. Rev. B - Condens. Matter Mater. Phys.*, vol. 56, no. 21, pp. 13757–13767, 1997.

[102] T. Ritschel *et al.*, “Pressure dependence of the charge density wave in 1T-TaS2 and its relation to superconductivity,” *Phys. Rev. B - Condens. Matter Mater. Phys.*, vol. 87, no. 12, pp. 1–5, 2013.

[103] X. L. Wu and C. M. Lieber, “Hexagonal domain-like charge density wave phase of TaS2 determined by scanning tunneling microscopy,” *Science (80-.).*, vol. 243, no. 4899, pp. 1703–1705, Mar. 1989.

[104] X. L. Wu and C. M. Lieber, “Direct observation of growth and melting of the hexagonal-domain charge-density-wave phase in 1T-TaS2 by scanning tunneling microscopy,” *Phys. Rev. Lett.*, vol. 64, no. 10, pp. 1150–1153, Mar. 1990.

[105] S. Martin, A. F. Hebard, A. R. Kortan, and F. A. Thiel, “Transport properties of Al65Cu15Co20 and Al70Ni15Co15 decagonal quasicrystals,” *Phys. Rev. Lett.*, vol. 67, no. 6, pp. 719–722, 1991.

[106] C. Uher, R. L. Hockey, and E. Ben-Jacob, “Pressure dependence of the c-axis resistivity of graphite,” *Phys. Rev. B*, vol. 35, no. 9, pp. 4483–4488, 1987.

[107] K. Matsubara, K. Sugihara, and T. Tsuzuku, “Electrical resistance in the c direction of graphite,” *Phys. Rev. B*, vol. 41, no. 2, pp. 969–974, 1990.

[108] M. Klanjšek *et al.*, “A high-temperature quantum spin liquid with polaron spins,” *Nat. Phys.*, vol. 13, no. 11, pp. 1130–1134, 2017.

[109] Y. Yu *et al.*, “Gate-tunable phase transitions in thin flakes of 1T-TaS2,” *Nat. Nanotechnol.*, vol. 10, no. 3, pp. 270–276, 2015.

[110] T. Ritschel, “Electronic self-organization in layered transition metal dichalcogenides,” 2015.

[111] S. H. Lee, J. S. Goh, and D. Cho, “Origin of the Insulating Phase and First-Order Metal-Insulator Transition in 1T-TaS2,” *Phys. Rev. Lett.*, vol. 122, no. 10, p. 106404, 2019.

[112] M. Bovet *et al.*, “Interplane coupling in the quasi-two-dimensional 1T-TaS2,” *Phys. Rev. B*, vol. 67, no. 12, p. 125105, Mar. 2003.

[113] P. Darancet, A. J. Millis, and C. A. Marianetti, “Three-dimensional metallic and two-dimensional

insulating behavior in octahedral tantalum dichalcogenides," *Phys. Rev. B - Condens. Matter Mater. Phys.*, vol. 90, no. 4, pp. 2–6, 2014.

[114] T. Ritschel *et al.*, "Orbital textures and charge density waves in transition metal dichalcogenides," *Nat. Phys.*, vol. 11, no. 4, pp. 328–331, 2015.

[115] L. V. Gasparov *et al.*, "Phonon anomaly at the charge ordering transition in 1T-TaS2," *Phys. Rev. B*, vol. 66, no. 9, p. 094301, Sep. 2002.

[116] L. Le Guyader *et al.*, "Stacking order dynamics in the quasi-two-dimensional dichalcogenide 1T-TaS2 probed with MeV ultrafast electron diffraction," *Struct. Dyn.*, vol. 4, no. 4, 2017.

[117] M. Naito, H. Nishihara, and S. Tanaka, "Nuclear Magnetic Resonance and Nuclear Quadrupole Resonance Study of 181Ta in the Commensurate Charge Density Wave State of 1T-TaS2," *J. Phys. Soc. Japan*, vol. 55, no. 7, pp. 2410–2421, 1986.

[118] A. Ribak *et al.*, "Chiral superconductivity in the alternate stacking compound 4Hb-Ta2," 2019.

[119] B. Dardel, M. Grioni, D. Malterre, P. Weibel, Y. Baer, and F. Lévy, "Temperature-dependent pseudogap and electron localization in 1T-TaS2," *Phys. Rev. B*, vol. 45, no. 3, pp. 1462–1465, 1992.

[120] F. J. Di Salvo, B. G. Bagley, J. M. Voorhoeve, and J. V. Waszczak, "Preparation and properties of a new polytype of tantalum disulfide (4Hb-TaS2)," *J. Phys. Chem. Solids*, vol. 34, no. 8, pp. 1357–1362, 1973.

[121] G. Wexler, A. Woolley, and N. Doran, "The Fermi surface of 1 T-VS2 and 4 Hb-TaS2," *Nuovo Cim. B Ser. 11*, vol. 38, no. 2, pp. 571–578, Apr. 1977.

[122] J. A. Wilson, F. J. Di Salvo, and S. Mahajan, "Charge-density waves and superlattices in the metallic layered transition metal dichalcogenides," *Adv. Phys.*, vol. 50, no. 8, pp. 1171–1248, Dec. 2001.

[123] I. Ekvall and J. J. Kim, "Atomic and electronic structures of the two different layers in 4Hb at 4.2 K," *Phys. Rev. B - Condens. Matter Mater. Phys.*, vol. 55, no. 11, pp. 6758–6761, 1997.

[124] E. Navarro-Moratalla *et al.*, "Enhanced superconductivity in atomically thin TaS 2," *Nat. Commun.*, vol. 7, no. 1, p. 11043, Apr. 2016.

[125] J. Lüdecke, S. van Smaalen, A. Spijkerman, J. L. de Boer, and G. A. Wiegers, "Commensurately modulated structure of 4Hb-TaSe2 determined by x-ray crystal-structure refinement," *Phys. Rev. B - Condens. Matter Mater. Phys.*, vol. 59, no. 9, pp. 6063–6071, 1999.

[126] A. Zong *et al.*, "Ultrafast manipulation of mirror domain walls in a charge density wave," *Sci. Adv.*, vol. 4, no. 10, 2018.

[127] R. H. Friend, R. F. Frindt, A. J. Grant, A. D. Yoffe, and D. Jerome, "Electrical conductivity and charge density wave formation in 4Hb TaS2 under pressure," *J. Phys. C Solid State Phys.*, vol. 10, no. 7, pp. 1013–1025, 1977.

[128] S. F. Meyer, *et al.*, "Properties of intercalated 2H-NbSe 2 , 4Hb-TaS 2 , and 1T-TaS 2," *J. Chem. Phys.*, vol. 62, no. 11, pp. 4411–4419, 1975.

[129] O. Ivashko *et al.*, "Charge-stripe order and superconductivity in Ir1-xPtxTe2," *Sci. Rep.*, vol. 7, no. 1, 2017.

[130] W. J. Wattamaniuk, J. P. Tidman, and R. F. Frindt, "Tunneling Conductivity in 4Hb-TaS2," *Phys. Rev. Lett.*, vol. 35, no. 1, pp. 62–65, Jul. 1975.

[131] H. Takatsu *et al.*, "Extremely large magnetoresistance in the nonmagnetic metal PdCoO2," *Phys. Rev.*

Lett., vol. 111, no. 5, pp. 1–5, 2013.

[132] S. Ghannadzadeh *et al.*, "Simultaneous loss of interlayer coherence and long-range magnetism in quasi-two-dimensional PdCrO 2," *Nat. Commun.*, vol. 8, pp. 6–11, 2017.

[133] C. Putzke *et al.*, "h/e Oscillations in Interlayer Transport of Delafossites," Feb. 2019.

[134] R. Schöllhorn, "Intercalation chemistry," *Phys. B+C*, vol. 99, no. 1–4, pp. 89–99, 1980.

[135] A. Lerf, "Storylines in intercalation chemistry," *Dalt. Trans.*, vol. 43, no. 27, pp. 10276–10291, 2014.

[136] H. Wang, H. Yuan, S. Sae Hong, Y. Li, and Y. Cui, "Physical and chemical tuning of two-dimensional transition metal dichalcogenides," *Chem. Soc. Rev.*, vol. 44, no. 9, pp. 2664–2680, 2015.

[137] S. Yamanaka, "Intercalation and superconductivity in ternary layer structured metal nitride halides (MNX: M = Ti, Zr, Hf; X = Cl, Br, I)," *J. Mater. Chem.*, vol. 20, no. 15, pp. 2922–2933, 2010.

[138] K. Takada, *et al.*, "A new superconducting phase of sodium cobalt oxide," *Adv. Mater.*, vol. 16, no. 21, pp. 1901–1905, Nov. 2004.

[139] S. S. Parkin and R. H. Friend, "3d transition-metal intercalates of the niobium and tantalum dichalcogenides ii. Transport properties," *Philos. Mag. B Phys. Condens. Matter; Stat. Mech. Electron. Opt. Magn. Prop.*, vol. 41, no. 1, pp. 95–112, 1980.

[140] Y. Jung, Y. Zhou, and J. J. Cha, "Intercalation in two-dimensional transition metal chalcogenides," *Inorg. Chem. Front.*, vol. 3, no. 4, pp. 452–463, Apr. 2016.

[141] S. F. Meyer, R. E. Howard, G. R. Stewart, J. V Acrivos, and T. H. Geballe, "Properties of intercalated 2H-NbSe 2 , 4Hb-TaS 2 , and 1T-TaS 2," *J. Chem. Phys.*, vol. 62, no. 11, pp. 4411–4419, 1975.

[142] M. B. Dines, "Intercalation of Metallocenes in the Layered Transition-Metal Dichalcogenides," *Science (80-.).*, vol. 188, no. 4194, 1975.

[143] E. W. Scheidt *et al.*, "On the nature of superconductivity in the anisotropic dichalcogenide NbSe2{CoCp2}x," *J. Phys. Condens. Matter*, vol. 27, no. 15, 2015.

[144] Y. Togawa *et al.*, "Chiral magnetic soliton lattice on a chiral helimagnet," *Phys. Rev. Lett.*, vol. 108, no. 10, 2012.

[145] Y. Togawa *et al.*, "Interlayer magnetoresistance due to chiral soliton lattice formation in hexagonal chiral magnet CrNb3S6," *Phys. Rev. Lett.*, vol. 111, no. 19, 2013.

[146] S. S. P. Parkin, E. A. Marseglia, and P. J. Brown, "Magnetic structure of Co 1/3 NbS 2 and Co 1/3 TaS 2," *J. Phys. C Solid State Phys.*, vol. 16, no. 14, pp. 2765–2778, May 1983.

[147] L. Corliss, N. Elliott, and J. Hastings, "Magnetic structures of the polymorphic forms of manganous sulfide," *Phys. Rev.*, vol. 104, no. 4, pp. 924–928, 1956.

[148] N. J. Ghimire, A. S. Botana, J. S. Jiang, J. Zhang, Y. S. Chen, and J. F. Mitchell, "Large anomalous Hall effect in the chiral-lattice antiferromagnet CoNb 3 S 6," *Nat. Commun.*, vol. 9, no. 1, 2018.

[149] M. Leroux, "Supraconductivité, Onde de Densité de Charge et Phonons Mous dans les dichalcogénures 2H-NbSe2 et 2H-NbS2, et le composé intermétallique Lu5Ir4Si10," Université de Grenoble, 2012.

[150] E. Martino *et al.*, "Sr 2 Pt 8-x As: A layered incommensurately modulated metal with saturated resistivity," *IUCrJ*, vol. 5, pp. 470–477, 2018.

[151] G. Binasch, P. Grünberg, F. Saurenbach, and W. Zinn, "Enhanced magnetoresistance in layered

magnetic structures with antiferromagnetic interlayer exchange," *Phys. Rev. B*, vol. 39, no. 7, pp. 4828–4830, 1989.

[152] N. L. Nair, E. Maniv, C. John, S. Doyle, J. Orenstein, and J. G. Analytis, "Electrical switching in a magnetically intercalated transition metal dichalcogenide," *Nature Materials*. 2019.

[153] N. Barišić *et al.*, "High-pressure study of transport properties in Co0.33NbS 2," *Phys. Rev. B - Condens. Matter Mater. Phys.*, vol. 84, no. 7, p. 75157, 2011.

[154] J. Melngailis, "Focused ion beam technology and applications," *J. Vac. Sci. Technol. B Microelectron. Process. Phenom.*, vol. 5, p. 469, 1987.

[155] P. J. W. Moll, "Focused Ion Beam Microstructuring of Quantum Matter," *Annu. Rev. Condens. Matter Phys*, vol. 9, pp. 147–162, 2018.

[156] A. Rigort and J. M. Plitzko, "Cryo-focused-ion-beam applications in structural biology," *Archives of Biochemistry and Biophysics*, vol. 581. Academic Press Inc., pp. 122–130, 01-Sep-2015.

[157] L. A. Giannuzzi and F. A. Stevie, "A review of focused ion beam milling techniques for TEM specimen preparation," *Micron*, vol. 30, no. 3, pp. 197–204, Jun. 1999.

[158] N. I. Kato, "Reducing focused ion beam damage to transmission electron microscopy samples," *Journal of Electron Microscopy*, vol. 53, no. 5. pp. 451–458, 2004.

[159] "Crystal Mounts and Loops | MiTeGen." [Online]. Available: https://www.mitegen.com/product/loops/. [Accessed: 22-Mar-2020].

[160] J. F. Knott, "STRENGTH AND TOUGHNESS OF STEELS.," 1982, pp. 181–198.

[161] M. D. Bachmann *et al.*, "Inducing superconductivity in Weyl semimetal microstructures by selective ion sputtering," *Sci. Adv.*, vol. 3, no. 5, p. e1602983, May 2017.

[162] S. N. Basahel, T. T. Ali, M. Mokhtar, and K. Narasimharao, "Influence of crystal structure of nanosized ZrO2 on photocatalytic degradation of methyl orange," *Nanoscale Res. Lett.*, vol. 10, no. 1, pp. 1–13, Feb. 2015.

[163] M. Nicklas, "Pressure Probes," in *Strongly correlated systems Experimental Techniques*, Springer, Berlin, Heidelberg, 2015, pp. 173–204.

[164] "Products | C&T Factory co.,Ltd." [Online]. Available: https://www.ctfactory.co.jp/product/. [Accessed: 22-Mar-2020].

[165] A. Eiling and J. S. Schilling, "Pressure and temperature dependence of electrical resistivity of Pb and Sn from 1-300K and 0-10 GPa-use as continuous resistive pressure monitor accurate over wide temperature range; Superconductivity under pressure in Pb, Sn and in," *J. Phys. F Met. Phys.*, vol. 11, no. 3, pp. 623–639, 1981.

[166] M. S. Torikachvili, S. K. Kim, E. Colombier, S. L. Bud'Ko, and P. C. Canfield, "Solidification and loss of hydrostaticity in liquid media used for pressure measurements," *Rev. Sci. Instrum.*, vol. 86, no. 12, p. 123904, Dec. 2015.

[167] E. Selvi, Y. Ma, R. Aksoy, A. Ertas, and A. White, "High pressure X-ray diffraction study of tungsten disulfide," *J. Phys. Chem. Solids*, vol. 67, no. 9–10, pp. 2183–2186, 2006.

[168] R. Aksoy, Y. Ma, E. Selvi, M. C. Chyu, A. Ertas, and A. White, "X-ray diffraction study of molybdenum disulfide to 38.8 GPa," *J. Phys. Chem. Solids*, vol. 67, no. 9–10, pp. 1914–1917, 2006.

[169] E. Selvi, R. Aksoy, R. Knudson, and Y. Ma, "High-pressure X-ray diffraction study of tungsten diselenide," *J. Phys. Chem. Solids*, vol. 69, no. 9, pp. 2311–2314, Sep. 2008.

List of Figures

Curriculum Vitae

Edoardo Martino

LinkedIn linkedin.com/in/-edoardo-martino-/
Skype: edoardomartino91

Rue pré-du-marché 23, CH-1004, Lausanne
edoardo.martino91@gmail.com
+41 78 829 18 63

Key skills:

Material engineer, condensed matter physicist and technological innovation enthusiast.
Experienced in the synthesis, understanding and applications of complex materials.
Passionate public speaker, scientific writer. Active in science outreach projects.

Research experiences

Research assistant
From Mar 2016
École polytechnique fédérale de Lausanne, Lausanne, Switzerland
Study of electronic and optical properties of 2D-materials

Visiting
Sept 2018
Brookhaven National Laboratory, Upton (NY), USA
Optical spectroscopy on High Temperature Superconductors and High-Entropy alloys

Internship
Mar 2015 - Aug 2015
École polytechnique fédérale de Lausanne, Lausanne, Switzerland
Study of transport coefficients in High Temperature Superconductor Bi-2212

Education

PhD in Physics
Mar 2016 — May 2020
École polytechnique fédérale de Lausanne (EPFL)
Laboratory Physics of Complex Matter—Light Fermions Spectroscopy group

Master
Oct 2013 - Dec 2015
Alta Scuola Politecnica
Managment of technological innovation

MSc
Oct 2013 - Sep 2015
Politecnico di Milano and Politecnico di Torino (double degree)
Materials Engineering and Nanotechnology

Exchange student
Sep 2014 - Jan 2015
Eidgenössische Technische Hochschule Zürich (ETH)
Exchange student in the Materials Science department

BSc
Oct 2010 - Jul 2013
Politecnico di Milano
Materials Engineering and Nanotechnology

Visiting student
Nov 2012
ParisTech Ecole des Ponts
Quantum mecchanics and Deterministic chaos

Professional Expertise

Software	Programming: Matlab, Python Automation and control: LabView Finite element simulation: COMSOL Microsoft Office suite, OriginLab, Vector graphics (Inkscape).
Hardware	Design, assembly and automation of experimental set-up Basic electronic and mechanical workshop skills
Transversal skills	Trained for public speaking (courses at EPFL) Problem solving under strict time/resources constrains Engaged in science communication via social media.
Experimental techniques	Electronic, Magnetic and thermodynamic characterization Optical spectroscopy, Raman scattering, X-ray diffraction Scanning electron microscopy (SEM) Focused ion beam (FIB) microfabrication Cryogenics - Measurements under extreme conditions (Low temperature, High pressure, High magnetic field)
Business/Management	**Degree:** Management of Technological Innovation (PoliMi, PoliTo) **Course:** Management of Innovation and Technology Transfer (EPFL) Intellectual property strategy

Languages

Italian	Mother tongue
English	Proficient user (C1 Level)
French	Intermediate user (B1 Level)

Honors and Awards

2019 Award: Outstanding teaching assistant, EPFL Department of Physics

2019 Selected for the 69th Lindau Nobel Laureate Meeting

2015 Scholarship: for master thesis abroad from Politecnico di Milano

2011 Scholarship: “Luigi and Wanda Amerio” Politecnico di Milano

2009 Award: “Darwin 2009” Molecular Biology department University of Milan.

Scientific talks (in bold are invited contributions)

2020
- **Seminar, Department of Physics Columbia University, New York, USA**
- **Seminar, Brookhaven National Laboratory, New York, USA**
- **Seminar, Energy department Politecnico di Milano, Milan, Italy**

2019
- E-MRS Spring Meeting, Nice, France
- Condensed Matter Workshop, Budapest University, Hungary
- CA2D, workshop on two-dimensional materials, Naples, Italy
- **Seminar, Physics department Universita la Sapienza, Rome, Italy**

2018
- Manep Workshop, Les Diablerets, Switzerland
- European Crystallography Metting (ECM31), Oviedo, Spain
- From Solid State to Biophysics IX, Cavtat, Croatia
- **Seminar, Synchrotron Soleil, Paris, France**
- AMBER-EPFL Joint workshop, Trinity College, Ireland

2017
- Swiss Physical Society (SPS) Meeting, Geneva, Switzerland

2016
- Swiss-Hungarian workshop, Lausanne, Switzerland

List of publications

- L. Martini, M. Bocchi, G. Angeli, M. Ascade, V. Rossi, A. Valzasina, C. Ravetta, S. Fratti, and **E. Martino**. 2015. "Live Grid Field-Testing Final Results of the First Italian Superconducting Fault Current Limiter and Severe 3-Phase Fault Experience." *IEEE Transactions on Applied Superconductivity* 25(3).
- O. Ivashko, L. Yang, D. Destraz, **E. Martino**, Y. Chen, C. Y. Guo, H. Q. Yuan, A. Pisoni, P. Matus, S. Pyon, K. Kudo, M. Nohara, L. Forró, H. M. Rønnow, M. Hücker, M. V. Zimmermann, and J. Chang. 2017. "Charge-Stripe Order and Superconductivity in Ir1-xPtxTe2." *Scientific Reports* 7(1).
- Crassee, **E. Martino**, C. C. Homes, O. Caha, J. Novák, P. Tückmantel, M. Hakl, A. Nateprov, E. Arushanov, Q. D. Gibson, R. J. Cava, S. M. Koohpayeh, K. E. Arpino, T. M. McQueen, M. Orlita, and A. Akrap. 2018. "Nonuniform Carrier Density in Cd3As2 Evidenced by Optical Spectroscopy." *Physical Review B* 97(12).
- **E. Martino**, A. Arakcheeva, G. Autès, A. Pisoni, M. D. Bachmann, K. A. Modic, T. Helm, O. V. Yazyev, P. J. W. Moll, L. Forró, and S. Katrych. 2018. "Sr2Pt8-XAs: A Layered Incommensurately Modulated Metal with Saturated Resistivity." *IUCrJ* 5.
- **E. Martino**, M. Bocchi, G. Angeli, M. Ascade, V. Rossi, A. Valzasina, A. Li Bassi, C. S. Casari, and L. Martini. 2018. "Assembly and Soldering Procedure of Nonstabilized YBCO Coils for 1000 A SFCL." *IEEE Transactions on Applied Superconductivity* 28(1).
- **E. Martino**, I. Crassee, G. Eguchi, D. Santos-Cottin, R. D. Zhong, G. D. Gu, H. Berger, Z. Rukelj, M. Orlita, C. C. Homes, and A. Akrap. 2019. "Two-Dimensional Conical Dispersion in ZrTe5 Evidenced by Optical Spectroscopy." *Physical Review Letters* 122(21).
- J. Hu, M. Caputo, E. B. Guedes, S. Tu, **E. Martino**, A. Magrez, H. Berger, J. H. Dil, H. Yu, and J. P. Ansermet. 2019. "Large Magnetothermopower and Anomalous Nernst Effect in HfTe5." *Physical Review B* 100(11).
- **E. Martino**, M. D. Bachmann, L. Rossi, K. A. Modic, I. Zivkovic, H. M. Rønnow, P. J. W. Moll, A. Akrap, L. Forró, and S. Katrych. 2019. "Persistent Antiferromagnetic Order in Heavily Overdoped Ca1-XLaxFeAs2." *Journal of Physics Condensed Matter* 31(48).
- D. Santos-Cottin, M. Padlewski, **E. Martino**, S. Ben David, F. Le Mardelé, F. Capitani, F. Borondics, M. D. Bachmann, C. Putzke, P. J. W. Moll, R. D. Zhong, G. D. Gu, H. Berger, M. Orlita, C. C. Homes, Z. Rukelj, and A. Akrap. 2020. " Probing Intraband Excitations in ZrTe 5 : A High-Pressure Infrared and Transport Study ." Physical Review B 101(12):1–10.
- Santos-Cottin, D., **E. Martino**, F. Le Mardelé, C. Witteveen, F. O. Von Rohr, C. C. Homes, Z. Rukelj, and A. Akrap. 2020. "Low-Energy Excitations in Type-II Weyl Semimetal Td- MoTe2 Evidenced through Optical Conductivity." *Physical Review Materials* 4(2).
- G. Tenasini, **E. Martino**, N. Ubrig, N. J. Ghimire, H. Berger, O. Zaharko, F. Wu, J. F. Mitchell, I. Martin, L. Forró, and A. F. Morpurgo 2020. "Giant anomalous Hall effect in quasi-two-dimensional layered antiferromagnet Co1/3NbS2". *Physical Review Research 2(2), 023051.*
- **E. Martino**, A. Pisoni, L. Ćirić, A. Arakcheeva, H. Berger, A. Akrap, C. Putzke, P. J. W. Moll, I. Batistić, E. Tutiš, L. Forró, K. Semeniuk. 2020. "Preferential out-of-plane conduction and quasi-one-dimensional electronic states in layered van der Waals material 1T-TaS2". *npj 2D materials and applications*, 4(7)
- **E. Martino**, D. Santos-Cottin, F. Le Mardelé, K. Semeniuk, F. Capitani, L. Forro, H. Berger, A. Akrap. 2020. "Strain tuned structural phase transition and optical switching in 1T-ZrS2 and 1T-ZrSe2". arXiv:2006.07141
- F. Le Mardelé, D. Santos-Cottin, **E. Martino**, K. Semeniuk, S. Ben David, F. Orbanic, M. Novak, Z. Rukelj, C. C. Homes, A. Akrap. 2020. "Optical conductivity of the type-II Weyl semimetal TaIrTe4". arXiv:2004.00147